博 士 学 位 論 文
Doctoral Thesis

論文題目

Thesis Title

Numerical Study of Undrained Cyclic Shear and Reconsolidation Behaviors of Granular Materials by 3D DEM

東 北 大 学 大 学 院 工 学 研 究 科

Graduate School of Engineering,

TOHOKU UNIVERSITY

専攻/Department: 土木工学専攻

学籍番号/ ID No: C0TD6006

氏 名 /Name: Mingjin Jiang

NUMERICAL STUDY OF UNDRAINED CYCLIC SHEAR AND RECONSOLIDATION BEHAVIORS OF GRANULAR MATERIALS BY 3D DEM

ABSTRACT: Earthquakes are one of the most destructive natural disasters, posing serious threats to human society. In addition to direct damage to building structures, the propagation of seismic waves may also affect the strength of the ground soil through undrained cyclic shear, thereby causing indirect damage to buildings and infrastructures. Specifically, when subjected to undrained cyclic loadings during an earthquake, saturated loose and medium-dense sand may gradually lose strength and then liquefy.

The common method for studying the seismic response of soil is laboratory element tests. However, most studies were conducted under unidirectional cyclic loading conditions, yet it had been recognized that the ground motion during an earthquake is multidirectional. Surface waves, including Love waves and Rayleigh waves, may predominate the ground surface motions during strong earthquakes and induce complicated multidirectional deformation. The relationship between soil liquefaction and surface waves had been confirmed. Nevertheless, because of the limitation of the loading pattern and observing method, the liquefaction behavior of granular materials under the propagation of surface waves has not been well understood in previous studies based on the physical element experiment and continuum modeling scheme. Besides the type of seismic waves, the strain level also has a significant influence on the seismic response of granular materials. However, most relevant studies were performed within the 20% strain level due to the limitation of the experimental apparatus. The response of granular materials subjected to undrained cyclic shear at a larger strain amplitude is still unknown. Except for the reduction in soil strength during undrained cyclic loadings, the settlement of ground after an earthquake may also cause severe damage to buildings and infrastructures. The volumetric strain during the resedimentation process accounts for a large part of the total volumetric strain during post-liquefaction reconsolidation. Whereas due to limitations on the accuracy of stress measurements near zero effective stress in physical testing, the nonlinear relationship between the void ratio and effective stress during the reconsolidation process is yet to be clarified.

To circumvent the limitation of traditional laboratory element tests and continuum modeling schemes, the above problems were qualitatively investigated using the three-dimensional discrete element method (DEM). In addition to not being limited by loading conditions and measurement accuracy, DEM also provides a convenient way to observe the response of granular assemblies from the particle scale. In this research, analysis from both macroscopic and microscopic scales was conducted to reveal the mechanism behind the response of granular materials.

To elucidate the behavior of granular materials under surface-wave deformation modes, a series of numerical tests were performed by 3D DEM under horizontally polarized shear- (SH-), Love-, and Rayleigh-wave strain conditions, where the equations governing the strain–time relationships were derived from elastic wave theory under the assumption of constant volume. The macroscopic and microscopic response of K_0-consolidated granular assemblies under Love- and Rayleigh-wave strain conditions was compared with that under SH-wave strain conditions. The results show that at the same strain level, the surface-wave strain condition, especially the Rayleigh-wave strain condition would generally make granular materials more vulnerable to liquefaction. Specifically, Rayleigh-wave strain conditions are the combination of pure shear mode and simple shear modes, while SH- and Love-wave strain conditions are simple shear modes and a combination of simple shear modes, respectively. Because the elongation direction of the particle skeleton was vertical in the K_0-consolidated specimen. The compression direction in pure shear mode was either consistent with or perpendicular to the structure elongation direction, whereas the deformation direction in simple shear mode deviated from the structure

elongation direction by an angle that varies with time. The different deformation modes resulted in different responses. The positive dilatancy behaviors under Rayleigh-wave strain conditions were more sensitive to the strain level than that in the SH- and Love-wave strain conditions. In addition, the increase in fabric anisotropy during cyclic loadings was especially significant under Rayleigh-wave strain conditions than under SH- and Love-wave strain conditions. The magnitude of the fraction of sliding contacts and fluctuation of coordination number under Rayleigh-wave strain conditions was also larger than that under other strain conditions. However, the initial liquefaction happened instantaneously when the coordination number approached approximately 2, independent of the loading path.

The undrained cyclic shear behavior of liquefiable granular materials at extremely large shear strain amplitude (> 20%) was studied by performing a series of 3D DEM simulations. Specifically, the undrained monotonic simple shear test with strain to 100% and undrained cyclic simple shear tests with strain amplitudes from 0.1% to 100% were conducted on a K_0-consolidated granular assembly. The results suggest that in undrained cyclic shear with a small strain amplitude (≤ 1%), the medium-dense granular assembly gradually lost its stiffness and liquefied eventually. When the shear strain amplitude became larger (≤ 10%), the shear stiffness recovered after the initial liquefaction as the shear strain application was continued. However, the shear stiffness recovery vanished, and the granular assembly completely liquefied as the undrained cyclic shear continued. Especially, the shear band formed in the granular assembly when the shear strain exceeded a certain value (about 40% in this study) during both undrained monotonic simple shear and undrained cyclic simple shear. The fluid-like state after initial liquefaction would only exist in a small shear strain range (about 20% in this study) after the strain loading direction reversion. After the shear band was formed, the granular structure outside the shear band become stable (the fraction of sliding contacts tended to be zero and the coordination number became constant), and the granular assembly reached a stable state of stress. In addition, the stable state of stress in undrained monotonic shear and undrained cyclic shear was different because of the different overall uniformities of the granular assembly.

The volumetric strain during the reconsolidation process that began at different residual effective stress states was investigated based on 3D DEM simulations. A monodisperse specimen and a polydisperse specimen (with Toyoura size distribution) were used in this study. The results indicated that the smaller the residual vertical effective stress, the larger the change in void ratio during the reconsolidation process. Especially, the post-liquefaction reconsolidation could be categorized into a liquefied and a solidified portion. In the liquefied portion, the void ratio decreased without a continuous increase in the effective stress. Furthermore, the volumetric strain during the liquefied portion accounts for a large proportion of the total volumetric strain during the reconsolidation process. In addition, the volumetric strain of the polydisperse specimen was larger than that of the monodisperse specimen during the liquefied portion and similar to that of the monodisperse specimen during the solidified portion. Finally, a larger change in pore uniformity was generally associated with a larger volumetric strain during the reconsolidation process.

ACKNOWLEDGMENTS

I am extremely grateful to my esteemed supervisors—Dr. Motoki Kazama, and Dr. Akiyoshi Kamura for their invaluable supervision, support, and tutelage during the course of my Ph.D. degree. I also thank them for their tolerance and understanding of the mistakes I have made in my work. Besides, I must express my gratitude to Dr. Yuki Yamakawa and Dr. Shotaro Yamada for their valuable comments and suggestions on my dissertation. Additionally, I would like to express my thanks to Mrs. Hiroko Onoda for her treasured support in my daily life and work. My gratitude extends to the WISE Program for sustainability in the Dynamic Earth (SyDE program) for the funding opportunity to undertake my studies at the Department of Civil and Environmental Engineering, Tohoku University. I am also grateful to Dr. Shuji Moriguchi, Dr. Yuichi Ono, Dr. Yuta Hara, Ms. Sachiko Yamagishi, and Ms. Takako Kasai for their help in the SyDE program. I would like to thank my friends and lab mates for the cherished time spent together in the lab. My appreciation also goes out to my family and friends in China for their encouragement and support throughout my studies. At last, I would like to express my heartfelt gratitude to my girlfriend—Aimin Song, who accompany and give me the courage and power to challenge the difficulties in my study and life.

Mingjin Jiang

Table of Contents

List of Figures

List of Tables

CHAPTER 1 INTRODUCTION

1.1. Background of the research

Earthquakes had brought immeasurable losses to human beings in the past and are still one of the natural disasters that pose serious threats to human society. Besides the direct damage to the building structure, the earthquake shaking may cause indirect damage to buildings and infrastructures by affecting the strength of the ground soil.

During the undrained cyclic loading caused by the earthquake, saturated loose and medium-dense sandy soil substantially loses strength and stiffness. The pore water gradually withstands the external loads initially carried by the soil skeleton. It is embodied in the decrease of effective stress and increase of excess pore water pressure on the

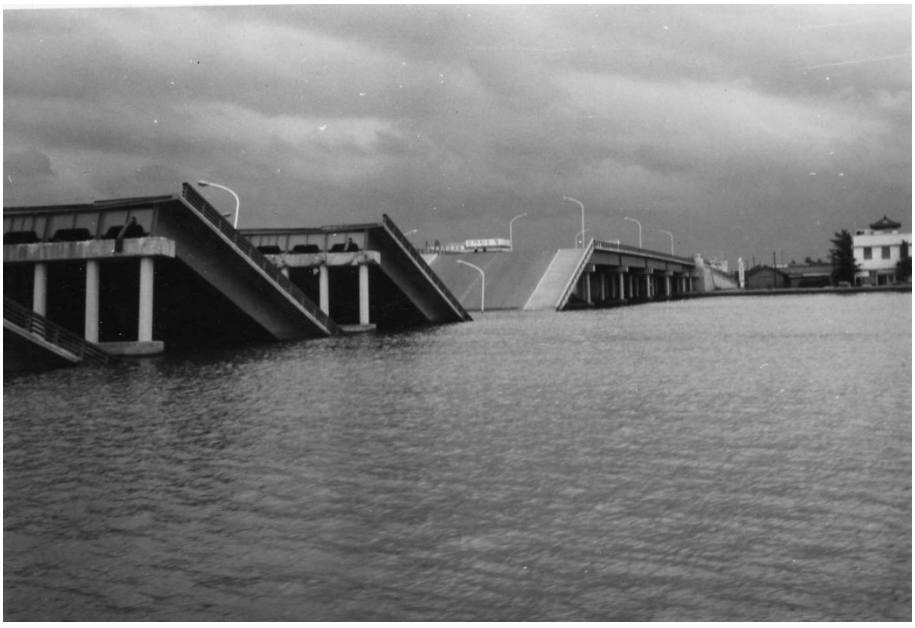

Fig. 1.1. Collapse of Showa Bridge due to liquefaction after the 1964 Niigata earthquake (Photo: Photographs and motion picture of the Niigata city immediately after the earthquake in 1964).

macroscale. As the effective stress decrease to zero, the soil skeleton cannot bear any load or deformation and behaves like a liquid, which is defined as soil liquefaction. The dramatic loss of strength in saturated sandy soil may cause the collapse or subsidence of buildings, the collapse of bridges (Fig. 1.1), lateral movement of the ground and road surfaces, etc.

During the 1964 Niigata earthquake and the 1964 Alaska earthquake, soil liquefaction occurred and caused severe and widespread damage, which attracted the attention of engineers and researchers. In recent decades, soil liquefaction has remained one of the most serious secondary disasters during earthquakes, including the 1995 Kobe earthquake (Tokimatsu and Asaka, 1998), the 2010 Chile earthquake (Verdugo and González, 2015), the 2011 off the Pacific Coast of Tohoku Earthquake (Kazama and Noda, 2012), and the 2018 Palu earthquake (Jalil et al., 2021). In the early days, the main concern of researchers was the prediction of sand liquefaction, that is, whether the site could liquefy. In addition, the countermeasure against soil liquefaction was also one of the main research directions. However, after the 1995 Kobe earthquake, it had been recognized that the cost of liquefaction countermeasures might be huge in some situations, and the concept of performance-based design (PBD) was put forward. In this approach, damage to the structure is permitted as long as the required performance of the structure is exhibited. Therefore, the evaluation of the ductility and the toughness of the soil to resist liquefaction (Kazama et al., 2000) and the prediction of the response of soil after liquefaction became important.

Most efforts to understand the seismic response of granular materials have been made through laboratory element tests (Seed et al., 1975; Yamamuro and Covert, 2001;

Yang and Sze, 2011; Chiaro et al., 2013; Kumar et al., 2020). Due to the limitation of loading patterns, it was difficult to reproduce some of the complex stress–strain conditions that may occur during real earthquakes. In the meantime, it is also difficult to observe the inside of the specimen in laboratory elemental tests, which makes it hard to reveal the intrinsic mechanism behind the experimental phenomenon. To overcome the shortcomings of traditional laboratory element tests, the discrete element method (DEM) proposed by Cundall and Strack (1979) has been widely used in the analysis of geotechnical problems (Iwashita and Oda 1998; Nakase et al. 1999; Morimoto et al. 2001; Sitharam and Dinesh 2003; Kazama et al. 2006; O'Sullivan et al. 2008; Katagiri et al. 2010; O'Sullivan 2011; Manne and Satyam 2015; Jiang et al. 2019). DEM provides a convenient way to study the behavior of granular material from both macroscopic and microscopic scales. It takes the materials as individual rigid bodies interacting through contact laws governed by Newton’s laws of motion. Besides the ability to look inside the material and obtain information on particle scale, DEM also provides an approach to reproducing complex multidirectional stress–strain loading conditions, e.g., Shamy and Zeghal (2006) evaluated the effects of multiple direction excitations on granular deposits based on an input kinetic energy using the 3D DEM; Wei et al. (2020) investigated the microstructure evolution of granular materials under multidirectional loading conditions with unidirectional, oval, circular, and figure-8 loading paths using the 3D DEM.

1.2. Statement of the problem

1.2.1. Surface waves

In the study of liquefaction, although it has long been recognized that the motion of the ground surface in an earthquake is multidirectional, most laboratory element tests were conducted under unidirectional cyclic loading conditions because of the difficulty in developing the corresponding test apparatus. Pyke et al. (1975) were the first to investigate problems associated with multidirectional loading conditions. They conducted several series of shaking table tests of dry sand in one, two, and three dimensions. Their results showed that the settlement might be significantly greater under multidirectional shaking compared with under unidirectional shaking, which implied that saturated sands under multidirectional loading conditions would be affected easily by liquefaction. Seed et al. (1975) quantitatively analyzed the effect of multidirectional shaking on the shear stress causing liquefaction by combining the results of the shaking table and cyclic simple shear tests on dry sand. The results indicated that the shear stress amplitude causing liquefaction under multidirectional shaking was less than that under unidirectional shaking, and that the multidirectional shaking effect could be considered equivalent to a 10% reduction in the shear stress amplitude. In subsequent studies, it was discovered that granular materials under multidirectional shearing were more vulnerable to liquefaction than those under unidirectional shearing, and that the multidirectional shearing effect varied by the loading path (Seed et al. 1978; Ishihara and Yamazaki 1980; Tokimatsu and Yoshimi 1982; Su and Li 2008; Nhan et al. 2017). However, previous experimental or DEM studies associated with multidirectional loading conditions still assumed that liquefaction was caused by the upward propagation of shear waves, multidirectional

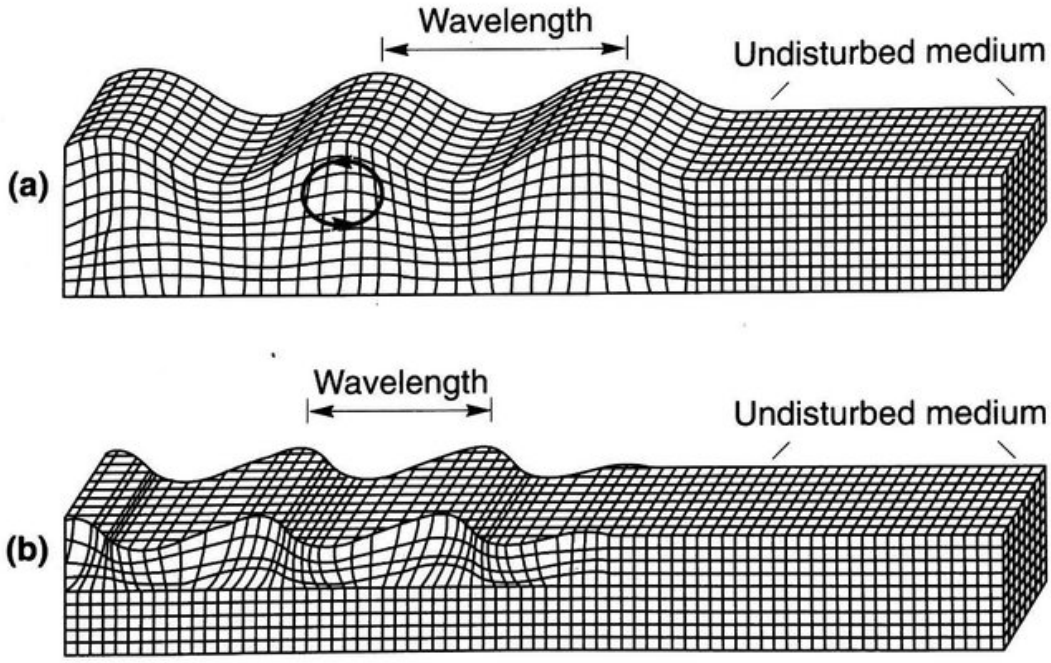

Fig. 1.2. Illustration of motion due to surface waves: (a) Rayleigh wave and (b) Love wave (after Bolt, 1993).

loadings were applied in the horizontal direction, and loading paths (e.g., alternate shear (Ishihara and Yamazaki, 1980) and figure-8 loading paths (Wei et al., 2020)) did not correspond to any realistic wave type.

Seismic waves can be divided into body waves and surface waves in terms of the spatial concentration of energy (Novotny, 1999). Body waves can propagate in the interior of a medium whereas surface waves are only concentrated along the surface of the medium. Body waves include longitudinal waves (P waves) and transverse waves (S waves), and surface waves can be further divided into Love waves and Rayleigh waves. Rayleigh waves can propagate near the surface of a homogeneous half-space while Love waves cannot. Love waves can only propagate near the surface of a medium where the S-wave velocity generally increases with the distance from the surface (Novotny, 1999). The ground subject to surface waves will produce a complex deformation, as shown in

Fig. 1.2. Rayleigh waves are elliptically polarized in the vertical plane determined by the surface normal and the direction of propagation. Particle motions in Love waves are transverse and parallel to the surface (Novotny, 1999; Pujol, 2003).

Generally, the ground surface motion during an earthquake may be regarded as the combined result of the propagation of body waves and surface waves (Hall et al. 1977). Compared to body waves, surface waves usually have larger amplitudes and longer periods (Novotny, 1999). In some cases, strong ground surface motions can be predominated by surface waves (Trifunac, 1971; Hall et al., 1977). Some field and theoretical evidence demonstrated that surface waves might be one of the causes of soil liquefaction. Hall et al. (1977) used a shear wave model and a Rayleigh wave model to predict the liquefaction potential of an idealized, homogeneous, undamped half-space. They found that the liquefaction risk near the surface for the two models was the same, but it decreased much more rapidly with depth for the Rayleigh wave model. The depth range predicted by the Rayleigh wave model was more consistent with the observed liquefaction cases than that predicted by the shear wave model. Gazetas and Yegian (1979) compared the dynamic response of various soil deposits under the influence of Rayleigh waves to that under the influence of vertical shear waves. They suggested that liquefaction could occur under Rayleigh wave propagation, and its potential was different from that under shear wave propagation, owing to the difference in the particle motions and distributions of shear stress with depth. After analyzing aerial photographs of the 1976 Tangshan Earthquake liquefaction sites, Wang et al. (1983) suggested that some types of liquefaction trajectories were induced by surface waves, e.g., a network pattern was probably formed by the reflection of surface waves within a quasi-parabolic river bend. Sugano and Yanagisawa (1992) used two experimental apparatuses to investigate the

cyclic undrained shear behavior of sands under the influence of surface waves. One is a hollow cylinder torsional shear test apparatus for Rayleigh wave propagation condition, and another is a newly developed bi-axial shear apparatus for Love wave propagation condition. Their results indicated that Love wave propagations may contribute to liquefaction. Cui et al. (2004) pointed out that Rayleigh waves should be an essential cause of liquefaction in shallow saturated sandy deposits beyond the epicentral region based on some field evidence and a preliminary theoretical analysis. They also analyzed the effect of Rayleigh wave propagation on sand liquefaction by using single and two-phase medium models and argued that currently used evaluation methods may overestimate the safety to some degree. Holzer and Youd (2007) demonstrated that Love waves contributed a significant portion of excess pore-water pressure to the liquefied layer at the Wildlife Liquefaction Array in the 1987 Superstition Hills earthquake after investigating the recording of the earthquake. Nakai et al. (2016) conducted a series of 2D elastoplastic effective stress analyses considering the effect of irregularly shaped bedrock. They stated that in the 2011 earthquake off the Pacific Coast of Tohoku, surface waves induced by inclined bedrock enhanced the liquefaction damage of Urayasu city through the complex interference between the Rayleigh waves and body waves, which is known as the “edge effect”. Staroszczyk (2016) used the finite element method to simulate the liquefaction of saturated sands under the influence of Rayleigh waves within the framework of a compaction theory, and analyzed the evolution of the characteristics of Rayleigh waves during the liquefaction process.

In previous studies, direct links between the liquefaction problem and surface waves were established. However, in these studies, surface waves were not extracted individually, or true surface wave deformation modes were not used. In addition, they

lack microscopic-scale observations. Therefore, the liquefaction behavior of granular materials under surface wave propagations has not yet been well understood.

1.2.2. Extremely large shear strain amplitudes

Besides the loading path, it has been recognized that both the monotonic and cyclic shear behavior of soils is highly dependent on the strain level. In monotonic shear, the soil under a given effective confining stress will ultimately reach a critical state as the shear strain increases. The critical state of soil was initially defined by Roscoe et al. (1958) as the state that "soils continue to deform at constant stress and constant void ratio". The common definition of critical state was given based on the equation below:

$$q = Mp' \tag{1.1}$$

$$v = \Gamma - \lambda \ln(p') \tag{1.2}$$

where q is the deviator stress; M is a frictional constant; p' is the mean effective pressure; v is the specific volume defined as $v = 1 + e$ and e is void ratio; Γ is the specific volume intercept at unit pressure; λ are the compression index. The critical state arrives when q, p', v keep constant. Under the undrained condition, the critical state is reached when the pore pressure and the effective stress remain constant during continued deformation (Schofield and Wroth 1968). Granular materials suffering from monotonic shearing with a large shear strain had been widely studied under the framework of the critical state (e.g., Li and Dafalias, 2012; Perez et al., 2016; Nguyen et al., 2021).

In cyclic shear, as the cyclic shear strain amplitude increases, the behaviors of soil

change from elastic to elastoplastic (Vucetic, 1994; Ishihara, 1996). However, most of the related studies were conducted within 20% strain level due to the limitation of laboratory apparatus (Umar et al., 2019). Correspondingly, the response of liquefiable soils subjected to undrained cyclic shear at an extremely larger strain amplitude is still unknown.

1.2.3. Volumetric strain during reconsolidation

Except for the reduction in soil strength during undrained cyclic loadings, the settlement of ground after the undrained cyclic loading may also cause severe damage to buildings and infrastructures. It is primarily attributed to soil volume change as a result of the drainage of pore water (reconsolidation), accompanied by excess pore water pressure dissipation. In terms of performance-based design, the amount of volumetric strain during or after liquefaction must be accurately predicted such that necessary countermeasures can be implemented. The volume contraction characteristics of saturated sand have been investigated via various cyclic undrained tests, followed by drained reconsolidation. Lee and Albaisa (1974) discovered that the volumetric strain during reconsolidation was affected by the particle size, relative density, and excess pore water pressure after cyclic shear. Nagase and Ishihara (1988) and Shamoto et al. (1996) reported that the reconsolidation volumetric strain was significantly associated with the maximum shear strain during cyclic shear. Tokimatsu and Seed (1987) as well as Ishihara and Yoshimine (1992) proposed simplified prediction models for post-liquefaction settlement based on experiment results. Sento et al. (2004) discovered that the reconsolidation volumetric strain demonstrated a higher correlation with the accumulated shear strain than the maximum shear strain generated during cyclic shear. Uzuoka et al. (2010)

proposed a prediction model for liquefaction and post-liquefaction settlement based on the minimum effective stress. Zhou et al. (2014) discovered that the compression index during reconsolidation was 1.3–1.5 times as great as that during consolidation and proposed a model for post-liquefaction settlement estimation based on an assumed initial stress.

The reconsolidation process after liquefaction can be categorized into liquified and solidified portions (Florin and Ivanov, 1961). The liquified portion is known as resedimentation (Zhou et al., 2014). A consensus was achieved, i.e., the volume contraction in the liquefied portion occupies a significant proportion of the total volume change during post-liquefaction reconsolidation. Therefore, understanding the resedimentation process is vital to the prediction of the total volume strain. However, owing to the limited measurement range in experiments, typically 10^{-1}–10^{0} kPa, the nonlinear relationship between the void ratio and effective stress during the reconsolidation process is yet to be clarified.

1.3. Objectives of this research

To clarify the three topics mentioned above, which are hard to be investigated by the ordinary physical element test, three DEM studies were conducted in this research. The objective of the research includes:

a) Clarify the undrained cyclic response of granular materials under surface-wave strain conditions (the deformation mode of a wave): Compare the liquefaction resistance and response of granular materials under surface-wave strain conditions

to that under SH-wave strain conditions. Furthermore, analyze the mechanism behind the macroscopic response of granular material under different strain conditions from a microscopic scale.

b) Investigate the undrained cyclic shear behavior of granular material at extremely large shear strain amplitude (up to 100%): Study the failure of medium-dense granular material under the undrained condition (volume remains constant) in large shear strain. Analyze the responses of the medium-dense granular assembly under cyclic simple shear with large strain amplitudes and compared them to those under the monotonic shear and cyclic shear with small strain amplitudes. Furthermore, explain the phenomenon from the microscopic scale.

c) Elucidate the behavior of granular materials during the reconsolidation process, especially during the resedimentation process: Investigate the evolution of void ratio and corresponding microscopic parameters during the reconsolidation process after undrained cyclic simple shear.

1.4. Layout of this dissertation

The outline of this research is given in Fig. 1.3. Following this Chapter, the literature review was performed to learn the previous study on liquefaction issues and methods for evaluating liquefaction resistance. The micromechanics of granular materials was also introduced in the literature review.

In Chapter 3, a detailed introduction to the 3D DEM code used in this study was

done, including the basic principle, contact model, boundary condition, timestep, macro and micro quantities, constant volume method, and quasi-static condition.

In Chapter 4, equations governing the strain–time relationship of SH, Love, and Rayleigh waves were derived from elastic wave theory under the assumption of constant volume. Then, a series of undrained cyclic shear simulations under SH- and surface-wave strain conditions was performed. The response and liquefaction resistance of granular materials under surface-wave strain conditions were compared to that under SH-wave strain conditions. Furthermore, the mechanism behind the macroscopic response of granular material under different strain conditions was analyzed from a microscopic scale.

In Chapter 5, the undrained monotonic and cyclic simple shear simulations were performed to investigate the undrained response of granular materials under large shear strain amplitudes. The influence of shear strain amplitude and loading type on the failure of granular was highlighted.

In Chapter 6, the simulation of reconsolidation began at different residual effective stress levels was performed. Attention was paid to the change in the void ratio and corresponding microscopic parameters of specimens during reconsolidation.

Chapter 7 presents a summary of conclusions drawn from this research, and recommendations for future research are given afterward.

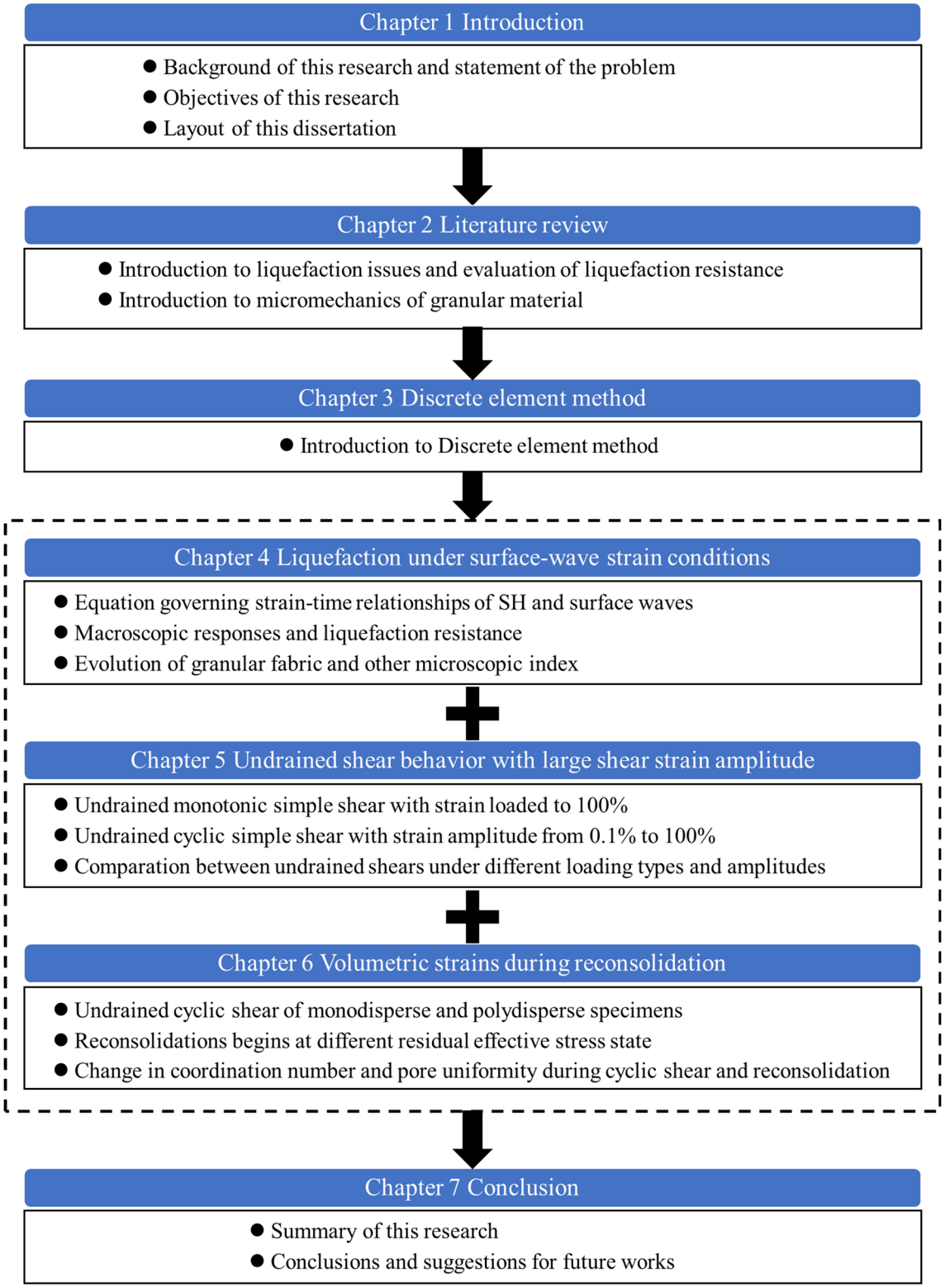

Fig. 1.3 Layout of this dissertation.

CHAPTER 2 LITERATURE REVIEW

2.1. Undrained cyclic shear behavior of granular materials

Granular materials subjected to undrained cyclic shear may undergo liquefaction. During the undrained cyclic loading, the mean effective stress decreases, and granular materials lose stiffness gradually. This state was called the *pre-liquefaction* phase. When the mean effective stress decreased to zero for the first time, the terminology—*initial liquefaction* was used to describe the state of granular materials. Depending on the behavior of granular material, liquefaction can be divided into *flow liquefaction* and *cyclic softening* during undrained cyclic loading. The assessment of liquefaction resistance is an indispensable part of engineering seismic design. Three general approaches, including the stress-based approach, strain-based approach, and energy-based approach had been used in evaluating the liquefaction resistance of soil in laboratory element tests.

2.1.1. Initial liquefaction and types of liquefaction failure

The oldest work on liquefaction was by Casagrande (1936). He pointed out that dense sand expands, and very loose sand reduces its volume during shearing tests, as shown in Fig. 2.1. In addition, the instability of saturated loose sand induced by a decrease of the effective stress and the shear strength was linked to the cyclic loading during an earthquake. He called the boundary between the case of volume decrease and increase the

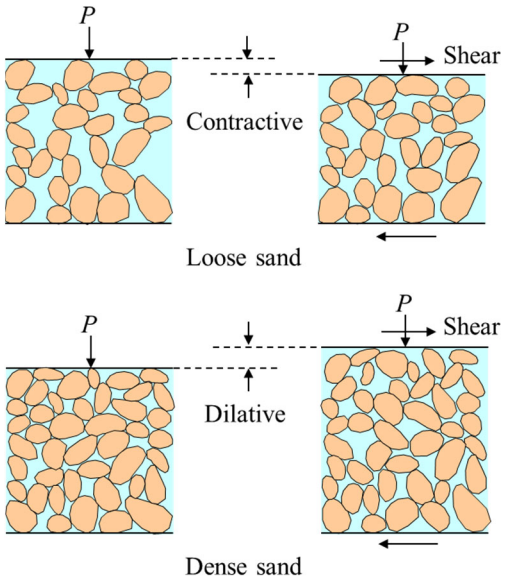

Fig. 2.1. Effects of shearing on the volume of soils.

critical density. If the density of sand is below the critical density and the voids in the sands are filled with water which cannot escape as quickly as the deformation is produced, the load on sand particles is transferred to the water during cyclic shear then the effective stress between sand particles decreases which impairs the stability of the sand mass. The description above was almost the same as the concept of liquefaction today.

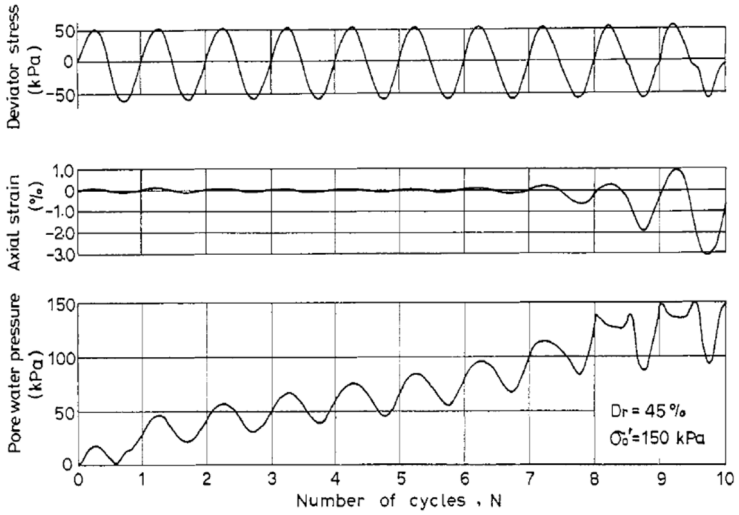

Fig. 2.2. Axial strain and pore water pressure build-up in the undrained cyclic triaxial test (after Ishihara, 1996).

Seed and Lee (1966) were the pioneers to summarize sand liquefaction systematically. In their research, isotropically consolidated saturated sands were applied repeated constant-amplitude cyclic deviatoric loads in a triaxial apparatus under undrained conditions. A typical result was shown in Fig. 2.2. It was observed that the axial strain and excess pore water pressure accumulated gradually during cyclic loading. Initial liquefaction refers to the first time that the excess pore water pressure equals the initial confining pressure. Based on experiment results, they summarized that the potential of liquefaction of saturated sand is determined by the void ratio, confining pressure, and magnitude of cyclic stress or strain.

Martin et al. (1975) developed a quantitative relationship between volume changes occurring during drained cyclic tests and the progressive increase of pore water pressure during undrained cyclic tests, which is schematically illustrated in Fig. 2.3. Point A is the initial state of the saturated sand specimen. During the drained cyclic simple shear test,

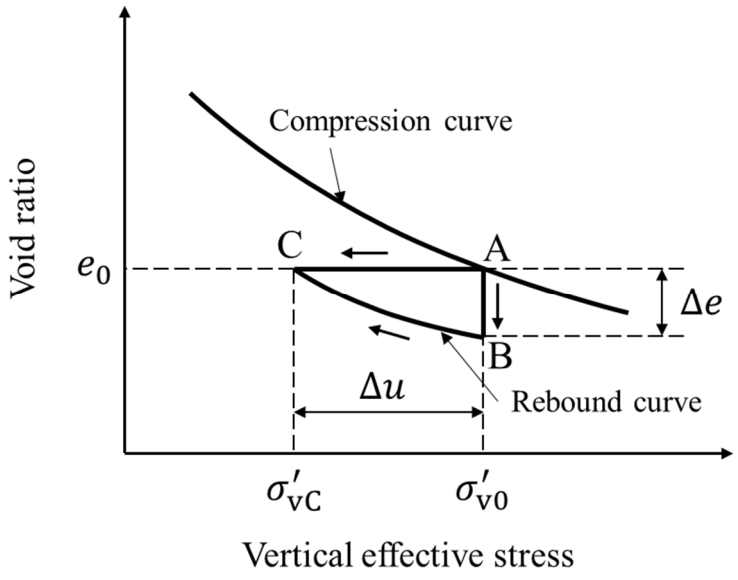

Fig. 2.3. Schematic diagram of the relationship between void ratio and vertical effective stress during initial consolidation, undrained cyclic shear loading, and reconsolidation.

since the vertical effective stress was kept constant, cyclic loading caused contraction of volume and manifested as the reduction in void ratio. This process can be represented by point A moving to point B in Fig. 2.3. During the undrained cyclic simple shear test, the volume of the sand specimen was kept constant (no change in void ratio) and cyclic loading caused an increase in the pore water pressure. This process can be represented by point A moving to point C. The volumetric contraction during drained cyclic loading can be counterbalanced by an elastic rebound of the soil skeleton due to a decrease in effective stress during undrained cyclic loading, their relationship can be represented by point B moving to point C. The use of this relationship enables the build-up of pore water pressure during cyclic loading to be computed theoretically using basic effective stress parameters of the sand. The initial liquefaction is the state where the effective stress reaches zero and the excess pore water pressure equals the initial vertical effective stress.

However, the effective stress near zero is hard to be controlled and measured in physical experiments. In some special conditions, e.g., multi-directional loading or uni-directional loading with initial shear stress higher than the applied cyclic shear stress, the excess pore water pressure is always less than the initial confining pressure (Boulanger et al, 1991). In addition, because of the measurement limitation, the specimen is assumed to be saturated when the B-value (the degree of saturation) is above 0.95, while in the case of a perfectly saturated specimen, the B-value should theoretically be 1.0. The imperfect saturation condition may also be a reason for the excess pore water pressure being always less than the initial effective confining pressure during undrained cyclic loading. Therefore, the Japanese Geotechnical Society (2013) defined the initial liquefaction as the state when excess pore water pressure builds up to 95% of the initial effective confining pressure (the effective stress is 5% of that in the initial state).

For silty sands, although the effective stress never becomes zero, it becomes close to zero and is accompanied by gradually increasing strain. In this state, the soil skeleton is considered to be destroyed. In such cases, the initial liquefaction criterion based on effective stress or excess pore water pressure is not applicable. New liquefaction criterions based on axial strain amplitude were put forward, e.g., Ishihara and Yamazaki (1980) suggested that the specimen experiencing 3% single amplitude axial strain for the first time is identified as initial liquefaction; Ishihara (1993) proposed that an axial strain of about 5% in double amplitude refers to the initial liquefaction state.

As stated above, liquefaction refers to the loss of strength in saturated, cohesionless soil or granular materials due to the build-up of pore water pressure during dynamic loadings (monotonic or cyclic). A definition of soil liquefaction is the transformation "from a solid state to a liquefied state as a consequence of increased pore pressure and reduced effective stress" (Definition of terms…, 1978). In other words, all the failure mechanisms of saturated soil resulting from the build-up of pore water pressure during undrained cyclic shear can be described by the term "liquefaction." However, depending on site and loading conditions, liquefied soils may experience liquid-like flow or limited soil deformation during undrained cyclic shear. Different types of post-liquefaction behavior will result in different kinds of damage; therefore, liquefaction should be carefully classified.

Liquefaction results from the volumetric contraction tendency of soil when subjected to shear stress/strain. The soil behavior during shear loading is highly reliant on the density of soil, as shown in Fig. 2.4. When loose, dry sands are sheared, the volume of the specimen tends to decrease. Therefore, when the loose sands are subjected to

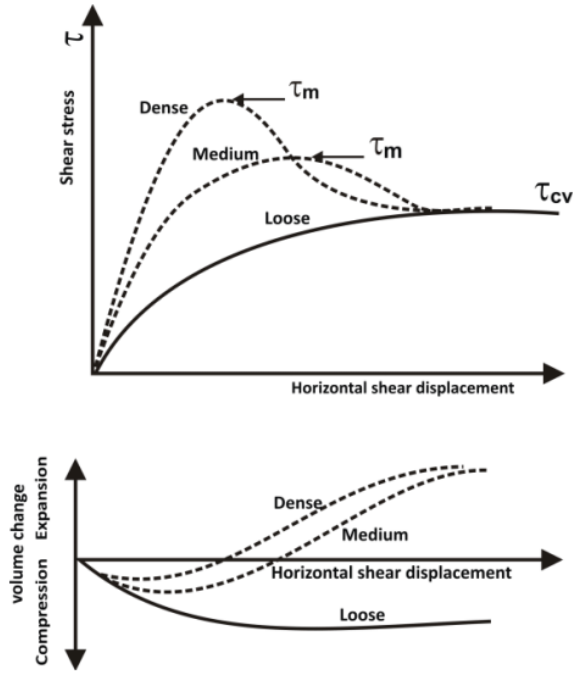

Fig. 2.4. Schematic diagram of the direct shear test result in loose, medium, and dense sands (after Das, 1983).

undrained cyclic shear, excess pore water pressure will built-up. When medium and dense, dry sands are sheared, the volume of the specimen may first decrease and then increase (sands first contract then dilate) as shear strain increases. Therefore, when the medium or dense sands are subjected to undrained cyclic shear in small shear strain amplitude, excess pore water pressure may be generated in each load cycle leading to softening of soil and accumulation of deformation. In contrast, when the shear strain amplitude is large, the dilation tendency of the soil skeleton will make the effective stress and shear resistance increase.

Liquefaction can occur in sands with different densities, while their mechanisms are different. Based on the mechanism of failure, a systematic description of liquefaction was given by Robertson and Fear (1996) and can be summarized as:

a) Flow liquefaction: When the static, driving shear stress exceeds the residual shear resistance, the saturated, contractive soil (e.g., loose sand) develops uncontrolled large deformation. The flow-type failure can be triggered by cyclic or monotonic shear loading.

b) Cyclic softening: excess pore water pressure build-up in soils and shear deformation accumulated during undrained cyclic shear. The shear deformation is limited and does not continue after cyclic loading ceases due to stiffness recovery. It can be further classified as cyclic liquefaction and cyclic mobility. Cyclic liquefaction occurs when cyclic shear stress exceeds the initial, static shear stress. A condition of zero effective stress may be achieved because of the reversal of shear stress. On the contrary, zero effective stress condition is not achieved in cyclic mobility because there is no shear stress reversal.

Flow liquefaction can only occur in loose soil while cyclic softening can occur in all types of soil. The difference between flow liquefaction and cyclic mobility is schematically illustrated in Fig. 2.5. It is noteworthy that in most cases, the distinction between cyclic softening and cyclic mobility is not deliberately distinguished (Castro, 1975; Seed, 1979; Elgamal et al., 2002; Wang and Wei, 2016; Banerjee et al., 2022). In this thesis, cyclic mobility and cyclic softening also refer to the same phenomenon.

The typical post-liquefaction phase of cyclic mobility is shown in Fig. 2.6. Shamoto et al. (1997) divide the shear strain in post-liquefaction into the component that dependent (non-zero effective stress) and independent (“zero” effective stress) of effective stress. Wang and Wei (2016) defined the stage that shear strain develops at a “zero” effective stress state as the “flow stage” and the stage that shear strain develops with the recovery

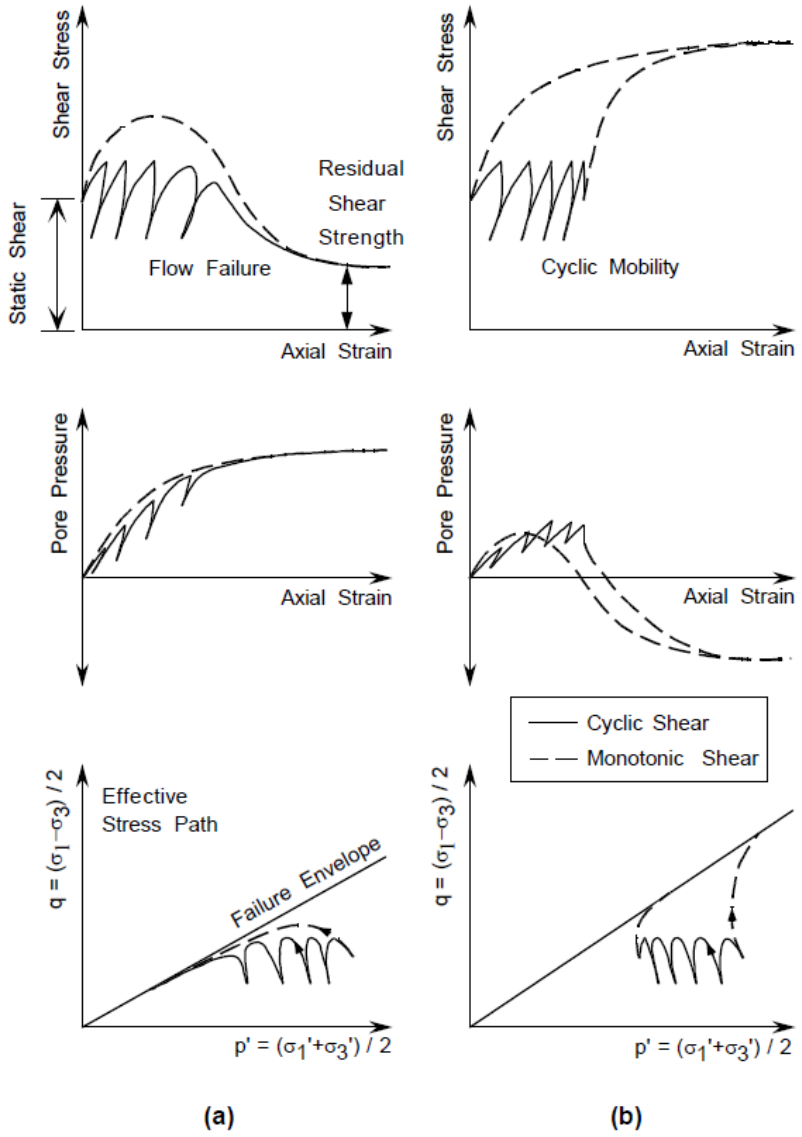

Fig. 2.5. Response of (a) contractive and (b) dilative saturated sands to undrained shear (after Rauch, 1997).

of effective stress as the “hardening stage”. The range of the “flow stage” enlarges with an increasing number of loading cycles, while the stress-strain hysteresis curves in the “hardening stage” are parallel to each other for loading or unloading. Therefore, the development of post-liquefaction shear strain is governed by the “flow stage”. Because of the stiffness recovery in the “hardening stage”, large shear strain usually does not occur in cyclic mobility. In addition, complete liquefaction is said to have occurred if the soil

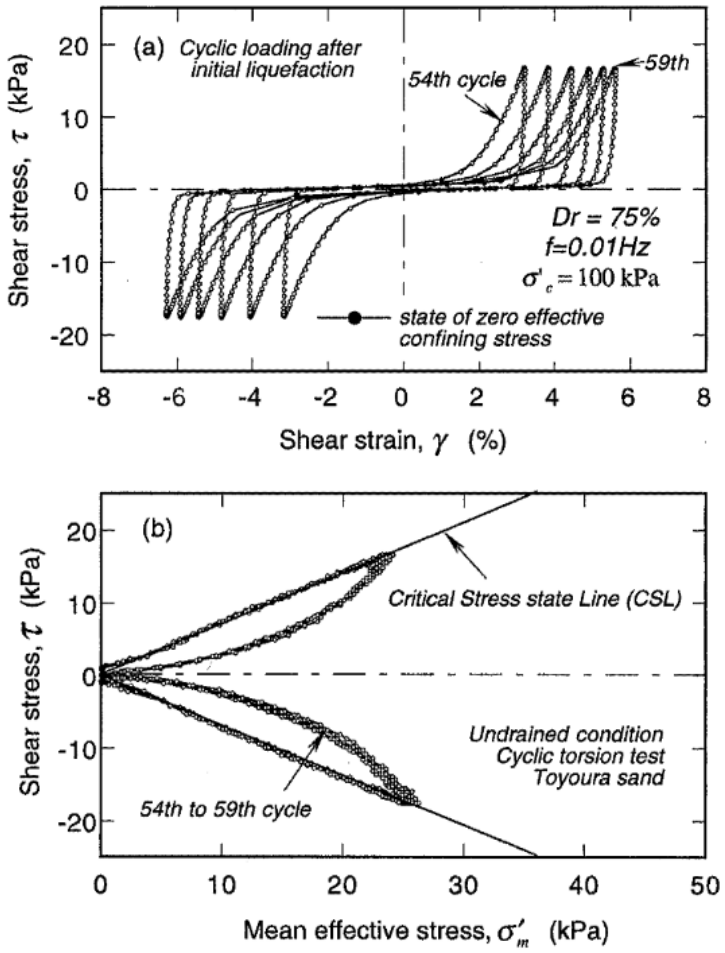

Fig. 2.6. Two post-liquefaction shear strain components in undrained cyclic torsional test (after Shamoto et al., 1997).

behaves like a liquid even subjected to a large shear strain (usually 20%) (Yoshida, 2020).

2.1.2. Assessment of liquefaction resistance

Assessment of liquefaction resistance (or liquefaction potential) is an indispensable part of engineering seismic design. There are three general approaches for evaluating the liquefaction resistance of soil in laboratory element tests: stress-based approach, strain-based approach, and energy-based approach.

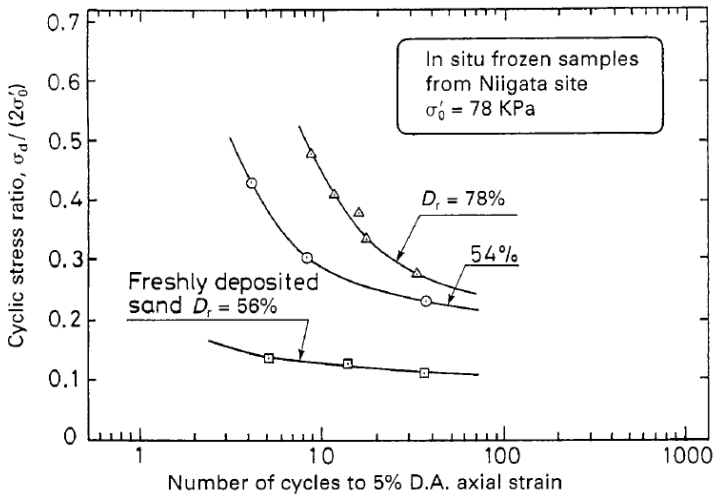

Fig. 2.7. Example of cyclic strength curve of undisturbed samples of sand (after Yoshimi et al., 1989).

The most widely used one is the stress-based approach. In the stress-based approach, stress-controlled cyclic tests are routinely performed to produce an empirical relationship between the applied uniform cyclic stress ratio (CSR) and the number of cycles required to trigger liquefaction. CSR is the ratio of shear stress amplitude to the initial confining stress. Achievement of a double amplitude of 5% shear strain is usually used as the failure criterion (trigger of liquefaction); however, sometimes the condition when the excess pore water pressure exceeds 95% or equals to 100% initial confining stress is taken as an alternative failure criterion to the double amplitude of strain. CSR that triggers liquefaction in a specified number of cycles (usually 20 cycles) is termed the cyclic resistance ratio (CRR), which is usually used to evaluate the liquefaction resistance of the soil. The relationship between CRR and the specific number of cycles is termed the cyclic strength curve (Ishihara, 1996; Kramer, 1996) or the liquefaction resistance curve (Towhata 2008). A typical cyclic strength curve is shown in Fig. 2.7.

Despite the popularity of stress-based procedures, multiple studies have shown that

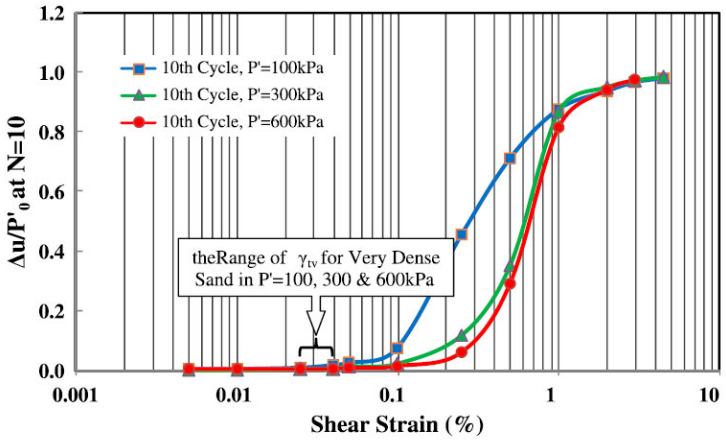

Fig. 2.8. Excess pore water pressure build-up vs. shear strain amplitude in the 10th cycle (after Heshmati et al., 2015).

excess pore water pressure better correlates to cyclic strain than to cyclic stress (e.g., Martin et al., 1975; Dobry et al., 1982; Byrne, 1991). Dobry et al. (1982) suggested that there is a threshold strain amplitude (γ_{tv}) below which no excess pore water pressure will generate in soils, regardless of the number of applied load cycles. They concluded that the threshold strain amplitude can be used to assess the liquefaction resistance. A typical curve of excess pore water pressure vs. shear strain amplitude is shown in Fig. 2.8.

However, in the engineering practice of liquefaction potential evaluation, both the stress-based approach and strain-based approach require the liquefaction resistance index to be compared with the shear stress/strain loading index (e.g., cyclic stress ratio, cyclic shear strain). In the calculation of the stress/strain loading index, the random seismic load should be converted to an equivalent number of uniform cycles. During this process, it is necessary to consider the effects of various seismic motion parameters (maximum amplitude, duration, waveform, ground dynamic response, ground depth, etc.) related to earthquake magnitude, fault distance, and ground characteristics. Such a conversion containing assumptions and approximations will decrease the evaluation accuracy of

liquefaction potential, especially when multiple components of ground motion are considered. Therefore, the energy-based approach regardless of the number of repetitions and waveform of the seismic motion was put forward.

Nemat-Nasser and Shokooh (1979) found that the excess pore water pressure developed in soil is directly related to the amount of dissipated energy during cyclic loading. Davis et al. (1982) proposed an evaluation method based on the concept of energy using seismic liquefaction survey data. This method considers the mechanism of saturated sandy soil liquefaction and assumes that the increase or decrease of pore water pressure is related to the energy dissipation in the soil during earthquakes. Towhata and Ishihara (1985) conducted undrained cyclic hollow cylindrical torsional shear tests and put a focus on the dissipated energy in soil specimens. They found a unique relationship between the cumulative dissipated energy and excess pore water pressure which is independent of loading history. Figueroa et al. (1994) performed a series of strain-controlled torsional shear tests which demonstrated that the cumulative dissipated energy per volume was closely connected to pore-pressure buildup. The cumulative dissipated energy per volume was affected by the void ratio and confining stresses but independent of shear strain amplitude (0.15–1.02%). Their relationship can be expressed by the function below:

$$\mathrm{Log}_{10}(\delta \mathrm{W}) = 5.697 + 0.00477\sigma'_{\mathrm{c}} - 4.339\mathrm{e} \tag{2.1}$$

where δW is the dissipated energy per unit volume; σ_c' is the initial effective confining pressure acting on the specimen; e is the void ratio. Kazama et al. (2000) carried out constant-strain-controlled cyclic triaxial tests and focused on the relationship between excess pore water pressure and energy-dissipation capacity obtained from stress-strain

loops even after initial liquefaction. In addition, they used dissipation energy as a scalar index to represent the degree of liquefaction and evaluated the ductility nature of soils based on it. Kokusho (2013) reviewed a data set of stress-controlled cyclic triaxial liquefaction test results by harmonic loading and found that the cumulative dissipated energy is correlated well with not only pore-pressure buildup but also induced strain, and with cumulative strain energy measured in the same test as well.

In the literature, the dissipated energy is usually calculated by the function below:

$$\mathrm{d}W = \sigma'_x \mathrm{d}\varepsilon_x + \sigma'_y \mathrm{d}\varepsilon_y + \sigma'_z \mathrm{d}\varepsilon_z + \tau_{xy}\mathrm{d}\gamma_{xy} + \tau_{yz}\mathrm{d}\gamma_{yz} + \tau_{zx}\mathrm{d}\gamma_{zx} \tag{2.2}$$

where dW is the increment of dissipated energy per unit volume; σ'_x, σ'_y, and σ'_z are the effective stresses acting along the x-, y-, and z-directions, respectively; τ_{xy}, τ_{yz}, and τ_{zx} are the shear stresses acting on the planes with normal vectors in the x-, y-, and z-directions, and parallel to the y-, z-, and x-axis, respectively. dε_x, dε_y, and dε_z are the normal strain differences in the x-, y-, and z-directions, respectively; and dγ_{xy}, dγ_{yz}, and dγ_{zx} are the engineering shear strain differences generated in the xy-, yz-, and zx-planes, respectively. In the cyclic triaxial test, Eq. (2.2) can be simplified as:

$$\mathrm{d}W = \sigma'_\mathrm{d}\mathrm{d}\varepsilon_\mathrm{a} \tag{2.3}$$

where σ'_d is the deviator stress and dε_a is the axial strain. The trapezoidal rule is usually used in the calculation of accumulated dissipated energy:

$$W = \frac{1}{2}\sum_{i=1}^{n-1}(\sigma'_{\mathrm{d},i+1} + \sigma'_{\mathrm{d},i})(\mathrm{d}\varepsilon_{\mathrm{a},i+1} + \mathrm{d}\varepsilon_{\mathrm{a},i}) \tag{2.4}$$

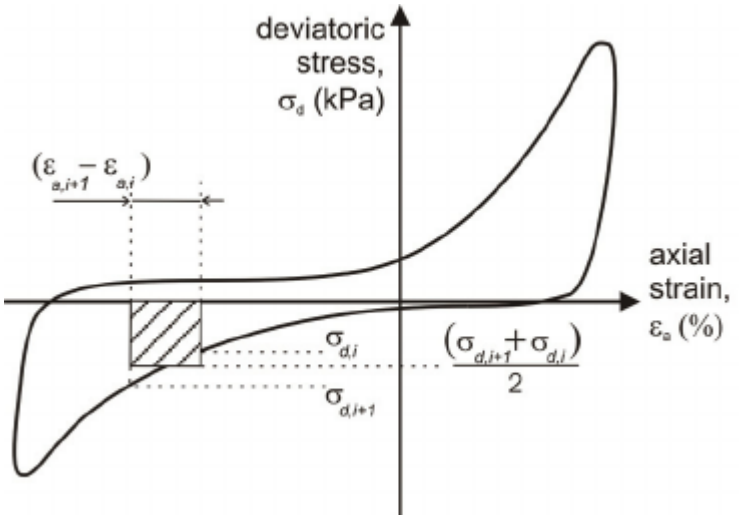

Fig. 2.9. Calculation of the amount of dissipated energy per unit volume using trapezoidal rule in cyclic triaxial tests (after Green et al., 2000).

where W is the accumulated dissipated energy; n is the number of applied load increments; $\sigma'_{d,i}$ and $\sigma'_{d,i+1}$ are the applied deviator stress at load increment i and $i + 1$, respectively; and $d\varepsilon_a$ and $d\varepsilon_{a,i+1}$ are the axial strain at load increment i and $i + 1$, respectively. Fig. 2.9 schematically illustrates the application of Eq. (2.4). In particular, the accumulated dissipated energy during one loading cycle is equal to the area bounded by the stress–strain hysteresis loop. In practice, the accumulated dissipated energy is commonly normalized by the initial mean effective stress (e.g., Kazama et al., 2000; Polit et al., 2013) or mean effective stress (e.g., Kokusho, 2013; Kokusho and Kaneko, 2018).

2.2. Micromechanics of granular materials

In geotechnical engineering, granular materials, including sands, are usually described by continuum-based methods, such as stress–strain relationship. However, granular materials are made up of distinct particles. The overall behavior of a granular

material is closely related to its microstructure during the loading processes. Therefore, from this perspective, the comprehension of microstructure evolution is a key concept for the change in granular material on the macroscopic scale (Cambou et al., 2016).

2.2.1. Representative volume element

As defined by Cambou et al. (2016), the scale of the granular material can be subdivided into the *microscopic scale, the mesoscopic scale, the aggregate mesoscopic scale*, and the *macroscopic scale*. The microscopic scale is the scale of particles and contacts between particles; the mesoscopic scale is the scale of local arrays defined as closed loops of particles in contact; the aggregate mesoscopic scale is defined as sets of local arrays sharing common texture characteristics (e.g., elongation degree and orientation); the macroscopic scale is the scale can be described by the representative volume element (REV), where continuum-based variables (e.g., stress tensor and strain tensor) and phenomenological constitutive laws are considered. A typical REV for granular assembly is shown in Fig. 2.10. The REV should satisfy: a) Large enough on the

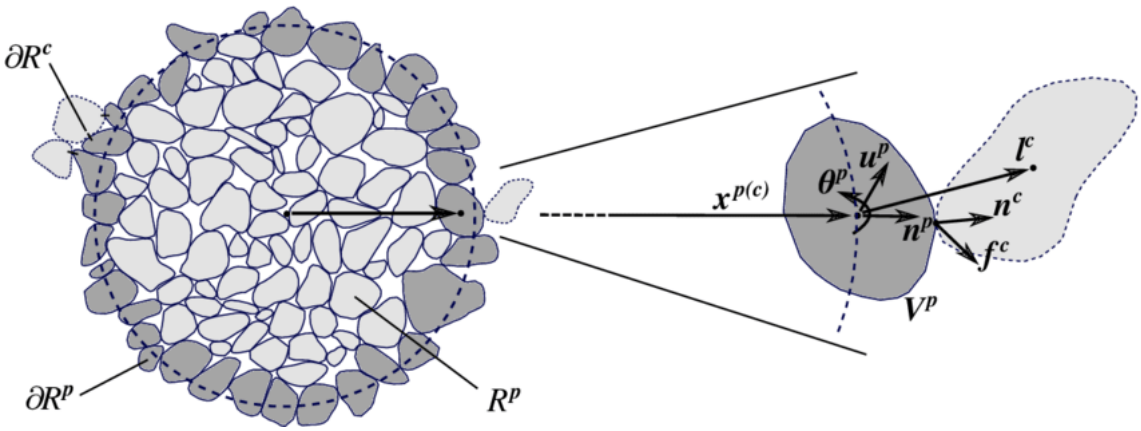

Fig. 2.10. Representative volume element for a granular assembly (after Karapiperis et al., 2021).

microscopic scale to contain enough particles and pores for statistical homogenization; b) Small enough on the macroscopic scale to be treated as a spatial point of the granular assembly; c) the scale of RVE does not vary with time and space.

Granular materials can be regarded as a discrete medium at the microscopic scale and a continuous medium at the macroscopic level. The key to the multi-scale analysis of granular materials is to establish the link between macroscopic and microscopic properties. The basic approach to determining the macro-micro connections of granular materials is the homogenization method as illustrated in Fig. 2.11. The homogenization process is based on three relations: localization operator (from macroscopic scale to microscopic scale), local constitutive law (relation between contact force and local displacements and rotations), and average operator (from microscopic scale to macroscopic scale). The main purpose of applying the homogenization method to granular materials is to "obtain a constitutive relation at the REV scale from information on the material behavior at the micro-scale and from the microstructure" (Cambou et al., 2016).

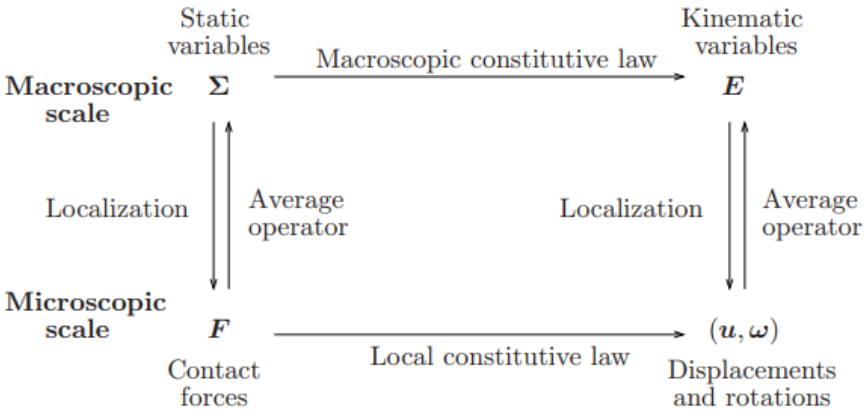

Fig. 2.11. General homogenization operators considering a micro-scale for granular materials (after Cambou et al. 2016).

2.2.2. Compactness and coordination number

The behavior of granular materials on the macroscopic scale is highly affected by their compactness. The compactness of a granular material is defined on the macroscopic scale (at RVE) by porosity, *n*, or void ratio, *e*:

$$n = \frac{V_\mathrm{v}}{V} \text{ and } e = \frac{V_\mathrm{v}}{V_\mathrm{s}} \tag{2.5}$$

where $V, V_\mathrm{v}, \text{and } V_\mathrm{s}$ are the total volume, the void volume, and the solid volume, respectively. Especially, $V = V_\mathrm{v} + V_\mathrm{s}$.

On the microscopic scale, the compactness can be described by the coordination number, *Z*, which is the mean number of neighbor particles in contact with each particle in a given granular assembly. The coordination number Z is given by:

$$Z = \frac{2N_\mathrm{c}}{N_\mathrm{p}} \tag{2.6}$$

where $N_\mathrm{c} \text{ and } N_\mathrm{p}$ are the total number of contact points and of particles in a given granular assembly, respectively. Several empirical relationships had been proposed to relate the variable defined on the macroscopic scale, porosity or void ratio, and the variable defined on the microscopic scale, coordination number (Field, 1963; Athanasiou-Grivas and Harr, 1980; Yanagisawa, 1983; Chang et al., 1990). Among these relationships, the function proposed by Chang et al. (1990) is the most widely used:

$$Z = 13.25 - 8e \tag{2.7}$$

where *e* ranges from 0.35 to 0.85. The connectivity of a granular material, which refers

to the set of force-bearing (active) contact, can also be described by the coordination number. However, it should be noted that the connectivity is a scalar index and does not reflect the difference in texture between two granular assemblies (Cambou, 2009). This means that granular packings with the same coordination number may have different textures. Therefore, higher-order indexes will be introduced hereinafter.

2.2.3. Contact normal and fabric

On the microscopic scale, the granular texture involves three vectors based on which other local geometrical variables can be defined (Cambou et al., 2009) as shown in Fig. 2.12: a) the *branch vector* $\vec{\ell}$ joining the centers of two contacted particles; b) the *contact vector* $\vec{c}$ joining the center of each particle to the particle center; c) the *contact normal* $\vec{n}$ defined as the unit vector normal to the contact plane π (tangential to the two particles at the contact point α). Especially, the vectors defined above have the same orientation when the particles are circular (2D space) or spherical (3D space).

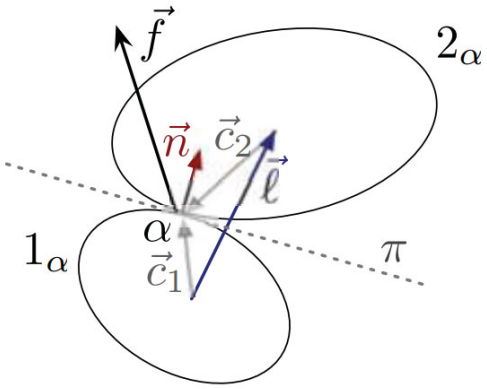

Fig. 2.12. Local vectors at the contact α between two particles (after Cambou et al., 2009).

The granular textural information is usually described based on the distributions of the vectors $\vec{\ell}, \vec{c},$ and $\vec{n}$ (Cambou et al., 2009). In the lowest order, scalar parameters (e.g., coordination number) concern the *connectivity* of the contact network; in the higher order, the spatial arrangement of particles and pore space distribution can be described by the *fabric tensor*.

The fabric of a granular assembly refers to the arrangement of particles, particle groups, and pore space distribution (Mitchell and Soga, 2005). The complex plastic behavior of granular materials in quasi-static deformation such as shear strength and dilatancy originates from the evolution of fabric (Arthur and Menzies, 1972; Cresswell and Powrie, 2004; Ventouras and Coop 2009; Fonseca et al., 2012). The fabric tensor is a tool to quantify the fabric of a granular assembly on the RVE scale, which is first proposed by Satake (1982). Satake (1982) defined the fabric tensor Φ_{ij} by the contact normal:

$$\Phi_{ij} = \frac{1}{N_\mathrm{c}} \sum_{k=1}^{N_\mathrm{c}} n_i^k n_j^k \tag{2.8}$$

where N_c is the total number of contacts; n_i^k and n_j^k denote the component of the k-th unit contact normal vector in the i and j direction, respectively. Chang and Gao (1996) defined the fabric based on branch vectors:

$$\Phi_{ij} = \frac{1}{N_\mathrm{c}} \sum_{k=1}^{N_\mathrm{c}} \ell_i^k \ell_j^k \tag{2.9}$$

where ℓ_i^k and ℓ_j^k denote the component of the k-th branch vector in the i and j direction, respectively. For single-sized circular (2D) or spherical (3D) particles, Eq. (2.8) and Eq.

(2.9) are equivalent. Although there are fabric tensors defined in higher orders (Kanatani, 1984; Chang and Misra, 1990), the second-order fabric tensor defined by Eq. (2.8) is the most widely used for its simplicity. In addition, fabric tensors can be used to express the anisotropy of fabric. Under 3D axisymmetric conditions, the anisotropy of fabric is commonly described by deviator fabric $\Phi_1 - \Phi_3$ (Thornton and Sun, 1993; Cui and O'Sullivan, 2006) or fabric ratio Φ_1/Φ_3 (Bardet, 1994), where $\Phi_1 \text{and } \Phi_3$ are the maximum and minimum principal fabric, respectively; A more general definition of deviator fabric Φ_d was proposed by Barreto et al. (2009):

$$\Phi_\mathrm{d} = \sqrt{\frac{[(\Phi_1 - \Phi_2)^2 + (\Phi_2 - \Phi_3)^2 + (\Phi_3 - \Phi_1)^2]}{2}} \tag{2.10}$$

Kanatani (1984) pointed out that fabric tensors can be described in the form below:

$$\Phi_{ij} = \int f(\boldsymbol{n}) n_i n_j \mathrm{d}\boldsymbol{n} \tag{2.11}$$

The distribution density $f(\boldsymbol{n})$ can be approximated by $F(\boldsymbol{n})$:

$$F(\boldsymbol{n}) = \frac{1}{4\pi}\left(1 + D_{ij} n_i n_j\right) \tag{2.12}$$

$$D_{ij} = \frac{15}{2}\left(\Phi_{ij} - \frac{1}{3}\delta_{ij}\right) \tag{2.13}$$

where D_{ij} is the parameter to describe the distribution density of contact normal; δ_{ij} is Kronecker delta. $D_1, D_2, \text{and } D_3$ represent the degree of anisotropy in the principal direction of the fabric. When $D_1 = D_2 = D_3 = 0$, the fabric is isotropic. The degree of anisotropy of fabric is also usually described by the second invariant of D_{ij} (Yang et al., 2022):

$$a_D = \sqrt{3J_2}$$
$$= \sqrt{\frac{3}{2} D_{ij} D_{ji}}$$
$$= \sqrt{\frac{15[(\Phi_1 - \Phi_2)^2 + (\Phi_2 - \Phi_3)^2 + (\Phi_3 - \Phi_1)^2]}{4}} \quad (2.14)$$

The definition of a_D is like the definition of equivalent stress. In addition, it can be found that a_D and Φ_d are equivalent.

Granular materials are porous mediums, and the pore between particles is also one of the major components of granular fabrics. Compared with contact-based fabric, the void-based fabric is less common. Among these limited studies, Oda et al. (1985) qualified the void space for granular packing using the scanning line method. Stake (1992) introduced a topological method to describe the granular packing based on contact points, branch vectors, and loops. Kuhn (1999) defined the loops in Stake (1992) as "void cells", as shown in Fig. 2.13(a). The void cells are surrounded by branch vectors of contacting particles. He modified the particle graph to include only those particles taking part in the

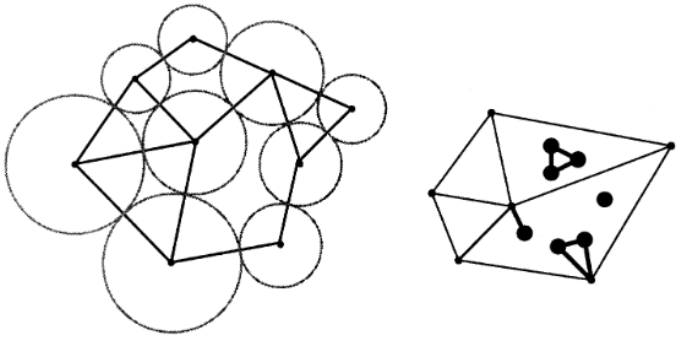

Fig. 2.13. Modified graph of particle arrangement (after Kuhn, 1999).

load-bearing framework of the granular assembly by disregarding the pendant, island, peninsula, and isolated particles, along with the branch vectors (Fig. 2.13 (b)). The fabric tensor $\boldsymbol{F}^i$ of the *i*-th void cell is then defined as:

$$\boldsymbol{F}^i = \frac{1}{2}\sum_{j=1}^{m^i} \boldsymbol{\ell}^{i,j} \otimes \boldsymbol{\ell}^{i,j} \tag{2.15}$$

where the *i*-th void cell has m^i branch vectors; $\boldsymbol{\ell}^{i,j}$ is the *j*-th branch vector in the *i*-th void cell. The height-to-width ratio of the *i*-th void cell is defined as $\alpha^i = \sqrt{F_{22}^i/F_{11}^i}$ (2D). The average height-to-width ratio of all void cells, $\hat{\alpha}$, is used as an anisotropy indicator. When $\hat{\alpha} = 1$, the void-based fabric is isotropic. Li and Li (2009) used a modified Delaunay-Voronoi tessellation technique to construct a "solid/void cell system" based on particle contact points. The fabric anisotropy of materials is defined on the average void cell as

$$\boldsymbol{G} = E_0 \oint_{\Omega} \bar{v}\,(\boldsymbol{n})\boldsymbol{n} \otimes \boldsymbol{n} \tag{2.16}$$

where E_0 is the normalization factor equals to 2π and 4π in the 2D and 3D space, respectively; $\bar{v}(\boldsymbol{n})$ is the average length of all the void vectors '$\boldsymbol{v}$' along the direction $\boldsymbol{n}$. $\boldsymbol{v}$ are the vectors connecting the void cell center and the contact points at the boundary.

However, those void-based fabrics rely on particle contacts. When granular materials are in the "zero" effective stress state after liquefaction, particles lost most of their contacts, and the construction of void cells based on contact points becomes meaningless.

Wang et al. (2016) proposed an index, mean neighborhood particle distance (MNPD) which does not rely on particle contacts, to reflect the amount of rearrangement needed for a liquefied granular assembly to reach a stable loading-bearing structure. In addition, MNPD also measures the extent of contact loss. In 2D space, MNPD is given by:

$$MNPD = \frac{1}{N}\sum_{k=1}^{N}\frac{D1^k + D2^k + D3^k}{3} \tag{2.17}$$

where N is the total number of particles in the granular assembly; $D1^k, D2^k,$ and $D3^k$ are the distance between the particle k and its three closest neighbor particles, as shown in Fig. 2.14. The reason why three closet neighbor particles are considered is that the coordination number should be equal to or larger than 3 for a particle to be mechanically stable in 2D space. The limitation of this index is that it is a scalar and cannot give information on void distribution (Bokkisa, 2019).

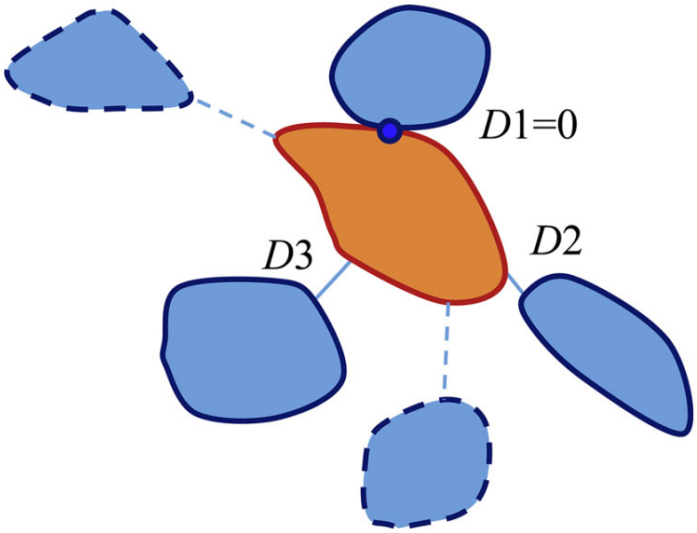

Fig. 2.14. Conceptual illustration of the surface-to-surface distance between a 2D particle and its three closest neighboring particles (after Wang et al., 2016).

Wang and Wei (2016) suggested that a particle is bound to the void space around it, to which the movement of the particle is only restricted during the deformation of granular assembly. The void space around the particle was determined from the Voronoi cell construction, as shown in Fig. 2.15. The void space around the particle 'i', is given by a convex polygon $C_1 - C_2 - C_3 - C_4 - C_5$. A new fabric index termed centroid distance D_c, was proposed to characterize the whole particle-void distribution:

$$D_c = \frac{1}{N_p}\sum_{i=1}^{N_p} D_c^i \text{ and } \boldsymbol{D}_c^i = \frac{\boldsymbol{P}^i - \boldsymbol{O}^i}{R_{50}} \tag{2.18}$$

where vector $\boldsymbol{P}^i$ and $\boldsymbol{O}^i$ are the mass center of the Voronoi cell and the mass center of the particle, respectively; R_{50} is the mean particle radius of the granular packing. $\boldsymbol{D}_c^i$ is centroid difference associated with particle i and defined to quantify the geometrical arrangement between the particle and its surrounding void. D_c can be used to quantitatively evaluate the uniformity of pore distribution.

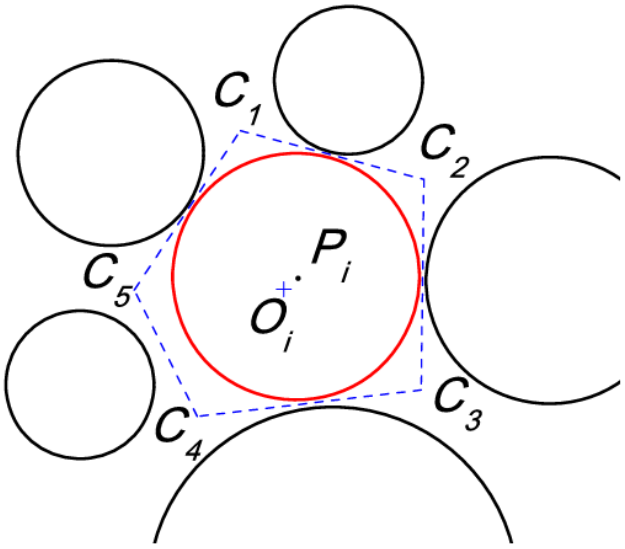

Fig. 2.15. Schematic illustration of the centroid distance (after Wang and Wei, 2016).

2.2.4. Force chain and stress tensor

Forces in a granular assembly are transmitted via force chains, and these force chains are interconnected to form a network. As illustrated in Fig. 2.16, on the one hand, the contact force networks are not uniformly distributed in the granular assembly; on the other hand, the forces transmitted in the network are also uneven. A contact force network comprising strong force chains bear the majority of the load. In some literature, the term "force chain" only refers to strong force chains (Radjai et al., 1998; Tordesillas et al., 2011). The number of strong force chains is small, and the weak force chains are distributed around and connected with the strong chains, which has an auxiliary effect on the stability of the strong force chains (Sun and Wang, 2009).

The direction of force chains is basically parallel to the direction of the external load. In weak force chains, the deformation of particles in contact points is extremely small. They have little resistance to tangential forces. In strong force chains, the deformation of particles in contact points is large because they bear a large portion of the

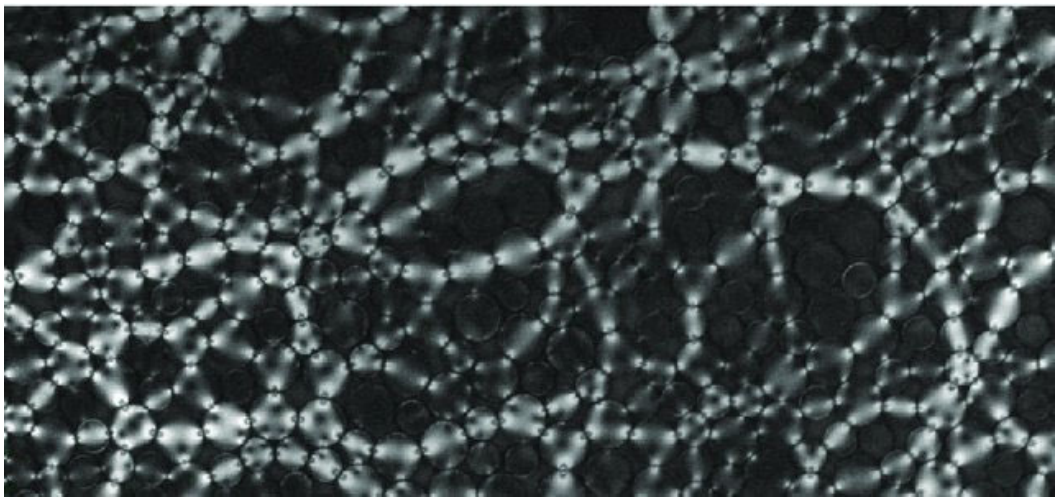

Fig. 2.16. Sample image of force chains in a quasi-2D granular material composed of photoelastic disks. Dark particles carry little force, and bright particles carry more (after Daniels, 2017).

external load. Therefore, strong force chains can withstand a certain amount of tangential forces. Obviously, the greater the friction coefficient of the particle surface and the contact force transmitted through the force chain, the greater tangential forces that the force chain can bear, which indicated that the force chain is more stable. In contrast, when the surface of particles is frictionless, the force chain cannot withstand any tangential force (Sun and Wang, 2009). Radjai et al. (1996) divided the contact force network into strong force and weak force networks based on the mean contact force. They found that the number of normal and tangential forces lower (higher) than their respective mean value decays as a power (exponential) law. Cambou et al. (2009) pointed out that in the quasi-static biaxial compressive test, the deviatoric stress component of the stress tensor originates from the strong contact force network while the weak contact force network only constitutes the spherical stress component. This foundation was verified by Thornton and Antony (1998) based on the triaxial compression DEM simulations. Thornton and Zhang (2010) pointed out that the amplitude of deviatoric stress also originates from the strong contact force network in a more general stress state.

Anisotropy exists in the force chain. Especially in the process of shearing, the phenomenon of non-uniform distribution of contact force is particularly significant. The direction of large contact forces will gradually tend to the direction of major principal stress, and a columnar structure will appear under certain conditions (Oda, 1972; Oda and Iwashita, 2000; Thornton and Zhang, 2010). The force chains are sensitive to the external load and geometric features of particle systems, and the force chain network varies widely. It should be noted that the quantified description of the force chain is still difficult (Sun and Wang, 2009; Tordesillas et al., 2011).

The discrete and heterogeneous features of granular material make the concept of the "stress tensor" defined in continuum material not directly applicable to granular materials. The definition of the stress tensor in granular material is closely related to the RVE. The general approach is to use the average operator (refer to Fig. 2.11) to derive the stress tensor from the contact force outside the RVE or the contact force in the RVE. The expression form of the average stress constructed according to the external contact force is based on the concept of the Cauchy stress tensor in continuum mechanics (Fortin et al., 2002, 2003; de Saxcé et al., 2004; Nicot et al., 2013). The most widely used definition of stress tensor in granular material is based on the contact force in the RVE. Christoffersen et al. (1981) gave the stress tensor defined by the contact force between particles by analyzing the contact force between particles in the granular material system and the equilibrium conditions of each particle, applying the principle of virtual work:

$$\sigma_{ij} = \frac{1}{V}\sum_{c=1}^{N_c} f_i^c \ell_j^c \tag{2.19}$$

where V is the volume of the RVE; N_c is the total number of contacts in the RVE; f_i^c is the component of the contact force in the i direction at contact point c; ℓ_j^c is the component of the branch vector in the j direction at contact point c. Equivalent results have been consistently reported in the literature (Love, 1927; Kanatani, 1981; Kruyt and Rothenburg, 1996; Bagi, 1996).

It should be noted that the definitions of force chain and stress tensor for granular materials are in the quasi-static state (Cambou et al., 2009, 2016).

CHAPTER 3 DISCRETE ELEMENT METHOD

In geotechnical engineering, the continuum modeling scheme, including the Finite Element method (FEM), is the most widely used numerical method in both practical design and research. The continuum modeling scheme mainly reflects the deformation characteristics of the geological material system from a macro perspective and tries to circumvent geometric complexity by using specific constitutive laws with equivalent material properties. Although the continuum modeling scheme has high computation efficiency and can be used for large-scale industrial applications, it cannot adequately consider the discrete nature of granular materials.

DEM is a discrete modeling scheme that was first proposed by Cundall and Strack (1979) to simulate the behavior of discrete materials, e.g., rock, and granular materials. DEM is essentially a first principle physics method that takes the materials as individual rigid bodies. Each particle is represented through a representative shape (usually circle or sphere) and size that interact with other particles or geometries. In the macroscopic scale, because the behavior of materials is governed by Newton's laws of motion, the constitutive model used in the continuum modeling scheme is not needed in DEM. The constitutive model in DEM, termed as "contact model", is defined in the particle or contact level, which indicates that DEM can capture the mechanical response features of granular material from the particle scale. In addition, DEM can reproduce the complex stress–strain loading condition which is difficult to achieve by laboratory element tests.

In this thesis, the business code, Rocky (ESSS., 2020), was used to conduct the numerical simulations.

3.1. Basic principle of discrete element method

In DEM, the sequence of calculations in one timestep can be summarized in Fig. 3.1. The DEM simulation generally starts with placing the particles and geometries (including boundary conditions) in the system. The material properties are input not only by directly defined inherent properties, including density, Young's modulus, and Poisson's ratio but also by specifying the contact model parameters, including friction coefficient and restitution coefficient. After the initial conditions (e.g., load or

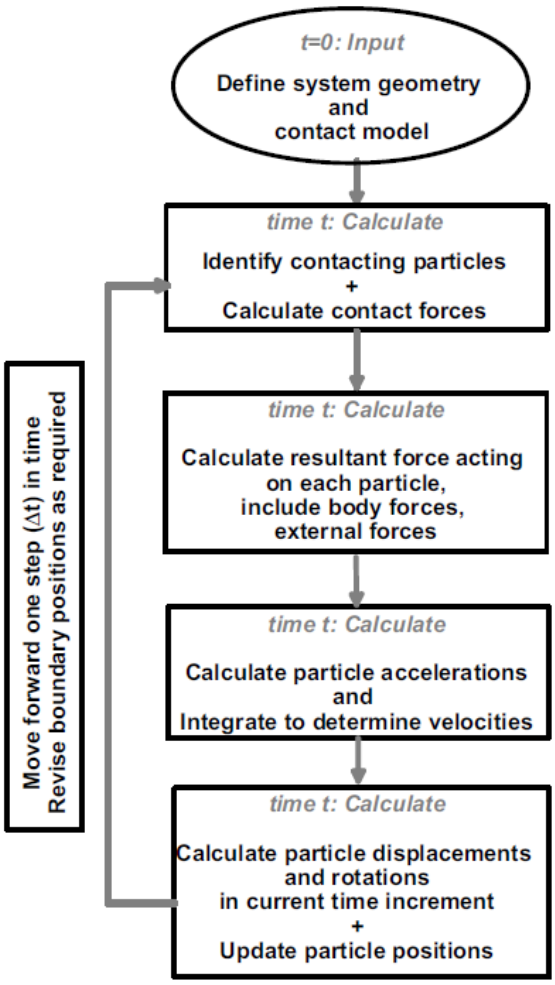

Fig. 3.1. Schematic diagram of sequence of calculations in a DEM simulation (after O'Sullivan, 2011).

deformation) are defined by the user, the simulation progresses for a specified number of time increments (timestep). At each timestep, contacts are detected to determine whether the individual particles interact with each other in the current time step. After contact detection was completed, the interparticle forces and moments related to the distance between contacting particles are identified by contact models. Having calculated those interparticle forces and moments, the resultant force and moment or torque applied to each particle, including body forces and external forces, can be determined. The translational motion and rotational motion (except when particle rotation is inhibited) of an individual particle in DEM are governed by Newton's second law of motion as shown below:

$$m_i \ddot{\boldsymbol{u}}_i = \boldsymbol{F}_i \tag{3.1}$$

$$I_i \ddot{\boldsymbol{\theta}}_i = \mathbf{M}_i \tag{3.2}$$

where m_i and $\ddot{\boldsymbol{u}}_i$ are the mass inertia and translational acceleration of particle *i*, respectively; $\boldsymbol{F}_i$ is the resultant force applied to particle *i*; I_i and $\ddot{\boldsymbol{\theta}}_i$ are the moment of inertia and angular acceleration of particle *i*; $\mathbf{M}_i$ is the resultant moment applied to particle *i*. The displacement and rotation of the particles over the current timestep then can be found through central-difference-type integration through time:

$$\ddot{\boldsymbol{u}}_i^t = \frac{\boldsymbol{u}_i^{t-\Delta t} - 2\boldsymbol{u}_i^t + \boldsymbol{u}_i^{t+\Delta t}}{\Delta t^2} \tag{3.3}$$

Substituting Eq. (3.3) into Eq. (3.1), we can get

$$\boldsymbol{u}_i^{t+\Delta t} = \Delta t^2 m_i^{-1}\left(\boldsymbol{F}_i^{t+\Delta t} - m_i \Delta t^{-2}\boldsymbol{u}_i^{t-\Delta t} + 2m_i \Delta t^{-2}\boldsymbol{u}_i^t\right) \tag{3.4}$$

where $\boldsymbol{u}_i^{t-\Delta t}, \boldsymbol{u}_i^t,$ and $\boldsymbol{u}_i^{t+\Delta t}$ are the translational displacement of particle *i* at time $t -$

$\Delta t, t,$ and $t + \Delta t$, respectively; $\boldsymbol{F}_i^{t+\Delta t}$ is the resultant force of particle *i* at time $t + \Delta t$; Δt is the timestep in the DEM simulation. Similarly, the angle of rotation of particle *i* at time $t + \Delta t$ is

$$\boldsymbol{\theta}_i^{t+\Delta t} = \Delta t^2 I_i^{-1}\left(\mathbf{M}_i^{t+\Delta t} - I_i \Delta t^{-2}\boldsymbol{\theta}_i^{t-\Delta t} + 2I_i \Delta t^{-2}\boldsymbol{\theta}_i^{t}\right) \tag{3.5}$$

where $\boldsymbol{\theta}_i^{t-\Delta t}$ and $\boldsymbol{\theta}_i^{t}$ are the angle of rotational of particle *i* at time $t - \Delta t$ and t, respectively; $\mathbf{M}_i^{t+\Delta t}$ is the resultant force of particle *i* at time $t + \Delta t$. Using Eq. (3.4) and (3.5), the particle position and orientation are updated. In the next timestep, the contact forces and moments are calculated using this updated information, and the series of calculations are repeated.

3.2. Contact model in DEM

The contact forces in any DEM algorism (including Rocky used in this thesis) consist of normal and tangential components. For spherical particles in 3D space, the contact plane is perpendicular to the line that connects the centers of two spheres. In the case of particle-to-boundary contact, the line connects the center of a sphere and the closest point of a triangle making up a boundary. The normal contact force is perpendicular to the contact plane while the tangential contact force is in the contact plane. The most widely used contact model includes Hertz-Mindlin nonlinear contact model and the linear spring dashpot-Coulomb limit model. However, using a nonlinear contact is computationally burdensome and it was pointed out that no significant improvement in

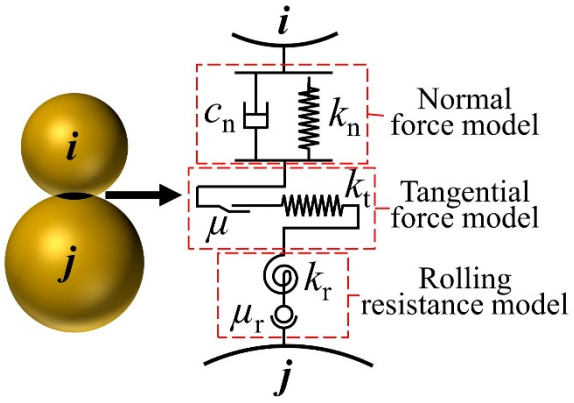

Fig. 3.2. Schematic of the interaction models (after Jiang et al., 2021).

assembly behavior when using the Hertz–Mindlin model to replace the linear-elastic contact model (Renzo and Maio, 2004). Therefore, the linear spring dashpot-Coulomb limit model was used in this thesis for its computational efficiency. In addition, rolling resistance was also usually used to restrict the rotation of spherical particles in DEM and is typically incorporated to represent the effect of non-sphericity (Iwashita and Oda, 1998; Ai et al., 2011; Coetzee, 2017; Gu et al., 2020). The contact models used in this thesis are schematically illustrated in Fig. 3.2. The normal force model, tangential force model, and rolling resistance model in Rocky are introduced as follows (ESSS., 2020):

3.2.1. Normal force model

The linear spring-dashpot model, which can be idealized as the parallel connection of a linear spring and a viscous dashpot, was first proposed in the seminal paper of Cundall and Strack (1979). The normal contact force in this model is composed of a linear elastic repulsive force and a damping force, that is

$$F_{\mathrm{n}} = k_{\mathrm{n}} s_{\mathrm{n}} + c_{\mathrm{n}} \dot{s}_{\mathrm{n}} \tag{3.6}$$

where k_{n} is the normal contact stiffness; c_{n} is the normal damping coefficient; s_{n} is the contact normal overlap; $\dot{s}_{\mathrm{n}}$ is the time derivative of the contact normal overlap. The normal contact stiffnesses are defined by the particle size and the bulk Young's modulus of contacting materials. For the contact of two particles, or of a particle with a boundary, the equivalent stiffnesses are defined as:

$$\frac{1}{k_{\mathrm{n}}} = \begin{cases} \dfrac{1}{k_{\mathrm{n,p_1}}} + \dfrac{1}{k_{\mathrm{n,p_2}}} & \text{for particle} - \text{particle contact} \\ \dfrac{1}{k_{\mathrm{n,p}}} + \dfrac{1}{k_{\mathrm{n,b}}} & \text{for particle} - \text{boundary contact} \end{cases} \tag{3.7}$$

where subscripts $\mathrm{p_1}$ and $\mathrm{p_2}$ identify the two contacting particles; subscripts p and b identify the contacting particle and boundary. The individual stiffnesses associated with a particle and with a boundary are computed, respectively, as:

$$k_{\mathrm{n,p}} = E_{\mathrm{p}} L \tag{3.8}$$

$$k_{\mathrm{n,b}} = E_{\mathrm{b}} L \tag{3.9}$$

where E_{p} and E_{b} are Young's modulus of particle and boundary materials, respectively; L is the particle size. The value of the normal damping coefficient c_{n} can be determined in a way that the viscous energy dissipation matches the energy dissipation of an inelastic collision, determined in turn by the value of the coefficient of restitution. In order to do this, the damping coefficient is defined in Rocky as follows:

$$c_n = 2\eta\sqrt{m^* k_{\mathrm{n}}} \tag{3.10}$$

where η is the damping ratio, a dimensionless parameter whose value is related to the restitution coefficient; m^* is the effective or equivalent mass for the contact, defined as:

$$\frac{1}{m^*} = \begin{cases} \frac{1}{m_1} + \frac{1}{m_2} & \text{for particle} - \text{particle contact} \\ \frac{1}{m} & \text{for particle} - \text{boundary contact} \end{cases} \tag{3.11}$$

where m_1 and m_2 are the masses of the contacting particles, whereas m is the mass of the particle in contact with a boundary. The functional relationship between the damping ratio η and the coefficient of restitution ε is:

$$\varepsilon = \begin{cases} \exp\left[-\frac{\eta}{\sqrt{1-\eta^2}}\left(\pi - \arctan\frac{2\eta\sqrt{1-\eta^2}}{1-2\eta^2}\right)\right] & \text{if } 0 \le \eta < \frac{1}{\sqrt{2}} \\ \exp\left(-\frac{\eta}{\sqrt{1-\eta^2}}\arctan\frac{2\eta\sqrt{1-\eta^2}}{2\eta^2-1}\right) & \text{if } \frac{1}{\sqrt{2}} \le \eta \le 1 \\ \exp\left[-\frac{\eta}{\sqrt{\eta^2-1}}\ln\frac{\eta+\sqrt{\eta^2-1}}{\eta-\sqrt{\eta^2-1}}\right] & \text{if } \eta > 1 \end{cases} \tag{3.12}$$

As can be seen in Fig. 3.3, Eq. (3.12) defines the restitution coefficient ε as a monotonic function of the damping ratio η.

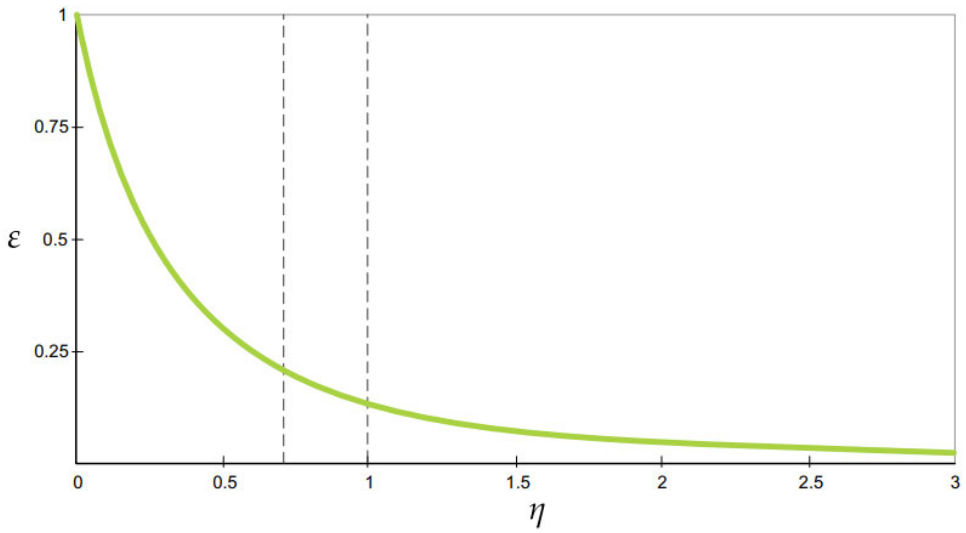

Fig. 3.3. Graph of the relationship between the damping ratio η and the restitution coefficient ε, given by Eq. (2.31) (after ESSS., 2020).

3.2.2. Tangential force model

The tangential force in the linear spring Coulomb limit model is elastic-frictional, which can be idealized as the series connection of a linear spring and a slider. Before reaching Coulomb's limit, the tangential force was considered purely elastic. Its value at time *t*, $\boldsymbol{F}_{\tau,\mathrm{e}}^{t}$, would be given by:

$$\boldsymbol{F}_{\tau,\mathrm{e}}^{t} = \boldsymbol{F}_{\tau,\mathrm{e}}^{t-\Delta t} - k_{\tau}\Delta\boldsymbol{s}_{\tau} \tag{3.13}$$

where $\boldsymbol{F}_{\tau,\mathrm{e}}^{t-\Delta t}$ is the value of the tangential force at the previous time; $\Delta\boldsymbol{s}_{\tau}$ is the tangential relative displacement of the particles during the timestep; k_{τ} is the tangential stiffness defined as:

$$k_{\tau} = r_{k}k_{\mathrm{n}} \tag{3.14}$$

where k_{n} is normal stiffness defined in Eq. (3.7); r_{k} is the tangential stiffness ratio. In this model, however, the tangential force cannot exceed Coulomb's limit. Therefore, the complete expression for the tangential force is:

$$\boldsymbol{F}_{\tau}^{t} = \min\left(\left|\boldsymbol{F}_{\tau,\mathrm{e}}^{t}\right|, \mu F_{\mathrm{n}}^{t}\right)\frac{\boldsymbol{F}_{\tau,\mathrm{e}}^{t}}{\left|\boldsymbol{F}_{\tau,\mathrm{e}}^{t}\right|} \tag{3.15}$$

where F_{n}^{t} is the contact normal force at time *t*; μ is the friction coefficient, defined as:

$$\mu = \begin{cases} \mu_{s} & \text{if no sliding takes place at the contact} \\ \mu_{d} & \text{if sliding does take place at the contact} \end{cases} \tag{3.16}$$

where μ_{s} and μ_{d} are the static and dynamic friction coefficients, respectively. The sliding is considered to be taking place on the contact the first time the magnitude of the tangential force $\boldsymbol{F}_{\tau,\mathrm{e}}^{t}$ exceeds the limit of μF_{n}^{t}. Once that force falls below the value of

μF_{n}^{t}, the contact is considered non-sliding again.

3.2.3. Rolling resistance

The linear spring rolling limit model is an elastic-plastic model reproducing the effects of rolling resistance, which be simplified as a series connection involving a rotation spring and a rotation slider. The rolling stiffness k_{r} is defined as:

$$k_{\mathrm{r}} = R_{\mathrm{r}}^{2} k_{\tau} \tag{3.17}$$

where k_{τ} is the tangential stiffness, defined in Eq. (3.14); R_{r} is the rolling radius, given by:

$$\frac{1}{R_{\mathrm{r}}} = \begin{cases} \dfrac{1}{|r_1|} + \dfrac{1}{|r_2|} & \text{for particle} - \text{particle contact} \\ \dfrac{1}{|r|} & \text{for particle} - \text{boundary contact} \end{cases} \tag{3.18}$$

where r_1 and r_2 are the rolling radii of the contacting particles, while r is the rolling radius of a particle in contact with the boundary. The rolling radius vector is defined as the vector joining the centroid of the particle and the contact point at a given time. If the rolling resistance were purely elastic, the rolling resistance moment $\mathbf{M}_{\mathrm{r,e}}^{t}$ would be updated incrementally in the following way:

$$\mathbf{M}_{\mathrm{r,e}}^{t} = \mathbf{M}_{\mathrm{r}}^{t-\Delta t} - k_{\mathrm{r}} \boldsymbol{\omega}_{\mathrm{rel}} \Delta t \tag{3.19}$$

where $\mathbf{M}_{\mathrm{r}}^{t-\Delta t}$ is the rolling resistance moment vector at the previous time; k_{τ} is the tangential stiffness defined in Eq. (3.17); $\boldsymbol{\omega}_{\mathrm{rel}}$ is the relative angular velocity vector,

which is defined as the difference between the angular velocities of two contacting particles or the angular velocity of a particle on a boundary, as the case may be. Δt is the simulation timestep. However, the updated rolling resistance moment defined in Eq. (3.19) is not used directly in the motion equation for the particles. The magnitude of the rolling resistance moment is limited by the value which is achieved at a full mobilization rolling angle. The limiting value is:

$$\mathrm{M}_{\mathrm{r,lim}} = \mu_{\mathrm{r}} R_{\mathrm{r}} F_{\mathrm{n}} \tag{3.20}$$

where μ_{r} is the rolling resistance coefficient; R_{r} is the rolling radius defined in Eq. (3.18); F_{n} is the contact normal force. The final expression for the rolling resistance moment in the Linear spring rolling limit model is:

$$\mathbf{M}_{\mathrm{r}}^{t} = \min\left(\left|\mathbf{M}_{\mathrm{r,e}}^{t}\right|, \mathrm{M}_{\mathrm{r,lim}}\right) \frac{\mathbf{M}_{\mathrm{r,e}}^{t}}{\left|\mathbf{M}_{\mathrm{r,e}}^{t}\right|} \tag{3.21}$$

3.3. Boundary condition

In continuum numerical modeling, the boundary condition is either displacement-restricted (or specified) or stress-specified. Similarly, displacement boundary and force boundary conditions in a DEM simulation can be achieved by fixing or specifying the coordinates of selected particles and by applying a specified force to selected particles. However, those displacement and force boundaries cannot easily be directly used with the discrete system including thousands of particles. Therefore, the analyst must apply those conditions to selected boundary particles as the system deforms (O'Sullivan, 2011). Here rigid walls and periodic boundary conditions were considered in this thesis.

3.3.1. Rigid boundary

The rigid boundary is the most widely used boundary type. Rigid boundaries are simply analytically described surfaces or geometries and can be used to simulate inclusions or machinery interacting with particles (O'Sullivan, 2011). These boundaries themselves do not have inertia and are only used to update the coordinates of particles, which to some extent is similar to the displacement boundary conditions in FEM. In addition, the motion of rigid walls is not affected by the external force acting on them. In typical DEM codes, including Rocky, there is no contact between rigid walls that intersect or touch. In other words, they do not interact with each other. In Rocky, the rigid wall is defined by triangular meshes in 3D space. The distance D between a particle centroid $(x^{\mathrm{p}}, y^{\mathrm{p}}, z^{\mathrm{p}})$ and the wall $ax + by + cz + d = 0$ is given by:

$$D = \frac{ax^{\mathrm{p}} + by^{\mathrm{p}} + cz^{\mathrm{p}} + d}{\sqrt{a^2 + b^2 + c^2}} \tag{3.22}$$

3.3.2. Periodic boundary

The DEM simulation of very large assemblies of particles can be simplified by using periodic boundaries, where only a selected subdomain, termed periodic cell, should be considered. The periodic cell surrounded by periodic boundary is usually a parallelogram in 2D and a parallelepiped in 3D spaces. There is a connection between the two boundaries in opposite directions, so that particles in the periodic cell are allowed to contact across periodic boundaries and move through the boundaries. Therefore, the periodic cell is surrounded by identical copies of itself, as shown in Fig. 3.4. Then, the granular material responds as if the periodic cell repeats itself infinitely in the directions

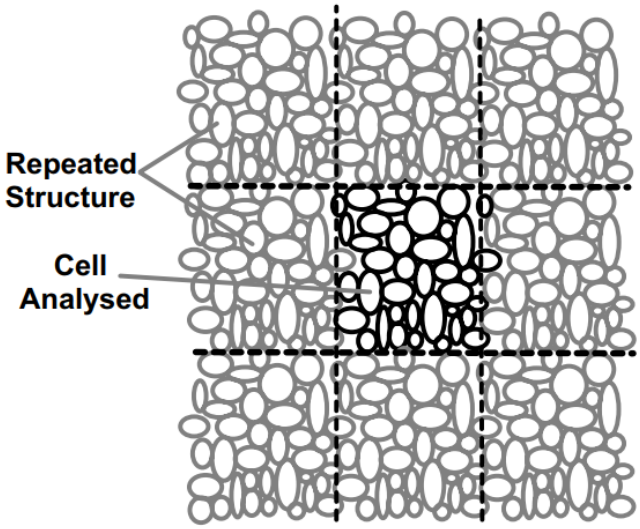

Fig. 3.4. Periodic boundaries (after O'Sullivan, 2011).

normal to each periodic cell face. Periodic boundaries are usually used to eliminate boundary effects and ensure homogenous deformation (each periodic cell is an RVE) (Cundall, 1988; Huang et al., 2014).

3.4. Timestep for the linear spring-dashpot model

Timestep is an important parameter concerning the numerical stability of DEM simulations. In the linear spring-dashpot model of Rocky, the calculation of timestep can be summarized into the following expression:

$$\Delta t = \frac{\pi}{2N_{\Delta t}^{l}}\sqrt{\frac{m^*}{k_{\mathrm{n}}}} \tag{3.23}$$

where m^* is the effective mass defined in Eq. (3.11); k_{n} is the normal stiffness defined in Eq. (3.7); $N_{\Delta t}^{l}$ is the minimum number of timesteps per loading cycle, which is set as

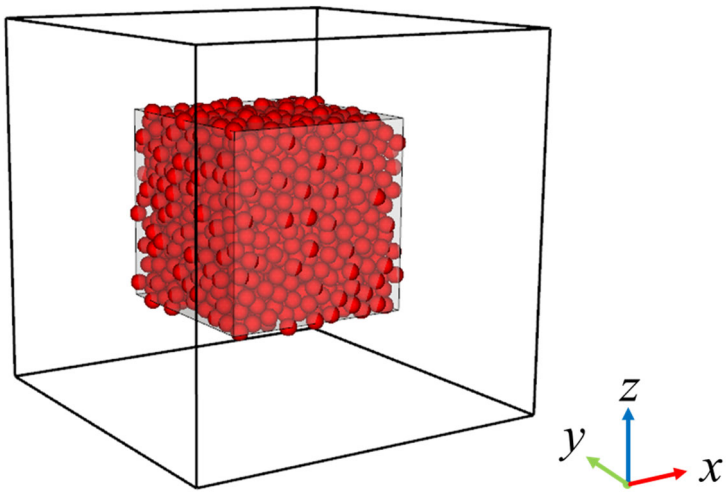

Fig. 3.5. Measurement cube in a granular assembly.

15 in this thesis ($N_{\Delta t}^{l}$ should be larger than 4).

3.5. Micro and macro quantities in DEM simulations

The micro and macro quantities, e.g., void ratio and stress tensor, in DEM code are generally measured by a measurement sphere or cube. In Rocky, the measuring cube is used, as shown in Fig. 3.5. A measurement cube can be further divided into several sub-cubes (bins).

3.5.1. Void ratio

The volume fraction, ϕ_i, of the bin i in the measurement cube is given by:

$$\phi_i = \frac{1}{V_i}\sum_{p=1}^{N_i} -\frac{m^p}{\rho^p} \tag{3.24}$$

where V_i is the volume of the bin i in the measurement region; N_i is the number of particles in the bin i; m^p is the mass of the particle p; ρ^p is the density of the particle p. The volume fraction in Rocky DEM represents the volume of the block occupied by particles. Since it takes into account the sum of the volume of all particles that have nodes (mass centroid) located inside the corresponding block, it can return a value above 1 in cases where the ratio between particle size and the block volume is small. The void fraction, or porosity of bin i, n_i, is given by:

$$n_i = 1 - \phi_i \tag{3.25}$$

the void ratio of bin i, e_i, is given by:

$$e_i = \frac{n_i}{\phi_i} \tag{3.26}$$

3.5.2. Stress tensor

The stress tensor of a particle p, σ_{ij}^p, is given by:

$$\sigma_{ij}^p = \frac{1}{V_p} \sum_{c=1}^{N_p^c} x_i^c f_j^c \tag{3.27}$$

where V_p is the volume of particle p; x_i^c is the contact location of pair ij; f_j^c is the contact force of pair ij; N_p^c is the number of contacts of particle p. The average stress tensor for the bin k is computed as:

$$\sigma_{ij}^{k} = \frac{1}{V_k}\sum_{p=1}^{N_k}\sigma_{ij}^{p}V_p \tag{3.28}$$

where V_k is the volume of bin k; V_p is the volume of particle p; N_k is the number of particles in the bin k; σ_{ij}^{p} is the stress tensor of particle p defined in Eq. (3.27).

3.5.3. Coordination number

The coordination number of particles in bin i, Z_i, is given by:

$$Z_i = \frac{2N_{\mathrm{c}}^{i}}{N_{\mathrm{p}}^{i}} \tag{3.29}$$

where N_{c}^{i} and N_{p}^{i} are the total number of contacts and particles in contacts in bin i, respectively. Since it considers only contacts located inside the corresponding block, some contacts (outside bin i) of particles that intersect the bin i boundary are not taken into account. Therefore, Z_i is smaller than the real coordination number Z defined in Eq. (2.6).

3.5.4. Fabric tensor

The contact-based fabric tensor in bin n is given by:

$$\Phi_{ij}^{n} = \frac{1}{N_{\mathrm{c}}^{n}}\sum_{k=1}^{N_{\mathrm{c}}^{n}} n_i^{n,k} n_j^{n,k} \tag{3.30}$$

where N_c^n is the total number of contacts in bin n; $n_i^{n,k}$ and $n_j^{n,k}$ denote the component of the k-th unit contact normal vector (inside bin n) in the i and j direction, respectively.

3.6. Constant volume method in DEM simulations

During the undrained cyclic loading, the pore fluid is generally assumed to be incompressible so that the granular assembly deforms without volume change. In DEM simulations, the volume of a granular packing is usually maintained constant during deformation to model an undrained condition. Then, the undrained response of a particle-fluid coupling system can be simulated without explicit consideration of the fluid phase. Because there is no real fluid phase in the constant volume (CV) method, the excess pore water pressure in an isotropically consolidated triaxial specimen is usually taken to be $\Delta u = \sigma_0 - \sigma_h$, where σ_0 and σ_h are the initial confining pressure and horizontal stress, respectively.

The CV method had been verified effective in laboratory element tests (Dyvik et al., 1987). However, a key assumption in this approach used in DEM is that the bulk modulus of the soil skeleton is much smaller than that of either the soil particle or the pore fluid (Yimsiri and Soga, 2010). The comparison of DEM simulations using the CV method to physical laboratory tests was conducted by some researchers, e.g., Ng and Dobry (1994) used the CV approach in a periodic cell during cyclic shear and find the result was qualitatively agreed with previously documented laboratory tests; Sitharam et al. (2009) conducted cyclic undrained triaxial compression simulation using the CV method and found that it is similar to the phenomenon in physical cyclic undrained

laboratory experiments. Recently, the CV method has been widely used in DEM simulation under undrained conditions (e.g., Sitharam et al., 2002, Shafipour and Soroush, 2008; Yimsiri and Soga, 2010; Asadzadeh and Soroush, 2017; Nguyen et al., 2021; Yang et al., 2022).

3.7. Quasi-static response in DEM simulations

In DEM simulation, the premise of the definition of stress tensor and force chain is that the granular assembly is in a quasi-static state. This means that this particle system is not flowing or close to a state of equilibrium (O'Sullivan, 2011). Stress waves will propagate through the particle system if the deformation of it is too fast, e.g., rapid particle flow. Under this condition, the equilibrium stress level is less than the stress measured instantaneously, and the assumption of RVE fails.

An index—inertial number, was pointed out by researchers, eg., da Cruz et al. (2005) and Radjai (2009), that can be used to judge whether the granular system is in a quasi-static state. The inertia number is the ratio of time in the microscopic scale t_{micro} to time in the macroscopic scale t_{macro}. t_{micro} refers to the duration of a particle of density ρ_s and of diameter d pass through a plane under pressure P. As $m{\sim}\rho_s d^3, a{\sim}\frac{d}{t_{\mathrm{micro}}^2}$, and $F{\sim}Pd^2$, substitute into Newton's law of motion defined in Eq. (3.1) yields

$$t_{\mathrm{micro}} = \frac{d}{\sqrt{P/\rho_s}} \tag{3.31}$$

where m is particle mass; a is particle acceleration; F is the total force acting on the

particle. t_{macro} is the reciprocal of the strain rate $\dot{\gamma}$. Therefore, the inertial number I, is expressed as

$$I = \frac{t_{\mathrm{micro}}}{t_{\mathrm{macro}}} = \frac{|\dot{\gamma}|d}{\sqrt{P/\rho_s}} \tag{3.32}$$

or

$$I = |\dot{\gamma}|\sqrt{\frac{m}{Pd}} \tag{3.33}$$

A small inertial number ($I \ll 1$) indicates that the macroscopic deformation of the granular system is significantly slower than the microscopic rearrangement of particles (Fei et al., 2020). In other words, the inertia forces acting on particles are much lower than the interparticle contact forces (O'Sullivan, 2011). In general, $I < 10^{-3}$ is widely used as the criteria to assess whether the granular material is in a quasi-static state (e.g., Soroush and Ferdowsi, 2011; Martin et al., 2020; Yang et al., 2022).

CHAPTER 4 LIQUEFACTION UNDER SURFACE-WAVE STRAIN CONDITIONS

4.1. Introduction

Strong ground surface motions may be predominated by surface waves, which will cause or aggravate liquefaction. To clarify the liquefaction behavior of granular materials under the influence of surface waves, a series of numerical tests based on the 3D DEM was performed for granular packing subject to SH-, Love-, and Rayleigh-wave strain conditions, that is, the strain paths generated by these waves without considering their natural characteristics (e.g., period and wavelength). Firstly, under the assumption of constant volume (undrained condition), the equation governing the strain–time relationships of SH, Love, and Rayleigh waves was derived from elastic wave theory. Subsequently, the undrained cyclic shear responses of K_0-consolidated specimens under different strain conditions (loading paths) were simulated using the 3D DEM. Finally, the liquefaction characteristics of specimens under different strain conditions were analyzed at both the macroscopic and microscopic scales.

4.2. SH- and Surface-wave strain conditions

4.2.1. SH-wave strain conditions

SH waves are shear waves with particle motion in the horizontal plane. As shown in Fig. 4.1, in a 3D Cartesian coordination system, assuming that SH waves propagate in

the *zx*-plane and its particle motion is along the *y*-direction, the displacement equation of SH waves in unbounded media can be expressed as follows (Pujol, 2003):

$$\boldsymbol{u}_{\mathrm{SH}} = A\boldsymbol{a}_y \exp\{\mathrm{i}[\omega t - k(lx + mz)]\} \tag{4.1}$$

where $\boldsymbol{u}_{\mathrm{SH}}$ is the displacement vector of a particle during the propagation of SH waves; A is the scalar factor determined by the boundary condition and propagation medium; $\boldsymbol{a}_y$ is the unit vector along the *y*-direction; i is the imaginary unit; ω is the angular frequency; t is the time; k is the wavenumber. Assuming $\boldsymbol{\beta}$ is the unit vector of the velocity of SH waves, l is the length of the vector component of $\boldsymbol{\beta}$ in the *x*-direction, and m is the length of the vector component of $\boldsymbol{\beta}$ in the *z*-direction. The strain can be derived from its corresponding displacement field as follows:

$$\begin{cases} \varepsilon_{xx} = \dfrac{\partial \boldsymbol{u}_x}{\partial x}, \varepsilon_{yy} = \dfrac{\partial \boldsymbol{u}_y}{\partial y}, \varepsilon_{zz} = \dfrac{\partial \boldsymbol{u}_z}{\partial z} \\ \gamma_{zx} = \dfrac{\partial \boldsymbol{u}_z}{\partial x} + \dfrac{\partial \boldsymbol{u}_x}{\partial z}, \gamma_{xy} = \dfrac{\partial \boldsymbol{u}_x}{\partial y} + \dfrac{\partial \boldsymbol{u}_y}{\partial x}, \gamma_{yz} = \dfrac{\partial \boldsymbol{u}_y}{\partial z} + \dfrac{\partial \boldsymbol{u}_z}{\partial y} \end{cases} \tag{4.2}$$

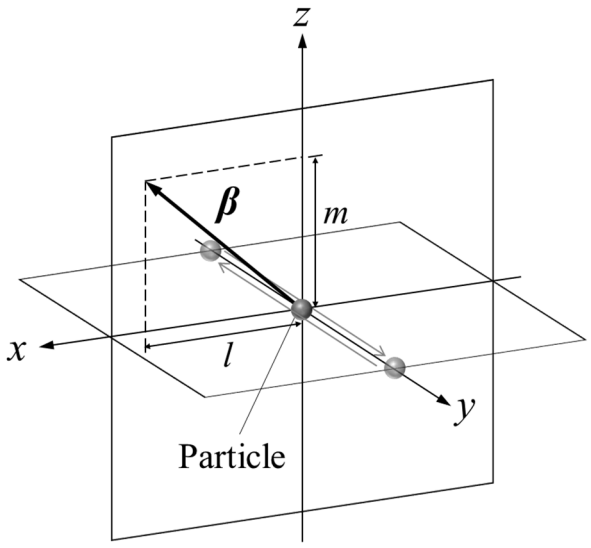

Fig. 4.1. Propagation of SH waves.

where ε_{xx}, ε_{yy}, and ε_{zz} are the normal strains in the *x*-, *y*-, and *z*-directions, respectively; γ_{zx}, γ_{xy}, and γ_{yz} denote the engineering shear strains in the *zx*-, *xy*-, and *yz*-planes, respectively; $\boldsymbol{u}_x$, $\boldsymbol{u}_y$, and $\boldsymbol{u}_z$ represent the components of the displacement field in the *x*-, *y*-, and *z*-directions, respectively. Therefore, the strain components of the SH wave are as follows:

$$\begin{cases} \gamma_{xy} = \dfrac{\partial \boldsymbol{u}_y}{\partial x} = Akl\sin[\omega t - k(lx + mz)] \\ \gamma_{yz} = \dfrac{\partial \boldsymbol{u}_y}{\partial z} = Akm\sin[\omega t - k(lx + mz)] \end{cases} \tag{4.3}$$

As shown in Eq. (4.3), the engineering shear strain of SH waves, which is based on a sine function, can be decomposed into two components (horizontal component γ_{xy} and vertical component γ_{yz}). In addition, the shear strain amplitude of each component is determined by the propagation direction of the SH waves. Although it is often assumed that liquefaction is due to the upward propagation of shear waves, in this study, two types of SH-wave strain conditions were considered: SH waves propagating horizontally and vertically upward. The former case is defined as the SHH-wave strain condition, in which

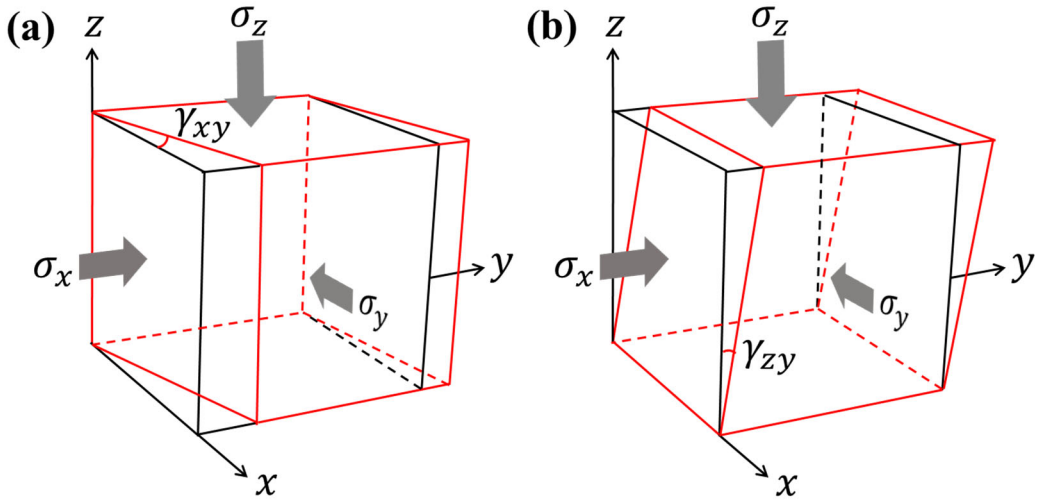

Fig. 4.2. Deformation of soil elements under (a) SHH-wave strain condition and (b) SHV-wave strain condition.

shear strain was applied in the *xy*-plane. The latter case is defined as the SHV-wave strain condition, in which shear strain was applied in the *yz*-plane. In natural ground (K_0-consolidated soil), the deformation of soil elements under SHH- and SHV-wave strain conditions are shown in Fig. 4.2. Because the normal stress in the vertical direction (σ_z) was much larger than that in the horizontal direction (σ_x and σ_y), the two conditions were not equivalent for different magnitudes of shear stress.

4.2.2. Love-wave strain conditions

In elastodynamics, Love waves occur owing to the interference of SH waves. In this study, Love waves were assumed to propagate through an isotropic elastic layer over a half-space, as shown in Fig. 4.3, where β is the shear wave velocity, ρ is the density, G is the shear modulus, and H is the interface depth. The subscripts 1 and 2 indicate the surface water-saturated sand layer and the bedrock half-space, respectively. G, ρ, and β satisfy:

$$\beta = \sqrt{\frac{G}{\rho}} \tag{4.4}$$

Assuming that the Love waves propagate along the *x*-direction, the displacement equation of Love waves in the isotropic elastic surface layer can be described as follows (Pujol, 2003):

$$\begin{cases} \boldsymbol{u}_{\mathrm{L}} = B\boldsymbol{a}_y \cos(\eta_1 kz)\exp\left[\mathrm{i}k(ct-x)\right];\ 0 < z < H \\ \eta_1 = \sqrt{\dfrac{c^2}{\beta_1^2} - 1} \end{cases} \tag{4.5}$$

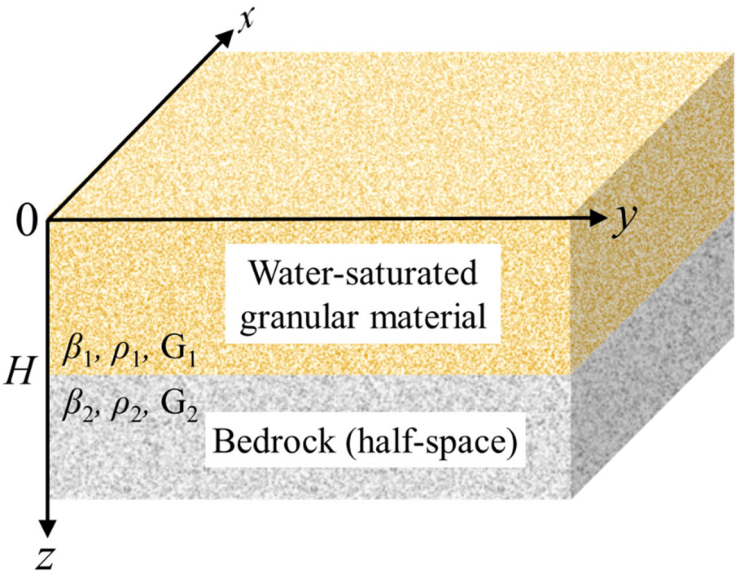

Fig. 4.3. Medium model for Love wave propagation.

where $\boldsymbol{u}_L$ is the displacement vector of a particle during the propagation of Love waves, B is the coefficient determined by the boundary condition and propagation medium, and c is the velocity of Love waves, which is between β_1 and β_2. Therefore, the strains of Love waves are expressed as follows:

$$\begin{cases} \gamma_{xy} = Bk\cos(\eta_1 kz)\sin(\omega t - kx) \\ \gamma_{yz} = -\eta_1 Bk\sin(\eta_1 kz)\cos(\omega t - kx) \end{cases} \tag{4.6}$$

As shown in Eq. (4.6), the engineering shear strain of Love waves can be decomposed into two components (horizontal component γ_{xy} and vertical component γ_{yz}). However, a phase difference of π/2 exists between the two components. Therefore, as shown in Fig. 4.4, in the natural ground, the soil element under the Love-wave strain condition is subject to shear strains in the vertical plane (yz-plane) and horizontal plane (xy-plane) simultaneously. The aspect ratio (AR) can be defined as the ratio of shear strain amplitude of two components in a specified depth z_0; hence, the AR of Love waves is expressed as follows:

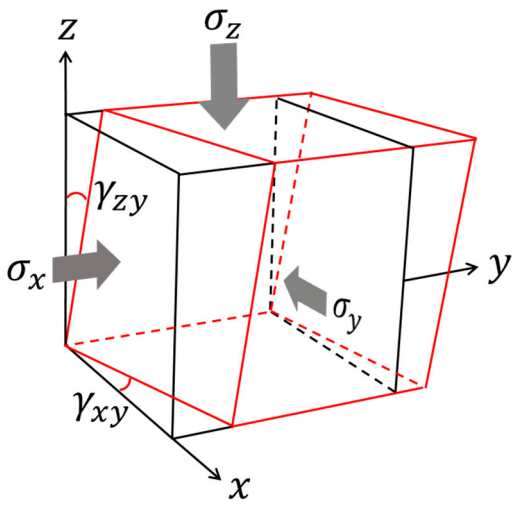

Fig. 4.4. Deformation of soil elements under Love-wave strain condition

$$\mathrm{AR} = \frac{\mathrm{Max}(\gamma_{yz})}{\mathrm{Max}(\gamma_{xy})} = \eta_1 \tan(\eta_1 k z_0) \tag{4.7}$$

Theoretically, the AR can be from 0 to infinity (∞). In fact, Love waves exhibit dispersion. This means that the velocity of the Love waves varies with the frequency. As a result, at a specified depth z_0, the shear strain amplitudes and AR of Love waves will be affected by their frequency.

Except for the dispersion features, Love waves typically have larger amplitudes and lower predominant frequencies than SH waves (Novotny, 1999). In this study, to simplify the problem, only the differences in the deformation mode, including the strain component, phase difference, and AR, were considered. Therefore, the deformations of the granular packings under different Love-wave strain conditions were assumed to be at the same frequency and strain level.

4.2.3. Rayleigh-wave strain condition

A Rayleigh wave is a surface wave including both longitudinal and transverse motions. However, due to its high non-linearity, an accurate mathematical formulation for Rayleigh waves in the real ground is very difficult to determine. In addition, the characteristics of Rayleigh waves change during the progressive weakening of the soil. Therefore, this paper does not attempt to seek the response of saturated soil during the propagation of real Rayleigh waves but aims to investigate the influence of the deformation modes resulting from Rayleigh waves on the liquefaction characteristics of granular materials, which is more practical in geotechnical engineering. Hence, in the following analyses, a relatively simple medium model was used, and the emphasis was placed on obtaining the possible deformation mode of the soil element under Rayleigh wave propagations, which was hereinafter referred to as the Rayleigh-wave strain conditions.

For simplification, it was assumed that Rayleigh waves propagate along the surface of a homogeneous, isotropic, and elastic solid half-space. As illustrated in Fig. 4.5(a), if the *xy*-plane coincides with the surface of the half-space, the scalar form of the displacement governing equation of Rayleigh waves traveling in the *x*-direction can be expressed as follows (Pujol 2003):

$$\begin{cases} u_x = Q\left[\exp(-\gamma_\alpha kz) - \left(1 - \dfrac{c^2}{2\beta^2}\right)\exp\left(-\gamma_\beta kz\right)\right]\sin(\omega t - kx) \equiv QU(z)\sin(\omega t - kx) \\ u_z = Q\gamma_\alpha\left[-\exp(-\gamma_\alpha kz) + \left(1 - \dfrac{c^2}{2\beta^2}\right)^{-1}\exp\left(-\gamma_\beta kz\right)\right]\cos(\omega t - kx) \equiv Q\gamma_\alpha W(z)\cos(\omega t - kx) \end{cases} \tag{4.8}$$

where u_x and u_z denote the displacement components of a particle in Rayleigh waves along

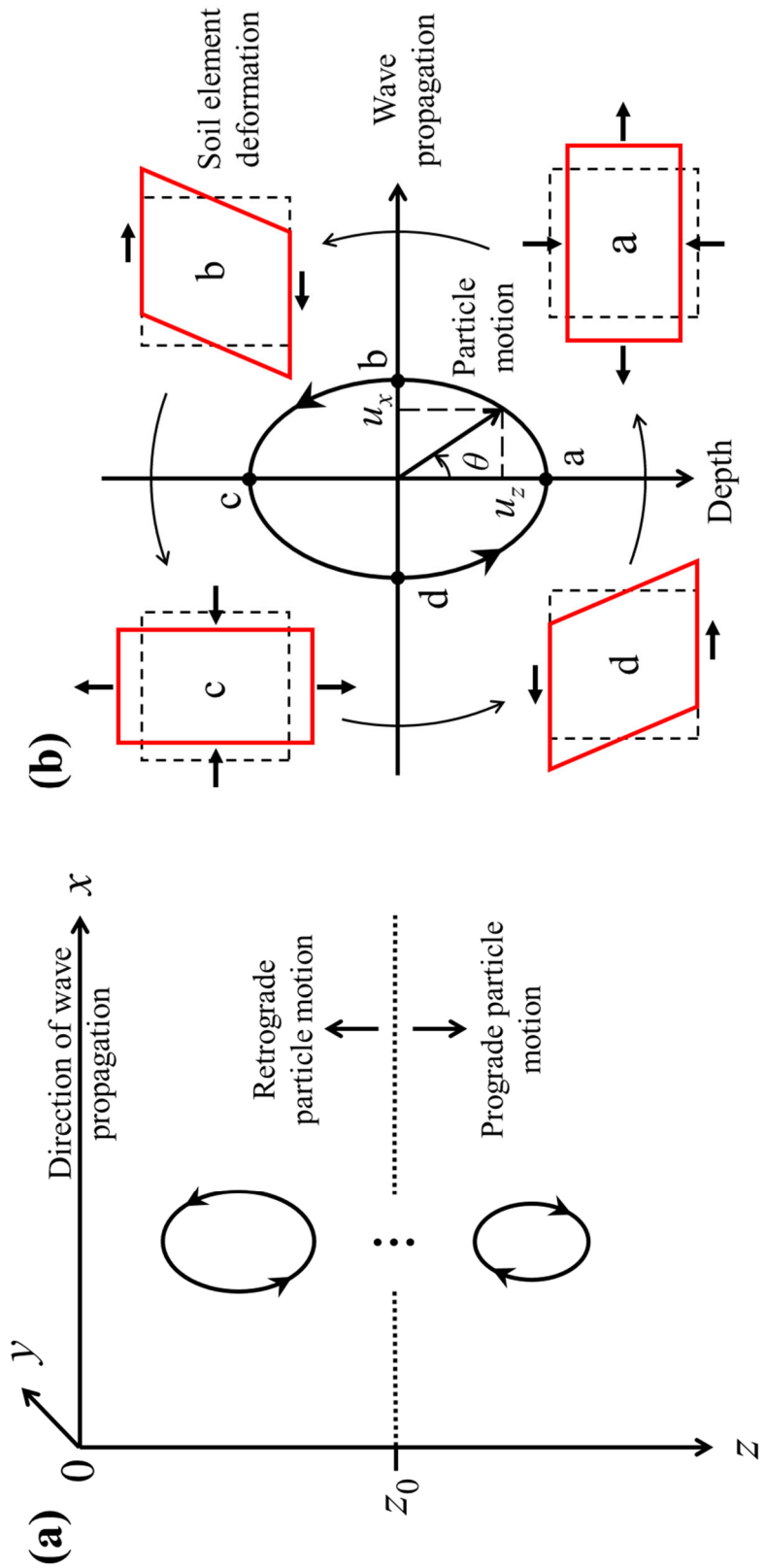

Fig. 4.5. Particle motion and soil element deformation generated by Rayleigh waves in a half-space: (a) particle motion as a function of depth and (b) particle motion and corresponding soil element deformation near the surface of the half-space.

the x- and z-directions, respectively, Q is a constant, k is the wavenumber, c is the velocity of the Rayleigh waves, ω is the angular frequency, t is the time, and γ_α and γ_β are defined as:

$$\gamma_\alpha = \sqrt{1 - c^2/\alpha^2}, \gamma_\beta = \sqrt{1 - c^2/\beta^2} \tag{4.9}$$

where α and β represent the velocities of P and SV waves, respectively, which are larger than c. As the stress vector across the medium surface is zero, Rayleigh waves should satisfy the following period equation:

$$(2 - c^2/\beta^2)^2 - 4\gamma_\alpha\gamma_\beta = 0 \tag{4.10}$$

From Eq. (4.8), it can also be determined that the motion of a particle in Rayleigh waves is elliptical on the zx-plane, as illustrated in Fig. 4.5. If k is constant, angle θ can be expressed as (Pujol 2003):

$$\tan\theta = \frac{u_x}{u_z} = \frac{U(z)}{W(z)\gamma_\alpha}\tan(\omega t - kx) \tag{4.11}$$

Since P waves travel faster than SV or Rayleigh waves, $W(z)$ and γ_α are positive. $U(z)$ is initially positive and becomes negative as z increases. Therefore, θ increases with t near the half-space surface, whereas it decreases with t when z exceeds z_0, where z_0 can be determined from $U(z_0) = 0$. This means that the particle motion is retrograde near the half-space surface and is prograde below threshold depth z_0, as illustrated in Fig. 4.5.

The strain components of a soil element caused by Rayleigh waves are given by:

$$\begin{cases} \varepsilon_x = \dfrac{\partial u_x}{\partial x} \\ \quad = -Qk\left[\exp(-\gamma_\alpha kz) - \left(1 - \dfrac{c^2}{2\beta^2}\right)\exp(-\gamma_\beta kz)\right]\cos(\omega t - kx) \\ \varepsilon_z = \dfrac{\partial u_z}{\partial z} \\ \quad = Qk\gamma_\alpha\left[\gamma_\alpha \exp(-\gamma_\alpha kz) - \gamma_\beta\left(1 - \dfrac{c^2}{2\beta^2}\right)^{-1}\exp(-\gamma_\beta kz)\right]\cos(\omega t - kx) \\ \gamma_{zx} = \dfrac{\partial u_x}{\partial z} + \dfrac{\partial u_z}{\partial x} \\ \quad = Qk\left\{-2\gamma_\alpha \exp(-\gamma_\alpha kz) + \left[\gamma_\beta\left(1 - \dfrac{c^2}{2\beta^2}\right) + \gamma_\alpha\left(1 - \dfrac{c^2}{2\beta^2}\right)^{-1}\right]\exp(-\gamma_\beta kz)\right\}\sin(\omega t - kx) \end{cases} \tag{4.12}$$

where ε_x and ε_z are the normal strains generated along the *x*- and *z*-directions, respectively, and γ_{zx} is the engineering shear strain occurring in the *zx*-plane. As illustrated in Fig. 4.5(b), the strain resulting from Rayleigh waves is planar. It consists of one shear strain and two normal strain components, and there is a phase difference of π/2 between the shear and normal strain components. Specifically, strain conditions with the above characteristics are called the Rayleigh-wave strain conditions in this thesis.

In the study of liquefaction, soils are generally assumed to be undrained, and the volume of the soil element remains constant during cyclic loading. Therefore, Rayleigh-wave strain conditions were hereinafter specified to be under a constant volume situation. Under this assumption, the bulk modulus *K* of the medium is considered to approach +∞. As $\alpha = \sqrt{[K + (4/3)\mu]/\rho}$, where μ is the shear modulus and ρ is the density of the medium, the velocity of the P waves, α also approaches +∞. Thus, ε_x and ε_z are equal in absolute value and opposite in sign. The ratio of the shear strain amplitude to the normal strain amplitude (RSN) under Rayleigh-wave strain conditions can be expressed as follows:

$$\mathrm{RSN} = \frac{\gamma_{\mathrm{amp}}}{\varepsilon_{\mathrm{amp}}} = \left| \frac{2\gamma_\alpha \exp(-\gamma_\alpha kz) - \left[\gamma_\beta \left(1 - \frac{c^2}{2\beta^2}\right) + \gamma_\alpha \left(1 - \frac{c^2}{2\beta^2}\right)^{-1}\right] \exp(-\gamma_\beta kz)}{\exp(-\gamma_\alpha kz) - \left(1 - \frac{c^2}{2\beta^2}\right) \exp(-\gamma_\beta kz)} \right| \quad (4.13)$$

where γ_{amp} is the amplitude of γ_{zx}, and $\varepsilon_{\mathrm{amp}}$ is the amplitude of ε_x and ε_z. Because $\varepsilon_x = -\varepsilon_z$, it can be derived from Eq. (4.12) that $\left(1 - \frac{c^2}{2\beta^2}\right) = \gamma_\alpha \gamma_\beta \left(1 - \frac{c^2}{2\beta^2}\right)^{-1}$. Therefore, Eq. (4.13) can be simplified as:

$$\mathrm{RSN} = \left| \frac{2\gamma_\alpha \exp(-\gamma_\alpha kz) - \frac{\gamma_\beta^2 + 1}{\gamma_\beta} \left(1 - \frac{c^2}{2\beta^2}\right) \exp(-\gamma_\beta kz)}{\exp(-\gamma_\alpha kz) - \left(1 - \frac{c^2}{2\beta^2}\right) \exp(-\gamma_\beta kz)} \right| \quad (4.14)$$

From Eq. (4.10), it can be derived that $\left(1 + \gamma_\beta^2\right)^2 = 4\gamma_\alpha \gamma_\beta$. Therefore, Eq. (4.14) can be simplified as:

$$\mathrm{RSN} = 2\gamma_\alpha \left| \frac{\exp(-\gamma_\alpha kz) - \frac{2}{\gamma_\beta^2 + 1} \left(1 - \frac{c^2}{2\beta^2}\right) \exp(-\gamma_\beta kz)}{\exp(-\gamma_\alpha kz) - \left(1 - \frac{c^2}{2\beta^2}\right) \exp(-\gamma_\beta kz)} \right| \quad (4.15)$$

Because $\left(1 - \frac{c^2}{2\beta^2}\right) = \frac{\gamma_\beta^2 + 1}{2}$, Eq. (4.15) can be simplified as:

$$\mathrm{RSN} = 2\gamma_\alpha \left| \frac{\exp(-\gamma_\alpha kz) - \exp(-\gamma_\beta kz)}{\exp(-\gamma_\alpha kz) - \left(1 - \frac{c^2}{2\beta^2}\right) \exp(-\gamma_\beta kz)} \right| = 2\gamma_\alpha \left| \frac{1 - \exp(\gamma_\alpha - \gamma_\beta kz)}{1 - \left(1 - \frac{c^2}{2\beta^2}\right) \exp(\gamma_\alpha - \gamma_\beta kz)} \right| \quad (4.16)$$

Because $\lim_{\alpha \to +\infty} \gamma_\alpha = 1$, it can be derived from Eq. (4.10) that $\lim_{\alpha \to +\infty} \gamma_\beta = 0.296$. Therefore, Eq. (4.16) can be simplified as:

$$\mathrm{RSN} = 2\left|\frac{\exp(0.704kz)-1}{1-0.544\exp(0.704kz)}\right|, z \in [0,+\infty) \tag{4.17}$$

As $k = 2\pi/\lambda_R$, where λ_R is the wavelength of the Rayleigh waves, RSN is a function of the relative depth, z/λ_R. It can be easily proved that RSN varies in the non-negative real number field (i.e., 0 ~ +∞). As illustrated in Fig. 4.6, RSN increases rapidly from 0 to +∞ within relative threshold depth z_0/λ_R, then decreases rapidly with relative depth, and finally converges to 3.68. Specifically, z_0/λ_R = 0.138. However, it should be noted that, although RSN depends on the λ_R in the Rayleigh waves, RSN in Rayleigh-wave strain conditions is not related to the real depth. RSN is only related to the shape of the strain path under Rayleigh-wave strain conditions. When RSN = 0, there is no shear strain component and the deformation of the soil element is in the pure shear mode; when RSN → +∞, there is no normal strain component and the deformation of the soil element is in the simple shear mode; and when $\mathrm{RSN} \in (0,+\infty)$, the deformation of the soil element is

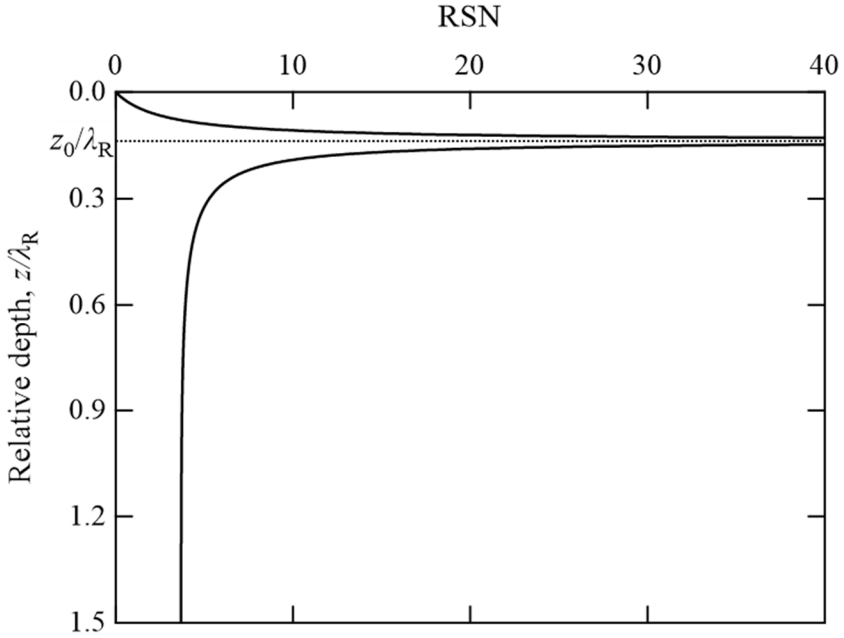

Fig. 4.6. Variation in RSN with relative depth.

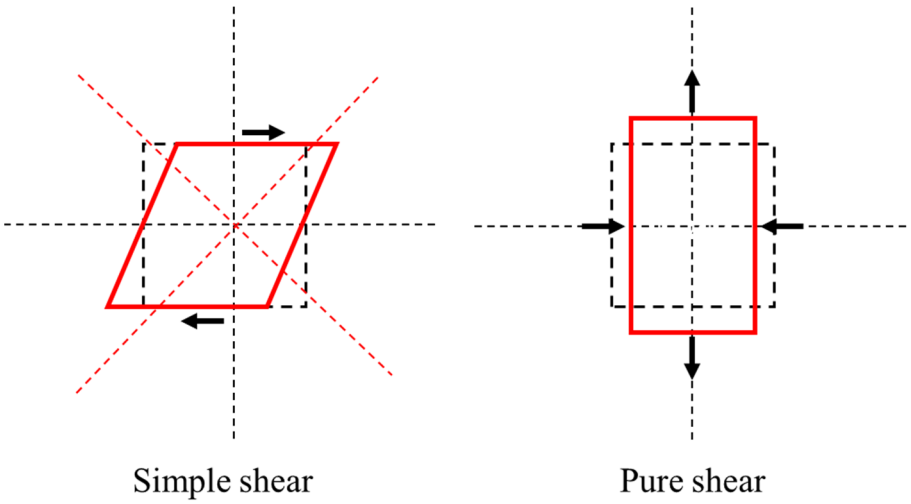

Fig. 4.7. Difference between simple shear and pure shear.

in the superposition mode of pure shear and simple shear. By the way, the difference between pure shear and simple shear is shown in Fig. 4.7. In the simple shear mode, parallel planes in a soil element remain parallel and maintain a constant distance, while being translated relative to each other. In the pure shear mode, the soil element is elongated in one direction while being shortened perpendicularly, and involve no principal strain rotation as in the simple shear mode.

4.3. DEM simulations

In this study, simulations were performed using the commercial code—Rocky (ESSS., 2020). Only spherical particles were used to improve the computation efficiency. The interaction model comprised a normal force, a tangential force, and a rolling resistance model, as introduced in Section 3.2. They were the linear spring dashpot model, linear spring Coulomb limit model, and linear spring rolling limit model, respectively.

4.3.1. Angle of repose test

The angle of repose (AoR) was used as the calibration criterion. The bulk response of the granular materials is simultaneously affected by the multiple microscopic properties. This means that the same AoR of the granular materials in the 3D DEM simulations can be achieved by different combinations of parameter values. According to Derakhshani et al. (2015), the coefficients of rolling and sliding friction are the two main parameters affecting the macroscopic properties. In other words, the friction coefficient μ and the rolling resistance coefficient μ_r have a direct influence on the reliability of the simulation results. Therefore, in this study, the values for some of the parameters were predetermined based on values in the literature. The friction coefficient μ = 0.5 was usually used in DEM simulations for granular materials (e.g., Sitharam and Dinesh, 2003; Soroush and Ferdowsi, 2011; Guo and Zhao, 2013; Wei et al., 2020), then only the rolling resistance coefficient required determination. A series of AoR tests were conducted numerically using the hollow cylinder method (Al-Hashemi and Al-Amoudi, 2018) to determine the rolling resistance coefficient. The hollow cylinder method was usually applied to determine the static angle of repose of a cohesionless material (Al-Hashemi and Al-Amoudi, 2018). The parameters used in the hollow cylinder method are shown in Table 4.1.

Table 4.1. Parameters used in the hollow cylinder method

Particles	
Diameter (mm)	0.4
Density (g/cm^3)	2.667
Young's modulus (N/m^2)	1.0×10^8
Poisson's ratio	0.3
Hollow cylinder (rigid wall)	
Young's modulus (N/m^2)	1.0×10^9
Diameter (mm)	10.8
Height (mm)	33.0
Base (rigid wall)	
Elastic modulus (N/m^2)	1.0×10^9
Length (mm)	60.0
Interactions between particles	
Static friction coefficient	0.5
Dynamic friction coefficient	0.5
Coefficient of restitution	0.3
Tangential stiffness ratio	1.0
Interactions between particles and rigid walls	
Static friction coefficient	0.5
Dynamic friction coefficient	0.5
Coefficient of restitution	0.3
Tangential stiffness ratio	1.0
Computational parameters	
Gravity (m/s^2)	9.81
Timestep (s)	1.56×10^{-7}

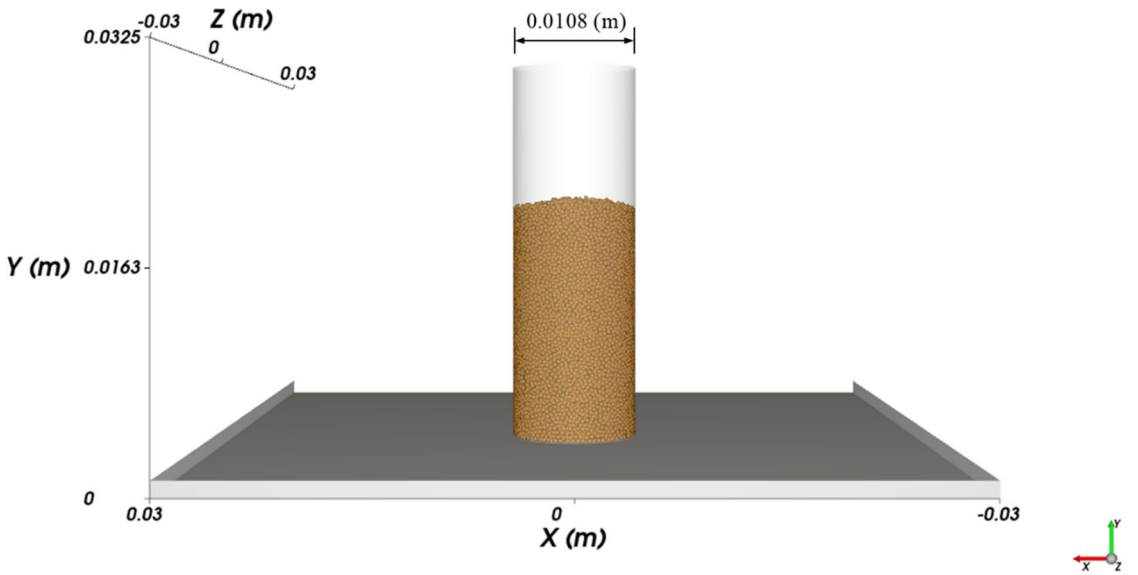

Fig. 4.8. Granular material in a hollow cylinder.

Firstly, the granular material was placed into a hollow cylinder which was on the base, as shown in Fig. 4.8. The friction coefficient between the particle and the boundary was the same as the friction coefficient between particles. Secondly, the hollow cylinder was subsequently pulled off of the base at speed of 5 mm/s. After particles stopped moving, the angle of repose could be obtained in post-processing. In the direction of the radius, a measurement cube was set up. The measurement cube was divided into 30 sub-cubes in the radial direction, as shown in Fig. 4.9. In each sub-cube, the maximum height of particles was counted. Furthermore, ignoring the maximum and minimum heights of the particles, the angle of repose of the particle material could be calculated by the least-squares method. Fig. 4.10 shows the relationship between the angle of repose and the rolling resistance coefficient when the static and dynamic friction coefficient equaled 0.5. Finally, the rolling resistance coefficient was set as 0.35, which resulted in a combination of parameter values corresponding to an AoR of 30.9°.

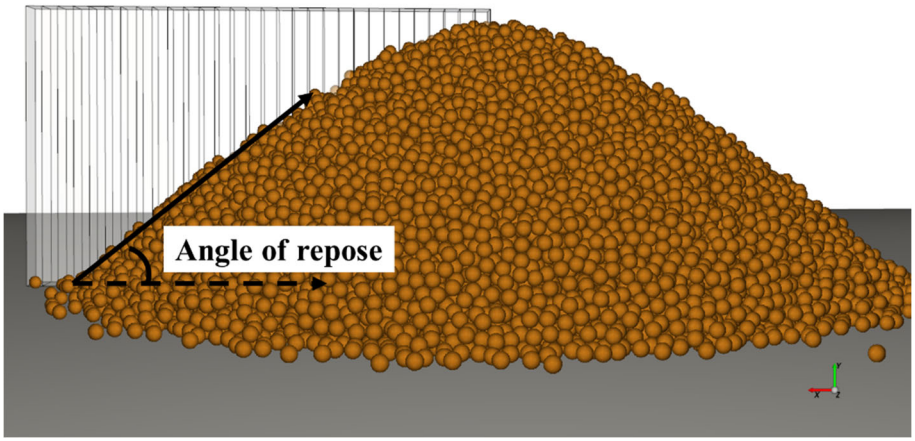

Fig. 4.9. Post-processing in Hollow cylinder method.

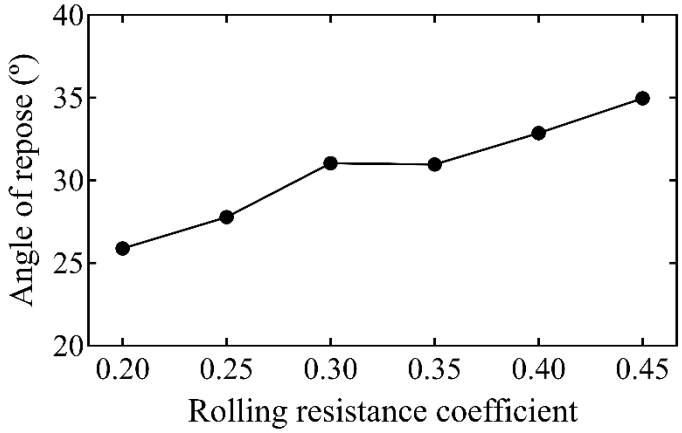

Fig. 4.10. Effect of rolling resistance coefficient on the angle of repose.

4.3.2. Specimen generation

After determining the parameters, the numerical specimens for the simulation tests were generated. Except for the friction coefficient between particles and rigid walls, the parameters concerning the particle, boundary, and interaction models were kept the same as that in the angle of repose tests. Each specimen was generated by following the procedure below: First, a rectangular cuboid volume element measuring 10 mm × 10 mm × 20 mm was formed by six frictionless boundary walls. Second, particles from an inlet

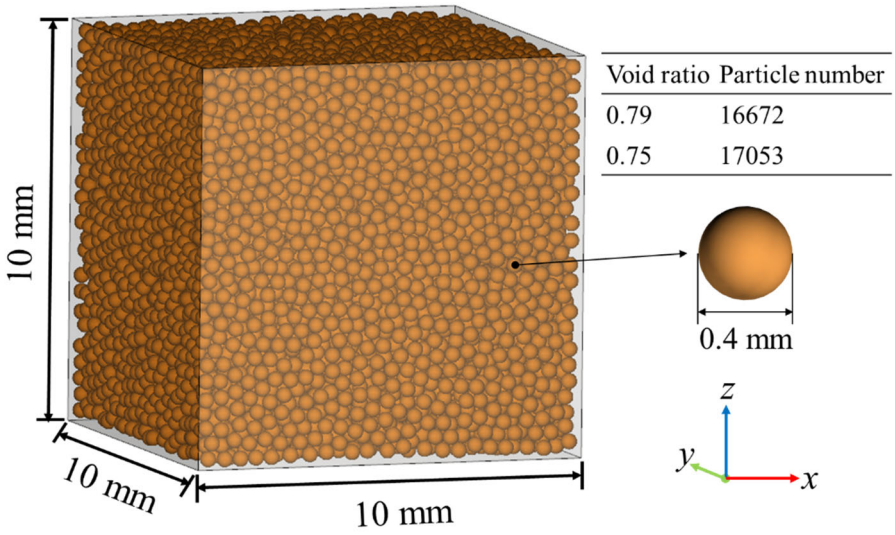

Fig. 4.11. A generated numerical specimen.

below the upper boundary wall were dispersed uniformly into the bottom of the space. During this process, the gravitational acceleration was set to 0.1 m/s^2 such that the particles would rebound slightly and a homogenous specimen would be obtained. Third, the volume element was compacted into a cube by moving the upper boundary wall downward at a constant speed of 0.2 mm/s. In this step, the rolling resistance coefficient was adjusted iteratively before compaction to ensure that the specimen reached a mean effective stress state of 100 kPa. Finally, the rolling resistance coefficient was set to 0.35 again. The generated specimen (granular packing) is shown in Fig. 4.11 and it was in the K_0-consolidation state. Specimens with void ratios of 0.79 (loose) and 0.75 (medium dense) were generated to represent soil elements of different bulk densities containing 16,672 and 17,053 particles, respectively. The K_0-values of the specimens with void ratios of 0.79 and 0.75 were 0.54 and 0.60, respectively. Specifically, $K_0 = (\sigma_x + \sigma_y)/2\sigma_z$, where σ_x, σ_y, and σ_z are the normal stresses acting in the x-, y-, and z-directions, respectively.

4.3.3. Simulation conditions

Nine types of cyclic strain were applied to the specimens to cover the strain features of SHH-wave strain condition, SHV-wave strain condition, Love-wave strain conditions with AR = 0.25, 1, and 4, and Rayleigh-wave strain conditions with RSN = 0, 0.25, 1, and 4, respectively. Especially, the Rayleigh-wave strain condition with an RSN = +∞, the Love-wave strain condition with an AR = +∞, and the SHV-wave strain condition are equivalent; the Love-wave strain condition with an AR = 0 equals the SHH-wave strain condition. The deformation of the specimens was achieved by moving the boundary walls. During cyclic loading, the specimen volume was kept constant to avoid the computational complexity of the fluid-coupled model (CV method). Furthermore, no gravity was applied to the sample to reproduce the particle suspension phenomenon in the liquefied state.

The accumulated equivalent strain, ε^*_{eqv} (Jiang et al., 2021), was adopted to evaluate the level of cumulative change in strains under different Rayleigh-wave strain conditions. It is defined as

$$\varepsilon^*_{\mathrm{eqv}} = \sum \sqrt{\frac{4}{3} J_{2\Delta\varepsilon}}$$

$$= \sum \sqrt{\frac{2}{9}\left[\left(\Delta\varepsilon_x - \Delta\varepsilon_y\right)^2 + \left(\Delta\varepsilon_y - \Delta\varepsilon_z\right)^2 + (\Delta\varepsilon_z - \Delta\varepsilon_x)^2\right] + \frac{1}{3}\left(\Delta\gamma_{xy}^2 + \Delta\gamma_{yz}^2 + \Delta\gamma_{zx}^2\right)} \quad (4.18)$$

where $J_{2\Delta\varepsilon}$ is the second invariant of the deviatoric strain increment tensor, $\Delta\varepsilon_x$, $\Delta\varepsilon_y$, and $\Delta\varepsilon_z$ are the normal strain increments in the *x*-, *y*-, and *z*-directions, respectively, and $\Delta\gamma_{xy}$, $\Delta\gamma_{yz}$, and $\Delta\gamma_{zx}$ are the engineering shear strain increments generated in the *xy*-, *yz*-, and *zx*-planes, respectively. The maximum shear strain amplitudes under the SHH- and SHV-

wave strain conditions were set to be 1.00%. The maximum strain amplitudes under other strain conditions were determined by making the increment in ε^*_{eqv} per loading cycle the same as that under the SHH- and SHV- wave strain conditions; they are summarized in Table 4.2.

Table 4.2. Maximum strain amplitudes under each strain condition

Condition	Maximum ε_x or ε_z	Maximum γ_{xy}	Maximum γ_{yz}	Maximum γ_{zx}
SHH	0.00%	1.00%	0.00%	0.00%
SHV	0.00%	0.00%	1.00%	0.00%
Love, AR = 0.25	0.00%	0.23%	0.93%	0.00%
Love, AR = 1	0.00%	0.64%	0.64%	0.00%
Love, AR = 4	0.00%	0.93%	0.23%	0.00%
Rayleigh, RSN = 0	0.50%	0.00%	0.00%	0.00%
Rayleigh, RSN = 0.25	0.49%	0.00%	0.00%	0.12%
Rayleigh, RSN = 1	0.41%	0.00%	0.00%	0.41%
Rayleigh, RSN = 4	0.83%	0.00%	0.00%	0.21 %

Fig. 4.12 illustrates the loading paths under each strain condition, in which γ is the shear strain, ε is the normal strain, including ε_x and ε_z ($\varepsilon_x = -\varepsilon_z$, and the direction of ε axis is consistent with ε_z). The strain amplitudes gradually increased from 0 to their maximum value within 10 cycles, and then remained constant. This loading method caused the applied strain to cover a wide range of amplitudes (El Shamy and Denissen, 2012), facilitating the elimination of the influence of different initial states under different ARs and RSNs on the controlled trials as well (the initial phases of γ_{yz} under Love-wave strain conditions with AR = 0.25 and 1, the initial phases of γ_{xy} under Love-wave strain condition with AR = 4) and γ_{zx} under Rayleigh-wave conditions are $\pi/2$). Since there was only one shear strain component or only normal strain components, the strain paths are vertical or

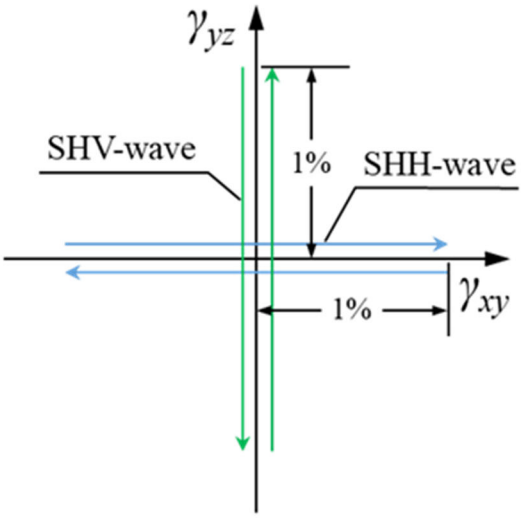

(a) SH-waves (simple shear)

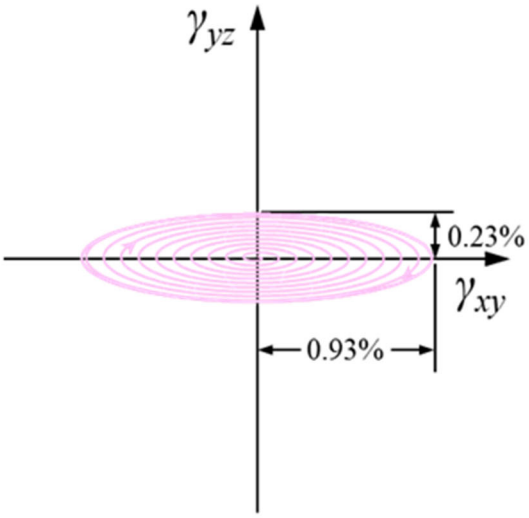

(b) Love-wave, AR = 0.25

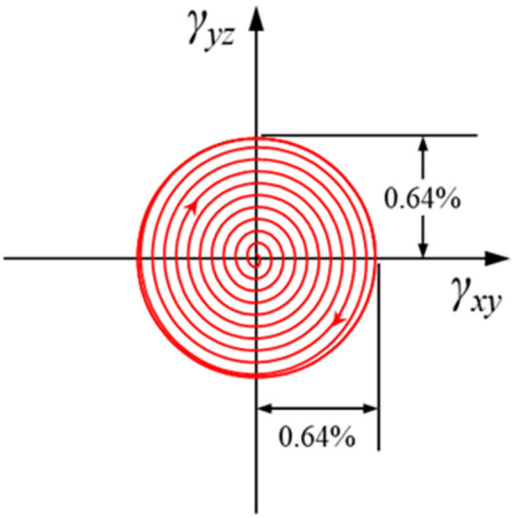

(c) Love-wave, AR = 1

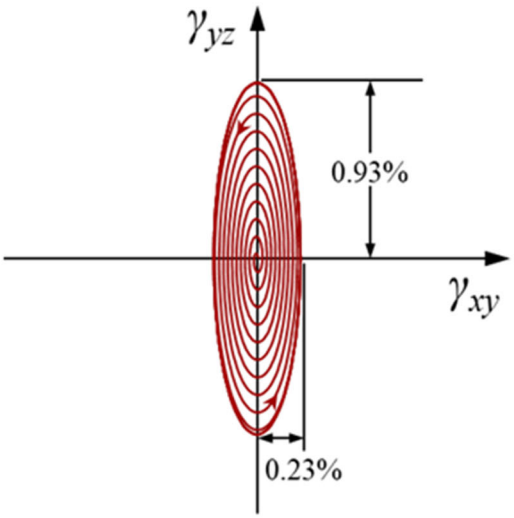

(d) Love-wave, AR = 4

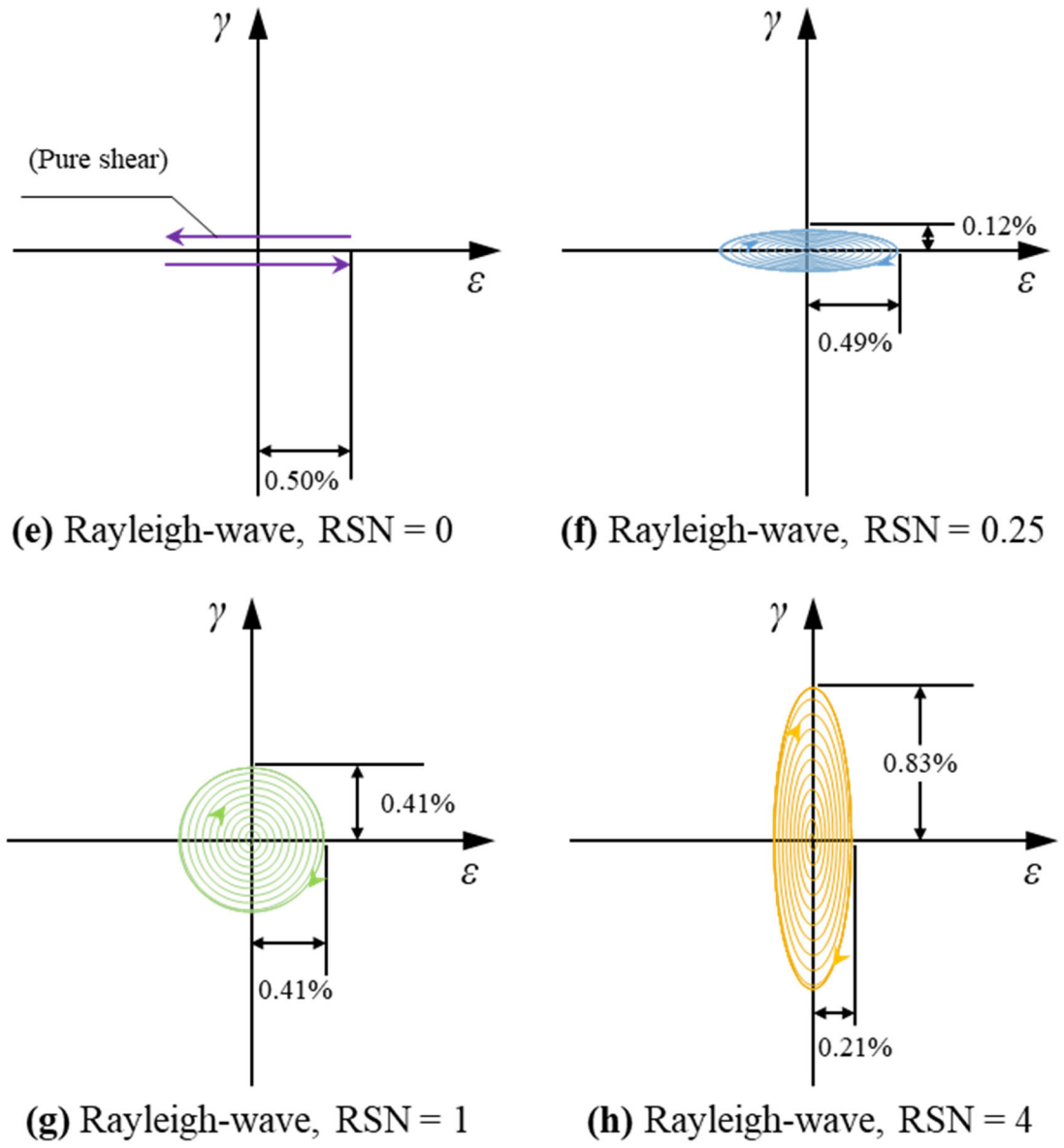

Fig. 4.12. loading paths under different strain conditions defined in this study (γ is the shear strain, and ε is the normal strain including ε_x and ε_z; $\varepsilon_x = -\varepsilon_z$ and the direction of the ε axis is consistent with ε_z).

horizontal lines under SH-wave strain conditions (Fig. 4.12(a)) and the Rayleigh-wave strain condition with RSN = 0 (Fig. 4.12(e)), respectively. In contrast, the strain paths are ellipses or circles under other strain conditions because two shear strain components (Love-wave strain conditions), or shear and normal strain components (Rayleigh-wave strain conditions with RSN = 0.25, 1, and 4) exist simultaneously and they are out of phase by π/2.

The simulations were run under quasi-static conditions, where the inertial effects were ignorable and there was no strain-rate dependency. In this study, the cyclic loadings were all applied at a frequency of 5 Hz. The strain rate applied on specimens at this frequency satisfies the $I = \dot{\varepsilon} d \sqrt{\rho / p'_{\mathrm{PT}}} < 2.5 \times 10^{-3}$ criterion (Perez et al., 2016), where I is the inertial number, $\dot{\varepsilon}$ is the strain rate, d is the diameter of the particles, ρ is the solid density, and p'_{PT} is the mean effective stress at the phase transformation.

4.4. Simulation results

4.4.1. Macroscopic scale

4.4.1.1. Stress–strain relationship

A measurement cube with a size of 9 mm × 9 mm × 9 mm was generated in the center of the specimen to measure the stress tensor. Fig. 4.13 shows the 3D shear stress relationship with the mean effective stress of the granular packings under each strain condition. The label of the x-axis represents mean effective stress. For SH- and Love-wave strain conditions, labels of the y-axis and of the z-axis are τ_{xy} and τ_{yz}, respectively (Fig. 4.13(a)–(j)); for Rayleigh-wave strain conditions (SHV-wave strain condition can

be regarded as the Rayleigh-wave strain condition with RSN = +∞), labels of the *y*-axis and of the *z*-axis are τ_{zx} (except for τ_{yz} in the SHV-wave strain condition) and $\sigma_v - \sigma_h$, respectively (Fig. 4.13(k)–(t)), where $\sigma_v = \sigma_{zz}$ and $\sigma_h = (\sigma_{xx} + \sigma_{yy})/2$. The change in the color of the paths from red to purple corresponds to a decrease in the mean effective stress from 100 kPa to approximately 0 kPa. Initially, because of the gradual application of shear strain, the shear stress (including stress $\sigma_v - \sigma_h$) amplitudes increased gradually with a slow decrease in the mean effective stress until the maximum shear stress amplitudes were attained. Subsequently, as the cyclic loading continued, the shear stress amplitudes and the mean effective stress decreased until initial liquefaction occurred. In this study, the initial liquefaction was defined by the mean effective stress being less than 10^{-3} kPa the first time. Generally, the larger the amplitude of the strain in one direction or plane, the larger the shear stress amplitude in this direction or plane, which results in the different shapes of stress paths under different strain conditions. The dilatancy behavior appeared during cyclic loadings under SH-, Love-, and Rayleigh-wave strain conditions. Especially, the dilatancy behaviors are more obvious under SH-and Rayleigh-wave strain conditions than under Love-wave strain conditions. Significantly, no obvious phase transformation was observed during cyclic loadings under the Love-wave strain condition with AR = 1, as shown in Fig. 4.13(g) and (h).

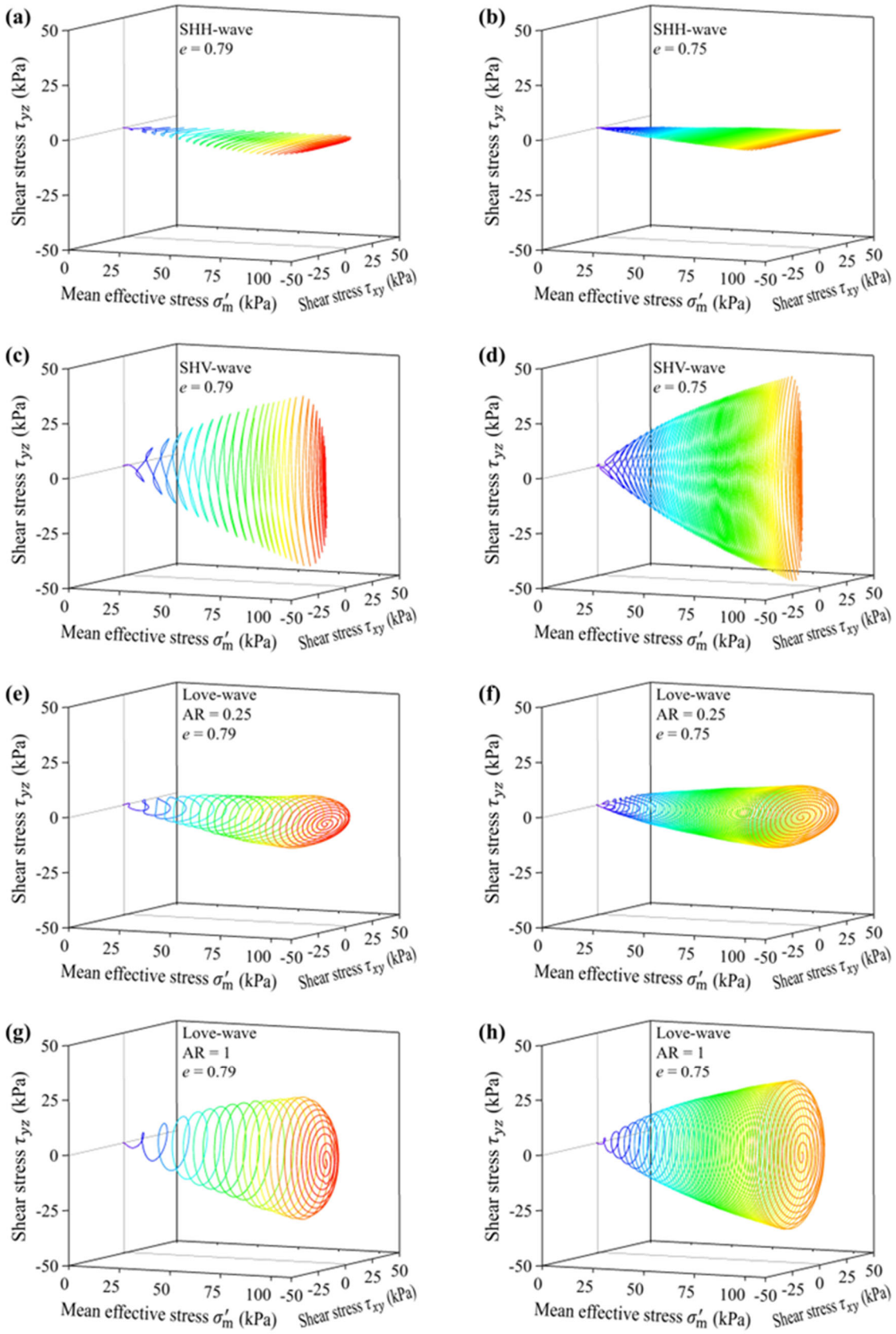
(a)
SHH-wave
e = 0.79
(b)
SHH-wave
e = 0.75
(c)
SHV-wave
e = 0.79
(d)
SHV-wave
e = 0.75
(e)
Love-wave
AR = 0.25
e = 0.79
(f)
Love-wave
AR = 0.25
e = 0.75
(g)
Love-wave
AR = 1
e = 0.79
(h)
Love-wave
AR = 1
e = 0.75
Shear stress τyz (kPa)
Mean effective stress σ′m (kPa)
Shear stress τxy (kPa)

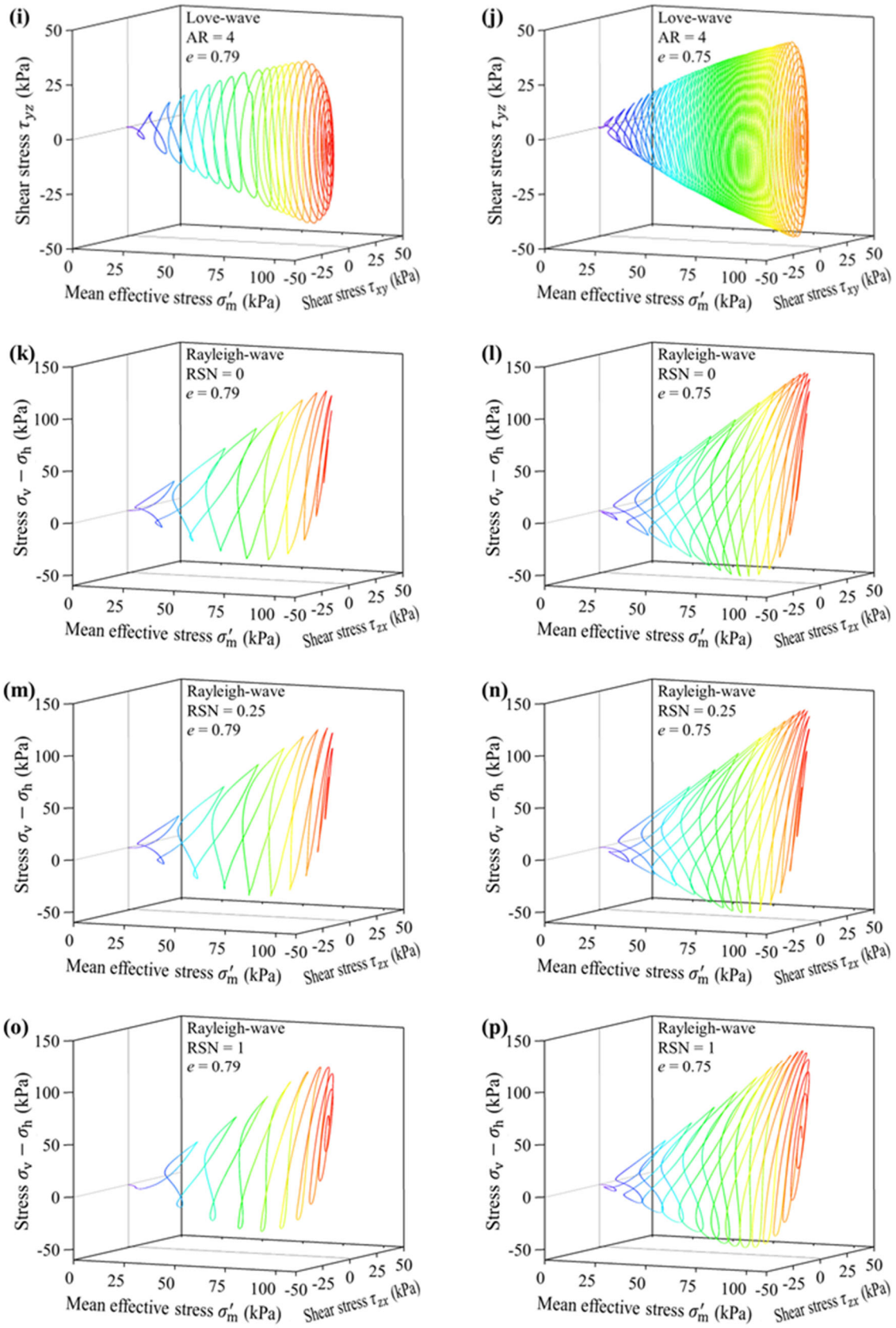
(i)
Love-wave
AR = 4
e = 0.79
Shear stress τyz (kPa)
Mean effective stress σ′m (kPa)
Shear stress τxy (kPa)
(j)
Love-wave
AR = 4
e = 0.75
Shear stress τyz (kPa)
Mean effective stress σ′m (kPa)
Shear stress τxy (kPa)
(k)
Rayleigh-wave
RSN = 0
e = 0.79
Stress σv − σh (kPa)
Mean effective stress σ′m (kPa)
Shear stress τzx (kPa)
(l)
Rayleigh-wave
RSN = 0
e = 0.75
Stress σv − σh (kPa)
Mean effective stress σ′m (kPa)
Shear stress τzx (kPa)
(m)
Rayleigh-wave
RSN = 0.25
e = 0.79
Stress σv − σh (kPa)
Mean effective stress σ′m (kPa)
Shear stress τzx (kPa)
(n)
Rayleigh-wave
RSN = 0.25
e = 0.75
Stress σv − σh (kPa)
Mean effective stress σ′m (kPa)
Shear stress τzx (kPa)
(o)
Rayleigh-wave
RSN = 1
e = 0.79
Stress σv − σh (kPa)
Mean effective stress σ′m (kPa)
Shear stress τzx (kPa)
(p)
Rayleigh-wave
RSN = 1
e = 0.75
Stress σv − σh (kPa)
Mean effective stress σ′m (kPa)
Shear stress τzx (kPa)

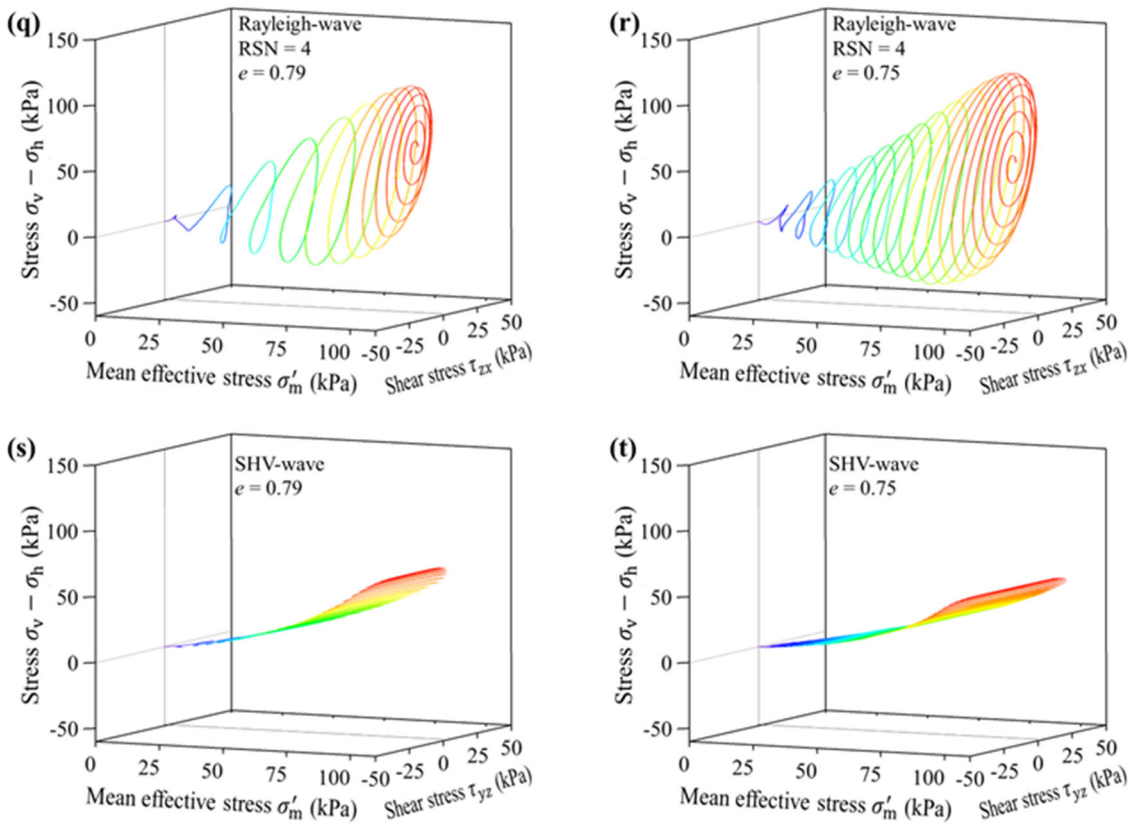

Fig. 4.13. Shear stress relationship with mean effective stress of granular packings under SH-, Love, and Rayleigh-wave strain conditions in 3D space.

The effective stress reduction ratio (ESRR) evolution with the accumulated equivalent strain during the cyclic loadings is illustrated in Fig. 4.14, in which the ESRR is defined by:

$$\mathrm{ESRR} = 1 - \frac{\sigma'_{\mathrm{m}}}{\sigma'_{\mathrm{m,0}}} \tag{4.19}$$

where σ'_{m} denotes the mean effective stress, and $\sigma'_{\mathrm{m,0}}$ is the initial mean effective stress. In this study, instead of the excess pore water pressure ratio, ESRR was used to express the extent of effective stress reduction. Because in the K_0-consolidated specimen, the amount of decrease in mean effective stress does not equal the amount of increase in excess pore water pressure. Furthermore, the CV method was used in simulations, in

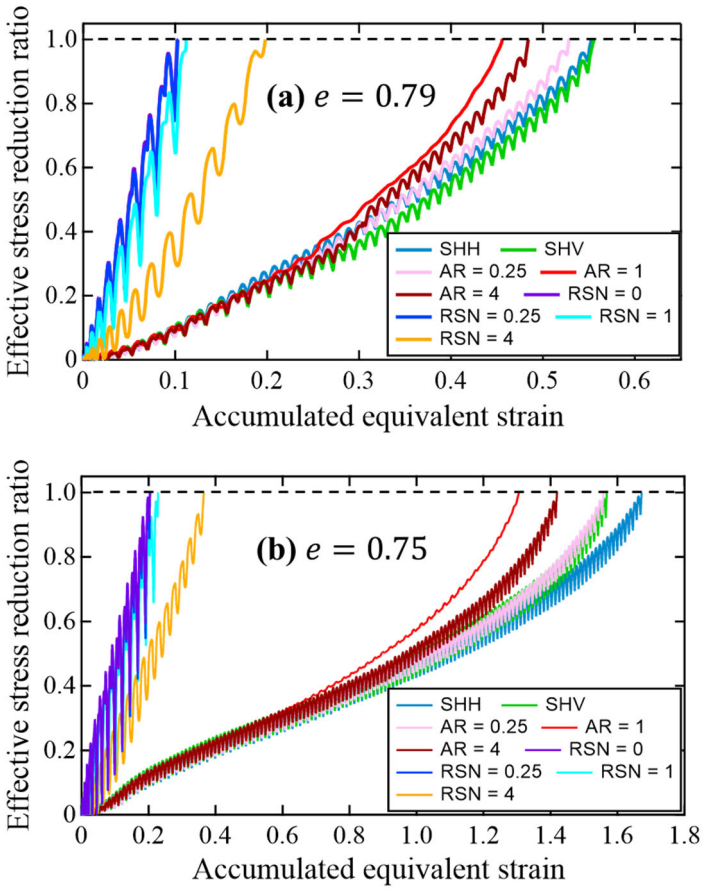

Fig. 4.14. Effective stress reduction ratio vs. accumulated equivalent strain.

which the fluid phase was not taken into consideration. Therefore, ESRR is a better choice than the excess pore water pressure ratio in this study.

SH- and Love-wave strain conditions are simple shear modes or a combination of simple shear modes. Under these strain conditions, regardless of the specimen density, when the ESRR was less than 0.4, the loading paths did not have a significant effect on the increase in the ESRR in terms of speed (accumulated equivalent strain). However, when beyond 0.4, the ESRR under Love-wave strain conditions increased more rapidly than that under SH-wave strain conditions. The liquefaction rate in terms of the accumulated equivalent strain under Love-wave strain conditions was highly influenced by AR. When AR = 1, which meant that the shear strain amplitudes in two planes are the same, the specimens liquefied the fastest. When AR was farther from 1 (being closer to 0 or $+\infty$), which meant that the larger the difference between shear strain amplitudes in two planes, the specimens liquefied at a slower rate. The Rayleigh-wave strain condition is a combination of simple shear mode and pure shear mode. Under Rayleigh-wave strain conditions, the evolution of the ESRR was significantly affected by the RSN. In general, the smaller the RSN, which meant the larger the amplitude of normal strains, the faster the liquefaction rate of specimens. However, when RSN $\leq$ 1, the specimen under different Rayleigh-wave strain conditions liquefied at a similar rate. Generally, the order of liquefaction rate in terms of the accumulated equivalent strain was Rayleigh-wave strain conditions > Love-wave strain conditions > SH-wave strain conditions.

In addition, fluctuations in the ESRR were observed during the cyclic loadings except for the Love-wave strain condition with AR = 1. This phenomenon concerning Love-wave strain conditions was consistent with the findings of Matsuda et al. (2011),

who concluded that the fluctuation in the effective stress (i.e., ESRR) was dominated by the change in the resultant shear strain Γ during cyclic loadings. In their experiments, shear strains in the vertical plane (γ_{xz} and γ_{yz}) were applied, and Γ is defined as

$$\Gamma = \sqrt{\gamma_{xz}^2 + \gamma_{yz}^2} \tag{4.20}$$

which shows the radial distance from the origin in the shear strain path of the vertical components. A larger amplitude of Γ will result in a larger fluctuation in the ESRR. In particular, in the case of multidirectional shear with two equal horizontal shear strain components and a phase difference of π/2, where Γ is a constant, the decrease in the effective stress ratio is smooth. In this study, although one of the shear strain components under the Love-wave strain condition was in the horizontal plane (γ_{xy}), the ESRR increased relatively smoothly when AR = 1. In addition, the fluctuation of the ESRR under the Love-wave strain condition with AR = 0.25 and 4 was larger than that under the Love-wave strain condition with AR = 1 but was similar to that under SH-wave strain conditions. Therefore, if replace γ_{xz} in Eq. (4.20) with γ_{xy}, it is reasonable to conclude that the fluctuation in the ESRR during cyclic loadings under the Love-wave strain condition was also affected by the amplitude of Γ.

The fluctuations in the ESRR under Rayleigh-wave strain conditions were much greater than those under Love- and SH-wave strain conditions. Uthayakumar and Vaid (1998) pointed out that the undrained response of loose sand strongly depends on the inclination of the major principal stress direction to the deposition direction. Similarly, under Rayleigh-wave strain conditions, the normal strain component ε_z was consistent with the deposition direction. A larger amplitude of normal strain components and a

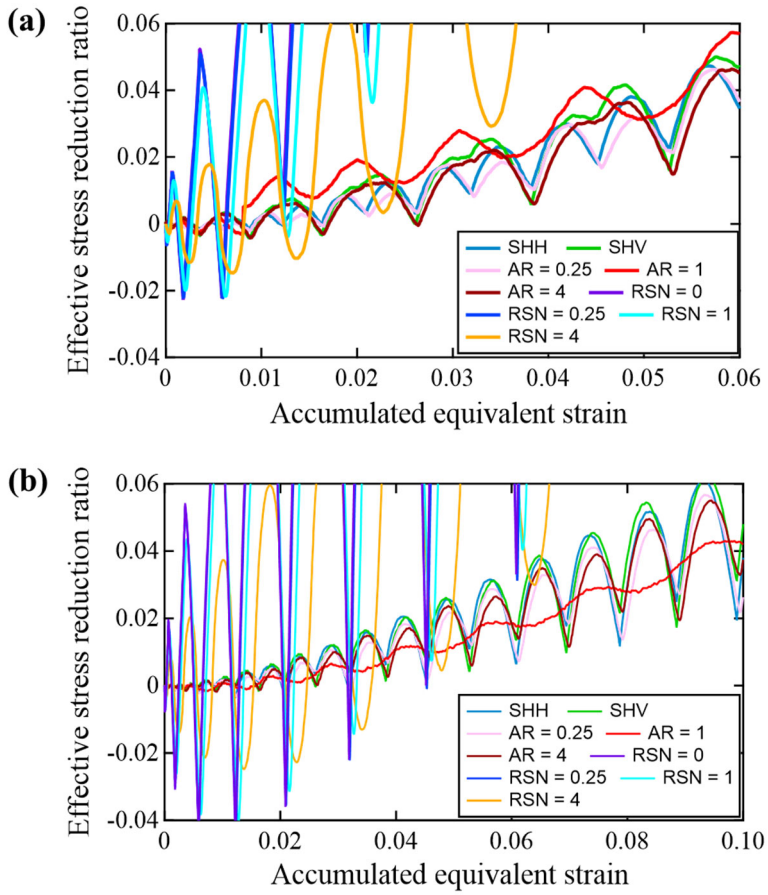

Fig. 4.15. Effective stress reduction ratio versus accumulated equivalent strain (a) e = 0.79 and (b) e = 0.75 in small strain amplitude range (enlarged part of Fig. 4.14).

smaller amplitude of the shear strain component would make the principal strain increment closer to the deposition direction, which will be discussed in Section 4.4.2.1 Therefore, compared to the SHV-wave strain condition (equal to the Rayleigh-wave strain condition with RSN = $+\infty$) without pure shear mode, the Rayleigh-wave strain conditions containing a pure shear mode had a larger fluctuation in the ESRR during cyclic loadings. This phenomenon was prominent in a small strain amplitude range, as illustrated in Fig. 4.15, which is the enlargement of a part of Fig. 4.14. These findings suggested that the positive dilatancy behavior of K_0-consolidated soils in the pure shear mode was more sensitive to the strain level than that in the simple shear mode.

Fig. 4.16 illustrates the relationship between the von Mises stress and the mean effective stress under different strain conditions. The von Mises stress, σ_{vM}, is given by:

$$\sigma_{vM} = \sqrt{\frac{1}{2}\left[\left(\sigma_x - \sigma_y\right)^2 + \left(\sigma_y - \sigma_z\right)^2 + (\sigma_z - \sigma_x)^2 + 6\left(\tau_{xy}^2 + \tau_{yz}^2 + \tau_{zx}^2\right)\right]} \quad (4.21)$$

As the specimens were in the K_0-consolidation state, the von Mises stress was not initially zero. In addition, the amplitude and average value of the von Mises stress during each cycle initially increased and then decreased with the gradual application of shear strain. An exception is that specimens with e = 0.79 under the SHH-wave strain condition and the Love-wave strain condition with AR = 0.25, as shown in Fig. 4.16(a), the average value of the von Mises stress of the granular packing with a void ratio of 0.79 during each cycle decreased from the first cycle. In addition, as shown in Fig. 4.16(a) and (b), the average values of the von Mises stress during each cycle under both the SHH-wave strain condition and the Love-wave strain condition with AR = 0.25 were smaller than those under either the SHV-wave strain condition or the Love-wave strain condition with AR = 4 when the mean effective stresses were approximately identical. These phenomena suggested that the proportion of the amplitude of the horizontal shear strain component (γ_{xy}) to the amplitude of the vertical shear strain component (γ_{yz}) affects the value of the von Mises stress. A higher proportion of the amplitude of the horizontal shear strain component would cause the granular packings to be subjected to smaller von Mises stresses in the K_0-consolidation state when the granular packings were in the same mean effective stress state.

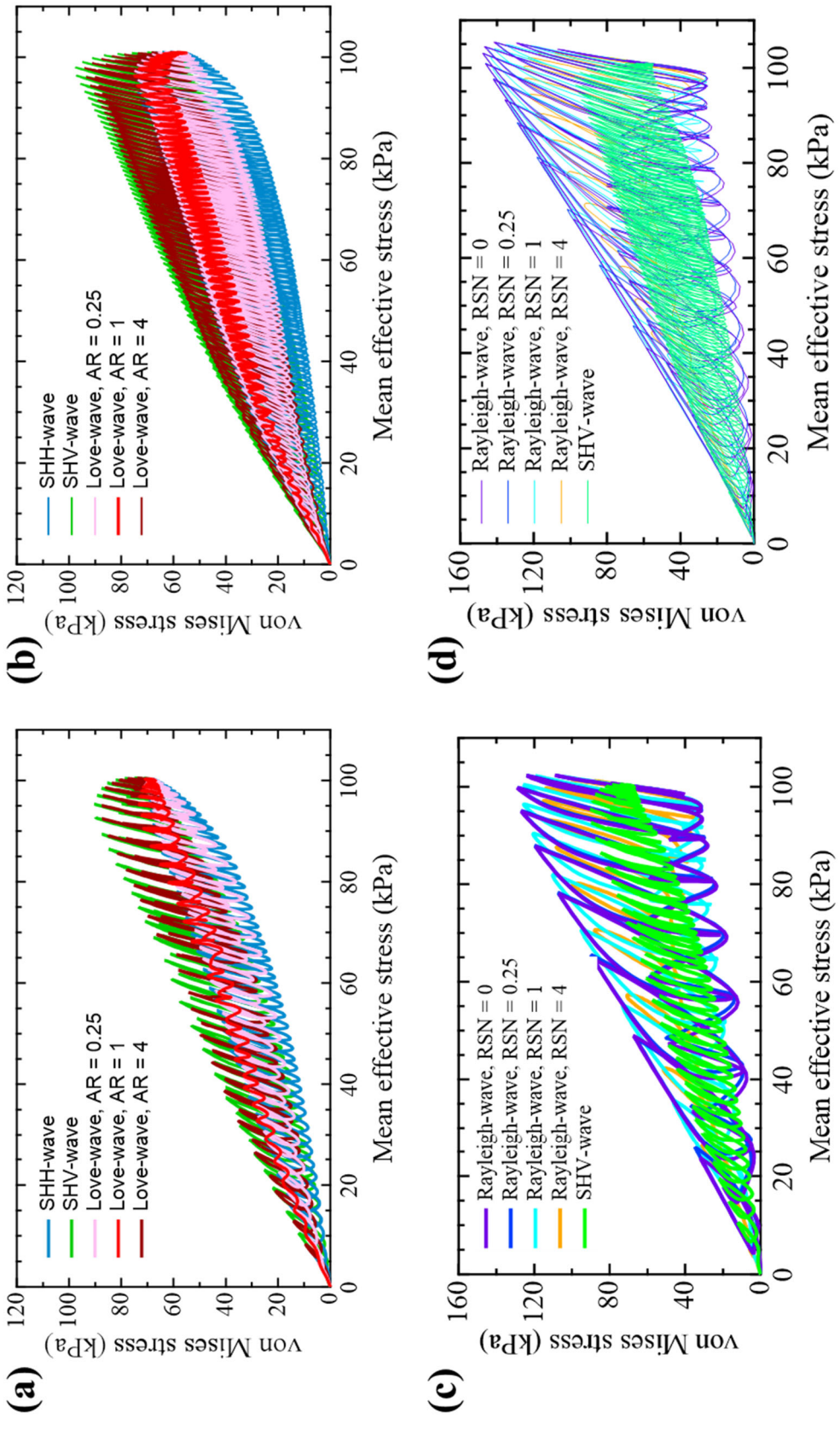

Fig. 4.16. von Mises stress relationship with mean effective stress of granular packings under (a) SH- and Love-wave strain conditions with $e = 0.79$; (b) SH- and Love-wave strain conditions with $e = 0.75$; (c) SHV- and Rayleigh-wave strain conditions with $e = 0.79$; (d) SHV- and Rayleigh-wave strain conditions with $e = 0.75$.

As shown in Fig. 4.16(a) and (b), the fluctuation in the von Mises stress under the Love-wave strain condition with AR = 1 was much smaller than that under the other conditions. In addition, the fluctuations in the von Mises stress under the Love-wave strain conditions with AR = 0.25 and 4 were smaller than those under the SHH- and SHV-wave strain conditions, respectively. This phenomenon was consistent with the fact that the fluctuations in Γ under the Love-wave strain conditions with ARs = 0.25 and 4 were smaller than those under the SH-wave strain conditions but much larger than that under the Love-wave strain condition with AR = 1. Because of the anisotropy originating from the K_0-consolidation, fluctuations in the von Mises stress were not zero in under the Love-wave strain condition with AR = 1. It was reasonable to conclude that the fluctuation in the von Mises stress under cyclic loading was affected by the fluctuation in Γ.

The specimens under Rayleigh-wave strain conditions containing a pure shear mode (RSN = 0, 0.25, 1, and 4) generally experienced a significantly larger magnitude of von Mises stress than those under the SHV-wave strain containing (equals Rayleigh-wave strain condition with RSN = $+\infty$) only simple shear model. In a certain mean effective stress state, the maximum von Mises stress that the specimens endured increased with a decrease in the RSN. In particular, the difference disappeared when RSN $\leq$ 1.

4.4.1.2. Liquefaction resistance

Fig. 4.17 illustrates the evolution of the ESRR with NDE at the end of each loading cycle until the initial liquefaction. In this study, the normalized accumulated dissipation energy (NDE), defined as the accumulated dissipation energy normalized by the initial mean effective stress, was used to evaluate the resistance of granular materials to liquefaction under different loading conditions. The ESRR increased with the NDE,

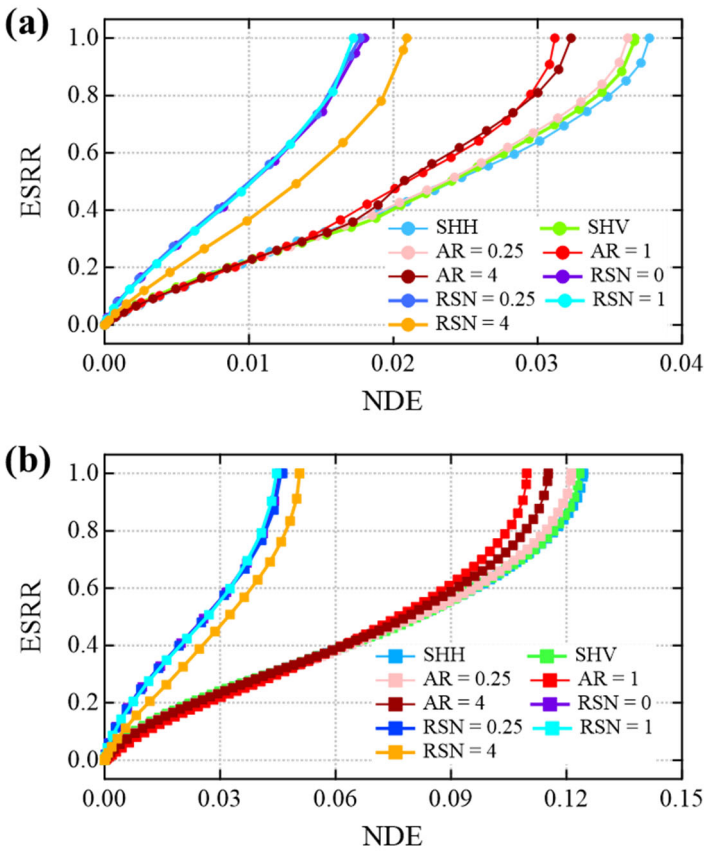

Fig. 4.17. Effective stress reduction ratio versus normalized accumulated dissipation energy up to initial liquefaction: (a) e = 0.79 and (b) e = 0.75.

which was similar to those shown in Fig. 4.14. When the ESRR was less than 0.4, the paths coincided under SH- and Love-wave strain conditions; when beyond 0.4, the ESRR increased more rapidly under the Love-wave strain conditions. Consequently, the granular packing under the Rayleigh-wave strain conditions and Love-wave strain conditions indicated a lower NDE when initial liquefaction occurred. Therefore, it can be concluded that granular materials under the surface-wave strain conditions were more vulnerable to liquefaction than those under the SH-wave strain conditions. In particular, the rate of decrease in the resistance to liquefaction under the Rayleigh- and Love-wave strain conditions was affected by the RSN and AR respectively.

To quantitatively evaluate the degree to which surface-wave strain conditions may affect the liquefaction resistance of granular materials, the NDEs at the initial liquefaction under Love- and Rayleigh-wave strain conditions were compared with those under SH-wave strain conditions, as shown in Fig. 4.18. The relative normalized accumulated dissipation energy (RNDE) was defined as the ratio of the NDE under each loading condition to that under the SHV-wave strain condition. Firstly, the histogram part of Fig. 4.18 shows that the looser specimen was more vulnerable to liquefaction under all strain conditions. Secondly, the degree of decrease in the liquefaction resistance was affected by the void ratio of the granular packings. Compared with the granular packing with a void ratio of 0.79, the granular packing with a void ratio of 0.75 had a larger reduction in the RNDE under the Love-wave strain conditions and Rayleigh-wave strain conditions. Therefore, it could be concluded that the decrease in liquefaction resistance was more

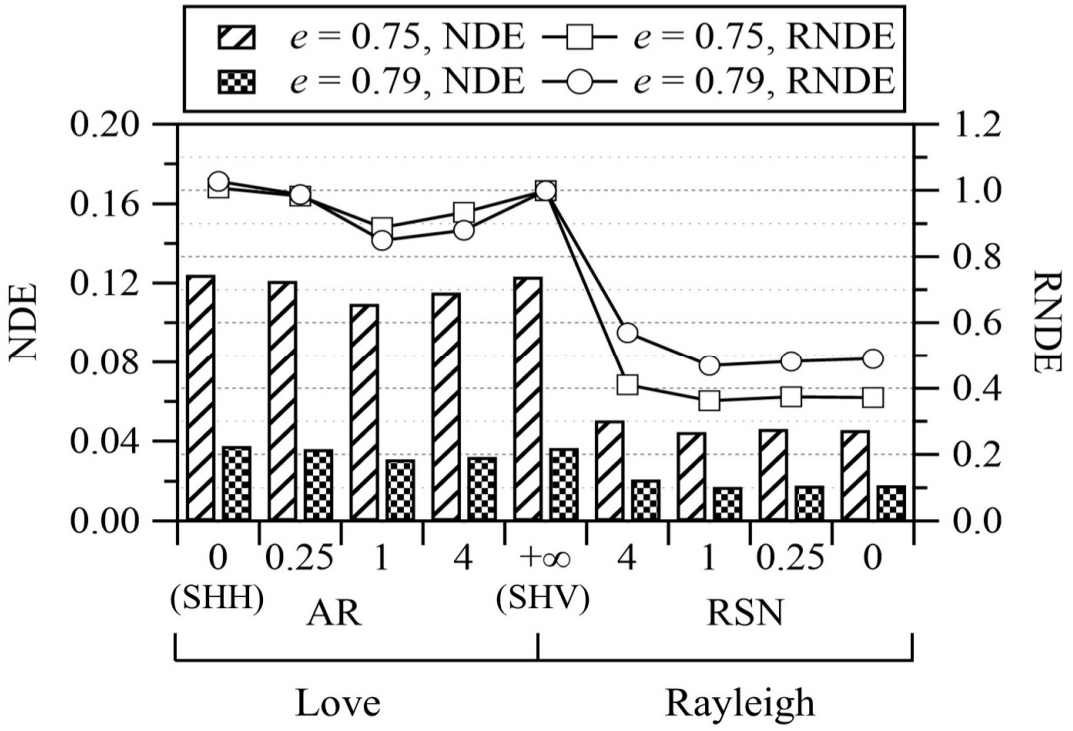

Fig. 4.18. Relationship of NDE and RNDE to AR/RSN at the initial liquefaction state.

remarkable for the denser specimen transitioning from under the SHV-wave strain condition to under the surface-wave strain conditions, especially to under Rayleigh-wave strain conditions. Lastly, as shown in the left part of Fig. 4.18, with an increase in the AR, the RNDE in the initial liquefaction firstly decreased and subsequently increased regardless of the void ratio. It reached the lowest value at AR = 1. In addition, the liquefaction resistance of granular materials under the SHH-wave strain condition was similar to that under the SHV-wave strain condition. In the right part of Fig. 4.18, as the RSN decreased from $+\infty$ to 0, the RNDE dropped rapidly and then increased slightly. The specimen was most vulnerable to liquefaction when RSN = 1, where specimens suffered a loss in liquefaction resistance of more than 50%. However, the difference in liquefaction resistance was negligible when RSN $\leq$ 1.

The liquefaction resistance of granular materials under Love-wave strain conditions was 80–100% of that under SH-wave strain conditions, whereas the liquefaction resistance of granular materials under Rayleigh-wave strain conditions might be lower than 50% of that under SH-wave strain conditions. Therefore, at the same strain level, it could be concluded that the Rayleigh-wave strain condition with a low RSN value would make granular materials more vulnerable to liquefaction than Love-wave strain conditions, and granular materials under Love-wave strain conditions were more likely to liquefy than under SH-wave strain conditions.

4.4.2. Microscopic scale

4.4.2.1. Normal contact force

The normal contact force-chain network, through which the external load is transferred, is an important aspect of granular assembly. It is fundamental in controlling the macroscopic behavior of granular materials. Generally, liquefaction is associated with the progressive degradation of the major force transmission network (Huang et al., 2019). Fig. 4.19 and Fig. 4.20 show the evolution of the normal contact force-chain network in the granular packing with a void ratio of 0.79 under both the SHV-wave strain condition and the Love-wave strain condition with AR = 1, respectively. The color indicates the maximum normal force borne by a particle. The chains formed by the particles that sustain a much larger maximum normal force than the surrounding particles can be regarded as the backbone force-chain, which transmits the majority of the load. As shown in Fig. 4.19, at points 0, 1, 3, 5, 7, and 9, when the shear strain was zero, the backbone force-chains were generally randomly orientated. However, owing to the effect of the K_0-consolidation, the force-chains in the *z*-direction were stronger than those in the horizontal direction (*x*- and *y*-directions). At points 2, 4, 6, and 8, when the shear strain was maximum (minimum), the normal force-chains were concentrated and aligned in the shorter diagonal direction in the *yz*-plane. This suggests that, with the development of shear strain, the dominant direction of the backbone force-chains rotated in the *yz*-plane and was consistent with the direction of the principal strain rotation. This rule was applicable to the Love-wave strain conditions, as shown in Fig. 4.20. In contrast, the dominant direction of the backbone force-chains under the Love-wave strain conditions rotated spatially.

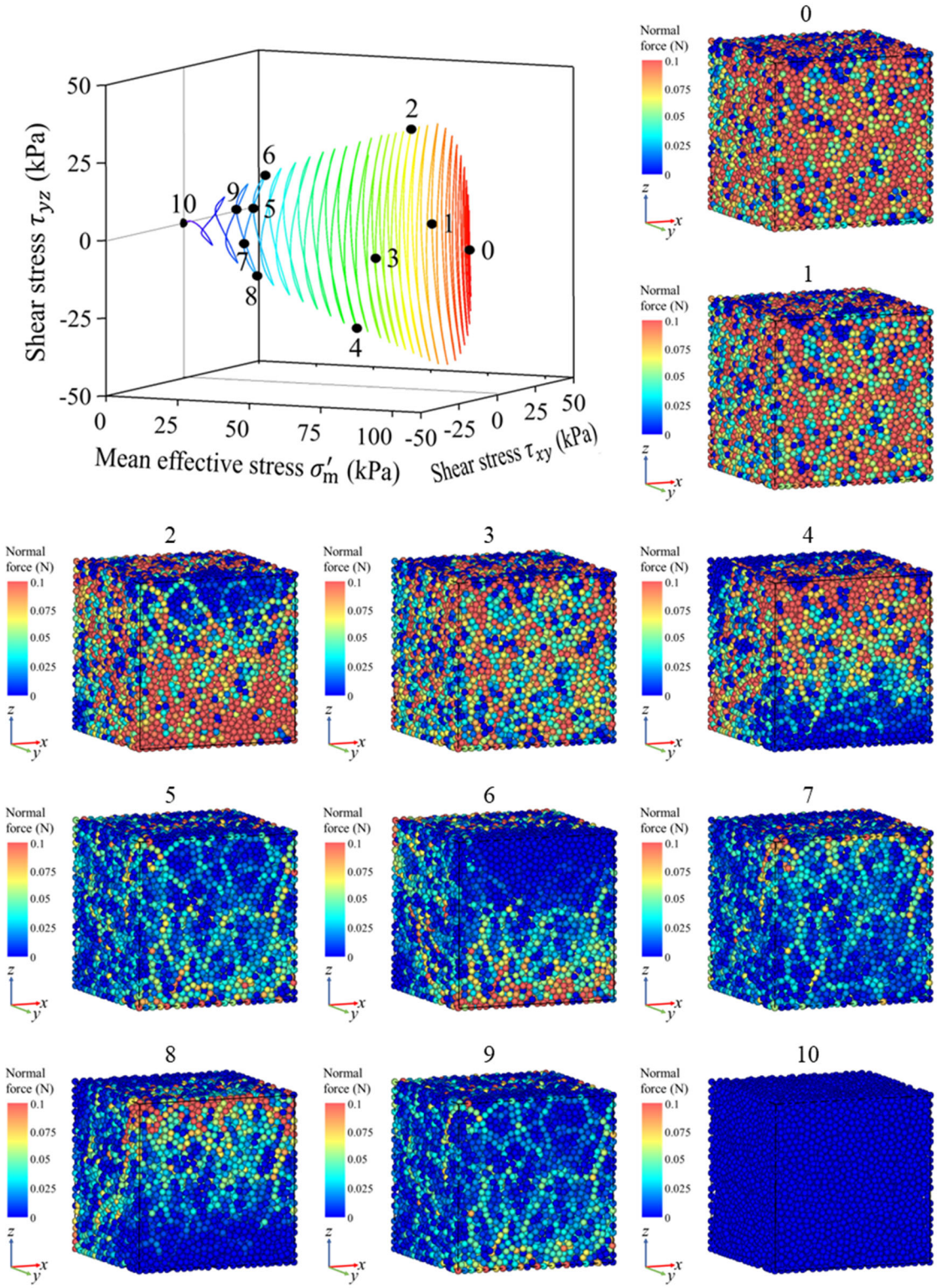

Fig. 4.19. Evolution of normal contact force-chain network under SHV-wave strain condition (e = 0.79).

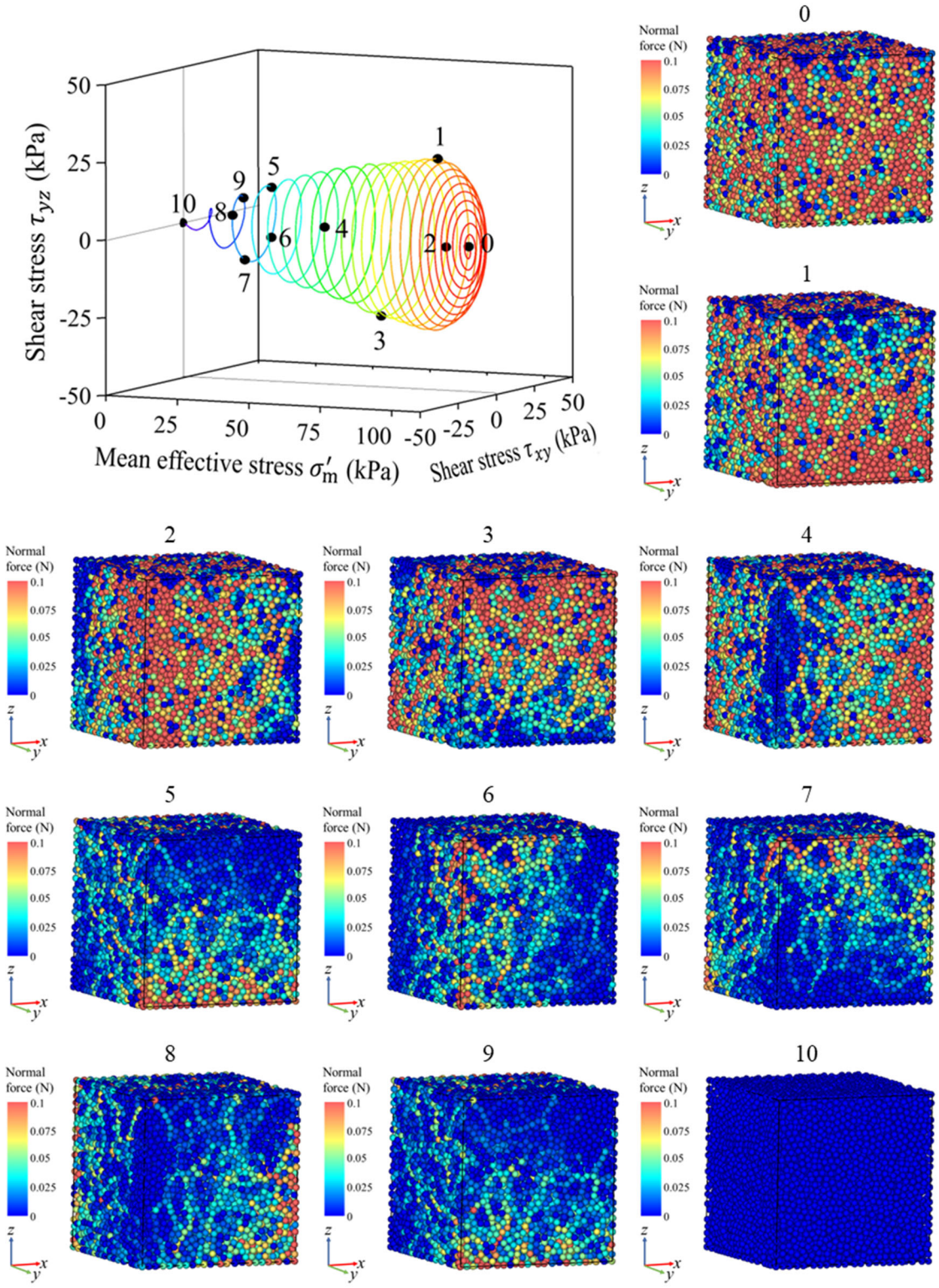

Fig. 4.20. Evolution of normal contact force-chain network under Love-wave strain condition with AR = 1 (e = 0.79).

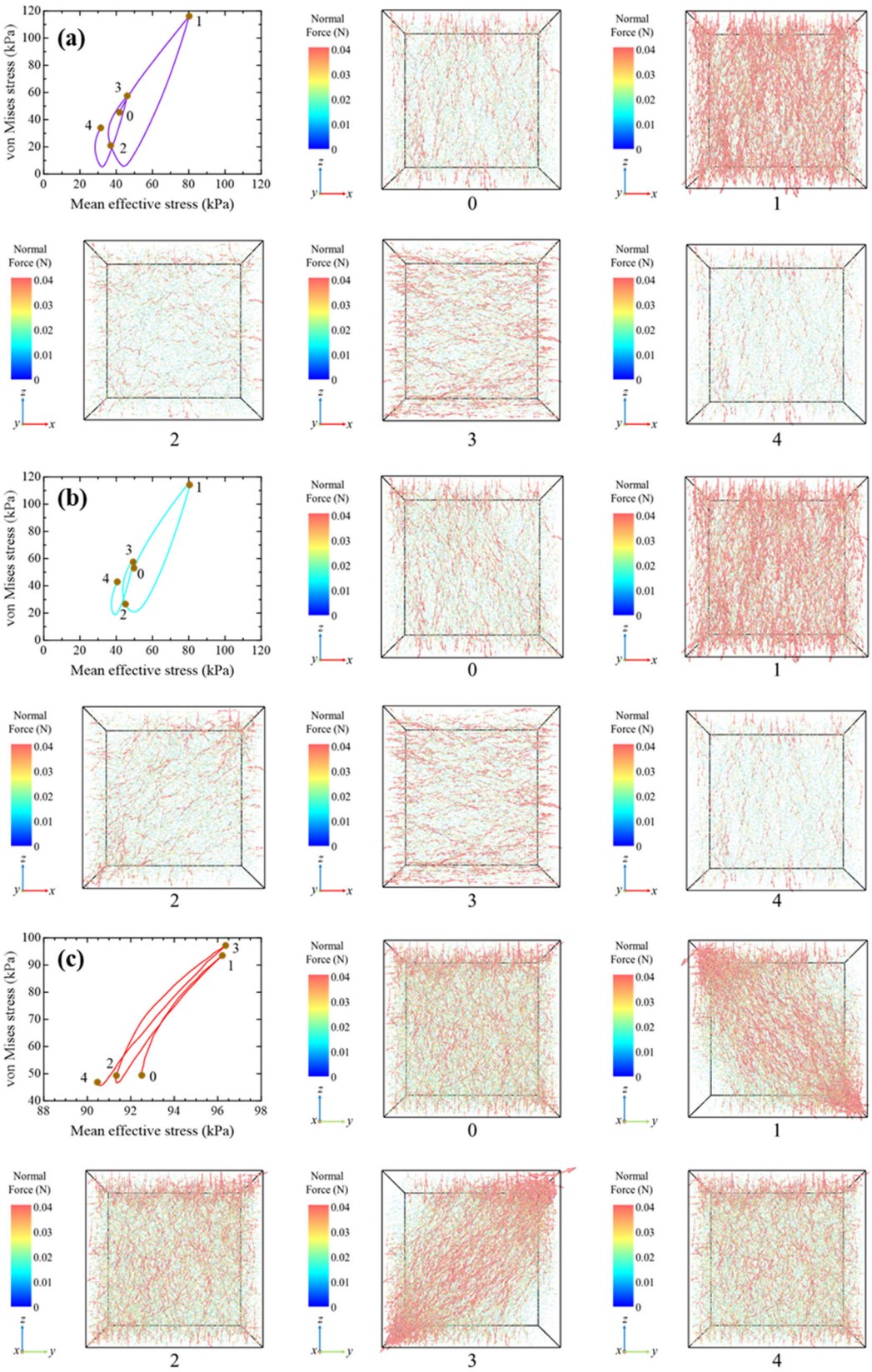

Fig. 4.21. Evolution of the distribution of normal contact forces from 2.0 s to 2.2 s under the Rayleigh-wave strain condition with (a) RSN = 0 and (b) RSN = 1, and (c) SHV-wave strain condition (e = 0.75, perspective projection).

Fig. 4.21 illustrates the evolution of the distribution of normal contact forces from 2.0 s to 2.2 s (the 11th cycle) under Rayleigh-wave strain condition with RSN = 0 (simple shear mode) and 1(simple shear mode + pure shear mode), and SHV-wave strain condition (pure shear mode). In the effective stress path plot, points 0, 1, 2, 3, and 4 divide the loading cycle into four equal parts according to the time interval. In the distribution map of normal contact forces, the color and size of the arrow indicate the magnitude of the normal contact forces. The magnitude and direction of the normal contact forces were not uniform in space and were altered during the cyclic loading process. Under the Rayleigh-wave condition with RSN = 0 (Fig. 4.21(a)), from points 0 to 1, with the compression in the *z*-direction and the extension in the *x*-direction, the strong normal contact forces were aligned in the vertical direction, corresponding to the positive dilatancy behaviors of the specimen. From points 2 to 3, with the extension in the *z*-direction and the compression in the *x*-direction, the orientation of the strong normal contact forces was horizontal, corresponding to a transition from negative to positive dilatancy behaviors of the specimens. Under the SHV-wave strain condition (Fig. 4.21(c)), from points 0 to 1 and points 2 to 3, strong normal contact forces were inclined diagonally with the shear strain application, corresponding to the positive dilatancy behavior of the specimen. Under other Rayleigh-wave strain conditions, the evolution of the force transmission network was affected by both the normal and shear strains. For example, under the Rayleigh-wave strain condition with RSN = 1 (Fig. 4.21(b)), strong normal contact forces were inclined or aligned with the principal strain directions, depending on the relative magnitude of normal strain and shear strain.

To quantitatively describe the magnitude and orientation of the contact forces during cyclic loading, the mean magnitude and proportion of the projection of contact

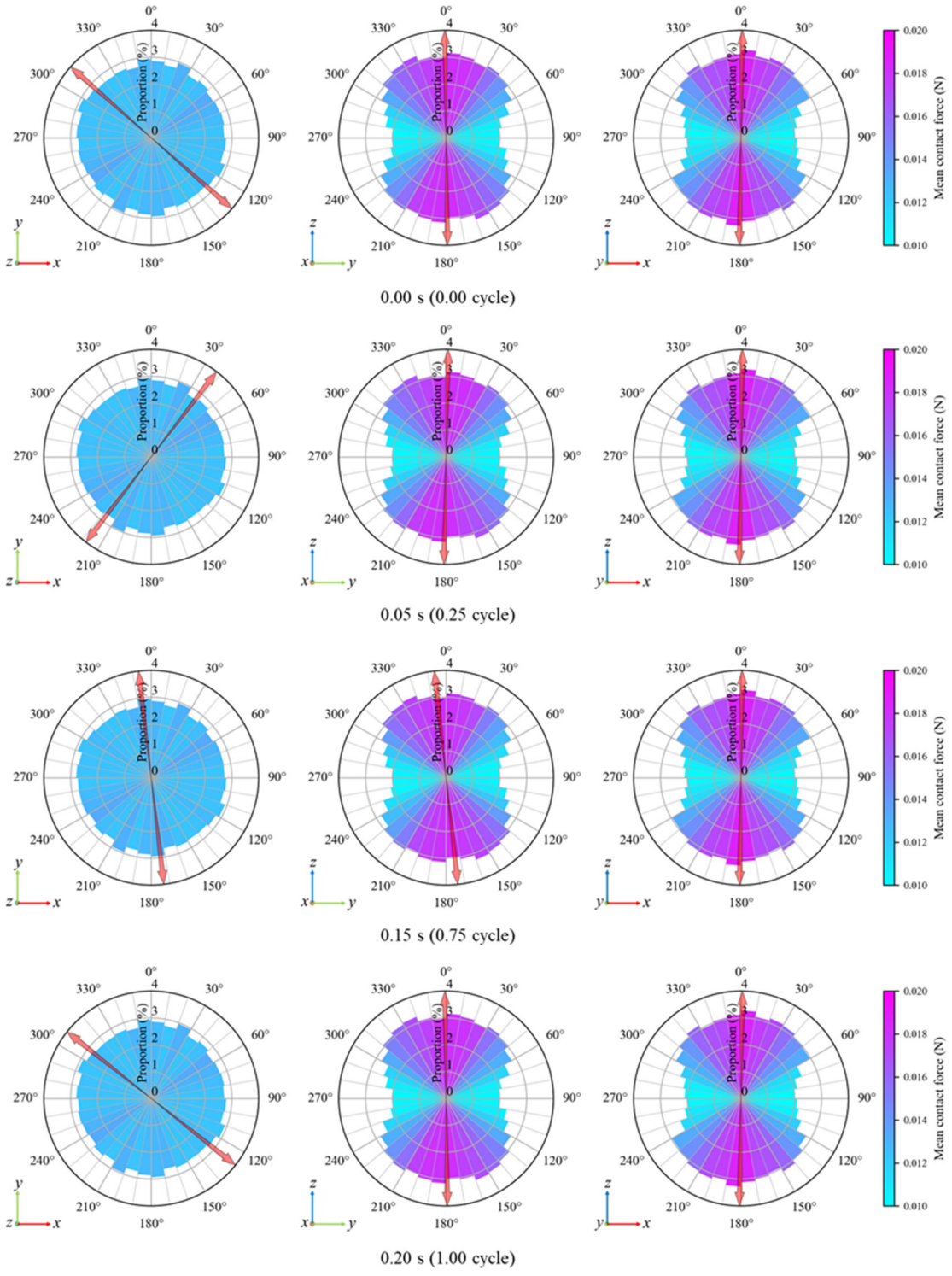

Fig. 4.22. Rose diagrams of contact normal forces and major principal stress direction under SHV-wave strain condition (e = 0.75).

forces on *xy*-,*yz*-,and *zx*-planes in a given direction are counted. The evolution of the magnitude and distribution of normal contact forces in the measurement cube of the specimen with $e = 0.75$ in the 1st and 11th cycle are illustrated and shown in Appendix I. The radial lines represent the contact force directions, and each concentric circle indicates the proportion of contact forces aligned in a particular direction range (10° per interval). The color of sector areas indicates the mean value of the projection of contact forces in each direction range on a given plane. The orange arrow illustrates the direction of the projection of major principal stress on each plane. The results suggested that:

a) At the initial state (0.00s), the distribution of contact forces was more inclined to the vertical direction, especially the strong normal contact forces. e.g., as shown in Fig. 4.22, in the 0.00s, the projections of contact forces on the *xy*-plane (horizontal plane) were almost uniformly distributed, while on the *yz*- and *zx*-plane (vertical plane), they mainly concentrated on the range between 300°–60° and 120°–240°. In addition, the mean contact forces in the range between 330°–30° and 150°–210° were greater than the average contact force in the other ranges. The major principal stress was almost in the vertical direction, which was consistent with the consolidation (compression) direction.

b) When the strain amplitude was small, the distribution of normal contact forces almost did not change or the distribution of the normal contact force recovered after the strain returned to the initial value, e.g., as shown in Fig. 4.22, under SHV-wave strain condition, from 0.00s (0.00 cycle, the shear strain is 0%) to 0.05s (0.25 cycle, the shear strain is 0.025%), the distribution of normal contact forces almost did not change. In the 0.15s (0.75 cycle, the shear strain is 0.075%), the distribution of normal contact forces changed little but recovered in the 0.20s (1.00 cycle, the shear strain is 0%). This explains

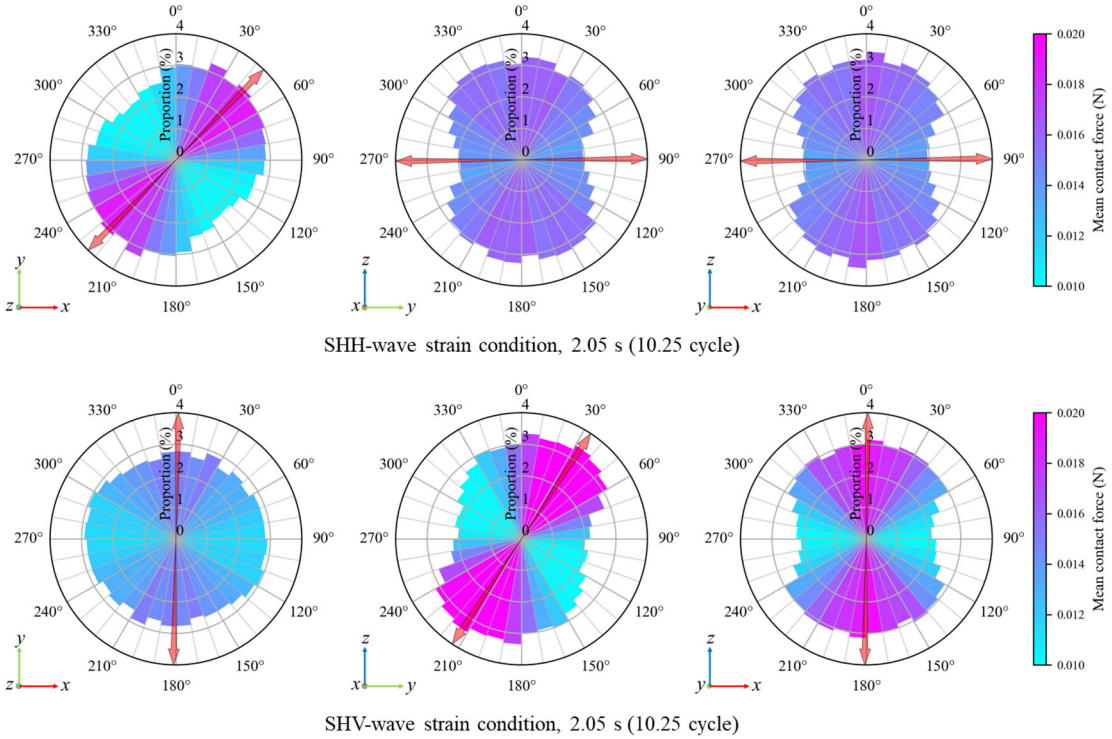

Fig. 4.23. Rose diagrams of contact normal forces and major principal stress direction of the specimen suffers from the largest shear strain under SHH- and SHV-wave strain conditions (e = 0.75).

the reason why the fluctuation in the ESRR was greater under Rayleigh-wave strain conditions than under other strain conditions, especially in a small strain amplitude range, as mentioned in section 4.4.1.1. Because the normal contact force tends to align in the vertical direction in the K_0-consolidation state, a given strain in the vertical direction will result in a larger increment of total contact forces if a contact point is assumed to be a spring.

c) The major principal stress direction was consistent with the direction of the principal strain rotation. In addition, strong normal contact forces were concentrated near the direction of major principal stress and tend to be distributed symmetrically along the direction of major principal stress, e.g., the distribution of normal contact forces of the

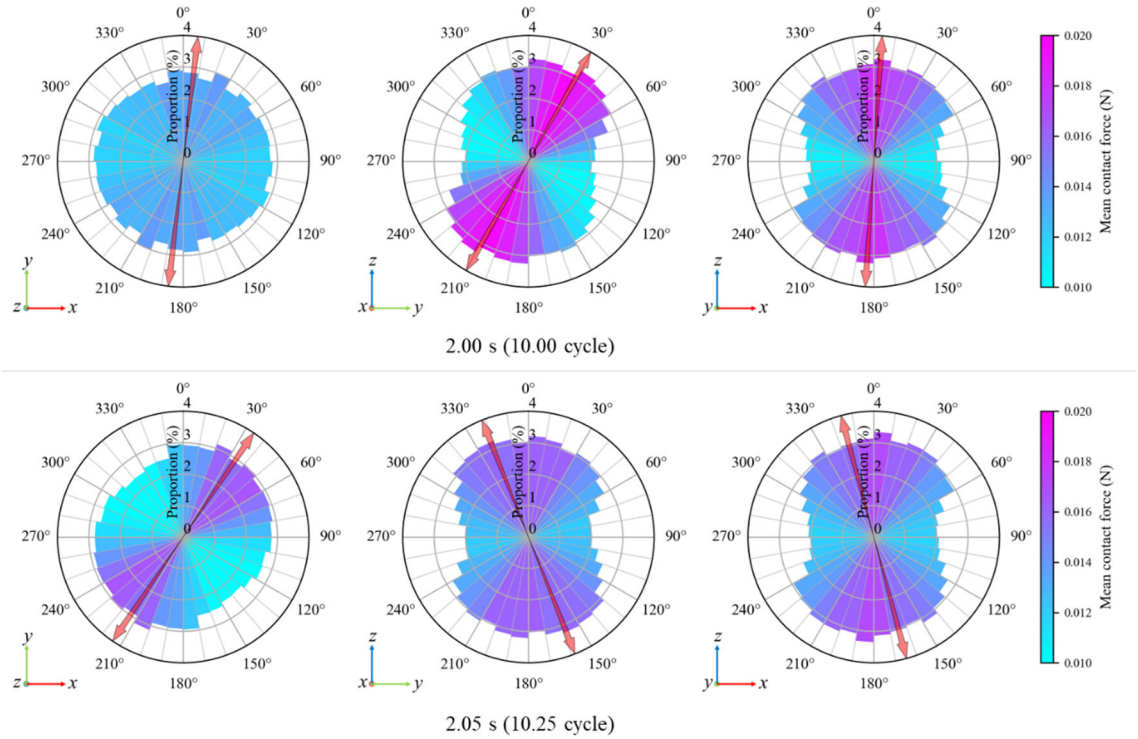

Fig. 4.24. Rose diagrams of contact normal forces and major principal stress direction of the specimen suffers from the largest shear strain in the vertical and horizontal planes under Love-wave strain condition with AR = 1 (e = 0.75).

specimen suffered from the largest shear strain under SHH- and SHV-wave strain conditions as shown in Fig. 4.23;

d) In the K_0-consolidation state, the shear strain in the vertical plane would result in a greater magnitude of the projection of normal contact forces on the same plane than the shear strain in the horizontal plane, e.g., suffered from the same shear strain amplitude, the magnitude of normal contact forces in the vertical plane under SHV-wave strain condition was greater than that in the horizontal plane under SHH-wave strain condition, as shown in Fig. 4.23. Also, under the Love-wave strain condition with AR = 1, the same phenomenon could be observed although the amplitudes of γ_{xy} and γ_{yz} were the same, as shown in Fig. 4.24. This explains the phenomenon that the proportion of the amplitude of the horizontal shear strain component (γ_{xy}) to the amplitude of the vertical shear strain

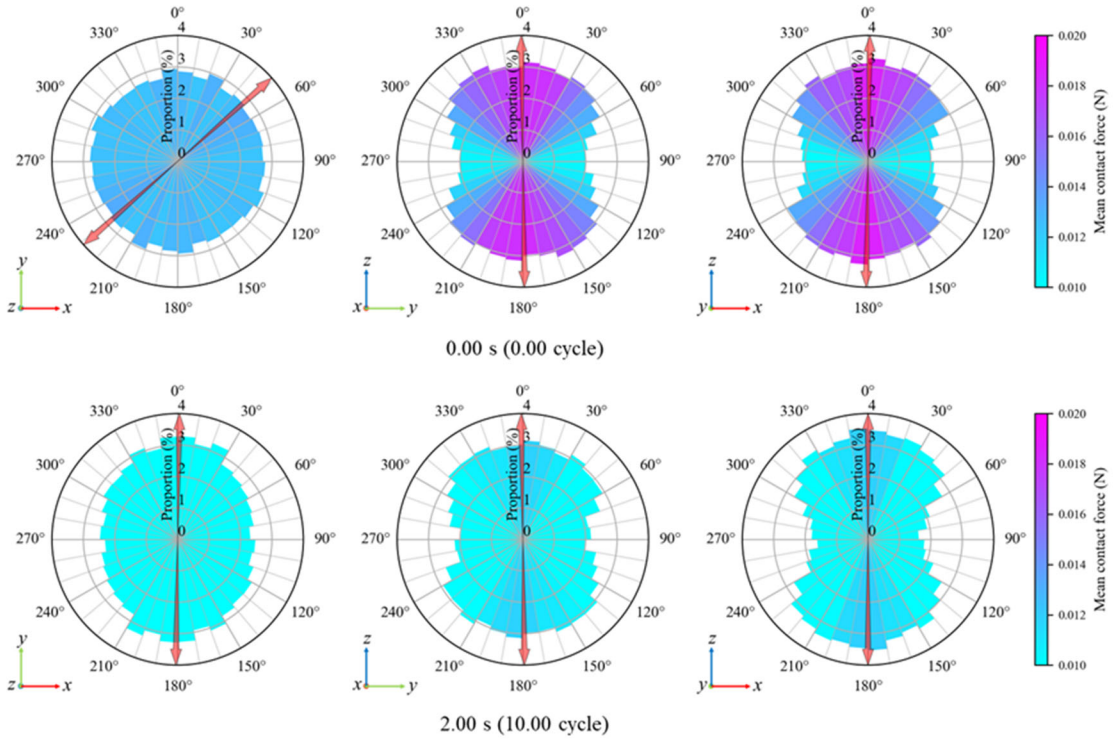

Fig. 4.25. Rose diagrams of contact normal forces and major principal stress direction at the start of 1st and 11th cycle under Rayleigh-wave strain condition with RSN = 0 (e = 0.75).

component (γ_{yz}) affected the value of the von Mises stress as mentioned in section 4.4.1.1.

e) The deformation-induced anisotropy became greater during cyclic loadings, e.g., the distribution of contact force under Rayleigh-wave strain condition with RSN = 0 was more concentrated in the vertical direction (normal strain is applied in zx-plane) in the 11th cycle than in the 1st cycle when the strain is zero, as shown in Fig. 4.25. What's more, the projections of contact forces on the xy-plane were more concentrated in the y-direction.

4.4.2.2. Fabric anisotropy

To quantitatively evaluate the anisotropy of the granular fabric during cyclic loadings, the fabric tensor Φ_{ij} proposed by Satake (1982) and deviator fabric Φ_{d} defined by Barreto et al. (2009) was used. As shown in Fig. 4.26(a) and (b), the amplitude

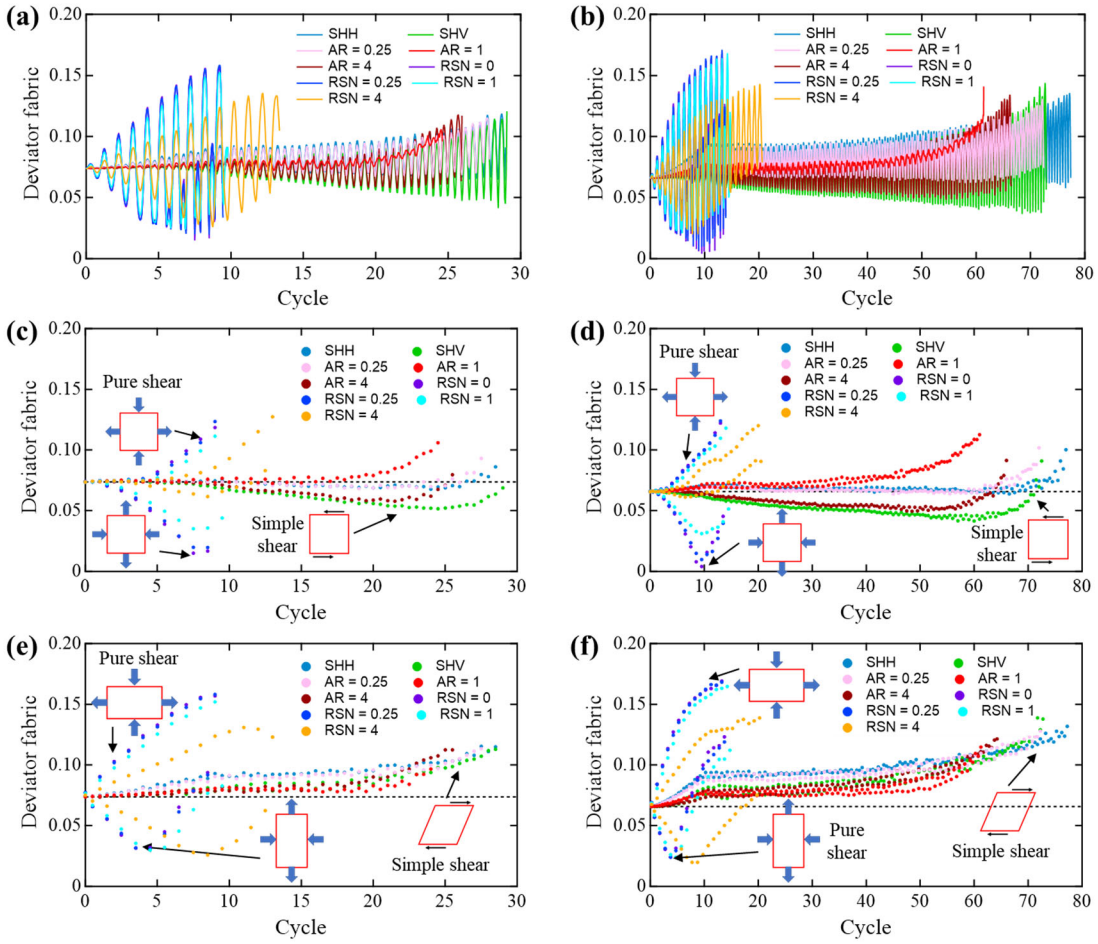

Fig. 4.26. Evaluation of fabric anisotropy during cyclic loadings (dashed line indicates the initial deviatoric fabric): (a) $e = 0.79$; (b) $e = 0.75$; (c) $e = 0.79$, every 0.5 cycle starting from 0.00s (zero normal strain positions for pure shear and zero shear strain positions for simple shear); (d) $e = 0.75$, every 0.5 cycle starting from 0.00s; (e) $e = 0.79$, every 0.5 cycle starting from one quarter of the 1st cycle (extrema normal strain positions for pure shear and extrema shear strain positions for simple shear); (f) $e = 0.75$, every 0.5 cycle starting from one quarter of the 1st cycle.

of the deviator fabric increased quickly before the 11th cycle, which suggested that the deformation-induced anisotropy was influenced by the strain amplitude. As the strain amplitude increased, the amplitude of fluctuation of anisotropy also became greater during cyclic loading. Especially for specimens under Rayleigh-wave strain conditions, the increase of anisotropy fluctuation was more significant than that under other strain

conditions. After the 10^{th} cycle, the strain amplitude was constant under each strain condition. However, the maximum values of the deviator fabric under all loading conditions continued to increase until liquefaction, while the evolutions of the minimum values of the deviator fabric under different loading conditions were different.

Fig. 4.26(c) and (d) show the deviator fabric of specimens every 0.5 cycle starting from 0.00s. Under Rayleigh-wave strain conditions, they indicate the degree of fabric anisotropy in the zero normal strains (ε_x and ε_z) and extrema (maximum and minimum) shear strain (γ_{zx}) positions (zero-strain positions for Rayleigh-wave strain condition with RSN = 0, i.e., pure shear). At the start of each cycle (loading in the *z*-direction and unloading in the *x*-direction), the fabric anisotropy of specimens became greater and greater; in the middle of each cycle (unloading in the *z*-direction and loading in the *x*-direction), the fabric anisotropy decreased at first then increased. Under the SHV-wave strain condition and Love-wave strain condition with AR = 4 (γ_{yz} = 0), the fabric anisotropy decreased at first and then increased before liquefaction. Under the SHH-wave strain condition and Love-wave strain condition with AR = 0.25 (γ_{xy} = 0), the fabric anisotropy almost kept constant at first and then increased before liquefaction. Under the Love-wave strain condition with AR = 1 (γ_{xy} = 0 and γ_{yz} is extrema), the fabric anisotropy increased at a very slow rate and then increased faster and faster before liquefaction.

Fig. 4.26(e) and (f) show the deviator fabric of specimens every 0.5 cycles starting from 0.05s (one-quarter of the 1^{st} cycle). Under Rayleigh-wave strain conditions, they indicate the degree of fabric anisotropy in the extrema normal strain (ε_x and ε_z) and zero shear strain (γ_{zx}) positions. At one-quarter of each cycle (ε_z is maximum and ε_x is minimum in a cycle), the fabric anisotropy of specimens became greater and greater; At three-

quarters of each cycle (ε_x is maximum and ε_z is minimum in a cycle), the fabric anisotropy decreased at first then increased. Under the SH- and Love-wave strain conditions, because the shear strain component with the larger amplitude was at the extremes (shear strain γ_{yz} = 0 and shear strain γ_{xy} was extrema for Love-wave strain condition with AR = 1), the fabric anisotropy at one-quarter and three-quarters of each cycle increases during cyclic loading.

In total, the strain-induced fabric anisotropy increased with cyclic loadings. The results above also indicated that the evolution of fabric anisotropy of a K_0-consolidated specimen was influenced by the strain amplitude and loading path. Specifically, the amplitude of the fluctuation of fabric anisotropy became greater as the strain amplitudes increased during cyclic loadings. The fabric anisotropy also relied on the direction of loaded strain. For pure shear (Rayleigh-wave strain condition with RSN = 0), the compression in the *z*-direction (vertical direction) would increase the fabric anisotropy while the compression in the *x*-direction (horizontal direction) would first reduce the fabric anisotropy; For simple shear (SH-wave strain conditions), the loading of shear strain would increase the fabric anisotropy. However, if the shear strain was applied on the *xy*-plane (horizontal plane), the loading history would first barely affect the fabric

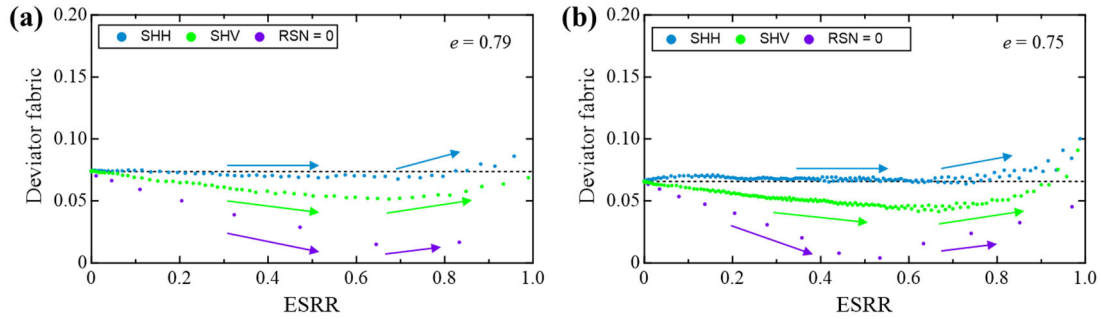

Fig. 4.27. Evolution of fabric anisotropy with ESRR in zero-strain positions (compression in horizontal direction for Rayleigh-wave strain condition): (a) e = 0.79; e = 0.75.

anisotropy when the shear strain was unloaded; if the shear strain was applied on the *yz*-plane (vertical plane), the loading history would first decrease the fabric anisotropy when the shear strain was unloaded. When the ESRR exceeds a threshold value located near 0.6, the fabric anisotropy in the zero-strain position which originally decreased with loading, then shifted to increase, as shown in Fig. 4.27. The common denominator for the decrease of fabric anisotropy in the zero-strain position was the non-coaxial nature of the strain application direction and initial major principal fabric direction, Φ_1.

The major strain application direction can be described by the principal eigenvector of the strain increment, $(\Delta\varepsilon)_1$. The strain increment $\Delta\varepsilon_{ij} = (\varepsilon_{ij})_n - (\varepsilon_{ij})_{n-1}$, where $(\varepsilon_{ij})_n$ and $(\varepsilon_{ij})_{n-1}$ are the strain tensor at the time t_n and t_{n-1}. In this research, the compression normal strain increment is positive in sign. The direction of $(\Delta\varepsilon)_1$ in the simple shear mode and the pure shear mode are shown in Fig. 4.28. In the simple shear, the angle between the direction of $(\Delta\varepsilon)_1$ and the direction of particle velocity is 45°; In the pure shear, the direction of $(\Delta\varepsilon)_1$ is consistent with the compression direction.

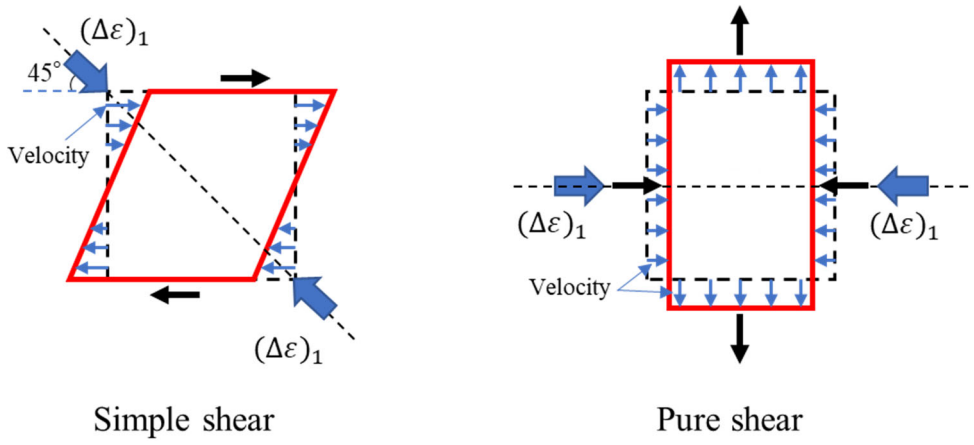

Fig. 4.28. Directions of $(\Delta\varepsilon)_1$ in simple and pure shear modes

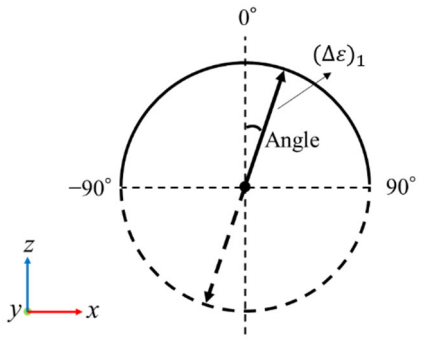

Fig. 4.29. Direction of the projection of $(\Delta\varepsilon)_1$ on the *xz*-plane limited to between −90° and 90°.

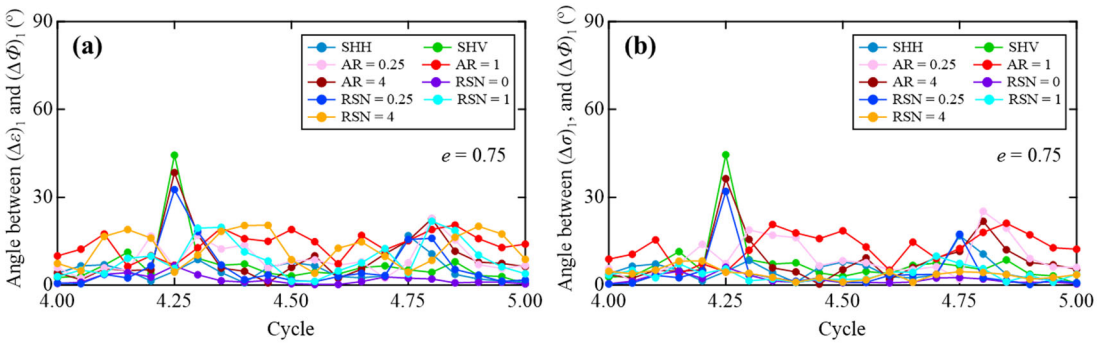

Fig. 4.30. Angle between: (a) $(\Delta\varepsilon)_1$ and $(\Delta\Phi)_1$; (b) $(\Delta\sigma)_1$ and $(\Delta\Phi)_1$.

The direction of the projection of a vector (e.g., $(\Delta\varepsilon)_1$) on a plane was limited to between −90° and 90° for convenience, as shown in Fig. 4.29. On the *xz*- or *yz*-plane, 0° indicated the vertical direction, while −90° and 90°indicated the horizontal direction. Because of the K_0-consolidation, the direction of the projection of initial structure elongation, or the major principal fabric, Φ_1, equaled −1.8° on the *zx*-plane and equaled 2.3° on the *yz*-plane, which was almost vertical. The direction of the projection of initial major principal stress, σ_1, equaled 0.9° on the *yz*-plane and equals −0.7° on the *zx*-plane, which was also almost vertical.

As shown in Fig. 4.30, during cyclic loading, the angles between $(\Delta\varepsilon)_1$ and $(\Delta\Phi)_1$ and the angle between $(\Delta\sigma)_1$ and $(\Delta\Phi)_1$ during cyclic loading maintained low values. It indicated that the direction of Φ_1 was influenced by $(\Delta\varepsilon)_1$ and $(\Delta\sigma)_1$ and

tend to be consistent with them. Fig. 4.31–Fig. 4.33 shows the direction of the projection of the direction of $(\Delta\varepsilon)_1$, $(\Delta\sigma)_1$ and Φ_1 under Rayleigh-wave strain condition with RSN = 0, SHH-wave strain condition, and SHV-wave strain condition on their strain application planes in different cycles. The directions of $(\Delta\varepsilon)_1$ and $(\Delta\sigma)_1$ were almost identical during cyclic loadings. The direction of Φ_1 was initially vertically and $(\Delta\varepsilon)_1$ on the horizontally plane had a limited influence on it. However, as the ESRR increased, the influence of $(\Delta\varepsilon)_1$ and $(\Delta\sigma)_1$ became stronger and the direction of Φ_1 tend to be the same as their directions. The effect of the direction of $(\Delta\varepsilon)_1$ gave an explanation for the phenomenon in Fig. 4.27.

As shown in Fig. 4.34(a), under the Rayleigh wave strain condition with RSN = 0, the direction of Φ_1 was almost vertical in the middle of each cycle when the ESRR was smaller than a threshold value located near 0.6. It indicated that at this time, the skeleton of specimen was still stable and capable to withstand a compressive deformation perpendicular to the direction of Φ_1 and extensional deformation along the direction of Φ_1. When the ESRR became larger than the threshold value, the direction of Φ_1 was almost horizontal in the middle of each cycle. This means that the direction of Φ_1 became consistent with the compression direction and perpendicular to the extension direction. Correspondingly, the fabric anisotropy in the middle of each cycle decreased when the ESRR was smaller than the threshold value because the initial fabric originated from K_0-consolidation was being destroyed, which was manifested as the decrease of Φ_1 and increase of Φ_2 and Φ_3 as shown in Fig. 4.34(b); when the ESRR was larger than the threshold value, the fabric anisotropy in the middle of each cycle increased because Φ_1 turned into the horizontal direction and increased, while Φ_3 in the vertical direction decreased.

Under the SHH-wave strain condition, because the shear strain application plane was horizontal, Φ_1 in the vertical direction was barely affected by the loading history at zero shear strain positions as shown in Fig. 4.35. When the ESRR was smaller than a threshold value located near 0.6, the change of Φ_2 and Φ_3 was also small, therefore, the fabric anisotropy at zero shear strain positions almost did not change; when the ESRR was larger than the threshold value, the increase of Φ_2 and decrease of Φ_3 caused the increase of fabric anisotropy at zero shear strain positions. Under the SHV wave strain condition, the shear strain application plane was vertical. As shown in Fig. 4.36 when the ESRR was smaller than a threshold value located near 0.6, the initial fabric was being destroyed as the decrease of Φ_1 at zero shear strain positions; when the ESRR was larger than the threshold value, the direction of Φ_1 became near to the direction of $(\Delta\varepsilon)_1$ and the magnitude of Φ_1 also increased with the decrease of Φ_3. Therefore, the fabric anisotropy at zero shear strain positions first decreased and then increased.

With the increase of fabric anisotropy and the direction of Φ_1 became closer to the directions of $(\Delta\varepsilon)_1$ and $(\Delta\varepsilon)_1$ during the loading of strain, the direction of Φ_1 also became closer to the directions of ε_1 and σ_1, as shown in Appendix II. Fig. 4.37 shows the angles between ε_1 and Φ_1 and between σ_1 and Φ_1 immediately before initial liquefaction under different strain conditions. Under Rayleigh-wave strain conditions, the angle between ε_1 and Φ_1 and between σ_1 and Φ_1 tended to be zero except when the direction of $(\Delta\varepsilon)_1$ and $(\Delta\varepsilon)_1$ were reversed. The smaller the shear strain amplitude, the smaller the angle, therefore, the strain-induced anisotropy under Rayleigh-wave strain conditions was higher than other conditions. Under SHH-wave strain conditions, the angle between ε_1 and Φ_1 and between σ_1 and Φ_1 also tended to be zero except when the direction of $(\Delta\varepsilon)_1$ and $(\Delta\varepsilon)_1$ were reversed; however, under SHV-wave strain

conditions, the angles were kept around 5° except when the direction of $(\Delta\varepsilon)_1$ and $(\Delta\varepsilon)_1$ were reversed; Under Love-wave strain conditions, although the direction of $(\Delta\varepsilon)_1$ was changing all the time, overall the angles also became close to zero.

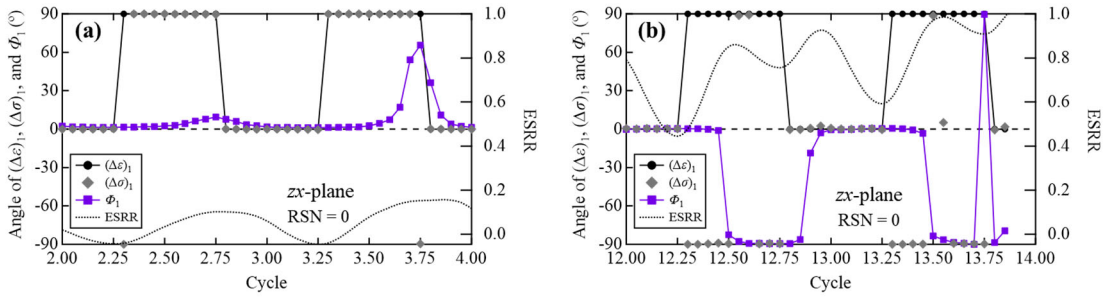

Fig. 4.31. Evolution of the projections of the directions of $(\Delta\varepsilon)_1$, $(\Delta\sigma)_1$, and Φ_1 on the *zx*-plane (e = 0.75), and their relationship with ESRR under Rayleigh-wave strain condition with RSN = 0 during: (a) 2–4 cycle; (b) 12–14 cycle.

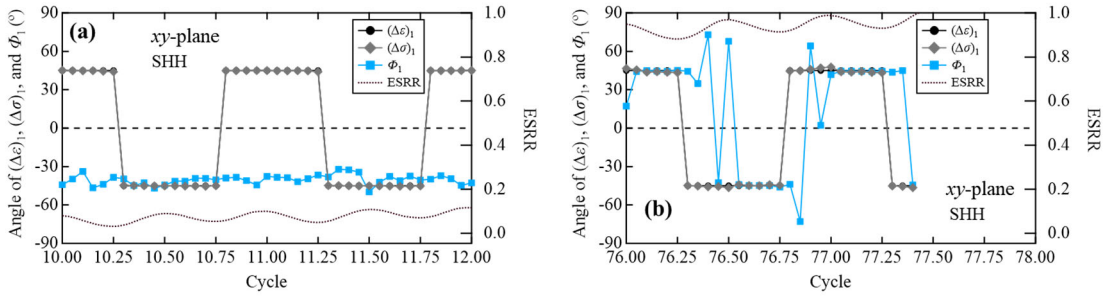

Fig. 4.32. Evolution of the projections of the directions of $(\Delta\varepsilon)_1$, $(\Delta\sigma)_1$, and Φ_1 on the *xy*-plane (e = 0.75), and their relationship with ESRR under SHH-wave strain condition (e = 0.75) during: (a) 10–12 cycle; (b) 76–78 cycle.

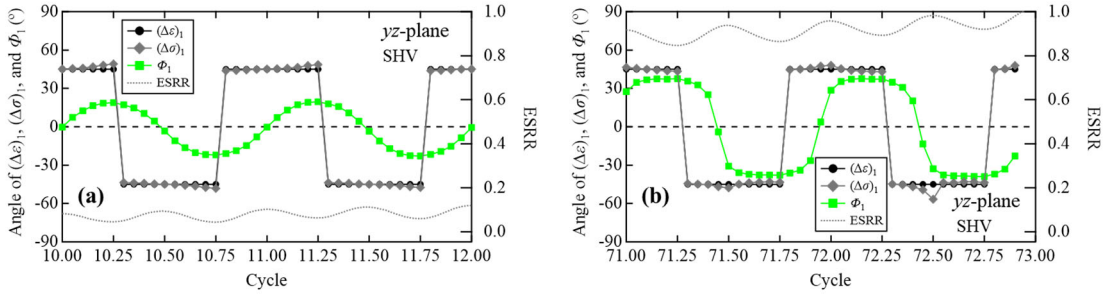

Fig. 4.33. Evolution of the projections of the directions of $(\Delta\varepsilon)_1$, $(\Delta\sigma)_1$, and Φ_1 on the *xy*-plane (e = 0.75), and their relationship with ESRR under SHH-wave strain condition (e = 0.75) during: (a) 10–12 cycle; (b) 76–78 cycle.

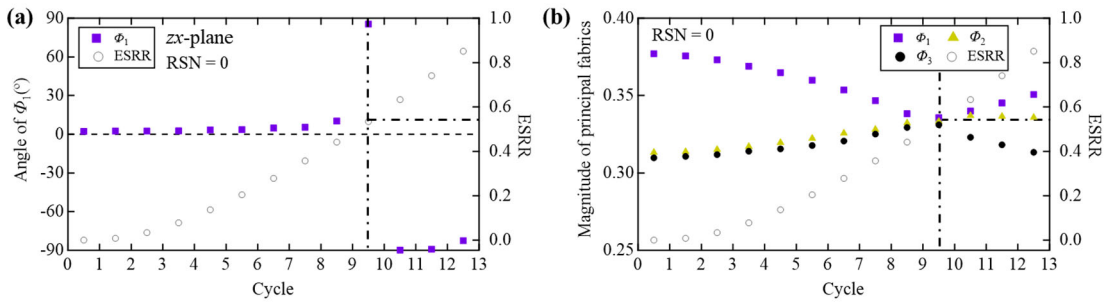

Fig. 4.34. (a) Projection of the direction of Φ_1 on the *zx*-plane and (b) magnitude of principal fabrics in the middle of each cycle under Rayleigh-wave strain condition with RSN = 0 (e = 0.75).

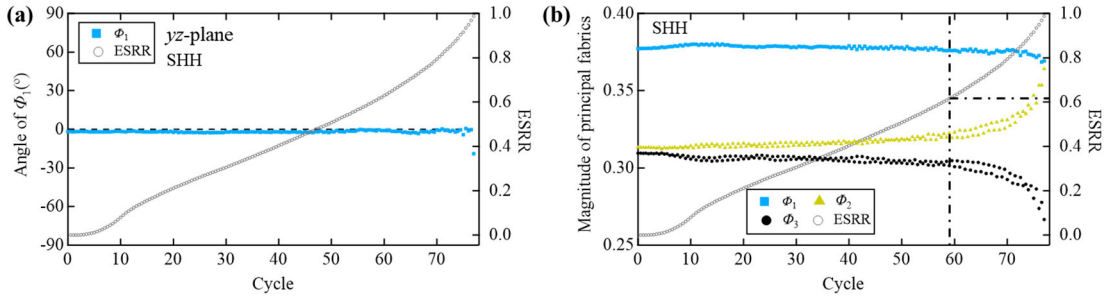

Fig. 4.35. (a) Projection of the direction of Φ_1 on the *yz*-plane and (b) magnitude of principal fabrics in zero-strain positions under SHH-wave strain condition (e = 0.75).

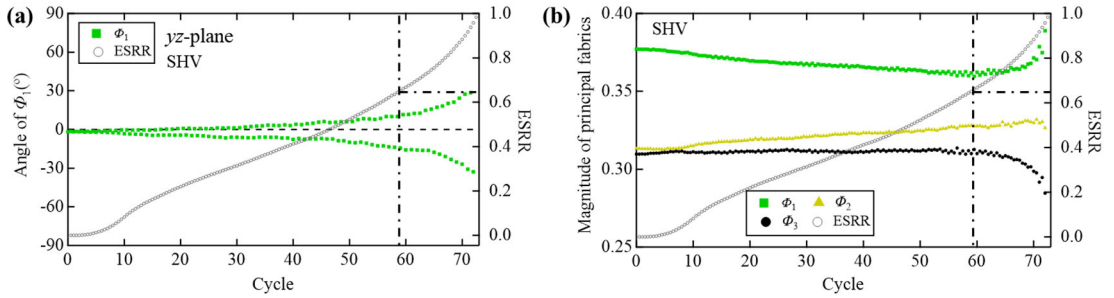

Fig. 4.36. (a) Projection of the direction of Φ_1 on the *yz*-plane and (b) magnitude of principal fabrics in zero-strain positions under SHV-wave strain condition (e = 0.75).

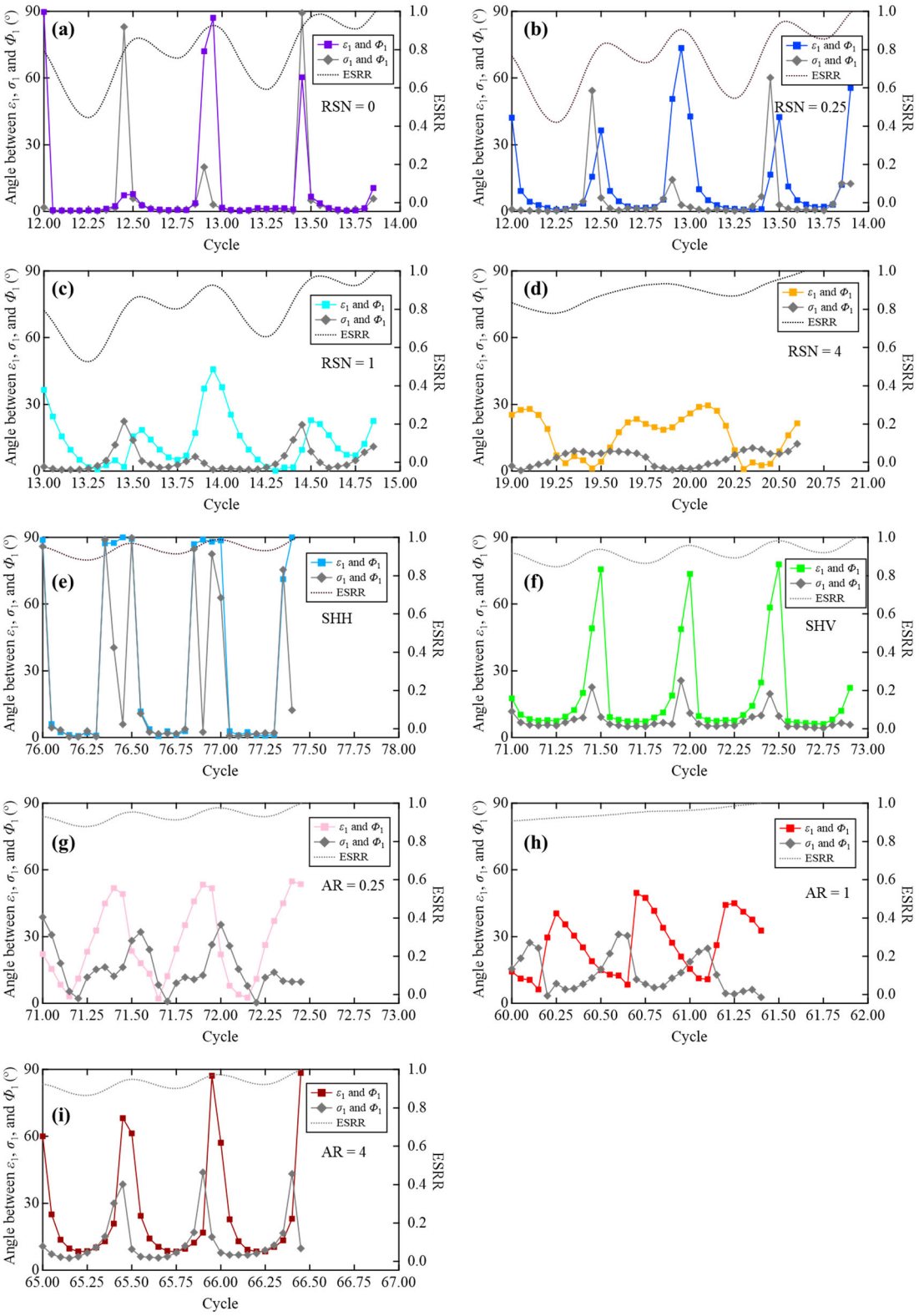

Fig. 4.37. Angles between ε_1 and Φ_1 and between σ_1 and Φ_1 immediately before initial liquefaction under different strain conditions (e = 0.75).

4.4.2.3. Structure stability

During the liquefaction process, with an increase in excess pore water pressure, the external load borne by the granular skeleton decreases, which is associated with the degradation of the major force transmission network (Huang et al., 2019). One characteristic manifestation of the structure losing stability is the failure of force chains. According to the tangential force model used in this study, when the static friction between particles cannot resist the tangential force, the particles in contact begin to slide. The force chain loses its stability if sliding occurs between particles in which it is involved. Therefore, the fraction of contacts that are sliding has an important influence on the stability of the granular structure.

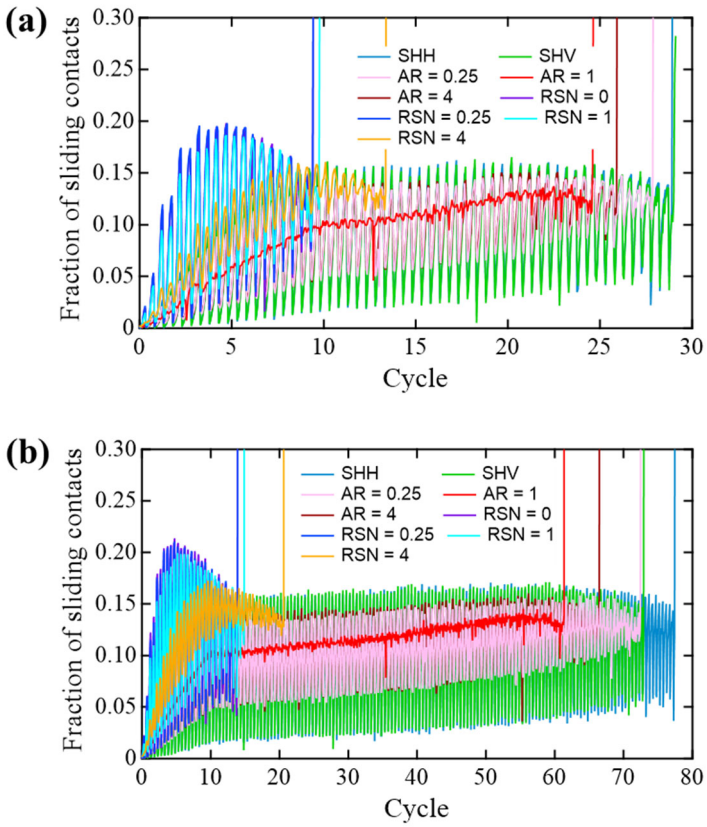

Fig. 4.38. Evolution of fraction of sliding contacts during cyclic loadings: (a) e = 0.79 and (b) e = 0.75.

Fig. 4.38 shows the evolution of the fraction of sliding contacts (FS) during cyclic loadings in each loading condition. Overall, FS increased during cyclic loadings, especially before the 11th cycle when the strain amplitude was increasing. When initial liquefaction happens, the FS dramatically increased to a high value. The maximum value of FS under Rayleigh-wave strain conditions was much larger than SH- and Love-wave strain conditions, which indicated that a higher proportion of slippage happens under Rayleigh-wave strain conditions during cyclic loadings. The decrease of FS within several cycles before liquefaction might be due to the low number of particle contacts as mentioned later and the higher proportion of surviving strong chains. Under SH- and Love-wave strain conditions, the fluctuation of FS during cyclic loadings was influenced by the resultant shear strain Γ. The fluctuation of FS under the Love-wave strain condition with AR = 1 was very small while that under SH-wave strain conditions was much larger.

In structural mechanics, when the number of unknown force or torque components equals the number of force balance equations, the structure system is isostatic; when the number of unknown force or torque components exceeds the number of force balance equations, the structure system is hyperstatic. The structure system can only maintain its stability when it is isostatic or hyperstatic. When accessing the stability of the granular system, the approach from a structural mechanics point of view, as mentioned above, is often drawn upon (e.g., Zhang and Makes, 2005; Huang et al., 2019). The load-bearing network of particles can only be maintained when the skeleton structure of the granular materials is relatively stable, which requires sufficient mechanically stable particles. The coordination number Z is widely used to assess the stability of a granular system. It is defined in sections 2.2.2 and 3.5.3 as $Z = 2N_c/N_p$, where N_c and N_p are the total contact and particle numbers in the measurement cube, respectively.

A contact without sliding and rolling can provide five constraints (three translational and two rotational). If the fraction of sliding contacts is f_s, the fraction of the rolling moment exceeding the rolling resistance moment is f_r, the total unknown force components in the granular system is $(5-2f_s-2f_r)N_{\mathrm{c}}$. As one particle has three translational and three rotational degrees of freedom, there are $6N_{\mathrm{p}}$ force balance equations in the granular systems. A granular system maintaining stability (isostatic or hyperstatic) requires $(5-2f_s-2f_r)N_{\mathrm{c}} \geq 6N_{\mathrm{p}}$. Therefore, the corresponding minimum coordination number is $Z_{\min} = 12/(5-2f_s-2f_r)$. If $f_s = 0$ and $f_r = 0$, $Z_{\min} = 2.4$; if $f_s = 1$ and $f_r = 0$, the moment balance equation can be ignored and $Z_{\min} = 6$. As a result, $Z_{\min}$ of a granular system range from 2.4 to 6.

Thornton (2000) suggested that the particle without contact or only one contact with neighbor particles does not contribute to the stability of the granular system. herein, he proposed the mechanical coordination number Z_{m} to describe the connectivity of the granular system. the mechanical coordination number is defined as:

$$Z_{\mathrm{m}} = \frac{\left(2N_{\mathrm{c}} - N_{\mathrm{p}}^{1}\right)}{N_{\mathrm{p}} - N_{\mathrm{p}}^{1} - N_{\mathrm{p}}^{0}} \tag{4.22}$$

where N_{p}^{1} and N_{p}^{0} are the number of particles with only one or no contacts, respectively. The relationship between the mechanical coordination number Z_{m} and coordination number Z is:

$$Z = Z_{\mathrm{m}} - (Z_{\mathrm{m}} - 1)\frac{N_{\mathrm{p}}^{1}}{N_{\mathrm{p}}} - Z_{\mathrm{m}}\frac{N_{\mathrm{p}}^{0}}{N_{p}} \tag{4.23}$$

Because $Z_{\min}$ of a granular system range from 2.4 to 6, Z is smaller than Z_{m} when the granular system is isostatic or hyperstatic.

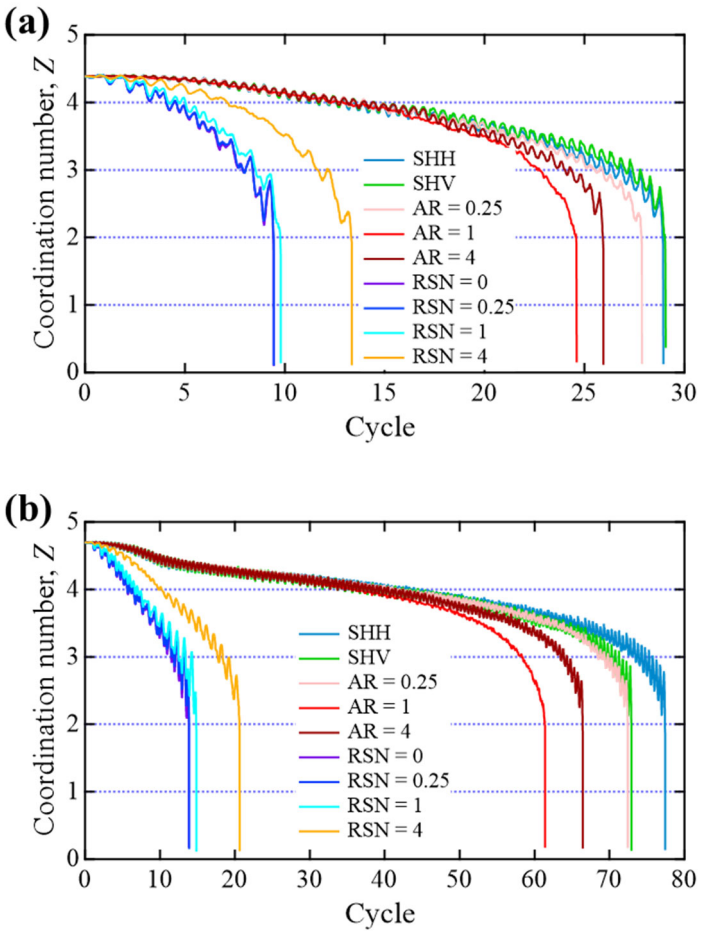

Fig. 4.39. Evolution of coordination number during cyclic loadings: (a) e = 0.79 and (b) e = 0.75.

However, the granular system is a collection of particles. When Z or Z_{m} is larger than its critical value, at which the granular system is isostatic, the granular system is stable. However, a larger Z or Z_{m} does not necessarily mean a more stable structure. The structural stability of the specimen with given a Z or Z_{m} is influenced on f_s, f_r, and its texture. Therefore, for the convenience of calculation, Z was used to reflect the overall degradation of a granular system during undrained cyclic loadings. As contacting particles disengage from each other, manifesting as a decrease in Z, the connectivity of the skeleton structure decreases, and the granular system gradually loses its stability until liquefaction.

Fig. 4.39 shows the evolution of Z under each loading condition. The initial value of Z was dependent on the void ratio of the granular packings, where a denser granular packing was associated with a larger initial value of Z. Under SH- and Love-wave strain conditions, before Z decreased to a value of approximately 4, the different loading conditions were similar in terms of decreasing speed. Below the critical value, Z decreased more rapidly under the Love-wave strain conditions than under the SH-wave strain conditions. This phenomenon was consistent with the ESRR results shown in Fig. 4.14.

In addition, after the ESRR exceeded the threshold (different for each strain condition) located near 0.6, Z decreased faster and faster, which was accompanied by a quick increase of fabric anisotropy at zero strain positions (zero normal strain positions for Rayleigh-wave strain conditions; zero shear strain position for SH-wave strain conditions; the position where the shear strain with large amplitude becomes zero under Love-wave strain conditions) as shown in Fig. 4.26(c) and (d). Iwashita and Oda (2020) determined that the increase in structural anisotropy accelerates the liquefaction of granular materials because the structure becomes extremely unstable when the major stress is rotated and deviates from the structure elongation direction under cyclic pure shear tests. Similarly, in strain-controlled tests, the direction of major strain application, $(\Delta\varepsilon)_1$, deviating from the structure elongation direction had a significant influence on the stability of the granular structure. The structure elongation direction could be represented by the direction of the major principal fabric Φ_1. As shown in Fig. 4.40, in both pure shear (Rayleigh-wave strain condition with RSN = 0) and simple shear (SHH- and SHV-wave strain condition), Z decreased when the direction of $(\Delta\varepsilon)_1$ deviated from the

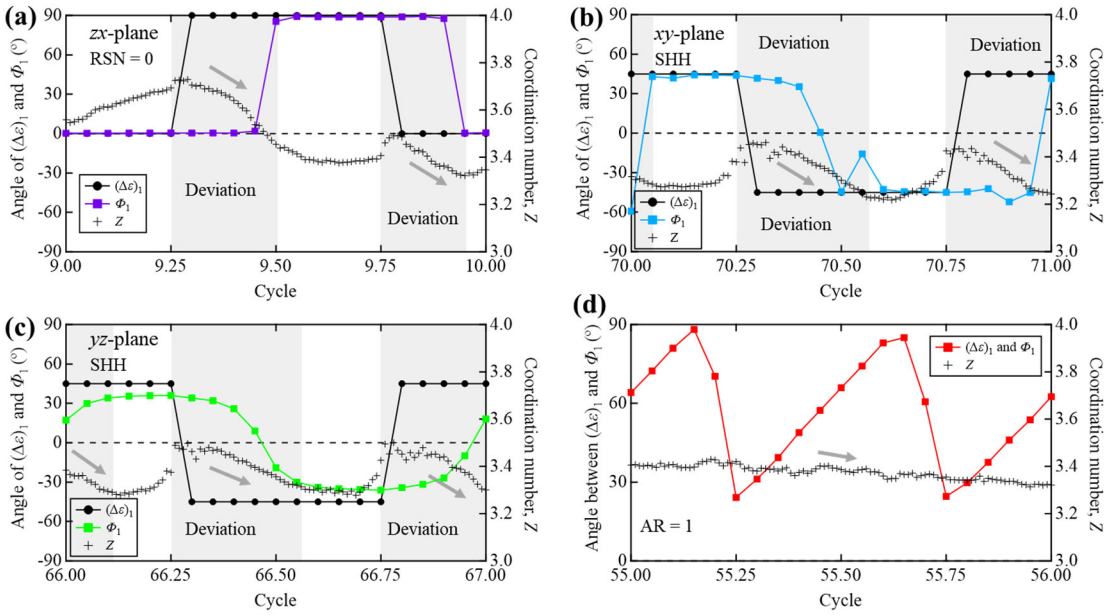

Fig. 4.40. Evolution of coordination number with change in directions of $(\Delta\varepsilon)_1$ and Φ_1 under: (a) Rayleigh-wave strain condition; (b) SHH-wave strain condition; (c) SHV-wave strain condition; (d) Love-wave strain condition with AR = 1.

direction of Φ_1. Especially, under Love-wave strain condition with AR = 1, the direction of $(\Delta\varepsilon)_1$ always deviated from the direction of Φ_1; therefore, Z almost decreased monotonically.

Compared to under SH- and Love-wave strain conditions, both the rate of decline and the amplitude of fluctuation of Z were larger under the Rayleigh-wave strain condition with RSN = 0. It indicated that the pure shear mode had a larger impact on the stability of a granular system than the simple shear mode or the combination of simple shear modes. When $\text{RSN} \leq 1$, the response of a granular system was governed by the pure shear mode; therefore, the evolutions of Z under Rayleigh-wave strain conditions with RSN = 0, 0.25, and 1 were similar. Under SH- and Love-wave strain conditions, the evolution of Z was also affected by the resultant shear strain. The fluctuation of Z was smaller under the strain condition with a smaller change in resultant shear strain. However,

regardless of the loading condition, when approaching approximately 2, Z decreased sharply, and the granular packing reached the initial liquefaction state.

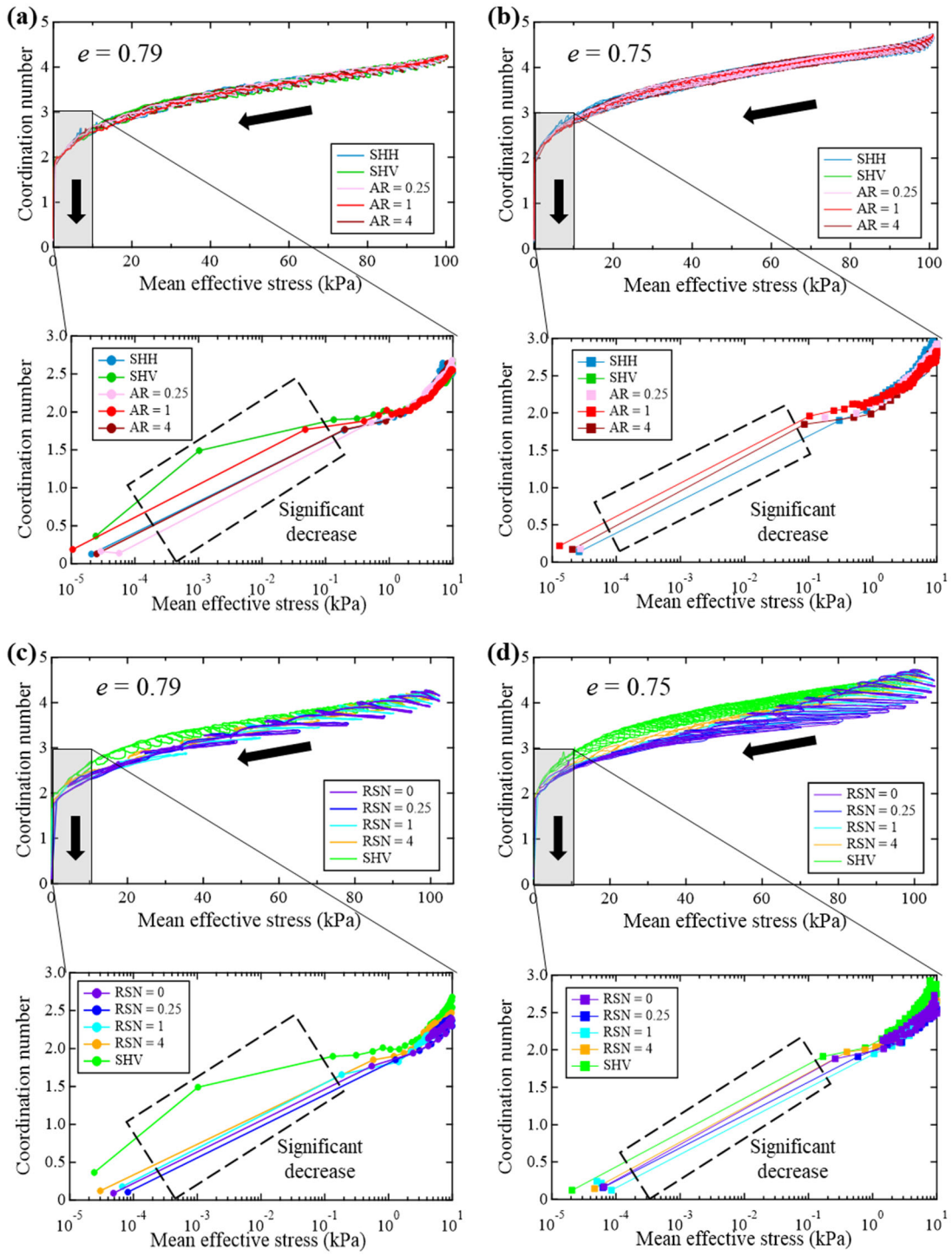

Fig. 4.41. Coordination number versus mean effective stress during cyclic loadings.

As shown in Fig. 4.41, Z was highly related to the mean effective stress. The gradual decrease in Z was accompanied by a decrease in mean effective stress. Especially, the mean effective stress decreased faster as Z became lower, suggesting that the skeleton structure's degradation accelerated the liquefaction of the specimens. As indicated in the enlarged part of the plot, regardless of the loading path, there was a sudden drop in the mean effective stress from approximately 10^{-1} to 10^{-5} kPa as Z fell below 2. As the time interval of the data output was 0.002 s, this process can be assumed to happen instantaneously. It is worth noting that the "zero mean effective state" was not reached after liquefaction because the interparticle contact had not completely disappeared.

4.5. Summary

To clarify the liquefaction behavior of granular materials under surface-wave strain conditions, the response of granular assemblies under Love- and Rayleigh-wave strain conditions was compared with that under SH-wave strain conditions by performing a series of 3D DEM numerical tests, where SH-, Love-, and Rayleigh-wave strain conditions are the deformation mode of SH, Love, and Rayleigh waves, respectively. Before conducting numerical tests, the equation governing the strain–time relationships of SH, Love, and Rayleigh waves was derived from elastic wave theory under the assumption of constant volume (undrained condition). Nine loading paths were applied to the specimens to cover the strain features of SHH-wave strain condition, SHV-wave strain condition, Love-wave strain conditions with AR = 0.25, 1, and 4, and Rayleigh-wave strain conditions with RSN = 0, 0.25, 1, and 4, respectively. The cyclic loadings were applied to the K_0-consolidated specimen until initial liquefaction. The main

conclusions are summarized as follows:

1. The deformation under SH-wave strain conditions is a simple shear mode; it under Love-wave strain conditions is a combination of simple shear modes; it under Rayleigh-wave strain conditions is a combination of simple shear mode and pure shear mode. The undrained response of a granular assembly is significantly affected by the loading paths. The fluctuation of ESRR and the magnitude of von Mises stress under Rayleigh-wave strain conditions is larger than that under SH- and Love-wave strain conditions. In addition, the resultant shear strain under Love-wave strain conditions has a significant influence on the fluctuation of ESRR and the magnitude of von Mises stress.

2. The liquefaction rate and resistance were evaluated by the accumulated equivalent strain and the NDE, respectively. Generally, at the same strain level, the Rayleigh-wave strain condition with a low RSN value would make granular materials more vulnerable to liquefaction than Love-wave strain conditions, and granular materials under Love-wave strain conditions are more likely to liquefy than under SH-wave strain conditions.

3. K_0-consolidation resulted in a structure whose normal contact forces, especially the strong normal contact forces, are more inclined to the vertical direction. As a result, vertical compression in the pure shear mode caused the magnitude and proportion of normal contact forces in the vertical direction to be much larger than in other directions. This means that, at the microscale, the positive dilatancy behavior in the pure shear mode was more sensitive to the strain level than that in the simple shear mode.

4. The fabric anisotropy increases during cyclic loadings. Especially, the increase

of fabric anisotropy is more significant under Rayleigh-wave strain conditions than that under other strain conditions. The evolution of fabric anisotropy under SH- and Love-wave strain condition highly relies on the plane in which shear strain is applied. With the degradation of the granular structure, the loading path has a larger influence on the evolution of structural anisotropy and rotation of structure elongation direction. The angle between ε_1 and Φ_1 and between σ_1 and Φ_1 tended to be a value near zero.

5. The increase in structural anisotropy and the degradation of the skeleton structure accelerated the liquefaction of granular materials. The fraction of sliding contacts increased, and the coordination number decreased during cyclic loadings. The magnitude of the fraction of sliding contacts and fluctuation of coordination number under Rayleigh-wave strain conditions is larger than that under SH- and Love-wave strain conditions. The evolution of the fraction of sliding contacts and fluctuation of coordination number under SH- and Love-wave strain conditions relies on the change in resultant shear strain during cyclic loading. However, regardless of the loading path, the initial liquefaction happened instantaneously when the coordination number approached approximately 2; It is noteworthy that the “zero mean effective states” was not reached in the initial liquefaction state.

CHAPTER 5 UNDRAINED SHEAR BEHAVIOR WITH LARGE SHEAR STRAIN AMPLITUDE

5.1. Introduction

The undrained cyclic shear behavior of granular material is highly dependent on the strain amplitude. However, the behavior of liquefiable granular materials under the undrained cyclic shear at extremely large shear strain amplitude (> 20%) had not been well understood because it is hard to achieve by actual physical element tests.

Generally, there are two states of shear deformation: pure shear and simple shear. As discussed in Chapter 4, the cyclic undrained responses of a granular assembly in pure shear mode and simple shear mode are quite different. As the simple shear mode is more suitable for the deformation of free-field horizontally layered ground during seismic events (Kammerer et al. 2001; Jefferies and Been, 2006), studies based on the simple shear mode are more representative. Therefore, the direct simple shear test was usually used to study the simple shear response of granular materials. The general method for determining the critical state requires information on all the stress components. However, on the one hand, the DSS tests, including the Royal Swedish Geotechnical Institute test type, Cambridge test type, and Norwegian Geotechnical Institute test type, are hard to measure the normal stress component in the horizontal direction; on the other hand, the critical state cannot be obtained before large shear deformation localization appears within shear bands (Fu and Dafalias, 2011), which may be hard to achieve in DSS tests.

To qualitatively evaluate the effect of very large shear strain (to 100%) on the cyclic

shear behavior of liquefiable granular materials, a series of undrained cyclic simple shear simulations was conducted in different cyclic shear strain levels by 3D DEM. It was found that the cyclic shear behavior of the specimens is highly affected by the cyclic shear strain amplitude. When the cyclic shear strain exceeds a certain amplitude, the shear band will be formed during both monotonic and cyclic loadings.

5.2. DEM simulations

5.2.1. Specimen generation

The simulations were also performed by Rocky as used in Chapter 4. Only spherical particles were used. The interaction model between particles comprises a normal force, a tangential force, and a rolling resistance model, as introduced in Section 3.2. A cubical assembly of spherical particles was generated from an inlet within a volume confined by

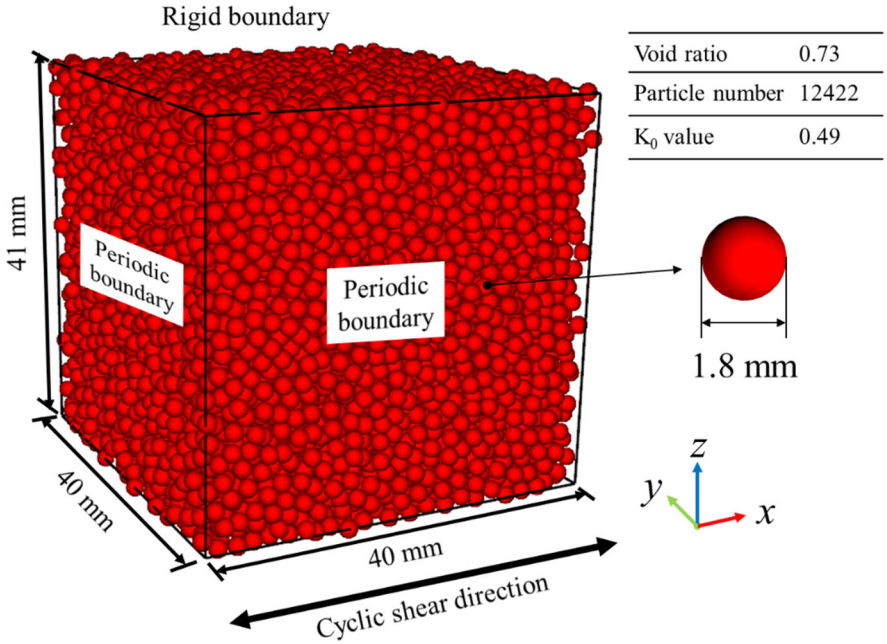

Fig. 5.1. Generated numerical specimen and boundary conditions.

periodic boundaries in the horizontal direction and rigid walls in the vertical direction, and then gradually compressed in the vertical direction to a K_0-stress state. The consolidated specimen is shown in Fig. 5.1 and the parameters used in the consolidation process are summarized in Table 5.1. The combination of the rolling resistance coefficient and friction coefficient in this simulation corresponded to an AoR of 30.43°. After consolidation, the gravity was set to zero and the mean effective stress of the granular assembly was 100 kPa. The measurement cube was located in the center of the specimen with a side length of 20 mm.

Table 5.1. Parameters used in the consolidation process

Particles	
Diameter (mm)	1.8
Density (g/cm^3)	2.65
Young's modulus (N/m^2)	1.0×10^9
Rolling resistance coefficient	0.3
Poisson's ratio	0.3
Rigid walls	
Young's modulus (N/m^2)	1.0×10^{11}
Interactions between particles	
Static friction coefficient	0.5
Dynamic friction coefficient	0.5
Coefficient of restitution	0.3
Tangential stiffness ratio	1.0
Interactions between particles and rigid walls	
Static friction coefficient	0.0
Dynamic friction coefficient	0.0
Coefficient of restitution	0.3
Tangential stiffness ratio	1.0
Computational parameters	
Gravity (m/s^2)	9.81
Timestep (s)	2.22×10^{-7}

5.2.2. Simulation conditions

Monotonic and cyclic undrained shear tests were conducted in this study. During undrained shear, the deformation of the specimen was achieved by moving the bottom rigid wall horizontally, and the volume of the specimen remained constant to simulate the undrained condition (CV method). In particular, the rotation and sliding between particle and rigid walls were forbidden to guarantee the application of shear strain. According to the $I = \dot{\varepsilon} d\sqrt{\rho/p'_{\mathrm{PT}}} < 2.5 \times 10^{-3}$ criterion (Perez et al., 2016), when $p'_{\mathrm{PT}} = 100$ kPa, the strain rate should satisfy $\dot{\varepsilon} < 8.5\ \mathrm{s}^{-1}$ to make the specimen under the quasi-static condition. Since no monotonic and cyclic undrained shear with single amplitude up to 100% had been conducted, to guarantee the quasi-static response of the granular assembly, a series of control tests with different strain rates were conducted to ensure that the strain rate used was suitable. It should be noted that the shear strain in this study was defined as $\gamma = \Delta l/H$, where Δl is the displacement of the bottom rigid wall and H is the height of the specimen.

5.2.2.1. Monotonic shear

The results of monotonic shear are shown in Fig. 5.2. Both shear stress and the mean effective stress increased with increasing shear strain, then decreased and arrived at

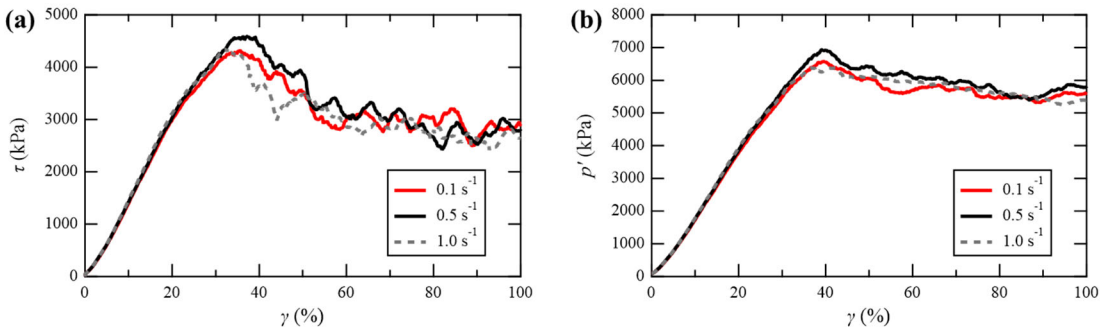

Fig. 5.2. (a) shear stress vs. shear strain; (b) mean effective stress vs. shear strain.

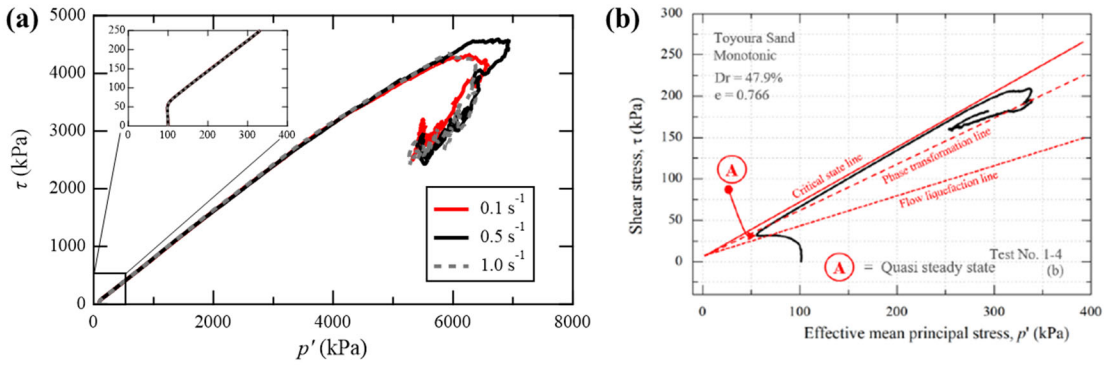

Fig. 5.3. Effective stress path during undrained monotonic loading: (a) simulation in this study; (b) laboratory test using large strain hollow cylindrical torsional shear apparatus (Umar et al., 2019).

a stable state of stress when the shear strain was around 60% (the shear stress and mean effective stress tend to be constant during continued deformation). In addition, the shear strain rate used in this study did not affect the response of the specimen. The stresses are extremely high during simulation, however, the maximum average overlap during loading was about 1.5%, which was less than 5% as suggested by Hanley et al. (2013). The volume change of the solid component of the specimen was ignorable. As shown in Fig. 5.3, except for the stress level, the results were analogous to those of a modified torsional shear test with applying shear strain up to 100% (Umar et al., 2019). It is noteworthy that the simulation with a shear strain rate of 0.1 s^{-1} would be used in subsequent analyses.

5.2.2.2. Cyclic shear

Cyclic shear strain with single amplitudes of 0.1%, 0.5%, 1%, 5%, 10%, 50%, and 100% was applied to the specimen, respectively. The responses of the specimen at different frequencies are shown in Fig. 5.4. The response of the specimen subjected to cyclic shear with amplitudes from 0.1% to 10% was not affected by the frequency used in this study due to the relatively low strain rate. The different responses in a low effective stress state arose from the unstable deformation, which is an intrinsic feature of cyclic

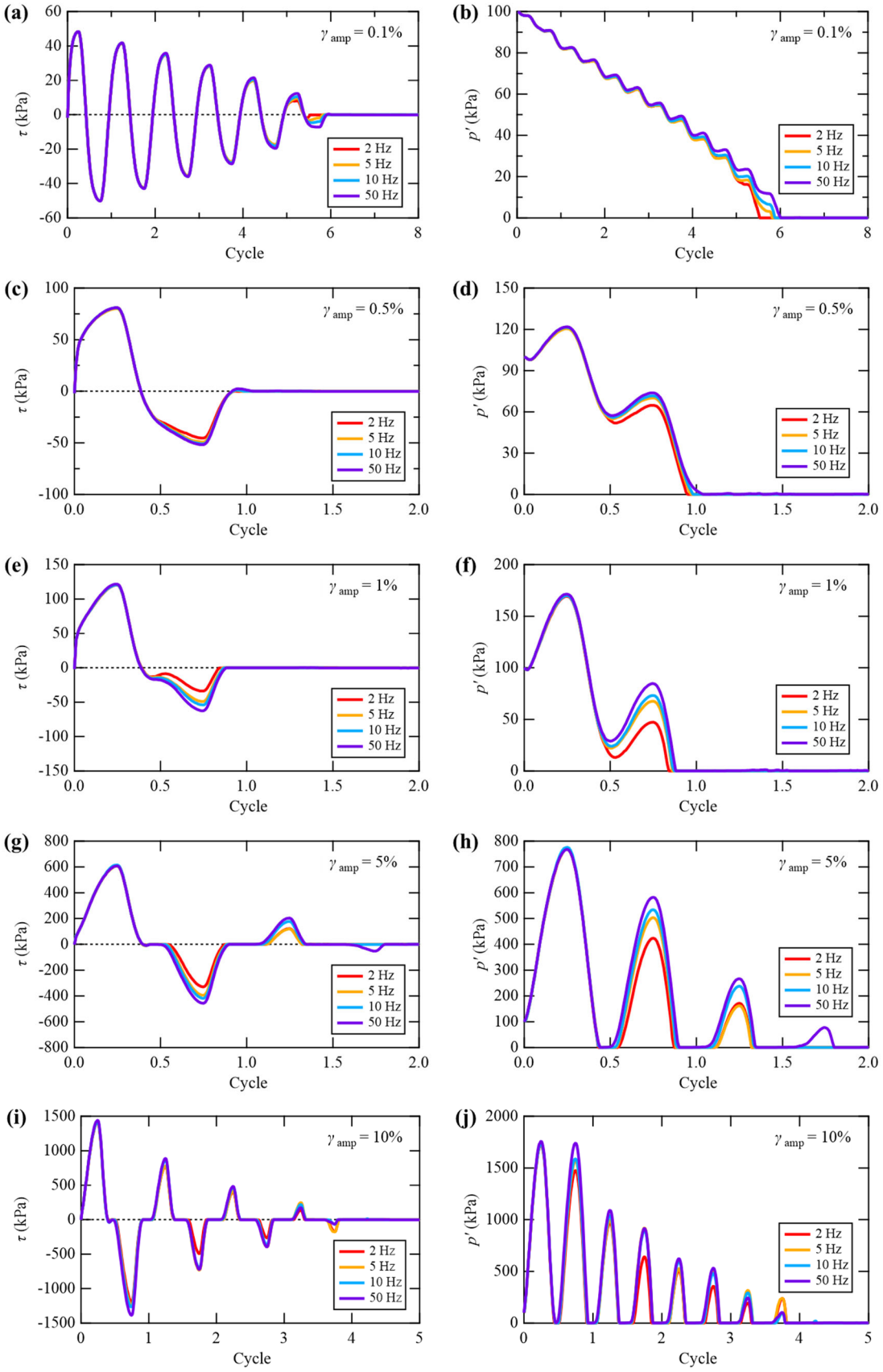
(a)
γ amp = 0.1%
τ (kPa)
Cycle
2 Hz
5 Hz
10 Hz
50 Hz
(b)
γ amp = 0.1%
p′ (kPa)
Cycle
(c)
γ amp = 0.5%
τ (kPa)
Cycle
(d)
γ amp = 0.5%
p′ (kPa)
Cycle
(e)
γ amp = 1%
τ (kPa)
Cycle
(f)
γ amp = 1%
p′ (kPa)
Cycle
(g)
γ amp = 5%
τ (kPa)
Cycle
(h)
γ amp = 5%
p′ (kPa)
Cycle
(i)
γ amp = 10%
τ (kPa)
Cycle
(j)
γ amp = 10%
p′ (kPa)
Cycle

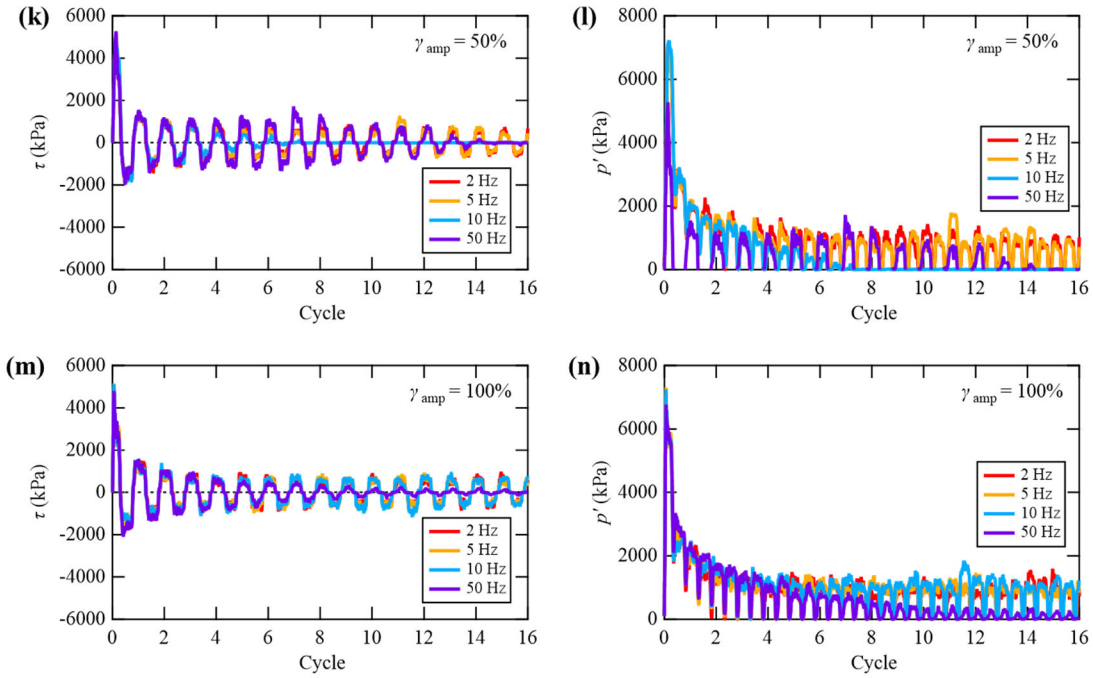

Fig. 5.4. Evolution of shear stress and mean effective stress during cyclic loading at different frequencies and amplitudes.

liquefaction and is not influenced by the loading rate (Yang and Taiebat, 2021).

The responses of the specimen subjected to cyclic shear strain with amplitudes of 50% and 100% at frequencies of 2 and 5 Hz were different from those at frequencies of 10 Hz and 50 Hz. The specimen finally liquefied at frequencies of 10 Hz and 50 Hz because of the relatively high strain rate. Therefore, the simulations with a frequency of 2 Hz were used in subsequent analyses after comprehensive consideration.

5.3. Simulation results

5.3.1. Monotonic shear

As shown in Fig. 5.5, the granular assembly was contractive when the shear strain

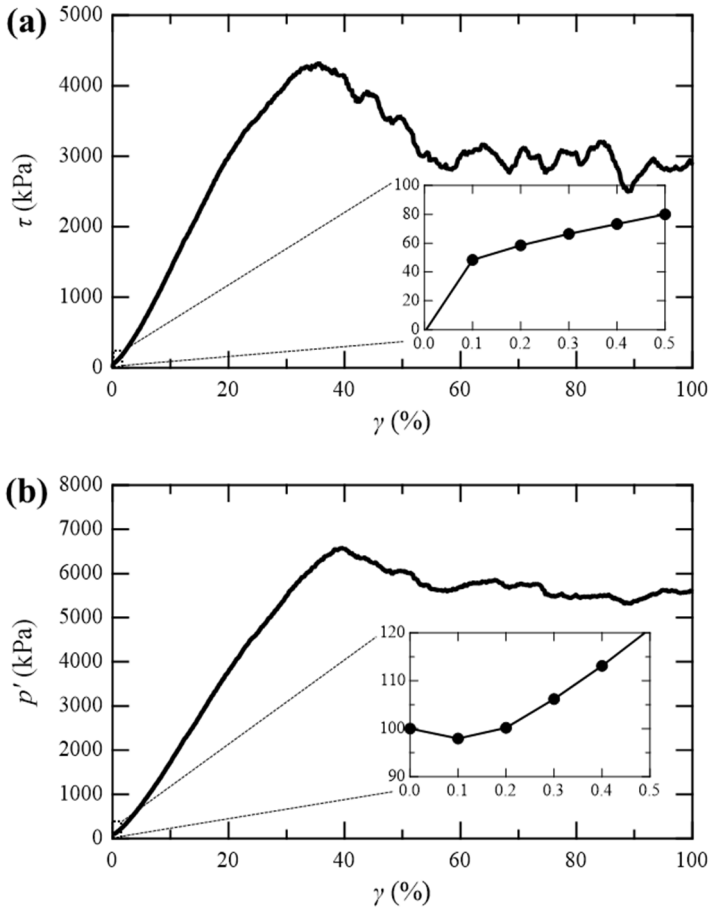

Fig. 5.5. Evolution of (a) shear stress and (b) mean effective stress during monotonic shear.

was in the range of 0–0.2%, and then turned into dilation behavior when the shear strain was large than 0.2%. The peak shear stress and mean effective stress were reached when the shear strain was about 40%. Subsequently, the shear stress and mean effective stress decreased and the granular assembly reached a stable state of stress when the shear strain was about 60%.

If divide the space between the top and bottom rigid walls into 20 equal layers, the mean velocity in the *x*-direction of each layer can be calculated by averaging the *x*-direction velocity of particles in that layer. Fig. 5.6(a) shows the mean velocity in the *x*-direction per layer for shear strains from 0% to 100%, where d_V is the vertical distance

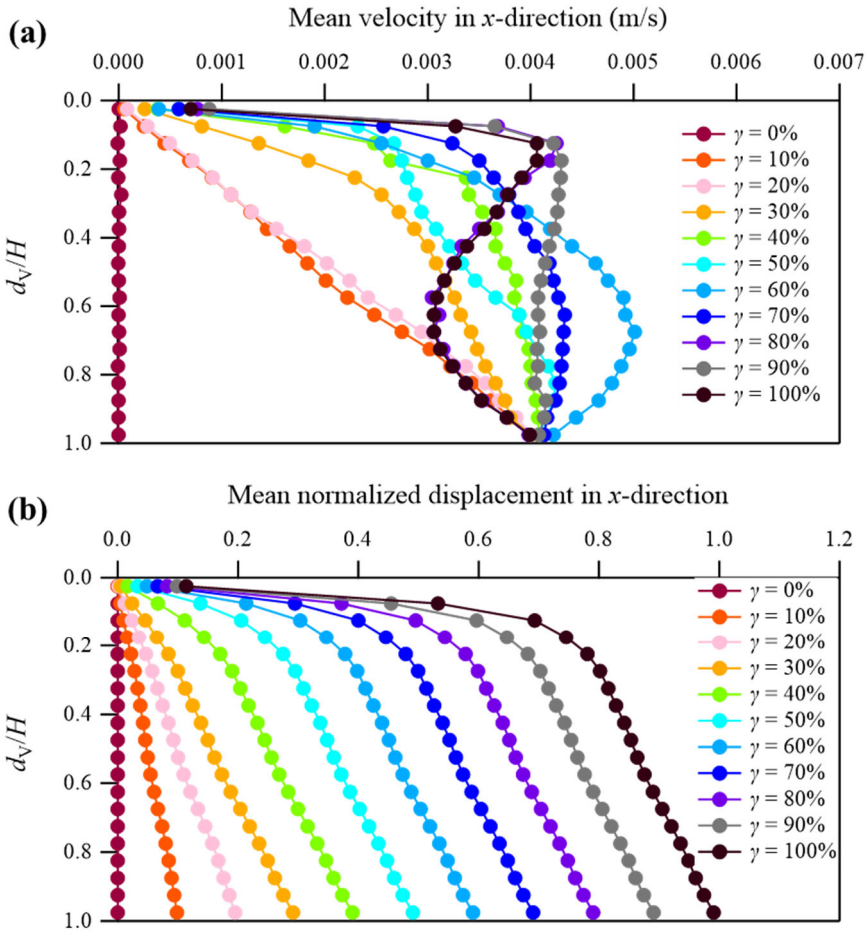

Fig. 5.6. (a) Mean velocity and (b) mean normalized displacement in the *x*-direction of particles per layer during monotonic shear.

from the midpoint of each layer to the top rigid wall, and H is the distance between the two rigid walls. As the bottom rigid wall was moving and the top rigid wall remained static, the velocity of particles contacting the bottom rigid wall was larger than those contacting the top rigid walls. When the shear strain was less than 30%, the distribution of particle velocity was like Planar Couette flow, in which the velocity field can be expressed by $u(d_V) = U\frac{d_V}{H}$, where U is the velocity of the bottom rigid wall. When the shear strain was larger than 20%, the distribution of particle velocity became uneven. The velocity gradient became larger near the top rigid wall and smaller in other parts of the specimen. Fig. 5.6(b) shows the distribution of the mean normalized displacement, which

is the mean displacement of particles in a layer normalized by the distance between the two rigid walls, in the *x*-direction. When the shear strain was larger than 30%, the mean normalized displacement in the *x*-direction below $d_V/H = 0.2$ are parallel at different strains, which indicated that the local shear strain concentrated near the top rigid wall and the shear band was formed. The phenomenon above was consistent with the observation of Lei et al. (2018) in the plane shear test.

The magnitudes and distributions of projections of normal contact forces on the *xz* in the measurement when the shear strain equals 0%, 10%, 50%, and 100% are illustrated in Fig. 5.7 (the magnitudes and distributions of projection of normal contact forces on the

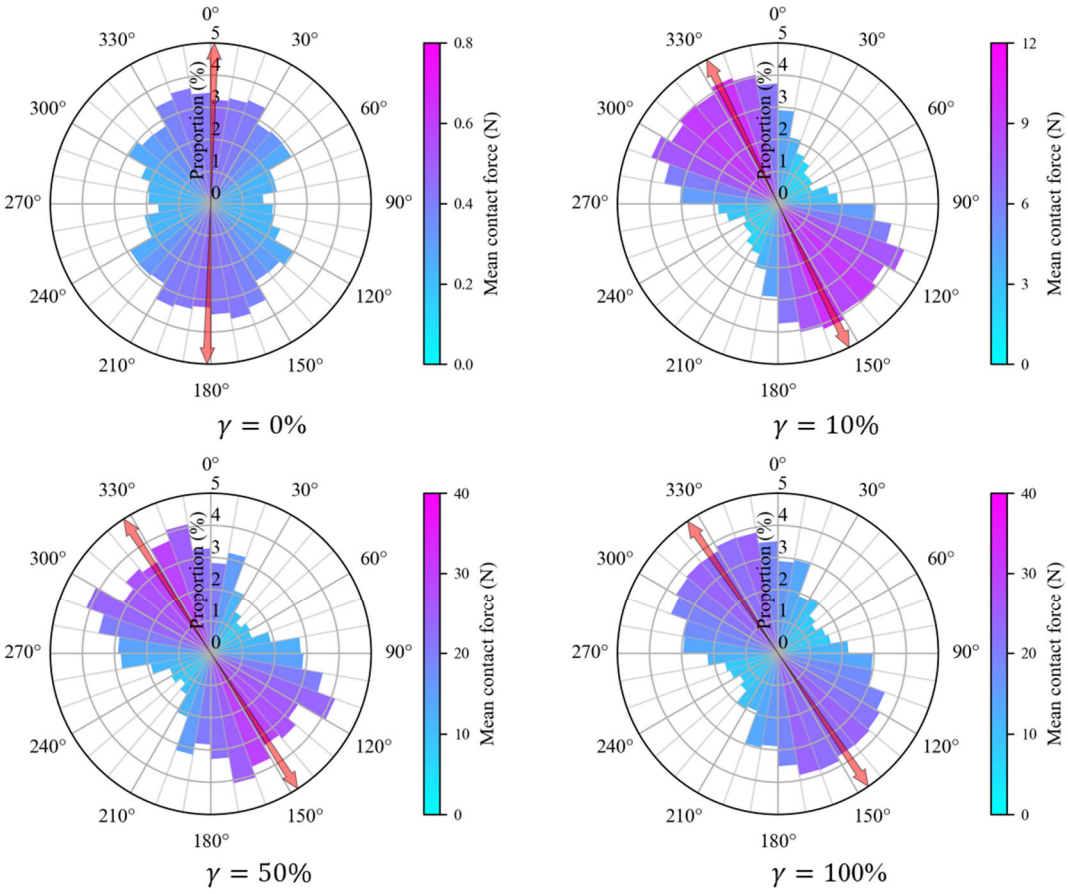

Fig. 5.7. Rose diagrams of projections of contact normal forces and major principal stress direction on the *zx*-plane during undrained monotonic shear.

zx-plane at 10% shear strain intervals are illustrated and shown in Appendix III). It should be noted that the measurement cube did not overlap the shear band during monotonic loading. The radial lines represent the contact force directions, and each concentric circle indicates the proportion of contact forces aligned in a particular direction range (10° per interval). The color of sector areas indicates the mean value of the projection of contact forces in each direction range on the *zx*-plane. The orange arrow illustrates the direction of the projection of major principal stress on the *zx*-plane.

Before shear strain was applied, the strong normal contact forces tended to align vertically because of K_0-consolidation. When the shear strain was applied, strong contact forces tended to rotate, and the magnitude of normal contact forces increased rapidly before the peak shear stress and peak mean effective stress were reached. The major principal stress direction rotated during monotonic shear and tended to be stable after the shear strain was greater than 10%. The normal contact forces tended to distribute symmetrically along the major principal stress in the stable state of stress. In addition, the normal contact forces became more concentrated near the major principal stress direction after reaching the stable state of stress. In addition, the magnitude of contact force near the major principal stress also became more uniform after entering the stable state.

Fig. 5.8 shows the evolution of some microscopic index, including the deviator fabric, the angle between the principal eigenvector of the deviatoric strain increment and the major principal fabric, the fraction of sliding contacts, and the coordination number during the undrained monotonic shear. It is noteworthy that the coordination number referred to the average coordination number of all the particles in the specimen, while the other microscopic indices were obtained from the range of the measurement cube. The

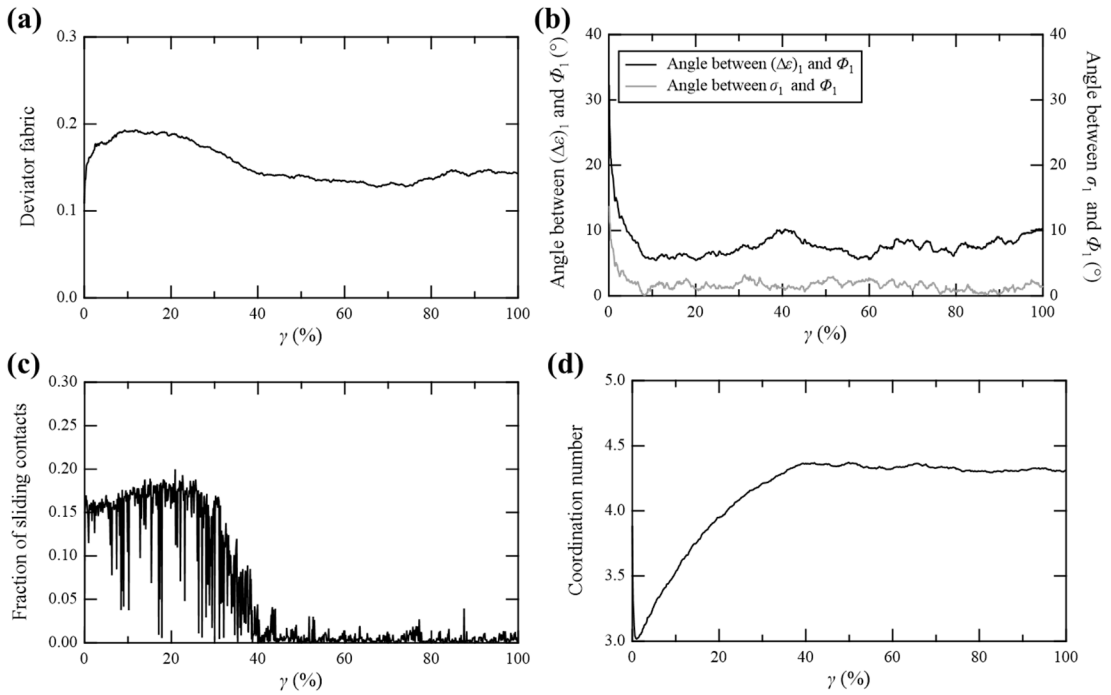

Fig. 5.8. Evolution of microscopic index during undrained monotonic shear: (a) deviator fabric vs. shear strain; (b) the angle between $(\Delta\varepsilon)_1$ and Φ_1 and between σ_1 and Φ_1 vs. shear strain; (c) fraction of sliding contacts; (d) coordination number vs. shear strain.

deviator fabric increased quickly and reached a peak when the shear strain was about 10%. Then it decreased and be stable after the specimen arrived at the stable state of stress. The angle between $(\Delta\varepsilon)_1$ and Φ_1 and between σ_1 and Φ_1 decreased to the minimum value when the shear strain was about 10% and tended to be stable when the deformation was continued. The value for the angle between $(\Delta\varepsilon)_1$ and Φ_1 was smaller than 10° and the value for the angle between σ_1 and Φ_1 was about 0°. It indicated that the structure elongation direction of the granular assembly became close to the direction of $(\Delta\varepsilon)_1$ and co-axial with σ_1 during 0–10% shear strain and tended to maintain the direction after 10% shear strain. The fraction of sliding contacts (FS) maintained a relatively high value when the shear strain was less than 20%, then decreased to about 0 during 20–40% shear strain. Finally, FS was maintained at about zero after 40% shear strain. The evolution trend of the FS was consistent with that of the deviator fabric. It

suggested that the granular fabric evolved rapidly in the range of 0–20% shear strain, and the evolution rate decreased in the range of 20%–40% shear strain. The granular fabric seemed to be stable after a 40% shear strain when the shear band was formed. The evolution trend of the coordination number was consistent with that of effective stress. The coordination number decreased initially because of the contractive behavior and then increased with the increase of mean effective stress. After the granular assembly reached a stable state of stress, the coordination number tended to remain constant. This phenomenon matched the point of view of Rothenburg and Kruyt (2004), who argued that the critical state is reached when rates of contact breakage and creation become equal (the critical state was reached in the shear band in this study).

5.3.2. Cyclic shear

The macroscopic responses of the granular assembly under undrained cyclic shear with different shear strain amplitude are shown in Fig. 5.9. As found in Section 5.3.1, under undrained monotonic shear, the behavior of granular aggregates was contractive for shear strains less than 0.2% and dilative for shear strains greater than 0.2%. Correspondingly, under undrained cyclic shear with an amplitude of 0.1%, the mean effective stress and shear stiffness decreased gradually, and the granular assembly eventually liquefied; under undrained cyclic shear with amplitudes of 0.5% and 1%, the mean effective stress initially deceased and then increased with shear strain as the behavior of the granular assembly changed from contraction to dilation at the phase transformation state. The mean effective stress and shear stress decreased as shear strain reversed, and the granular assembly eventually liquefied; under undrained cyclic shear

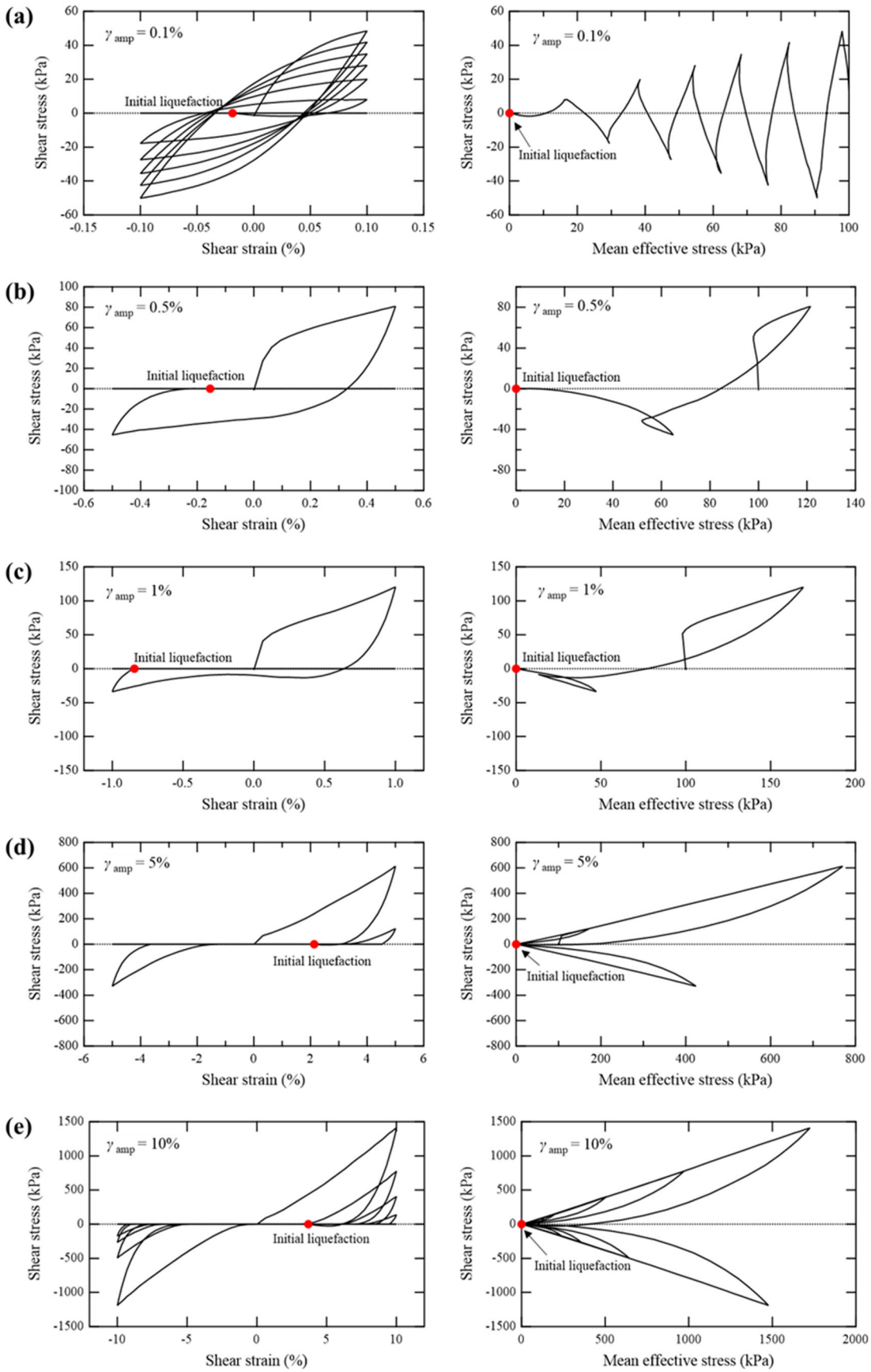
(a)
γ amp = 0.1%
Initial liquefaction
Shear stress (kPa)
Shear strain (%)
γ amp = 0.1%
Initial liquefaction
Shear stress (kPa)
Mean effective stress (kPa)
(b)
γ amp = 0.5%
Initial liquefaction
Shear stress (kPa)
Shear strain (%)
γ amp = 0.5%
Initial liquefaction
Shear stress (kPa)
Mean effective stress (kPa)
(c)
γ amp = 1%
Initial liquefaction
Shear stress (kPa)
Shear strain (%)
γ amp = 1%
Initial liquefaction
Shear stress (kPa)
Mean effective stress (kPa)
(d)
γ amp = 5%
Initial liquefaction
Shear stress (kPa)
Shear strain (%)
γ amp = 5%
Initial liquefaction
Shear stress (kPa)
Mean effective stress (kPa)
(e)
γ amp = 10%
Initial liquefaction
Shear stress (kPa)
Shear strain (%)
γ amp = 10%
Initial liquefaction
Shear stress (kPa)
Mean effective stress (kPa)

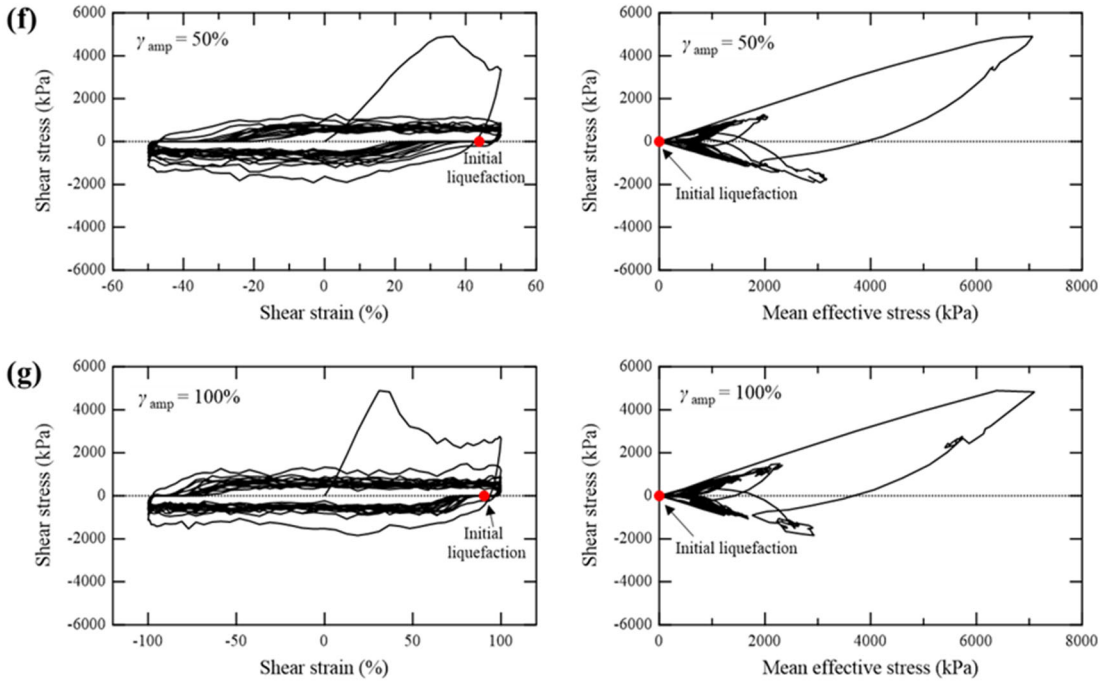

Fig. 5.9. shear stress vs. shear strain and effective stress path: (a) γ_{amp} = 0.1%; (b) γ_{amp} = 0.5%; (c) γ_{amp} = 1%; (d) γ_{amp} = 5%; (e) γ_{amp} = 10%; (f) γ_{amp} = 50%; (g) γ_{amp} = 100%.

with amplitudes of 5% and 10%, the dilative behavior of the granular assembly became stronger. Especially, the shear stiffness recovered after the initial liquefaction when the shear strain application was continued. However, the magnitude of shear stiffness that recovered after initial liquefaction also decreased gradually. Finally, the granular assembly was completely liquefied (shear stiffness no longer recovered); under undrained cyclic shear with amplitudes of 50% and 100%, the initial liquefaction occurred. However, the fluid-like state only existed within 20% shear strain after the reversal of shear strain during cyclic loading, and the shear stress recovered and maintained constant as shear strain continued. Especially, the magnitude of this unchanged shear stress was almost the same despite the shear strain amplitude and much lower than that under undrained monotonic shear, as shown in Fig. 5.10. If the displacement of the particles was set to zero at the beginning of the 11th cycle, the mean normalized displacements in the *x*-

direction of particles per layer in the first quarter of the 11th cycle are shown in Fig. 5.11(a)

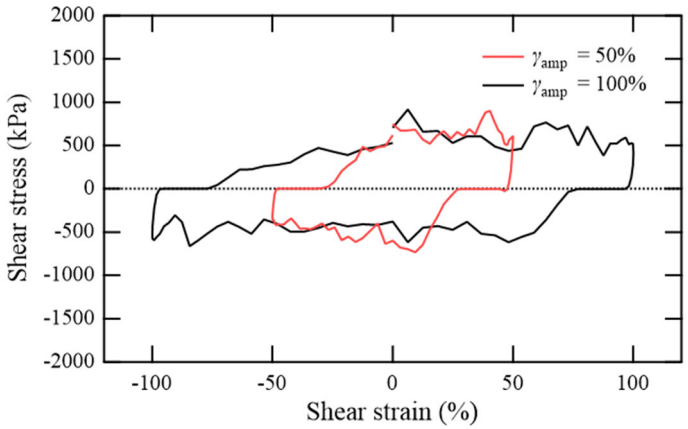

Fig. 5.10. Shear stress vs. shear strain under undrained cyclic shears with amplitudes of 50% and 100% during the 11th cycle.

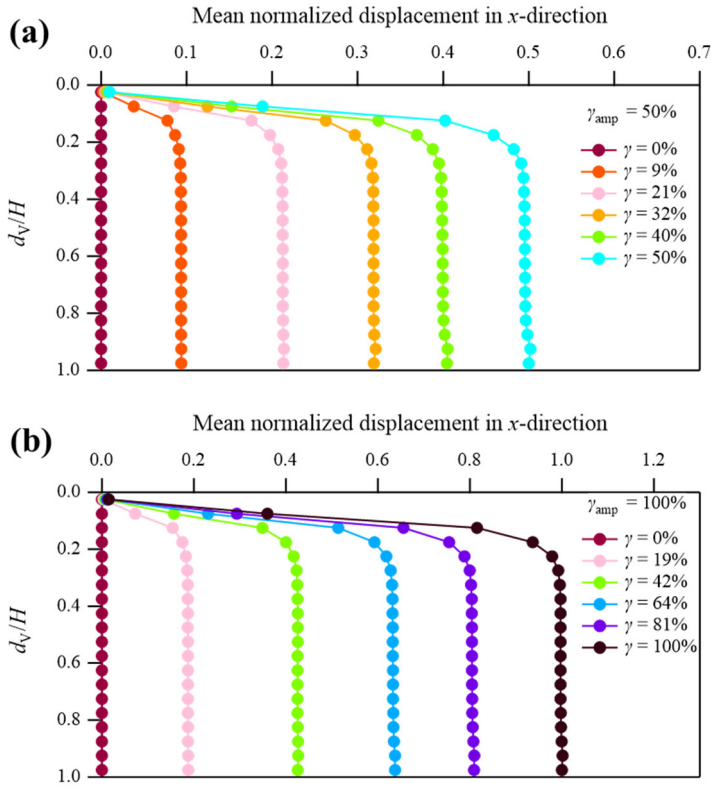

Fig. 5.11. Mean normalized displacement in the *x*-direction of particles per layer under undrained cyclic shear with amplitude of (a) 50% and (b)100% in the first quarter of the 11th cycle.

and (b). The shear band also formed near the top boundary during the cyclic loading, as the gradient of mean normalized displacement in the *x*-direction of particles was large near the top rigid boundary but almost zero in other parts of the specimen. This "strain localization" phenomenon during undrained cyclic shear was also observed in the hollow cylinder torsional shear test in which the double shear strain amplitude was loaded up to 100% (Kiyota et al., 2008).

The evolution of deviator fabric, the angle between $(\Delta\varepsilon)_1$ and Φ_1 and between σ_1 and Φ_1, FS, and coordination number during undrained cyclic shear are shown in Fig. 5.12–Fig. 5.15, respectively. The deviator fabric increased during the loading process and decreased during the unloading process before initial liquefaction. As shown in Fig. 5.12(a), (b), and (c), after entering the flow-like state, the fabric tensor based on particle contacts became invalid and the deviator fabric oscillated violently with continued application of shear strains. When the shear stiffness recovered after initial liquefaction during cyclic loadings, as shown in Fig. 5.12(e), (f), and (g), the deviator fabric became stable. Especially, these stable deviator fabrics in Fig. 5.12(f) and (g) are almost the same—about 0.15. As shown in Fig. 5.13, the angle between $(\Delta\varepsilon)_1$ and $(\Delta\varepsilon)_1$ and between σ_1 and Φ_1 deceased during the application of shear strain. When the direction of $(\Delta\varepsilon)_1$ and σ_1 were reversed, the angles increased sharply. This phenomenon was consistent with the observation in the SHV-wave strain condition in Chapter 4. Especially, as shown in Fig. 5.13(e), (f), and (g), when the shear stiffness recovered after initial liquefaction, the angle between $(\Delta\varepsilon)_1$ and Φ_1 and between σ_1 and Φ_1 dramatically became about 5° and about 2°, respectively. It indicated that the elongation direction of granular fabric formed during the shear stiffness recovery process after liquefaction was almost consistent with the $(\Delta\varepsilon)_1$ and σ_1.

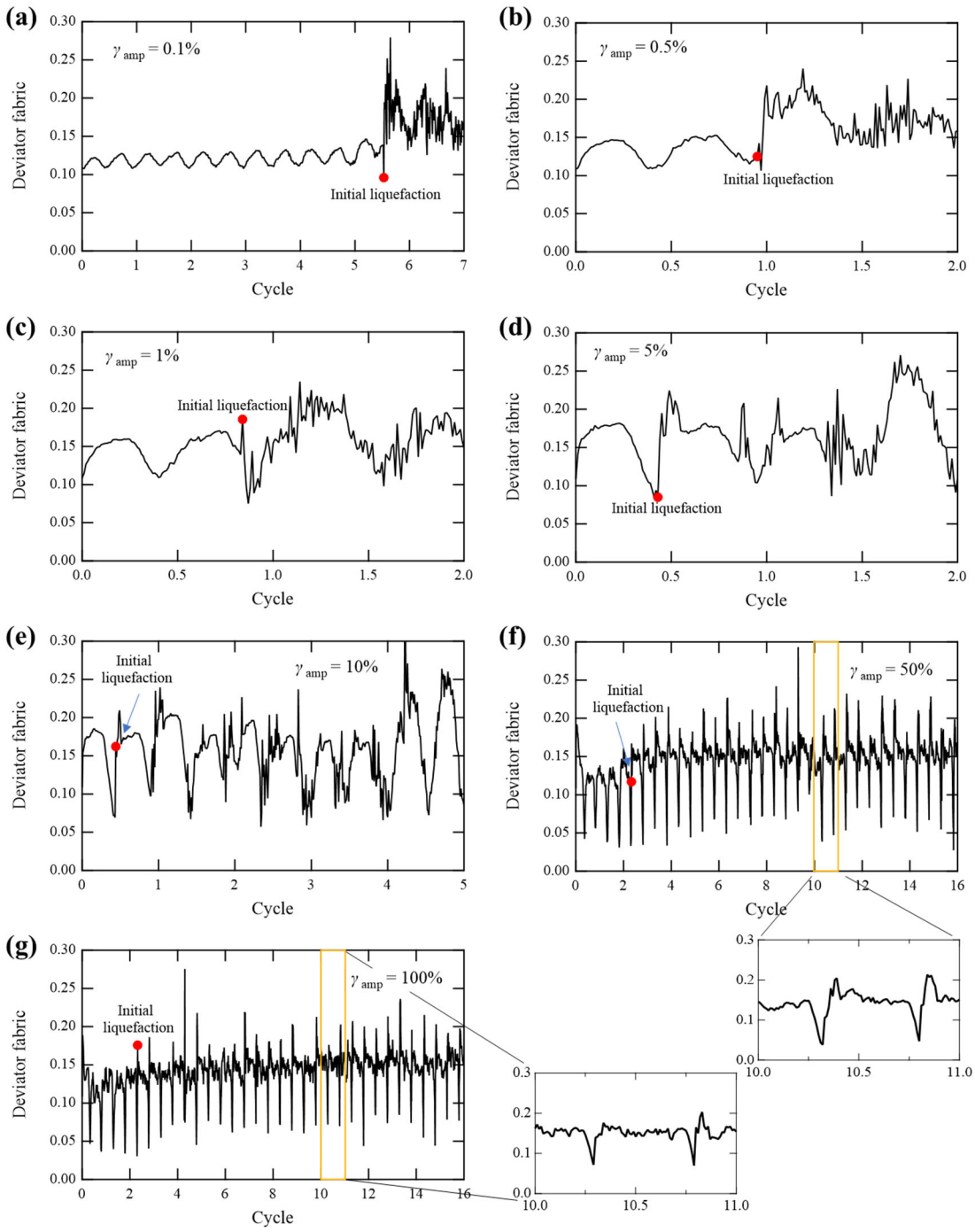

Fig. 5.12. Evolution of deviator fabric during undrained cyclic loadings: (a) γ_{amp} = 0.1%; (b) γ_{amp} = 0.5%; (c) γ_{amp} = 1%; (d) γ_{amp} = 5%; (e) γ_{amp} = 10%; (f) γ_{amp} = 50%; (g) γ_{amp} = 100%.

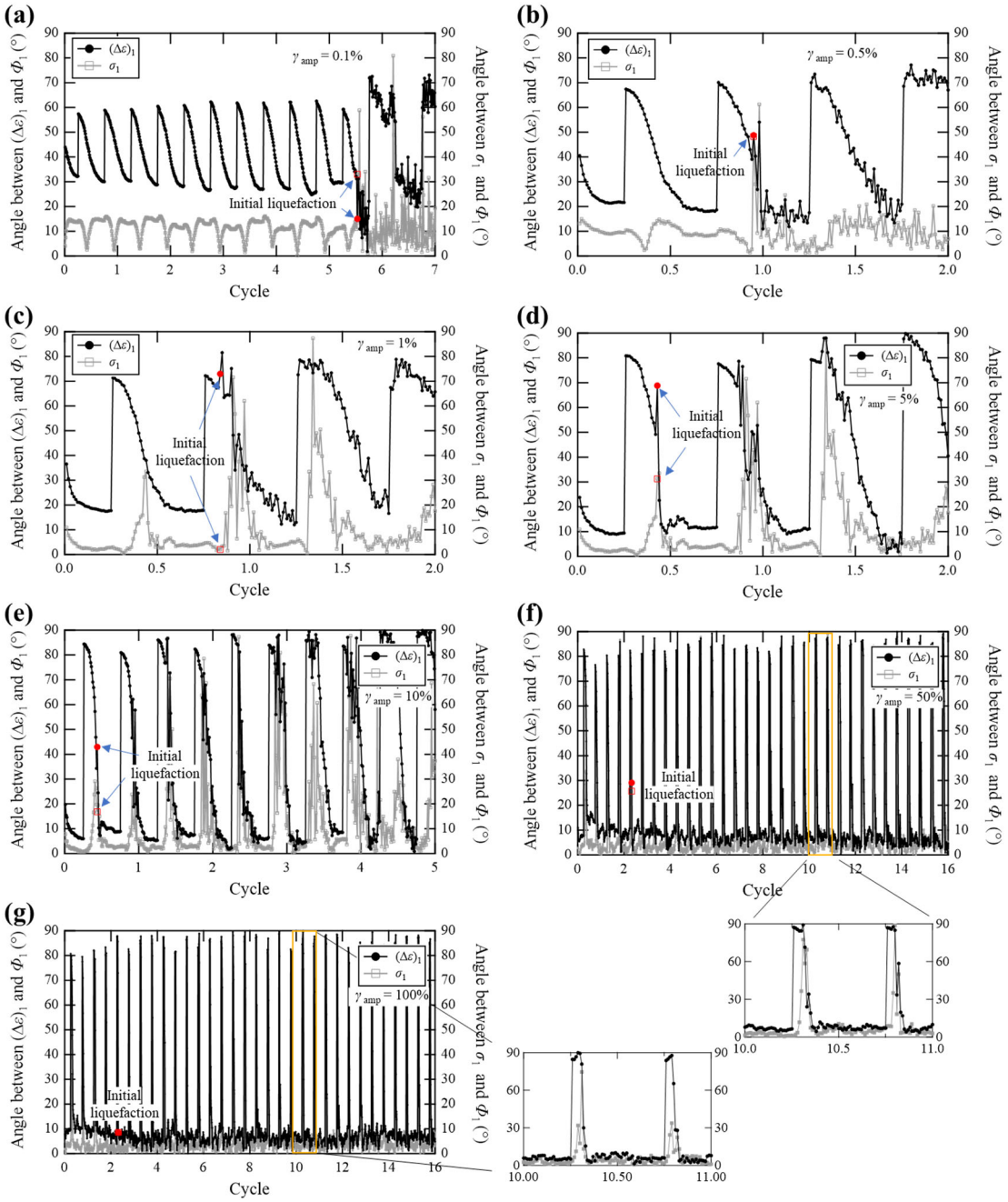

Fig. 5.13. Evolution of the angle between $(\Delta\varepsilon)_1$ and Φ_1 and between σ_1 and Φ_1 during undrained cyclic loadings: (a) γ_{amp} = 0.1%; (b) γ_{amp} = 0.5%; (c) γ_{amp} = 1%; (d) γ_{amp} = 5%; (e) γ_{amp} = 10%; (f) γ_{amp} = 50%; (g) γ_{amp} = 100%.

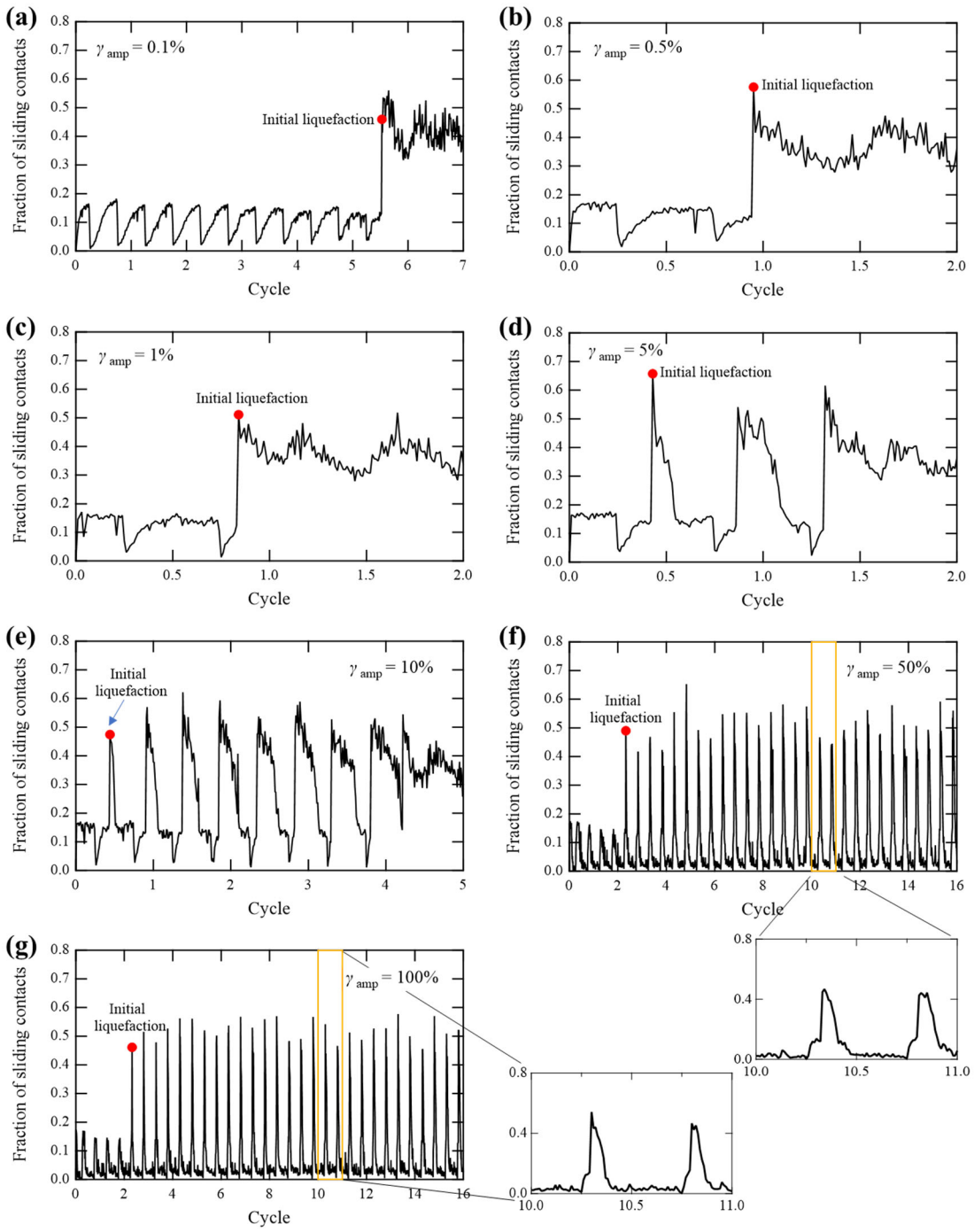

Fig. 5.14. Evolution of fraction of sliding contacts during undrained cyclic loadings: (a) γ_{amp} = 0.1%; (b) γ_{amp} = 0.5%; (c) γ_{amp} = 1%; (d) γ_{amp} = 5%; (e) γ_{amp} = 10%; (f) γ_{amp} = 50%; (g) γ_{amp} = 100%.

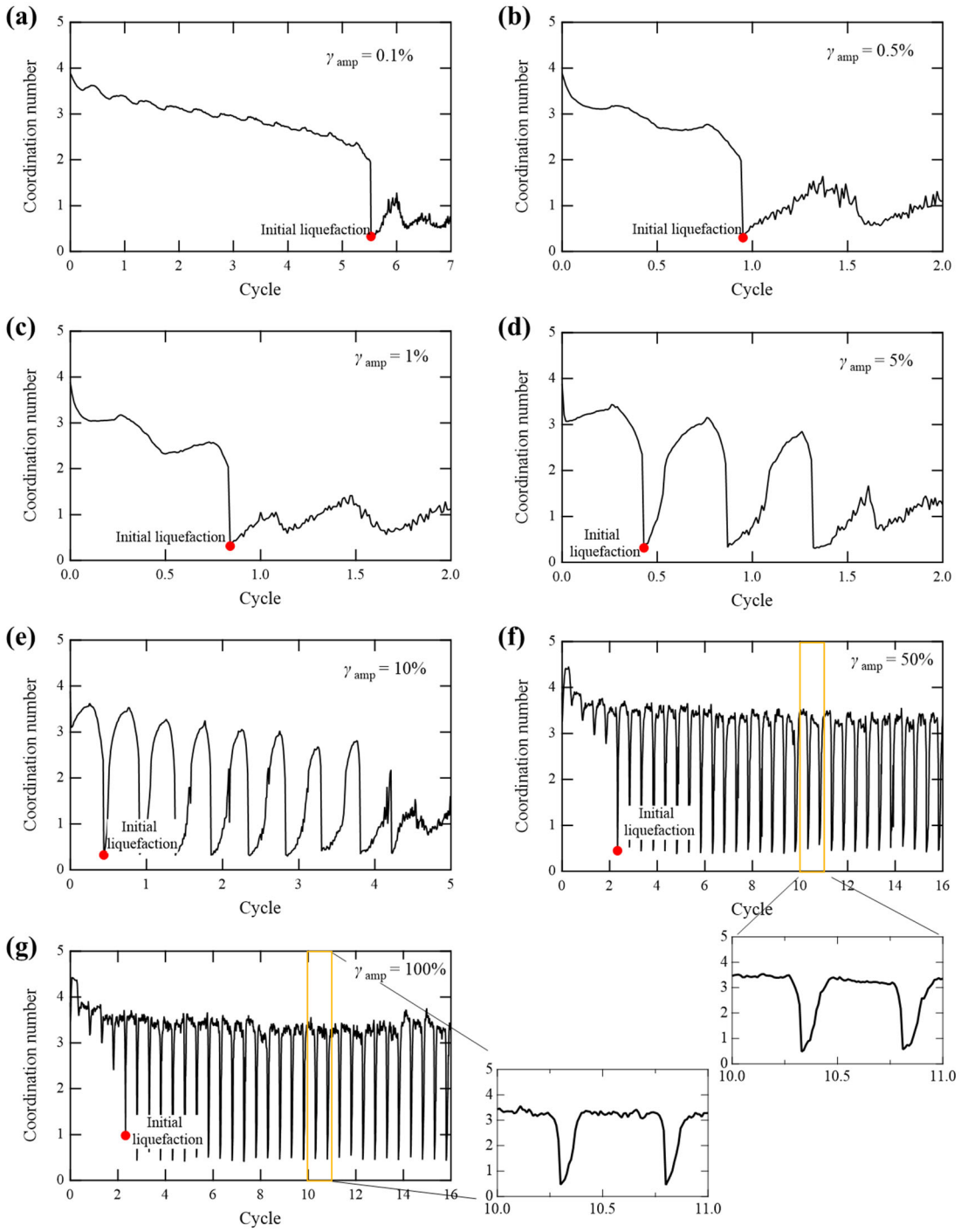

Fig. 5.15. Evolution of coordination number during undrained cyclic loadings: (a) γ_{amp} = 0.1%; (b) γ_{amp} = 0.5%; (c) γ_{amp} = 1%; (d) γ_{amp} = 5%; (e) γ_{amp} = 10%; (f) γ_{amp} = 50%; (g) γ_{amp} = 100%.

As shown in Fig. 5.14, FS increased during the application of shear strain and decreased sharply when the direction of shear strain application reversed. Especially, when initial liquefaction occurred, FS dramatically increased to a high value. In the flow-like state after initial liquefaction, as shown in Fig. 5.14(a), (b), and (c), FS maintained high values as most of the particle contacts are unstable collisions. When shear stiffness recovered after initial liquefaction, as shown in Fig. 5.14(d) and (e), FS decreased to a relatively low value. When the shear band formed after shear stiffness was recovered, as shown in Fig. 5.14(f) and (g), FS decreased to a value close to 0. It indicated that the particle contacts within the measurement cube, which was outside the shear band, were stable.

As shown in Fig. 5.15, the coordination number decreased gradually during cyclic loading. When the cyclic shear strain amplitude was smaller than 1%, as shown in Fig. 5.15(a), (b), and (c), the specimen liquefied with the coordination number dramatically decreasing from about 2 to a value near 0, which was consistent with the phenomenon observed in Chapter 4. However, under undrained cyclic shear with relatively large shear strain amplitude, as shown in Fig. 5.15(d), (e), (f), and (g), the coordination number dramatically decreases from a value larger than 2, even 3, to a value near 0. In the flow-like state after initially initial liquefaction, as shown in Fig. 5.15(a), (b), and (c), the coordination number remained below 2 although shear strain was applied. When shear stiffness recovered after initial liquefaction, as shown in Fig. 5.15(d), (e), (f), and (g), the coordination number also increased and then became stable and larger than 2, which suggested that when the shear stiffness recovered, a stable structure would form outside the shear band and the critical state would be reached in the shear band.

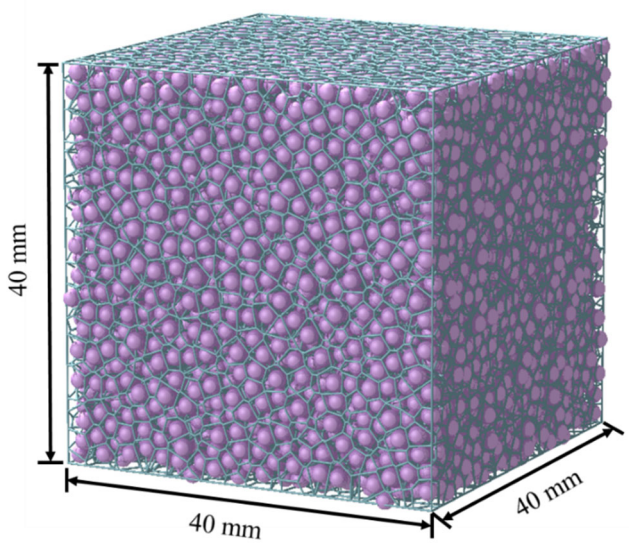

Fig. 5.16. Voronoi tessellation on the granular assembly.

Undrained cyclic shear will result in the degradation of the granular skeleton, which is accompanied by the dissipation of a large void, and the granular assembly became more uniform (Wang and Wei, 2016; Wei et al., 2019). The centroid distance, D_c, which is based on "particle-void cells" and was proposed by Wang and Wei (2016), was used in this study to evaluate the uniformity of the specimen. The "particle-void cell" was computed using Voronoi tessellation by an open-source software library, Voro++ (Rycroft 2009). Fig. 5.16 Shows the Voronoi tessellation on the granular assembly. The whole space can be divided into polyhedral regions composed of convex planes, which are called Voronoi cells. The centroid difference associated with a particle is defined by $\boldsymbol{D}_c^i = (\boldsymbol{P}^i - \boldsymbol{O}^i)/R_{50}$, where $\boldsymbol{P}^i$, $\boldsymbol{O}^i$ are the position vector of the mass centroids of the particle and the Voronoi cell surrounding it; R_{50} is the mean radius of the granular assembly. The centroid distance, D_c, is the average magnitude of the centroid difference. Generally, a large value of D_c indicates that the void spaces are distributed inhomogeneously or relatively large local pores existed in the specimen (Wang and Wei, 2016).

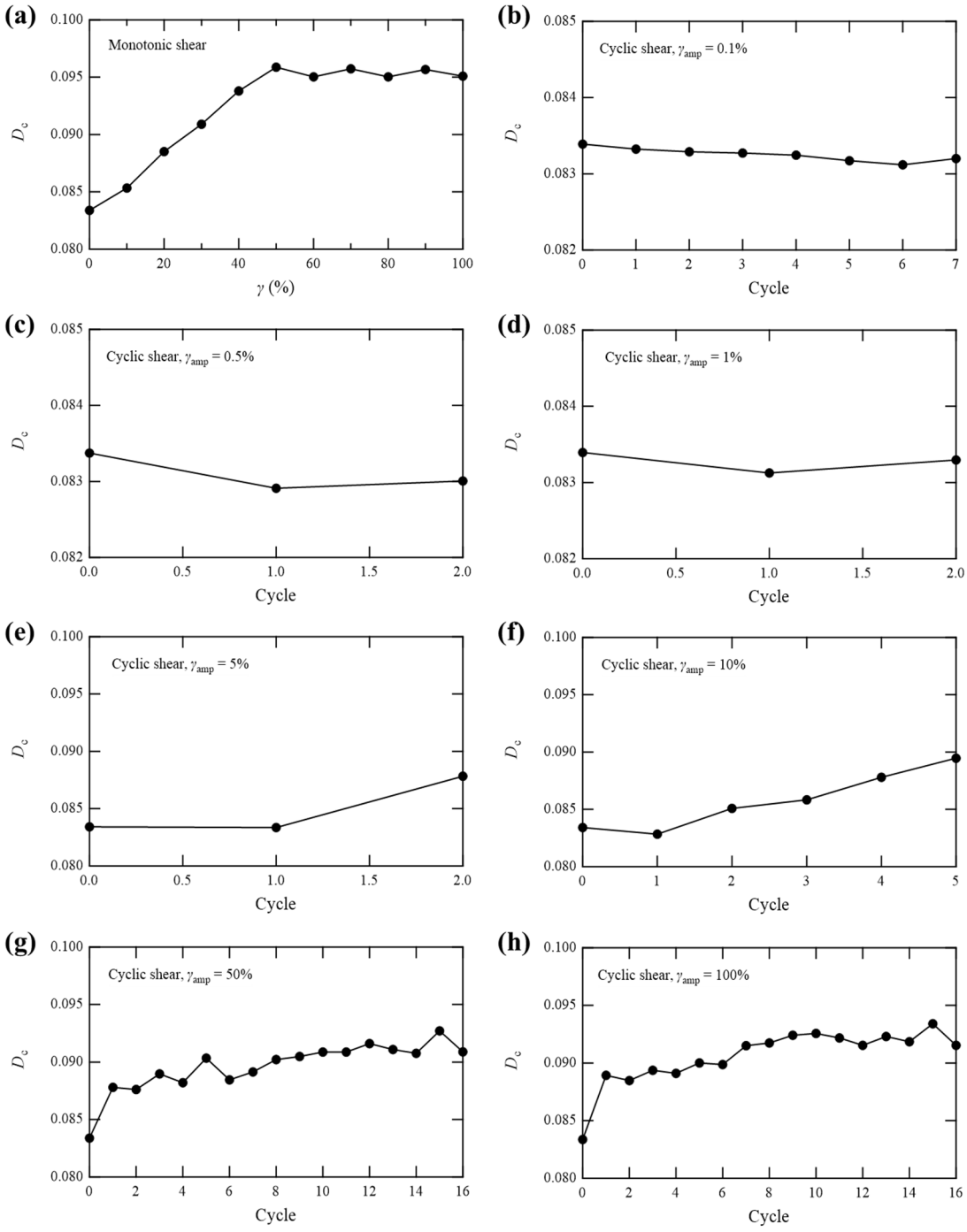

Fig. 5.17. Evolution of centroid distance during undrained shear (every 10% shear strain or 1 cycle).

As shown in Fig. 5.17(a), during undrained monotonic shear, D_c increased with shear strain application initially and then remained almost constant after the shear strain was larger than 50%. According to the evolution of effective stress during undrained monotonic shear shown in Fig. 5.5, the evolution of D_c suggested that the granular assembly became more inhomogeneous when the effective stress increased. As the effective stress became constant after the shear band formed, the uniformity of the granular assembly also remained constant.

As shown in Fig. 5.17(b)–(f), during undrained cyclic shear, D_c decreased during cyclic loading initially and then increased. By comparing with Fig. 5.4, it could be concluded that the granular assembly became more homogenous as the effective stress decreased. However, in the fluid-like state after initial liquefaction, the granular assembly became inhomogeneous because of the continued application of shear strain. Especially, the larger the shear strain applied, the more inhomogeneous the granular assembly during the fluid-like state after initial liquefaction.

As shown in Fig. 5.17(g) and (h), because the effective stress at the end of each cycle was larger than that at the initial state, D_c at the end of each cycle was also larger than that at the initial state (at the end of each cycle, the shear band was formed). Especially, D_c tended to be constant after initial liquefaction; however, it was lower than that under the undrained monotonic shear when the shear band formed. It indicated that when the shear band was formed, the granular assembly, on the whole, was more homogeneous under undrained cyclic shear after initial liquefaction than that under undrained monotonic shear. As mentioned in Fig. 5.10, the stable states of stress during undrained monotonic shear and undrained cyclic shear are different. This phenomenon

originated from the different granular fabrics when the shear band was formed. Although the void ratio of the granular specimen was constant, the void ratios within the shear band and out of the shear band were different because the granular fabrics were different during cyclic shear and monotonic shear. As the granular assembly was more homogeneous during undrained cyclic shear than during undrained monotonic shear when the shear band was formed, the granular particle in the narrow shear band can move more easily. Therefore, the effective stress in the stable state during undrained cyclic shear was lower than that during undrained monotonic shear.

It should be noted that the liquefaction phenomenon and occurrence of shear band in undrained cyclic simple shears with extremely large amplitude are predicated on the

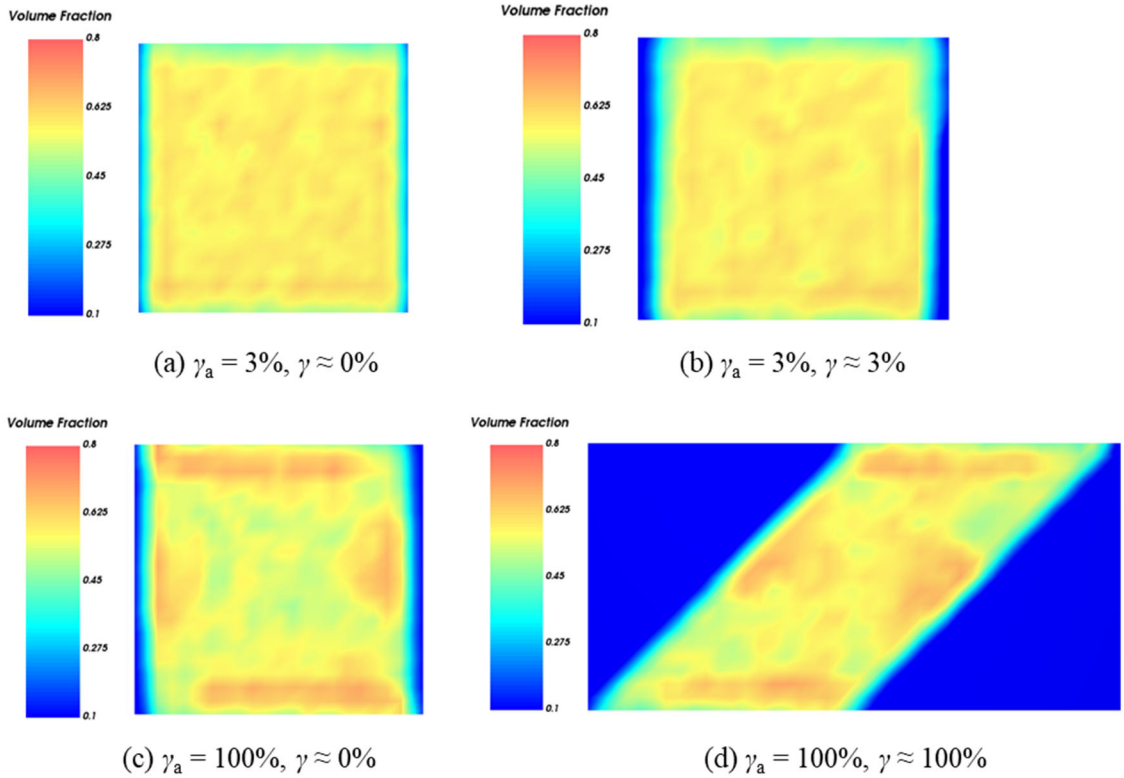

Fig. 5.18. Evolution of volume fraction in the specimen confined by rigid walls during undrained cyclic shear with amplitude of (a) 3% in zero-strain position; (b) 3% in maximum-strain position; (c) 100% in zero-strain position; (d) 100% in maximum-strain position (Jiang et al., 2020).

ideal boundary condition achieved by the periodic boundary, which means that there is no influence from the boundary, e.g., membrane, rigid boundary. Jiang et al. (2020) performed a series of 3D DEM undrained cyclic simple shear simulations with large shear amplitude using rigid boundaries. In their research, when the shear amplitude exceeded 45%, all the specimens did not liquefy, and the shear band also did not appear. In contrast, because the shortest distance between the lateral boundaries was shortened, the specimen became inhomogeneous and was subjected to excessive mean effective stress, which was far from the experimental results using actual soil particles. As shown in Fig. 5.18, when the shear strain amplitude was 3%, the granular assembly was relatively homogeneous during cyclic shear, while when the shear strain amplitude was 100%, the granular assembly was extremely inhomogeneous. In this research, as shown in Fig. 5.19, since there is no boundary effect (because of the presence of periodic boundaries) in lateral directions, the granular assembly was more homogeneous than in the case of using rigid boundaries in Fig. 5.18, and the shear band was formed near the top boundary (the volume fraction of the shear band was lower than that of the nearby area). The stress–strain relationship of the specimen depended on the characteristics of the shear band.

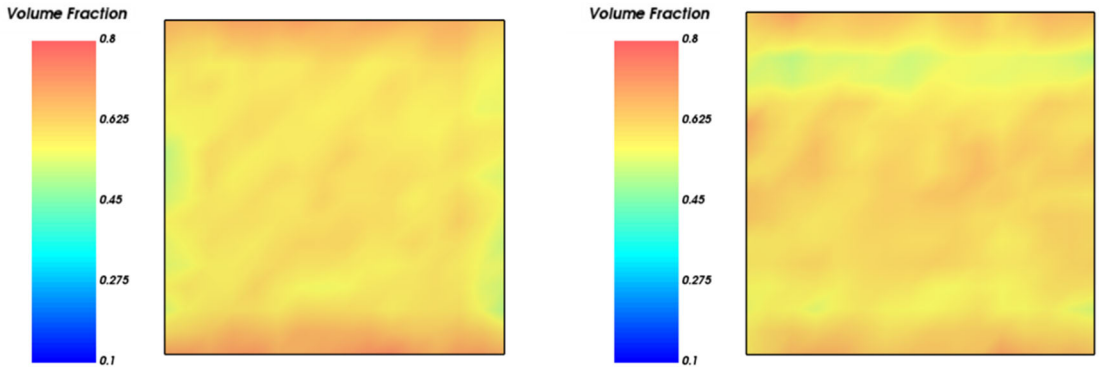

(a) Initial state (b) End of cycle 10

Fig. 5.19. Evolution of volume fraction in *zx*-plane in the specimen using periodic boundary during undrained cyclic shear with amplitude of 100% at (a) initial state and (b) the end of cycle 10.

5.4. Summary

A series of 3D DEM simulations under undrained monotonic and cyclic simple shears was performed until 100% shear strain amplitudes. The granular assembly was K_0-consolidated, and the periodical boundary was used to eliminate the influence of boundary effects in the large deformation. The main conclusions are summarized as follows:

1. During both undrained monotonic simple shear and undrained cyclic simple shear, when the shear strain exceeds a certain value and there is no influence of boundary effects, the uniform shear deformation in the element will disappear and the shear band will be formed. After the shear band was formed, the granular structure outside the shear band become stable, and the granular assembly reached a stable state of stress.

2. When the cyclic shear strain amplitude is small (≤ 1%), the medium-dense granular assembly will gradually lose shear stiffness, accompanied by the gradual decrease of effective stress, and liquefy at last. When the shear strain amplitude becomes larger (≤ 10%), the shear stiffness will recover after the initial liquefaction as the shear strain application is continued. However, the recovered shear stiffness also decrease gradually until the granular assembly was completely liquefied. When the shear strain amplitude exceeds a certain value (about 50%), the fluid-like state after initial liquefaction only exists in a small shear strain range (about 20%) after the direction of shear strain application is reversed. The shear stiffness will recover as the shear strain application is continued, and the granular assembly reaches a stable state of stress as the shear band was formed during cyclic loadings.

3. The fabric anisotropy increases during the loading process and decreases during

the unloading process. When the shear strain exceeds a certain value, the fabric anisotropy tends to be constant. The major principal fabric direction (Φ_1) tends to be close to the direction of shear strain application (principal eigenvector of the strain increment, $(\Delta\varepsilon)_1$) and major principal stress (σ_1) during the loading process and became constant when the shear strain exceeds a certain value. FS increases during the application of shear strain and decreases dramatically when the direction of shear strain application reverses. When the stable state of stress arrived, FS outside the shear band tends to be zero. The coordination number increases with the increase of effective stress and decreases with the decrease of effective stress. The coordination number will decrease dramatically from a value larger than 2 to a value near zero when the initial liquefaction occurs. In the flow-like state after initial liquefaction, the coordination number was below 2; however, when shear stiffness recovered, the coordination number will recover and become larger than 2.

4. The granular assembly became inhomogeneous during undrained monotonic shear when the effective stress increased. During undrained cyclic shear, the granular assembly becomes homogeneous as the effective stress decrease. After initial liquefaction, because the granular structure was destroyed, the granular assembly becomes inhomogeneous at flow-like when shear strain application is continued. When the shear band was formed, the whole granular assembly become more inhomogeneous than the initial state. However, compared to under the undrained monotonic shear, the granular assembly under the undrained cyclic shear is more homogenous when the shear band was formed. This explained the different stable states of stress between undrained monotonic shear and cyclic shear as the void ratios in the narrow shear band are different.

CHAPTER 6 VOLUMETRIC STRAINS DURING RECONSOLIDATION

6.1. Introduction

The reconsolidation of ground after undrained cyclic shear during an earthquake may also cause severe damage to buildings and infrastructures. However, the nonlinear relationship between the void ratio and effective stress during reconsolidation, especially the resedimentation process, was not well investigated due to the limitation of laboratory tests. A series of 3D DEM simulations was conducted to investigate the reconsolidation characteristics of granular materials after undrained cyclic shear, and the results were analyzed based on the macroscopic and microscopic responses.

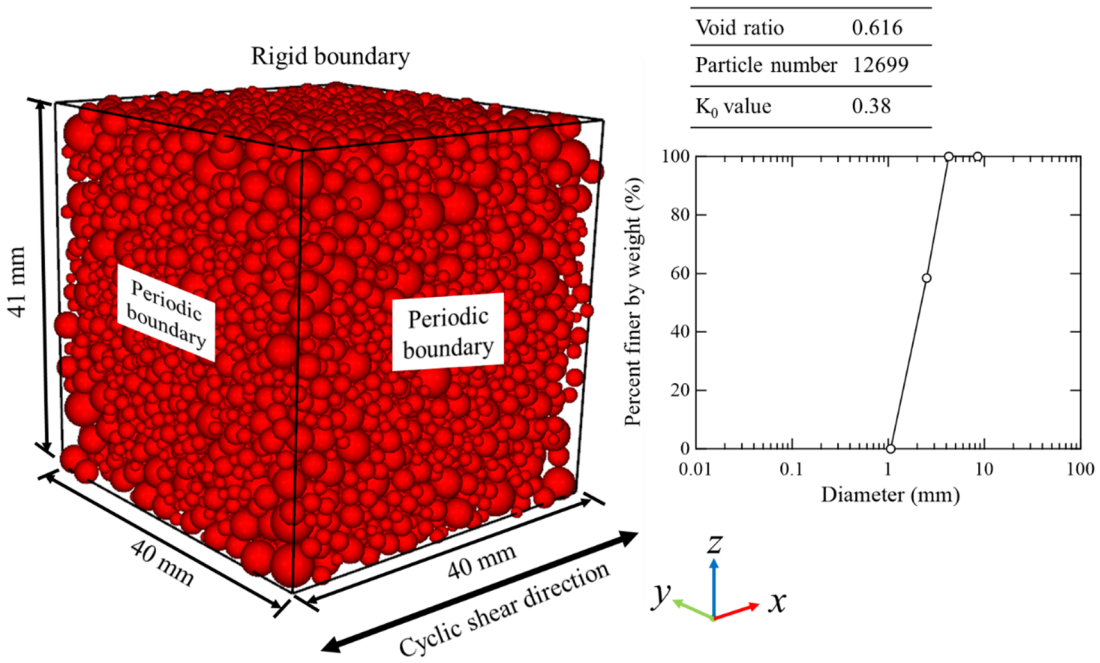

Fig. 6.1. Granular assembly composed of multi-sized particles and its corresponding PSD curve.

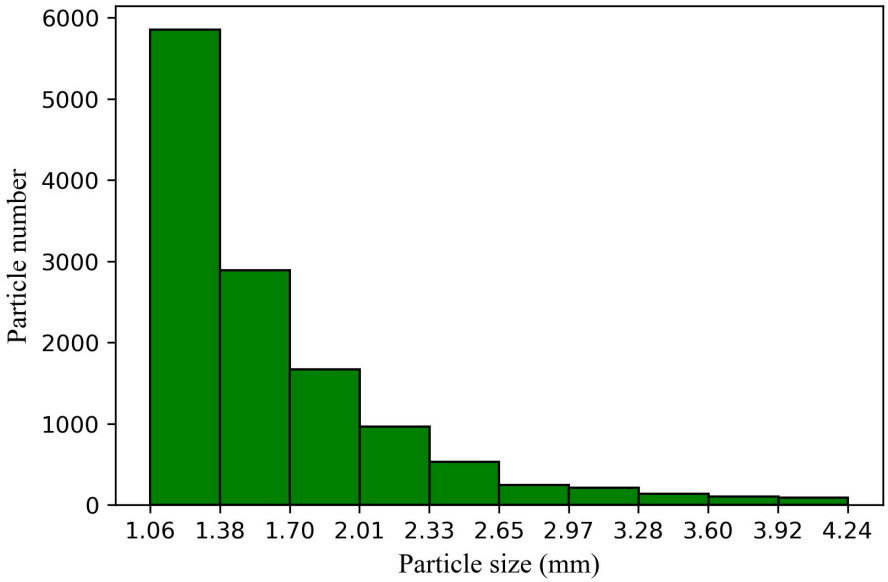

Fig. 6.2. Histogram of particle size in the specimen with Toyoura size distribution.

6.2. DEM simulations

6.2.1. DEM models

In this study, both single-sized particles and multi-sized particles were used. The specimen composed of single-sized particles is the same as what was used in Chapter 5. The specimen composed of multi-sized particles and its corresponding particle size distribution (PSD) curve are shown in Fig. 6.1. The particle sizes are 10 times that of Toyoura sands and it was called Toyoura size distribution. Especially, particles with a diameter lower than 0.106 mm are deleted in this study to improve the computation efficiency. The particle number in a given particle size range in the specimen with Toyoura size distribution is shown in Fig. 6.2. The average particle size of both the Single size distribution and the Toyoura size distribution is 1.8 mm. In particular, the two specimens are generated using the same method as introduced in Chapter 5. The

parameters in the two specimens are the same except for the particle size, particle number, void ratio, and K_0 value. The AoR corresponding to the Toyoura size distribution is 31.38°, which is a little higher than that corresponding to the Single size distribution (30.43°).

6.2.2. Undrained cyclic shear

The undrained cyclic shear was strain-controlled by moving the bottom rigid wall. The shear strain amplitude was 0.1%. As mentioned in Chapter 5, the responses of the granular assembly during undrained cyclic shear with a shear strain amplitude of 0.1% are the same at frequencies of 2 Hz and 5 Hz. Therefore, to save computation time, the undrained cyclic shears were conducted at the frequency of 5Hz.

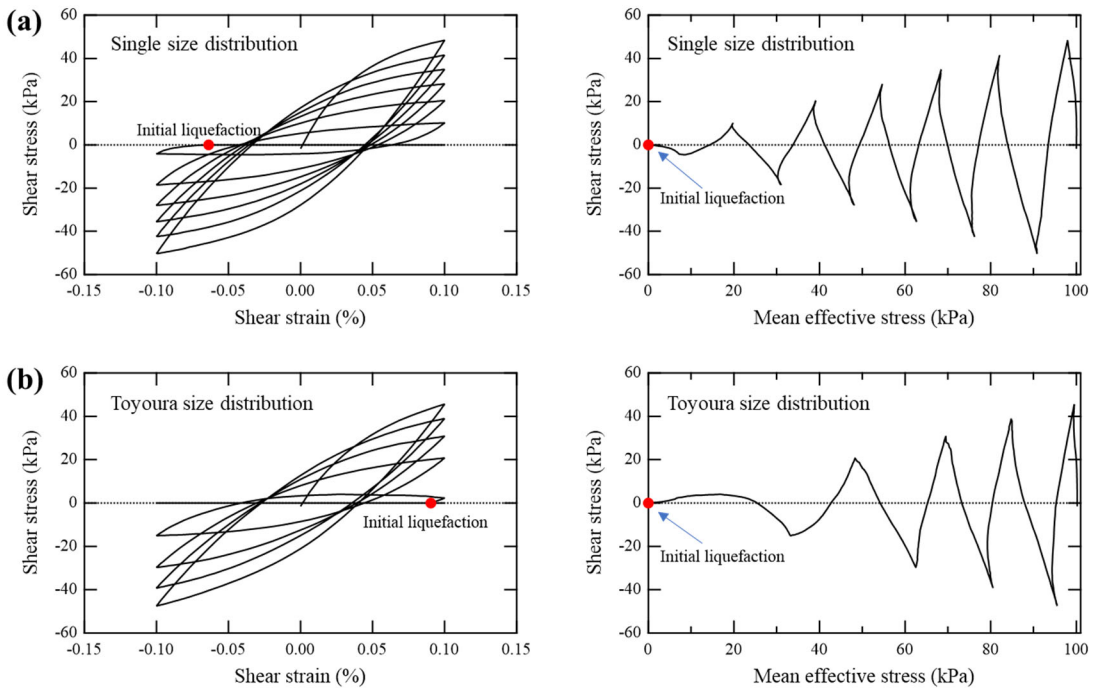

Fig. 6.3. Shear stress vs. shear strain and effective stress during cyclic loadings: (a) specimen with Single size distribution; (b) specimen with Toyoura size distribution.

The macroscopic responses of two specimens during undrained cyclic loading are shown in Fig. 6.3, which was consistent with the pattern obtained from laboratory element tests. The shear stiffness and effective stress decreased during undrained cyclic shear and the two specimens liquefied ultimately. In addition, there is no shear stiffness recovery after initial liquefaction after shear strain application was continued.

6.2.3. Reconsolidation

The reconsolidations were conducted from the end of each cycle, which was achieved by moving the top rigid wall downward. The reconsolidation was completed when the vertical effective stress σ'_v recovered to the initial value σ'_{v0}, which was 151.3 kPa in the monodisperse specimen and 170.2 kPa in the polydisperse specimen. To clarify the effect of strain rate on the volumetric strain during reconsolidation, a series of reconsolidation tests using the monodisperse specimen, both before initial liquefaction and after initial liquefaction, was conducted with different strain rates.

As shown in Fig. 6.4(a), the evolutions of the void ratio during reconsolidation

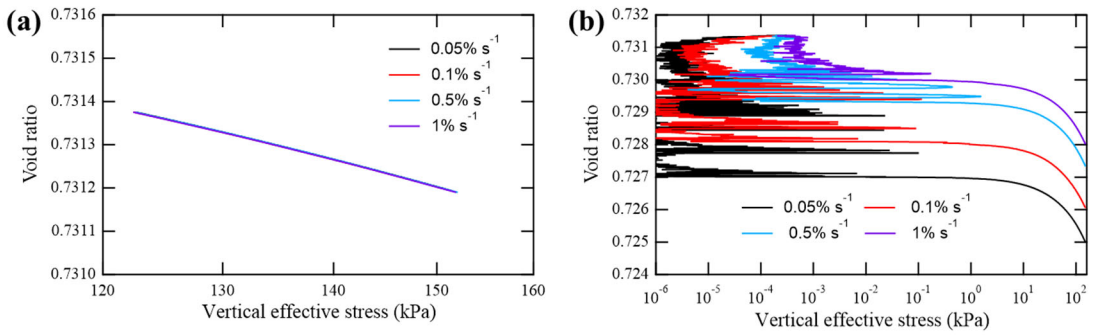

Fig. 6.4. Evolution of void ratio during reconsolidation: (a) reconsolidation before initial liquefaction; (b) reconsolidation after initial liquefaction

started before initial liquefaction at different strain rates were identical. However, during the reconsolidation started after initial liquefaction, the changes in void ratio during the very small effective stress state were different, although the slope of the $e - \log \sigma'_v$ are almost identical after σ'_v was larger than 10^{-1} kPa. It indicates the strain rate only used in this study only affects the reconsolidation during a very small effective stress range. Considering the computation efficiency, a strain rate of 0.05% was used in this study.

As shown in Fig. 6.5, during undrained cyclic shear, σ'_v decreased gradually. As σ'_v the first time below 1×10^{-3} kPa, the granular assembly was assumed to be initially liquefied. The reconsolidation started from the end of each cycle, and the corresponding value of σ'_v are shown in Fig. 6.5 and marked by red dots. The red dots did not completely coincide with the curve because the curve corresponds to the undrained cyclic shear until initial liquefaction occurred (corresponding to the reconsolidation that began at the end of the 6th cycle in the specimen with Single size distribution and at the end of 5th cycle in the specimen with Toyoura size distribution), while the reconsolidations initiated at other effective stress states were different simulations performed from the state prior to undrained cyclic shearing.

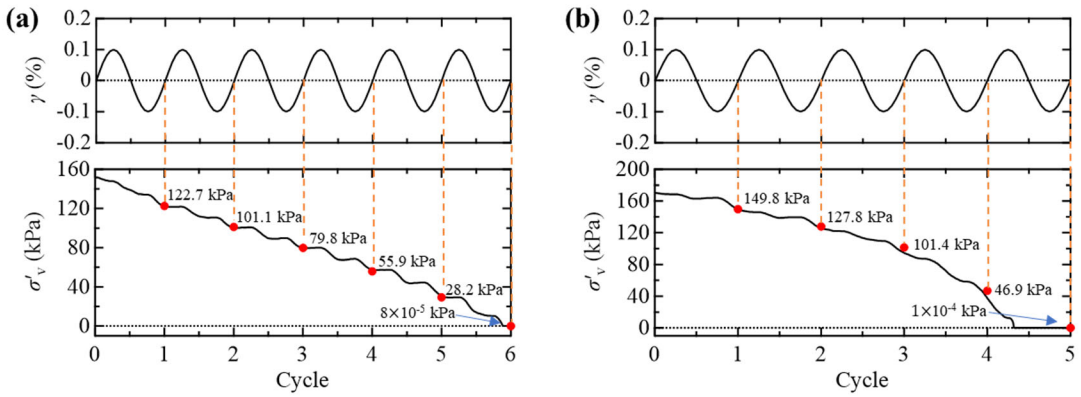

Fig. 6.5. Reconsolidation beginning at different cycles: (a) specimen with Single size distribution; (b) specimen with Toyoura size distribution.

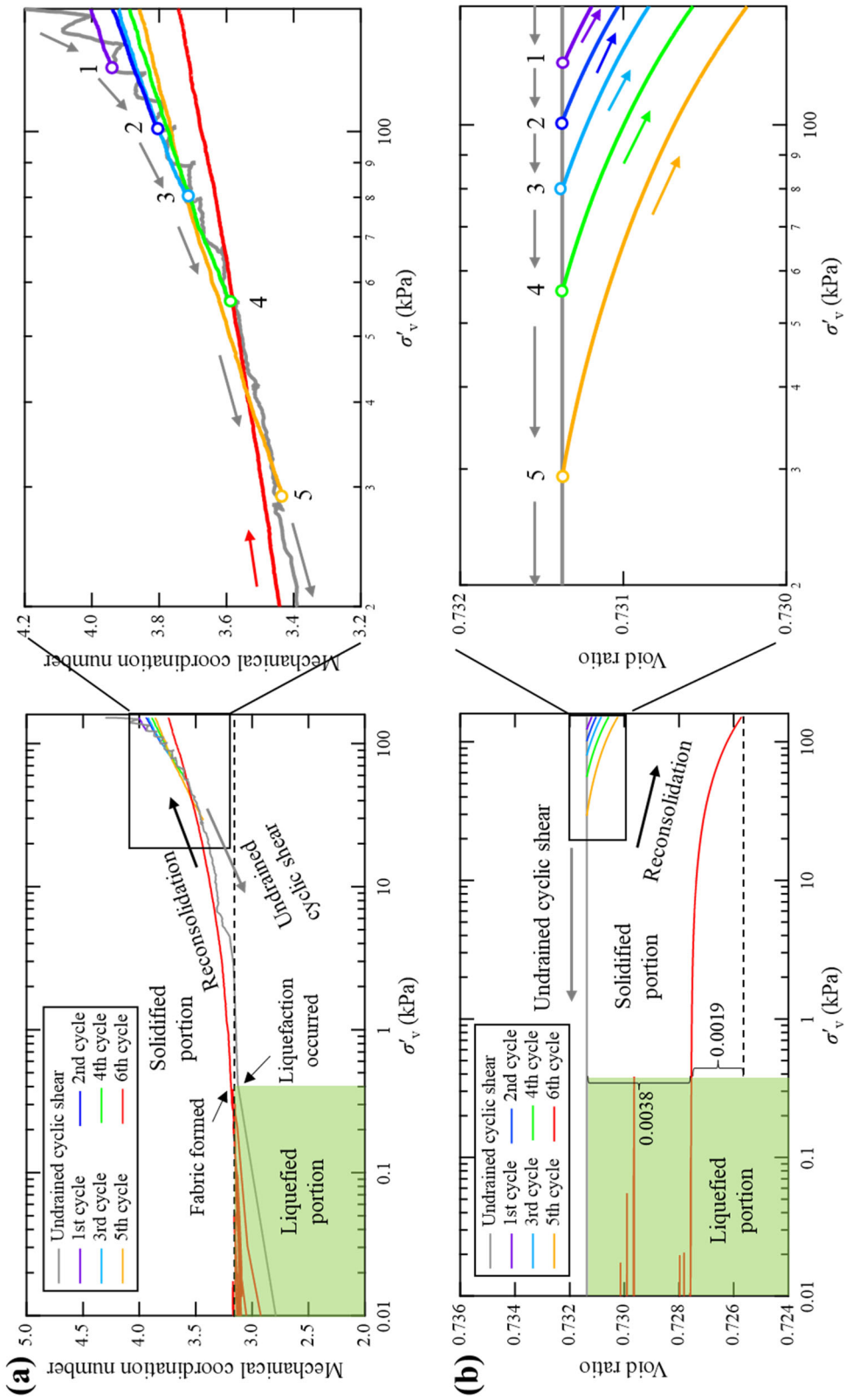

Fig. 6.6. Evolution of (a) mechanical coordination number and (b) void ratio with vertical effective stress during undrained cyclic shear and reconsolidation processes began at the end of each cycle in the specimen with Single size distribution.

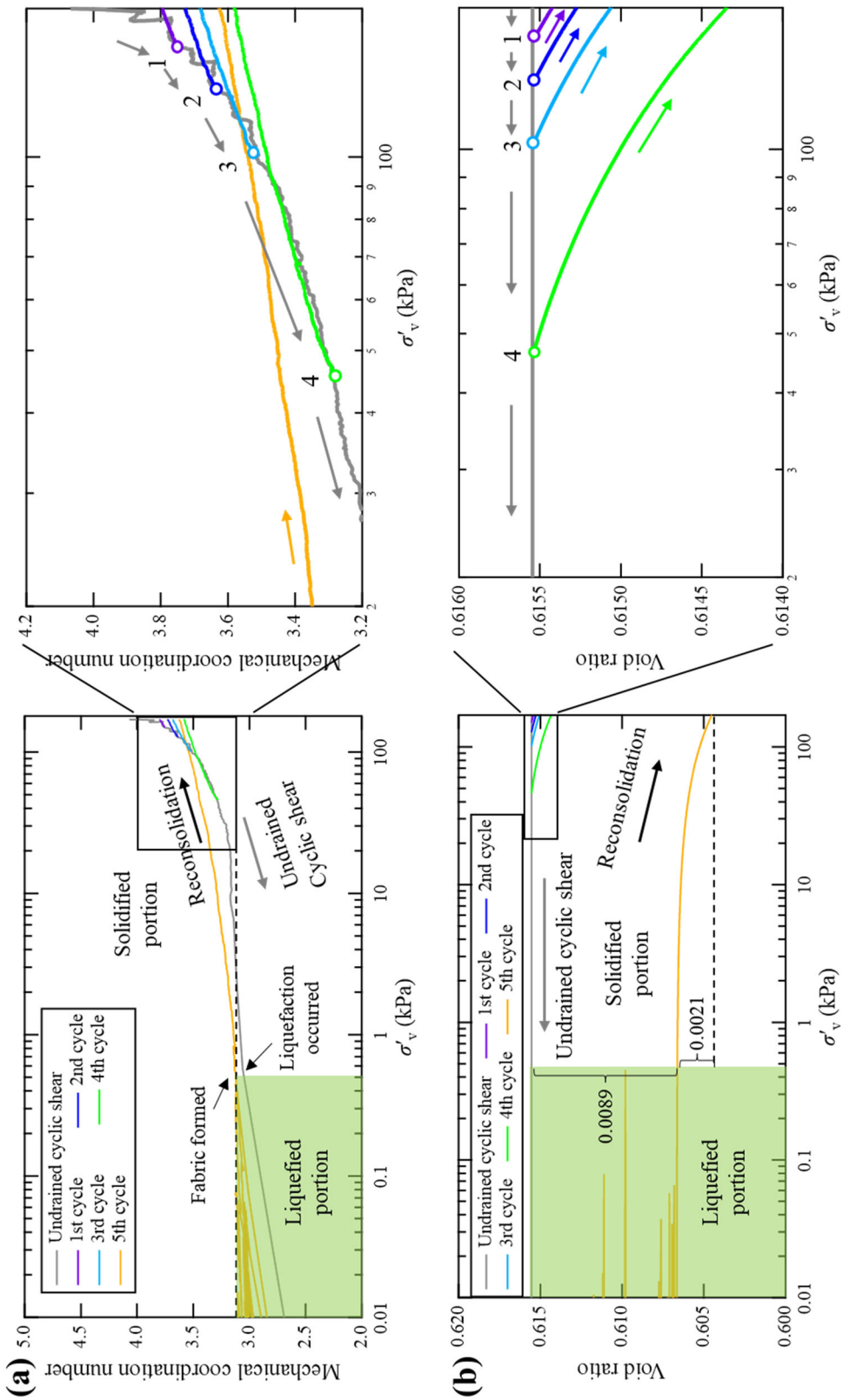

Fig. 6.7. Evolution of (a) mechanical coordination number and (b) void ratio with vertical effective stress during undrained cyclic shear and reconsolidation processes began at the end of each cycle in the specimen with Toyoura size distribution.

6.3. Simulation results

Fig. 6.6 and Fig. 6.7 show the evolution of mechanical coordination number and void ratio during undrained cyclic shear and reconsolidation processes in the monodisperse specimen and polydisperse specimen, respectively. The mechanical coordination number (Thornton, 2000) was introduced in Section 4.4.2.3, which rules out the influence of particles that have no or only one contact with other particles. Before cyclic loading, the mechanical coordination number of the monodisperse specimen was 4.3; the mechanical coordination number of the polydisperse specimen was 4.1. For the monodisperse specimen, the initial liquefaction happened when the mechanical coordination number became less than a threshold value located near 3.2; Similarly, for the polydisperse specimen, the threshold mechanical coordination number was also about 3.2. In addition, during the undrained cyclic shear, there was no change in void ratio because the volume of the specimen remained constant during simulations.

During the reconsolidation process, interparticle contacts that vanished during undrained cyclic shear were restored, which manifested as an increase in the mechanical coordination number; however, the mechanical coordination number remained lower than before undrained cyclic loading. One of the reasons is that the K_0 value after

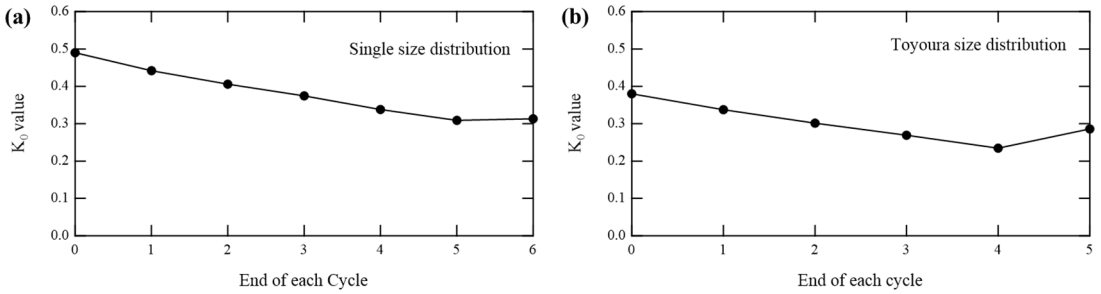

Fig. 6.8. K_0 value at the initial state and after reconsolidation that began at the end of each cycle in the specimens with (a) Single size distribution and (b) Toyoura size distribution.

reconsolidations was different. As shown in Fig. 6.8, The K_0 value after reconsolidation became lower when the reconsolidation process began at a lower residual effective stress state before initial liquefaction. Because the vertical effective stress was equal after reconsolidation, a lower K_0 value implied a smaller mean effective stress.

In the liquefied cases (The 6th cycle in the monodisperse specimen and the 5th cycle in the polydisperse specimen), when the mechanical coordination number was less than the threshold value located near 3, the vertical effective stress did not increase as the void ratio decreased. It was regarded as the liquefied portion of reconsolidation in this study, which indicates that the contact between particles was primarily in the form of impact, and a stable structure had not been formed. In the solidified portion, both the mechanical coordination number and the vertical effective stress increased as the void ratio decreased, and a stable structure was gradually formed. In addition, owing to the measurement limitations, the boundary between the liquefied and solidified portion observed in previous laboratory tests (Uzuoka et al., 2010; Zhou et al., 2014) was larger than that observed in this study (less than 1 kPa), and the phenomenon that the void ratio decreased extremely slowly when the magnitude of vertical effective stress less than 10^0 kPa in the solidified portion of reconsolidation had not been observed.

The change in void ratio during reconsolidation depended on the residual effective stress. In both specimens, the lower the residual vertical effective stress, the larger the change in void ratio during the reconsolidation process. The change of void ratio during the reconsolidation process that began at the end of each cycle before initial liquefaction and the corresponding recompression indices are listed in Table 6.1 and Table 6.2. The recompression index $C_r = (e_0 - e)/\log_{10}(\sigma'_{v0}/\sigma'_v)$, where e_0 is the void ratio at the

start of reconsolidation, e is the void ratio after reconsolidation, σ'_{v0} is the vertical effective stress after reconsolidation, and σ'_v is the vertical effective stress at the start of reconsolidation. Although the recompression index was affected by the residual effective stress (usually the larger the residual effective stress, the larger the recompression index), this affection was very small. In addition, for reconsolidations starting before initial liquefaction, the recompression indices of the monodisperse specimen are similar to that of the polydisperse specimen.

Table 6.1. Recompression indices of the monodisperse specimen

Reconsolidation after	$e_0 - e$	$\log_{10}(\sigma'_{v0}/\sigma'_v)$	C_r
1 cycle	0.00018	0.091	0.0020
2 cycles	0.00035	0.175	0.0020
3 cycles	0.00053	0.278	0.0019
4 cycles	0.00080	0.433	0.0019
5 cycles	0.00114	0.715	0.0016

Table 6.2. Recompression indices of the polydisperse specimen

Reconsolidation after	$e_0 - e$	$\log_{10}(\sigma'_{v0}/\sigma'_v)$	C_r
1 cycle	0.00012	0.055	0.0022
2 cycles	0.00027	0.125	0.0022
3 cycles	0.00048	0.225	0.0022
4 cycles	0.00120	0.560	0.0021

In the liquefied cases, the change in void ratio during the liquefied portion accounts for a large proportion of the total change in void ratio during reconsolidation. Especially, the change in void ratio during the liquefied portion was affected by the particle size distribution. In the specimen with Single size distribution, the change in void ratio was

0.0038 during the liquefied portion and 0.0019 during the solidified portion of the reconsolidation process began at the end of the 6th cycle; In the specimen with Toyoura size distribution, the change in void ratio was 0.0089 during the liquefied portion and 0.0021 during the solidified portion of the reconsolidation process began at the end of the 5th cycle. The change in void ratio during the liquefied portion was larger in the specimen with Toyoura size distribution than in the specimen with Single size distribution. However, the change in void ratio during the solidified portion was similar between the Toyoura size distribution specimen and the Single size distribution specimen. It indicated that volumetric strain during the solidified portion was much less affected by the particle size distribution than that during the liquefied portion. Of course, as mentioned in Section 6.2.3, the void ratio change in the liquefied portion would be also affected by the strain

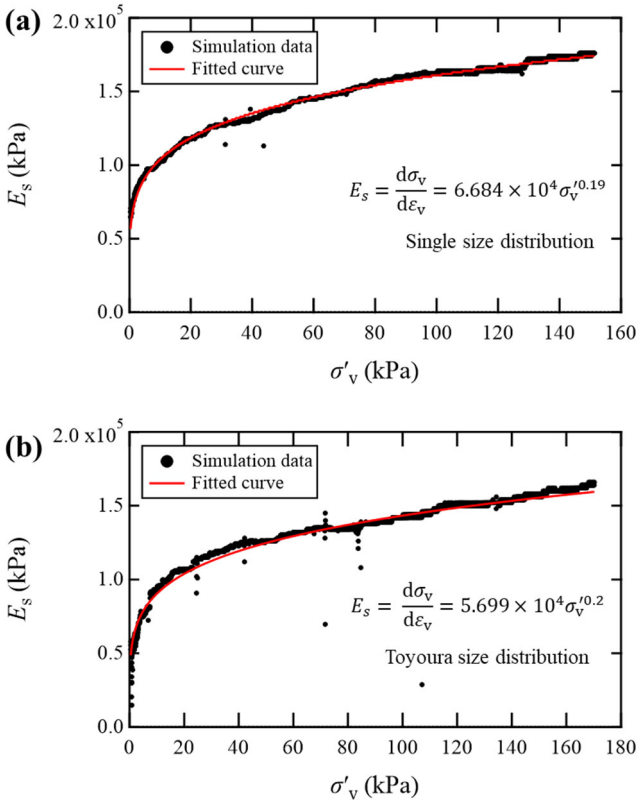

Fig. 6.9. Evolution of compression modulus during the solidified portion of reconsolidation process in the (a) monodisperse specimen and (b) polydisperse specimen.

rate of reconsolidation, which was ignored in this study.

Based on the principle of effective stress, the stiffness and strength of soil depend on the effective stress. The elastic modulus was usually expressed as proportional to the power of the effective stress (Yoshida, 2020). Fig. 6.9 shows the relationship between vertical effective stress and compression modulus E_s during the solidified portion of the reconsolidation process, where $E_s = \mathrm{d}\sigma'_{\mathrm{v}}/\mathrm{d}\varepsilon_v$, and ε_v is the volumetric strain. The compression modulus E_s was proportional to the power of 0.2 the vertical effective stress. The relationship between $\mathrm{d}\sigma'_{\mathrm{v}}$ and $\mathrm{d}\varepsilon_v$ could be expressed by:

$$\mathrm{d}\sigma'_{\mathrm{v}} = E_{sc}{\sigma'_{\mathrm{v}}}^{m}\mathrm{d}\varepsilon_v \tag{6.1}$$

where E_{sc} is a constant depending on the specimen and m is about 0.2. Integrating Eq. (6.1), the volumetric strain during the solidified portion of the reconsolidation process, ε_{vs}, could be expressed by:

$$\varepsilon_{vs} = \frac{1}{E_{sc}(1-m)}\left({\sigma'_{\mathrm{v}}}^{1-m} - {\sigma'_{\mathrm{v0}}}^{1-m}\right) \tag{6.2}$$

where σ'_{v0} is the vertical effective stress when entering the solidified portion. In this study, σ'_{v0} was about 0.42 kPa. Fig. 6.10 shows that the fitted curve closely follows the pattern of the original data points.

The proportion of particles that have no contact or only one contact with other particles was called unstable particle proportion in this study. As shown in Fig. 6.11, the unstable particle proportion in the polydisperse specimen was generally higher than that in the monodisperse specimen. Correspondingly, as shown in Fig. 6.12, the coordination number in the polydisperse specimen was generally lower than that in the monodisperse

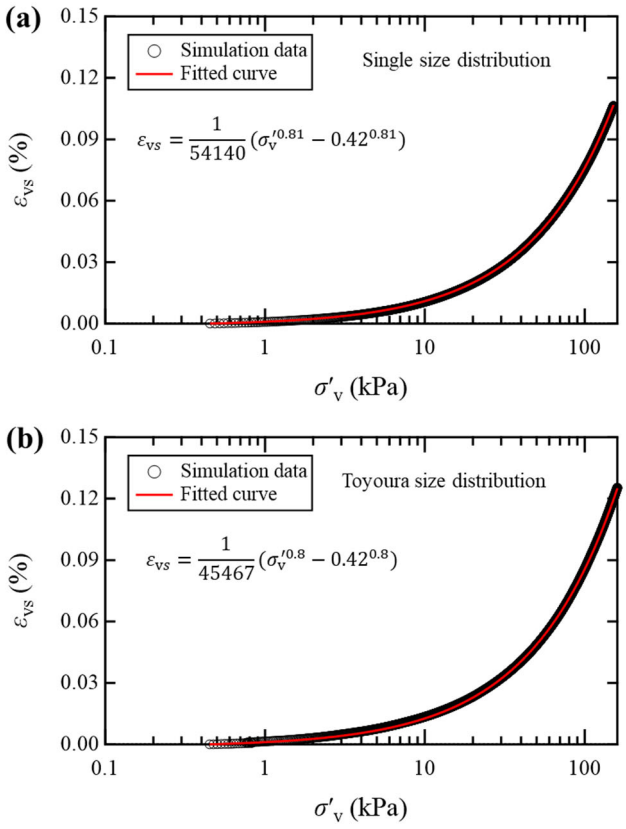

Fig. 6.10. Relationship between the vertical effective stress and volumetric strain during the solidified portion of reconsolidation process in the (a) monodisperse specimen and (b) polydisperse specimen.

specimen. In both specimens, the unstable particle proportion increased sharply when liquefaction occurs; during the reconsolidation process, the unstable particle proportion did not decrease with the decrease of void ratio in the liquefied portion; when the specimens achieved the solidified portion, the unstable particle proportion was almost the same as when it reached liquefaction. It suggested that the formation of a stable granular skeleton requires a certain proportion of mechanically stable particles, and the proportion is higher in the monodisperse specimen than in the polydisperse specimen. In the solidified portion, the unstable particle proportion decreased with the decrease of void ratio and the increase of effective stress; however, the unstable particle proportion after reconsolidation was still higher than that before undrained cyclic shear.

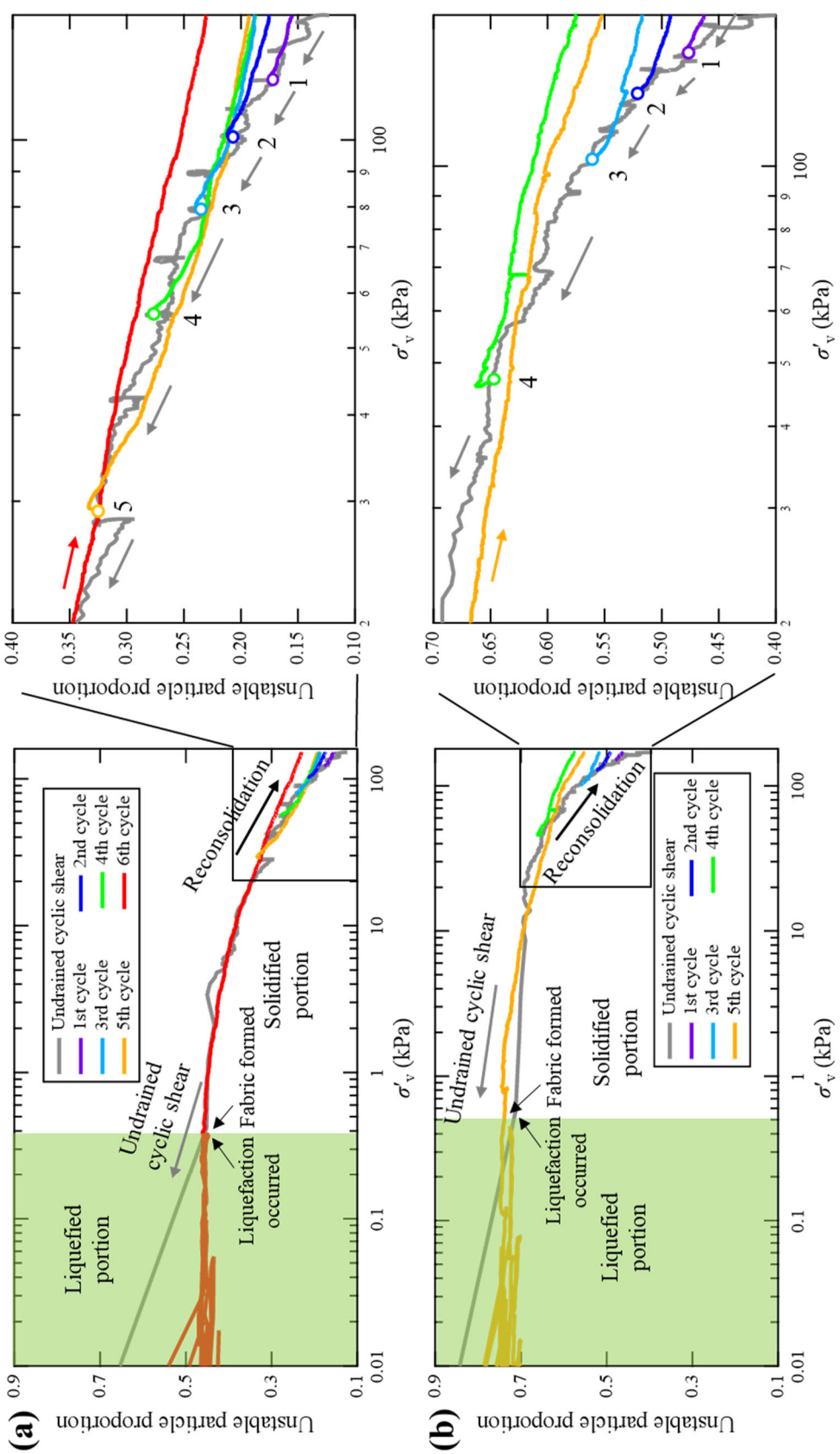

Fig. 6.11. Evolution of unstable particle proportion in the specimen with: (a) Single size distribution; (b) Toyoura size distribution.

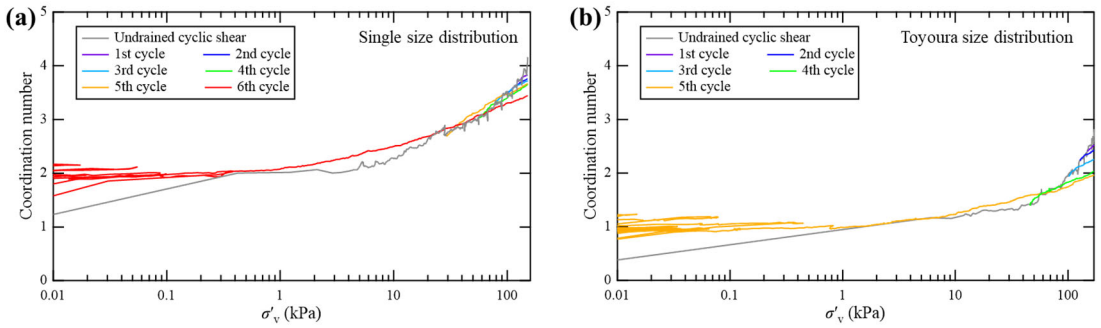

Fig. 6.12. Evolution of coordination number of the specimen with (a) Single size distribution and (b) Toyoura size distribution.

In the specimen with Toyoura size distribution, as shown in Fig. 6.13, particles with different sizes had different coordination number levels. Generally, a larger particle size implied a larger coordination number level during both undrained cyclic shear and reconsolidation processes. Especially, as shown in Fig. 6.13(a), the coordination number of the particles with sizes from 1.06 to 1.38 mm was lower than the overall coordination number of the specimen as shown in Fig. 6.12(b). Considering that about half of the particles were in this size range, the results indicated that the suspended particles are mainly of small sizes. These small, suspended particles move more flexibly and they are more difficult to participate in the construction of the force transmission network compared with larger size particles. This phenomenon should be the reason why the volume strain of the Toyoura size distribution specimen in the liquefied portion is greater than that of the Single size distribution specimen.

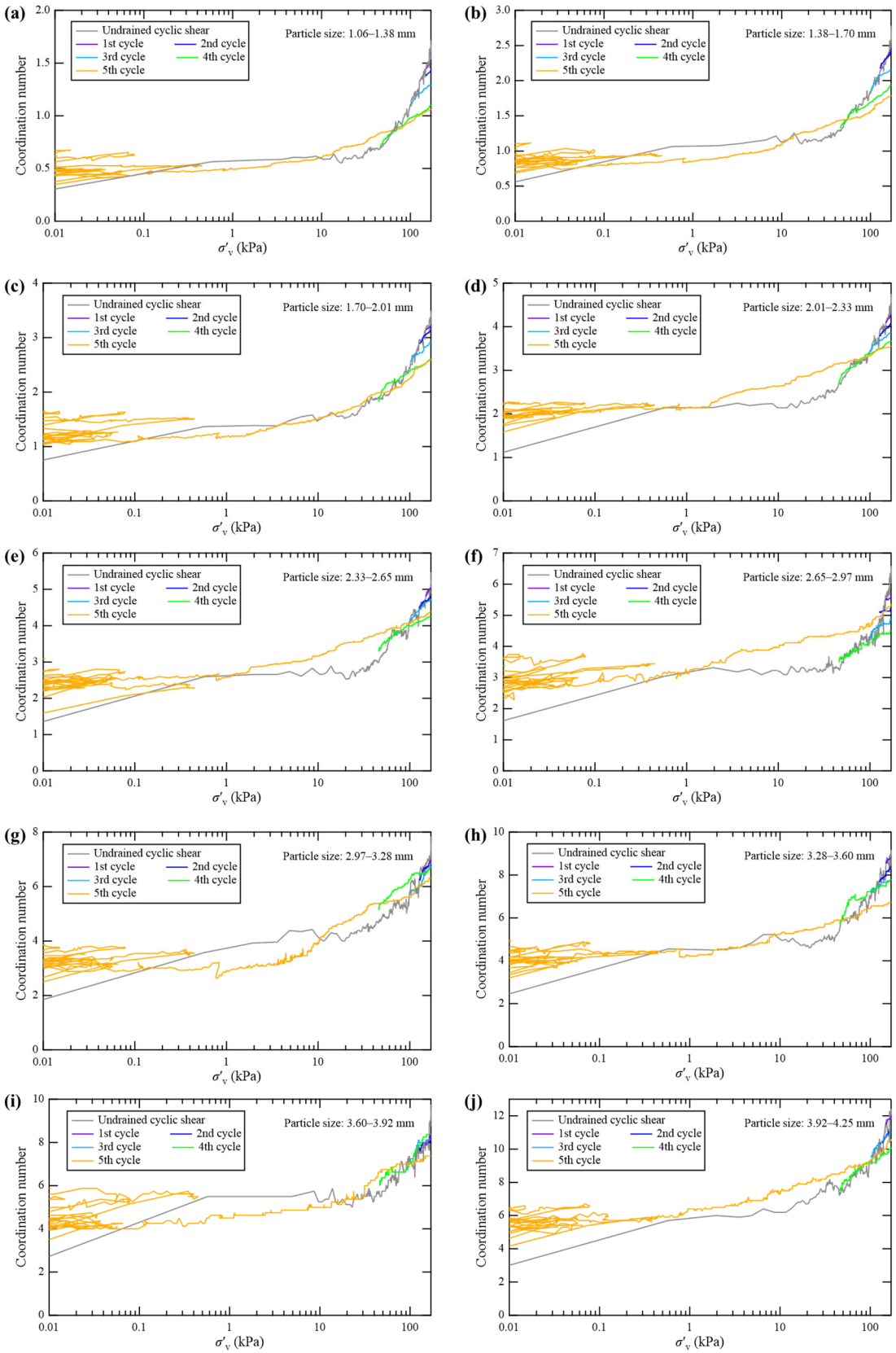

Fig. 6.13. Evolution of coordination number of particles with different sizes in the specimen with Toyoura size distribution.

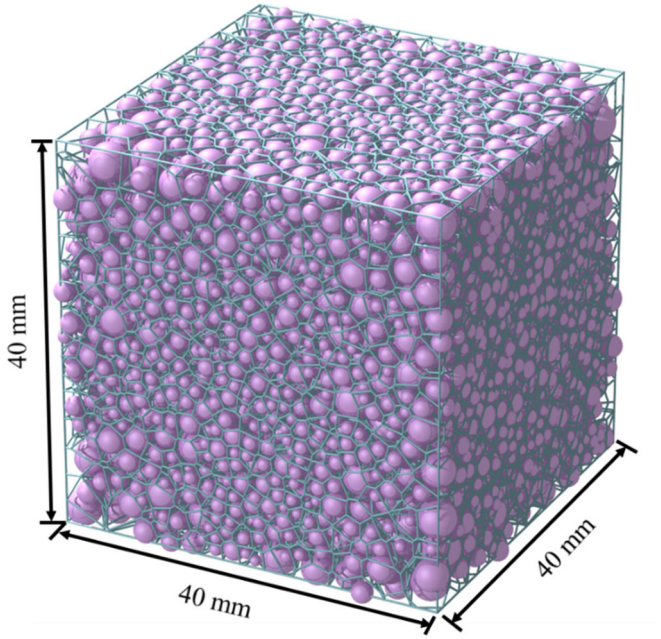

Fig. 6.14. Voronoi radical tessellation on the specimen with Toyoura size distribution.

Wei et al. (2019) indicated that the degree of pore uniformity was closely associated with the volume contraction characteristics of sands. The centroid distance, D_c as mentioned in Chapter 5, was used to evaluate the degree of pore uniformity. A low value of D_c generally indicates that the void spaces are distributed homogeneously, and no relatively large local pores existed in the specimen (Wang and Wei, 2016). The open-source software library, Voro++ (Rycroft 2009) was used to obtain the "particle-void cell" in the same way as in Chapter 5. Especially, Voronoi radical tessellation was used to handle the polydisperse specimen, as shown in Fig. 6.14.

The results of centroid distance are shown in Fig. 6.15. On the whole, the centroid distance decreased as the cycle increased. It indicated that in both the monodisperse specimen and polydisperse specimen, the granular assembly became more homogeneous during undrained cyclic shear. In the monodisperse specimen, during the reconsolidation process, the centroid distance increased. Particularly, the lower the residual effective

stress when the reconsolidation began (large cycle number), the larger the increase in the centroid distance during the reconsolidation process. In the liquefied case, the centroid distance at the vertical effective stress of 1.0×10^{-3} kPa closest to the solidified portion was recorded. The result suggested that most of the increase in inhomogeneity occurred during the liquefied portion, which was consistent with the change in void ratio. In the polydisperse specimen, the granular assembly would become either homogeneous or inhomogeneous. Especially in the liquefied case, most of the increase in homogeneity occurs during the liquefied portion, which is consistent with the change in void ratio. The different evolutions of centroid distance during reconsolidation in the monodisperse

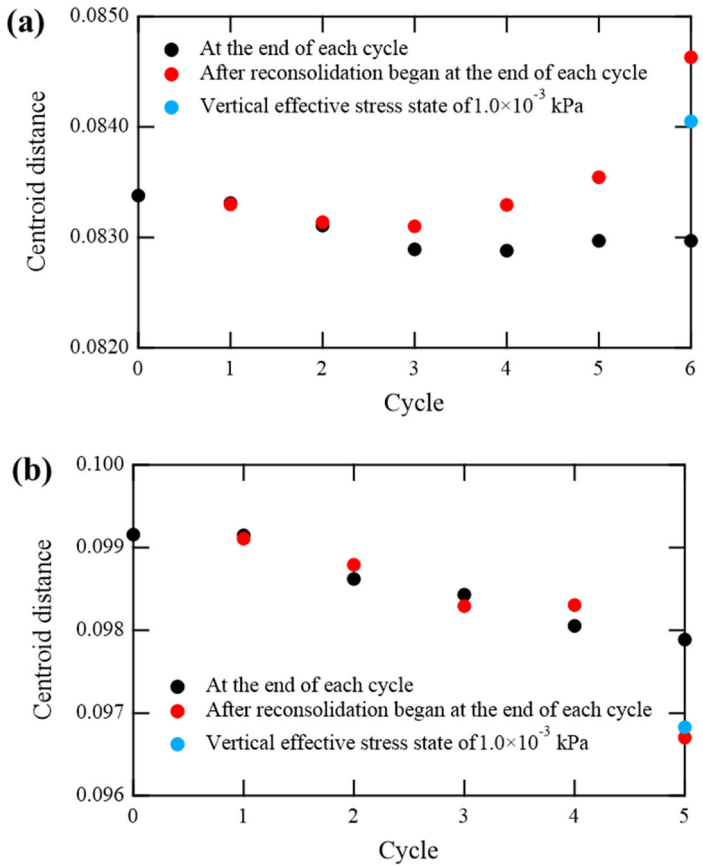

Fig. 6.15. Evolution of centroid distance during undrained cyclic shear and after reconsolidations in the specimen with: (a) Single size distribution and (b) Toyoura size distribution.

specimen and polydisperse specimen probably due to different proportions of unstable particle. As the unstable particle proportion of the polydisperse specimen was much higher than that of the monodisperse specimen. the random motion of the mechanically unstable particles during reconsolidation would affect the uniformity of the specimen. Therefore, the centroid distance might increase or decrease during cyclic shear. In addition, the initial inhomogeneity of the polydisperse specimen was larger than that of the monodisperse specimen, this may be one of the reasons that the monodisperse specimen became inhomogeneous and the polydisperse specimen became homogeneous during the reconsolidation after initial liquefaction.

6.4. Summary

To avoid the measuring limitation of laboratory tests, a series of 3D DEM simulations was performed to investigate the reconsolidation characteristics of K_0-consolidated granular materials. Both monodisperse and polydisperse specimens were used in this study. The drainage rate effect was disregarded by applying volumetric strain at a constant and low rate without gravity. The main conclusions are as follows:

1. The post-liquefaction reconsolidation process can be categorized into a liquefied and a solidified portion. In the liquefied portion, the void ratio decreased without an increase in the effective stress. In the solidified portion, the void ratio decreased as the effective stress increased; however, the void ratio decreased extremely slowly at a stress level of less than 10^0 kPa.

2. The residual effective stress significantly affected the volumetric strain during reconsolidation after an undrained cyclic shear. The smaller the residual vertical effective stress, the larger the change in void ratio during the reconsolidation process. Especially, the volumetric strain during the liquefied portion accounts for a large proportion of the total volumetric strain during the reconsolidation process. The particle size distribution has a great influence on the volumetric strain during the liquefied portion of the reconsolidated process, whereas has little effect on the volumetric strain during the solidified portion of the reconsolidation process. During the liquefied portion of the reconsolidation process, the volumetric strain of the polydisperse specimen is greater than that of the monodisperse specimen.

3. The mechanical coordination number decreased gradually during undrained cyclic shear and increased during the reconsolidation process. However, the mechanical coordination number after the reconsolidation was lower than that in the initial state. In particular, the specimen with Toyoura size distribution generally has a higher unstable particle proportion than the specimen with Single size distribution. Moreover, the evolution of unstable particle proportion is opposite to that of the mechanical coordination number.

4. The pore uniformity increased during undrained cyclic shear in both monodisperse and polydisperse specimens. During the reconsolidation process, the pore uniformity in the monodisperse increased, whereas the polydisperse granular assembly may be either homogenous or inhomogeneous. In addition, despite the sign, a larger change in centroid distance is generally associated with a larger volumetric strain during the reconsolidation process.

CHAPTER 7 CONCLUSION

7.1. Summary

Earthquakes are one of the natural disasters that pose severe threats to human society. One of the ways earthquakes cause damage is the undrained shearing of soil under the propagation of seismic waves.

In traditional laboratory element tests, it is hard to reproduce some of the complex stress–strain conditions that occur during real earthquakes, and the microscopic behavior and corresponding parameters of a granular assembly during cyclic loadings are difficult to observe and measure. In addition, the continuum modeling scheme is unable to capture the discrete nature of granular materials. Therefore, 3D DEM was used in this research, which helps to reveal the intrinsic essence mechanism behind the failure phenomenon of granular materials.

This research aimed to conduct a qualitative study on the failure and reconsolidation behavior of granular material due to undrained shear, and analysis was performed from both macroscopic and microscopic scales to reveal the mechanism behind the response of granular materials.

In Chapter 4, the responses of granular assemblies under surface-wave strain conditions and SH-wave strain conditions were studied. The equations governing the strain–time relationships of SHH, SHV, Love, and Rayleigh waves were derived from the elastic wave theory. And the undrained deformation mode of a soil element under the propagation of SHH, SHV, Love, and Rayleigh waves are called SHH-, SHV-, Love-, and

Rayleigh-wave strain conditions in this study. Nine different loading paths were applied to the K_0-consolidated specimens to cover the strain characteristics under different strain conditions. The accumulated equivalent strain was used to ensure the strain level at different loading conditions are identical. The volume of granular assembly remained constant during cyclic loadings to model the undrained condition, and cyclic loadings were applied until the initial liquefaction occurred.

In Chapter 5, both undrained monotonic simple shear and the undrained cyclic simple shear tests were conducted on a K_0-consolidated granular assembly using 3D DEM. A relatively slow strain rate was used to ensure the quasi-static responses of the granular assembly. During the undrained monotonic simple shear, the shear strain was applied until 100%. During the undrained cyclic shear, cyclic loadings with a shear strain amplitude of 0.1%, 0.5%, 1%, 5%, 10%, 50%, and 100% were applied to the granular assembly. Periodical boundaries were used in this study to eliminate the boundary effects that originate from large shear strain conditions.

In Chapter 6, the volumetric strain during the reconsolidation process that began at different residual effective stress states and with no residual shear strain was studied. A K_0-consolidated monodisperse specimen and a K_0-consolidated polydisperse specimen were used in this study. Both the undrained cyclic shear and reconsolidation were conducted under zero-gravity conditions. The strain rate during reconsolidation was controlled at a low value to reduce the effect of the reconsolidation rate on the volumetric strain.

7.2. Conclusions

7.2.1. Study on the response of granular material under surface-wave strain conditions

The liquefaction behavior of granular material under the propagation of surface waves had not been clarified due to their complex deformation mode. In this study, the macroscopic and microscopic response of K_0-consolidated granular assemblies under Love- and Rayleigh-wave strain conditions was compared with that under SH-wave strain conditions by performing a series of 3D DEM numerical tests. Nine loading paths, which correspond to the SHH-wave strain condition, SHV-wave strain condition, Love-wave strain conditions with AR = 0.25, 1, and 4, and Rayleigh-wave strain conditions with RSN = 0, 0.25, 1, and 4, respectively, were applied to the granular assemblies. The cyclic loadings were applied until initial liquefaction. The following main conclusions were achieved from the 3D DEM study:

1. The undrained response of a granular assembly is significantly affected by the loading paths. The fluctuation of ESRR and the magnitude of von Mises stress under Rayleigh-wave strain conditions is larger than that under SH- and Love-wave strain conditions. In addition, the resultant shear strain under Love-wave strain conditions has a significant influence on the fluctuation of ESRR and the magnitude of von Mises stress.

2. Generally, at the same strain level, the Rayleigh-wave strain condition with a low RSN value would make granular materials more vulnerable to liquefaction than Love-wave strain conditions, and granular materials under Love-wave strain conditions are more likely to liquefy than under SH-wave strain conditions.

3. K_0-consolidation resulted in a structure whose elongation direction is vertical. As a result, the positive dilatancy behavior in the pure shear mode was more sensitive to the strain level than that in the simple shear mode.

4. The fabric anisotropy increases during cyclic loadings, which is especially significant under Rayleigh-wave strain conditions than under other strain conditions. As the granular structure degraded, the loading path has a larger influence on the evolution of structural anisotropy and rotation of structure elongation direction. The angle between ε_1 and Φ_1 and between σ_1 and Φ_1 tended to be a value near zero

5. The increase in structural anisotropy and the degradation of the skeleton structure accelerated the liquefaction of granular materials. The magnitude of the fraction of sliding contacts and fluctuation of coordination number under Rayleigh-wave strain conditions is larger than that under SH- and Love-wave strain conditions. The evolution of the fraction of sliding contacts and fluctuation of coordination number under SH- and Love-wave strain conditions relies on the change in resultant shear strain during cyclic loading.

6. Regardless of the loading path, the initial liquefaction happened instantaneously when the coordination number approached approximately 2; It is noteworthy that the "zero mean effective states" was not reached in the initial liquefaction state.

7.2.2. Study on the undrained behavior of granular materials with different shear strain amplitude

Due to the limitation of laboratory apparatus, the behavior of liquefiable granular

material under undrained cyclic shear with very large shear strain amplitudes is still unknown. To clarify the shear strain amplitude on the undrained behavior of granular materials without the influence of boundary effects, a series of 3D DEM simulations under undrained monotonic and cyclic simple shears was performed until 100% shear strain amplitudes using periodic boundaries in lateral directions. The main results of this study can be summarized as follows:

1. During both undrained monotonic simple shear and undrained cyclic simple shear, the shear band was formed when the shear strain exceeds a certain value. After the shear band was formed, the granular structure outside the shear band become stable, and the granular assembly reached a stable state of stress.

2. Under the cyclic shear with a small strain amplitude (≤ 1%), the medium-dense granular assembly will gradually lose its shear stiffness and liquefy eventually. When the shear strain amplitude becomes larger (≤ 10%), the shear stiffness will recover after the initial liquefaction as the shear strain application is continued. However, the shear stiffness recovery will vanish as the undrained cyclic shear continued. When the shear strain amplitude exceeds a certain value (about 50%), the fluid-like state after initial liquefaction will only exist in a small shear strain range (about 20%) after the strain loading direction reversion. The shear stiffness will recover as the shear strain application is continued, and the granular assembly reaches a stable state of stress as the shear band was formed during cyclic loadings.

3. The fabric anisotropy increases during the loading process and decreases during the unloading process. When the shear strain exceeds a certain value, the fabric anisotropy tends to be constant, and the major principal fabric direction tends to be close to the

direction of shear strain application and the direction of major principal stress. When the stable state of stress arrived, the skeleton of the part of the granular assembly outside the shear band became stable, as FS outside the shear band tended to be zero and the coordination number outside the shear band became constant. The coordination number will decrease dramatically from a value larger than 2 to a value near zero when the initial liquefaction occurs. In the flow-like state after initial liquefaction, the coordination number was below 2; however, after shear stiffness recovered, the coordination number will become larger than 2.

4. The granular assembly became inhomogeneous during undrained monotonic shear when the effective stress increased. During undrained cyclic shear, the granular assembly becomes homogeneous as the effective stress decrease. The stable states of stress during undrained monotonic shear and undrained cyclic shear with large strain amplitudes are different. This is because the overall uniformities of the granular assembly in the two stable states are different. Therefore, the void ratios in the narrow shear bands are not identical.

7.2.3. Study on the reconsolidation after undrained cyclic shear

In laboratory tests, the effective stress near zero is hard to be measured exactly, and the behavior of granular materials during reconsolidation is difficult to observe from the particle scale. To overcome these limitations, a series of 3D DEM simulations was performed. The reconsolidation characteristics of K_0-consolidated monodisperse and polydisperse granular materials were investigated in this study. The drainage rate effect

was disregarded by applying volumetric strain at a constant and low rate without gravity. The main conclusions are as follows:

1. The post-liquefaction reconsolidation process can be categorized into a liquefied and a solidified portion. In the liquefied portion, the void ratio decreased without an increase in the effective stress. In the solidified portion, the void ratio initially decreased extremely slowly at a stress level less than 10^0 kPa, then the void ratio decrement become quicker and eventually stable as the effective stress increased.

2. The residual effective stress significantly affected the volumetric strain during reconsolidation after an undrained cyclic shear. The smaller the residual vertical effective stress, the larger the change in void ratio during the reconsolidation process. Especially, the volumetric strain during the liquefied portion accounts for a large proportion of the total volumetric strain during the reconsolidation process. During the liquefied portion of the reconsolidation process, the volumetric strain of the polydispersed specimen is greater than that of the monodisperse specimen. However, the particle size distribution has little effect on the volumetric strain during the solidified portion of the reconsolidation process.

3. The monodisperse specimen had a greater coordination number than the polydisperse specimen (with Toyoura size distribution). The coordination number decreased gradually during undrained cyclic shear and increased during the reconsolidation process. In particular, the polydisperse specimen generally has a higher unstable particle proportion than the monodisperse specimen. Moreover, the evolution of unstable particle proportion is opposite to that of the mechanical coordination number.

.

4. The pore uniformity increased during undrained cyclic shear in both monodisperse and polydisperse specimens. During the reconsolidation process, the pore uniformity in the monodisperse increased, whereas the polydisperse granular assembly may be either homogenous or inhomogeneous. In addition, despite the sign, a larger change in centroid distance is generally associated with a larger volumetric strain during the reconsolidation process.

7.3. Suggestions for future works

The studies in this thesis are qualitative. Some conditions were not considered or cannot be fulfilled by the commercial code used in this research. Therefore, the following recommendations are suggested for future study:

1. All the numerical specimens used in this were K_0-consolidated, and the K_0 value cannot be controlled. To evaluate the initial anisotropy on the simulation results, future studies on the specimen with different K_0 values are recommended.

2. The rolling resistance model cannot completely replace the role of particle shape. As the particle shape plays an important role in the dilatancy behavior, it is recommended to consider the effect of particle shape on the basis of this paper, e.g., compared with SH-wave strain conditions, the relative liquefaction resistance of granular materials with different particle shapes may be different under surface-wave strain conditions.

3. In the study about reconsolidation, the reconsolidation was assumed to happen on level ground, and the reconsolidation began at the end of each cycle. As a result, the

effect of initial static shear, which corresponds to sloping ground, was not considered. In addition, the shear stresses at the end of each cycle are not necessarily 0, which deviated from the assumption of level ground. The stress-controlled test is recommended for future study.

REFERENCES

Ai, J., Chen, J. F., Rotter, J. M., and Ooi, J. Y., 2011. Assessment of rolling resistance models in discrete element simulations. *Powder Technology*, 206(3), 269–282.

Al-Hashemi, H. M. B., and Al-Amoudi, O. S. B., 2018. A review on the angle of repose of granular materials. *Powder Technology*, 330, 397–417.

Arthur, J. R. F. and Menzies, B. K., 1972. Inherent anisotropy in a sand. *Géotechnique*, 22, 115–128.

Asadzadeh, M., and Soroush, A., 2017. Macro-and micromechanical evaluation of cyclic simple shear test by discrete element method. *Particuology*, 31, 129–139.

Athanasiou-Grivas, D., and Harr, M. E., 1980. Particle contacts in discrete materials. *Journal of the Geotechnical Engineering Division*, 106(5), 559–564.

Bagi, K., 1996. Stress and strain in granular assemblies. *Mechanics of materials*, 22(3), 165–177.

Banerjee, A., Puppala, A. J., and Hoyos, L. R., 2022. Liquefaction Assessment in Unsaturated Soils. *Journal of Geotechnical and Geoenvironmental Engineering*, 148(9), 04022067.

Bardet, J. P., 1994. Observations on the effects of particle rotations on the failure of idealized granular materials. *Mechanics of materials*, 18(2), 159–182.

Barreto, D., O'Sullivan, C., and Zdravkovic, L., 2009. Quantifying the evolution of soil fabric under different stress paths. In: *AIP Conference Proceedings*, 1145(1), 181–184.

Bokkisa, S. V., 2019. Fabric evolution in 3D discrete element modelling of soil liquefaction (Doctoral dissertation).

Bolt, B. A., 1993. *Earthquakes: Newly Revised and Expanded*. New York: W. H.Freeman and Company.

Boulanger, R. W., Seed, R. B., Chan, C. K., Seed, H. B. and Sousa, J., 1991. Liquefaction behavior of saturated sands under uni-directional and bi-directional monotonic and cyclic simple shear loading. *Geotechnical Engineering Report No. UCB/GT/91-08*, University of California, Berkeley.

Byrne P.M., 1991. A cyclic shear-volume coupling and pore pressure model for sand. Proceedings, *2nd International Conference on Recent Advances in Geotechnical Earthquake Engineering and Soil Dynamic*s, St. Louis, Vol. 1, pp. 47–55.

Cambou, B., Jean, M., and Radjaï, F., 2009. *Micromechanics of granular materials*. John Wiley & Sons.

Cambou, B., Magoariec, H., and Nguyen, N. S., 2016. *Granular Materials at Meso-scale: Towards a Change of Scale Approach*. Elsevier.

Casagrande, A., 1936. Characteristics of cohesionless soils affecting the stability of slopes and earth fills. *J. Boston Society of Civil Engineers*, 23(1), 13–32.

Castro, G., 1975. Liquefaction and cyclic mobility of saturated sands. *J. Geotech. Eng. Div*. ASCE. 101(GT6), 551–569.

Chang, C. S., and Gao, J., 1996. Kinematic and static hypotheses for constitutive modelling of granulates considering particle rotation. *Acta Mechanica*, 115(1), 213–229.

Chang, C. S., and Misra, A., 1990. Packing structure and mechanical properties of granulates. *Journal of engineering mechanics*, 116(5), 1077–1093.

Chang, C., Misra, A., and Sundararam, S., 1990. Micromechanical modelling of cemented sands under low amplitude oscillations, *Géotechnique*, 40(2), 251–263.

Chiaro, G., Kiyota, T. and Koseki, J., 2013. Strain localization characteristics of loose saturated Toyoura sand in undrained cyclic torsional shear tests with initial static shear. *Soils Found*., 53 (1), 23–34.

Christoffersen, J., Mehrabadi, M. M., and Nemat-Nasser, S., 1981. A micromechanical description of granular material behavior. *Journal of Applied Mechanics*. 48(2), 339–344

Coetzee, C. J., 2017. Calibration of the discrete element method. *Powder Technology*, 310, 104–142.

Cresswell, A. and Powrie, W., 2004. Triaxial tests on an unbonded locked sand. *Géotechnique*, 54, 107–115.

Cui, J., Men, F., and Wang, X., 2004. Soil liquefaction induced by Rayleigh wave. *13th World Conference on Earthquake Engineering*.

Cui, L. and O'Sullivan, C., 2006. Exploring the macro- and microscale response characteristics of an idealized granular material in the direct shear apparatus, *Geotechnique*, 56, 455–468.

Cundall, P. A. and Strack, O. D., 1979. A discrete numerical model for granular assemblies. *Géotechnique.* 29 (1), 47–65.

Cundall, P., 1988. Computer simulations of dense sphere assemblies. *Studies in Applied Mechanics*. Elsevier.

da Cruz, F., Emam, S., Prochnow, M., Roux, J. N. and Chevoir, F., 2005. Rheophysics of dense granular materials: Discrete simulation of plane shear flows. *Phys. Rev. E*. 72, 254–271.

Daniels, K. E., 2017. The role of force networks in granular materials. In *EPJ Web of Conferences*. 140, 01006. EDP Sciences.

Das, M. B., 1983. *Advanced Soil Mechanics*, Hemisphere Publishing Corp., McGraw-Hill, London

Davis R. O. and Berrill J. B., 1982. Energy dissipation and seismic liquefaction of sands. *Earthquake Engineering & Structural Dynamics*. 10:59–68.

de Saxcé, G., Fortin, J., and Millet, O., 2004. About the numerical simulation of the dynamics of granular media and the definition of the mean stress tensor. *Mechanics of Materials*, 36(12), 1175–184.

Definition of terms related to liquefaction., 1978. Com. on Soil Dynamics, Geotech. Engrg. Div. J. *Geotech Engrg. Div*., ASCE, Vol. 104, No. GT9, September, pp. 1197–1200.

Derakhshani, S. M., Schott, D. L., and Lodewijks, G., 2015. Micro-macro properties of quartz sand: experimental investigation and DEM simulation. *Powder Technology*. 269, 127–138.

Di Renzo, A., and Di Maio, F. P., 2004. Comparison of contact-force models for the simulation of collisions in DEM-based granular flow codes. *Chemical engineering science*, 59(3), 525–541.

Dobry R., Ladd R., Yokel F., Chung R., and Powell D., 1982. Prediction of pore water pressure buildup and liquefaction of sands during earthquakes by the cyclic strain method. NBS Building Science Series 138, National Bureau of Standards, Washington, DC.

Dyvik, R., Berre, T., Lacasse, S., and Raadim, B., 1987. Comparison of truly undrained and constant volume direct simple shear tests. *Géotechnique.* 37, 3–10.

El Shamy, U., and Zeghal, M., 2006. Response of liquefiable granular deposits to multi-direction shaking. In *GeoCongress 2006: Geotechnical Engineering in the Information Technology Age*. 1–5.

Elgamal, A., Yang, Z., and Parra, E., 2002. Computational modeling of cyclic mobility and post-liquefaction site response. *Soil Dynamics and Earthquake Engineering*, 22(4), 259–271.

ESSS, 2020. ROCKY: user's manual, version 4.4.

Fei, J., Jie, Y., Sun, X., and Xiong, H., 2020. Physical interpretation of shear-rate behaviour of soils and geotechnical solution to the coefficient of start-up friction with low inertial number. *Scientific Reports*, 10(1), 1–9.

Field, W. G., 1963. Towards the statistical definition of a granular mass. *Proc. 4th A. and NZ cont. on Soil Mech*., 143–148.

Figueroa J. L., Saada A. S., Liang L., and Dahisaria N. M., 1994. Evaluation of soil liquefaction by energy principles. *Journal of Geotechnical and Geoenvironmental Engineering*, ASCE. 120(9),1554–69.

Florin V. A., and Ivanov P. L., 1961. Liquefaction of saturated sandy soils. In: *Proceedings of the 5th International Conference on Soil Mechanics and Foundation Engineering*, 107–111. Paris.

Fonseca, J., O'Sullivan, C., Coop, M. R. and Lee, P. D., 2012. Non-invasive characterization of particle morphology of natural sands. *Soils and Foundations*, 52, 712–722.

Fortin, J., Millet, O., and de Saxcé, G., 2002. Mean stress in a granular medium in dynamics. *Mechanics Research Communications*, 29(4), 235–240.

Fortin, J., Millet, O., and de Saxcé, G., 2003. Construction of an averaged stress tensor for a granular medium. *European Journal of Mechanics-A/Solids*, 22(4), 567–582.

Fu, P., and Dafalias, Y. F. (2011). Fabric evolution within shear bands of granular materials and its relation to critical state theory. *International Journal for numerical and*

analytical methods in geomechanics, 35(18), 1918–1948.

Gazetas, G. C., and Yegian, M. K., 1979. Shear and Rayleigh waves in soil dynamics. *Journal of the Geotechnical Engineering Division*, 105(12), 1455–1470.

Green, R. A., Mitchell, J. K., and Polito, C. P., 2000. An energy-based pore pressure generation model for cohesionless soils. In Proceedings of the John Booker Memorial Symposium–Developments in Theoretical Geomechanics, 16–17 November 2000. Balkema, Rotterdam, the Netherlands. pp. 383–390.

Gu, X., Zhang, J., and Huang, X., 2020. DEM analysis of monotonic and cyclic behaviors of sand based on critical state soil mechanics framework. *Computers and Geotechnics*, 128, 103787.

Guo, N., and Zhao, J., 2013. The signature of shear-induced anisotropy in granular media. *Computers and Geotechnics*, 47, 1–15.

Hall, J. R., Shukla, D. K., and Kissenpfennig, J. F., 1977. *Shear Stress Distribution due to Shear and Raleigh Wave Propagation at Deep Soil Sites.*

Hanley, K. J., Huang, X., O'Sullivan, C., and Kwok, F., 2013. Challenges of simulating undrained tests using the constant volume method in DEM. In *AIP conference proceedings* (Vol. 1542, No. 1, pp. 277–280). American Institute of Physics.

Heshmati, A. A., Shahnazari, H., and Sarbaz, H., 2015. The cyclic threshold shear strains in very dense clean sand, *European Journal of Environmental and Civil Engineering*, 19(7), 884-899.

Holzer, T. L., and Youd, T. L., 2007. Liquefaction, ground oscillation, and soil deformation at the Wildlife Array, California. *Bulletin of the Seismological society of America*. 97(3), 961–976.

Huang, X., Hanley, K. J., O'Sullivan, C., and Kwok, F.C., 2014. Effect of sample

size on the response of DEM samples with a realistic grading. *Particuology*, 15(1), 107–115.

Huang, X., Hanley, K. J., Zhang, Z., and Kwok, C. Y., 2019. Structural degradation of sands during cyclic liquefaction: Insight from DEM simulations. *Computers and Geotechnics*, 114, 103139.

Ishihara, K., 1993. Liquefaction and flow failure during earthquakes. *Géotechnique*, 43(3), 351–451.

Ishihara, K., 1996. *Soil behaviour in earthquake geotechnics*. Clarendon Press Oxford.

Ishihara, K., and Yamazaki, F., 1980. Cyclic simple shear tests on saturated sand in multidirectional loading. *Soils and Foundations*, 20(1), 45–59.

Ishihara, K., and Yamazaki, F., 1980. Cyclic simple shear tests on saturated sand in multi-directional loading. *Soils and Foundations*. 20(1). 45–59.

Ishihara, K., and Yoshimine, M., 1992. Evaluation of settlements in sand deposits following liquefaction during earthquakes. Soils and foundations 32(1), 173–188.

Iwashita, K., and Oda, M., 1998. Rolling resistance at contacts in simulation of shear band development by DEM. *Journal of engineering mechanics*, 124(3), 285–292.

Iwashita, K., and Oda, M., 2020. Numerical simulation of granular materials subjected to cyclic loading under constant volume by modified distinct element method. In: *Powders and Grains 2001*, pp. 251–254.

Jalil, A., Fathani, T. F., Satyarno, I., and Wilopo, W., 2021. Liquefaction in Palu: the cause of massive mudflows. *Geoenvironmental Disasters*, 8(1), 1–14.

Japanese Geotechnical society, Ground Survey Standards and Criteria Committee,

2013. *Ground investigation method and commentary*. Japanese Geotechnical society.

Jefferies, M., and Been, K., 2006. *Soil Liquefaction: A Critical State Approach*. Taylor & Francis.

Jiang, M., Kamura, A., and Kazama, M., 2020. Undrained cyclic simple shear simulation of liquefiable granular particles subjected to large shear strains up to 100% by 3D DEM. *Japanese Geotechnical Society Special Publication*, 8(3), 53–58.

Jiang, M., Kamura, A., and Kazama, M., 2021. Comparison of liquefaction behavior of granular material under SH-and Love-wave strain conditions by 3D DEM. *Soils and Foundations*, 61(5), 1235–1250.

Jiang, M., Zhang, A., and Li, T., 2019. Distinct element analysis of the microstructure evolution in granular soils under cyclic loading. *Granular Matter*, 21(2), 1–16.

Kammerer, A. M., Wu, J., Riemer, M., Pestana, J. M. and Seed, R. B., 2001. Use of cyclic simple shear testing in evaluation of the deformation potential of liquefiable soils. *Proceedings Fourth International Conference on Recent Advances in Geotechnical Earthquake Engineering and Soil Dynamics*. San Diego, California, 1–6.

Kanatani, K. I., 1981. A theory of contact force distribution in granular materials. *Powder Technology*, 28(2), 167–172.

Kanatani, K., 1984. Distribution of directional data and fabric tensors. *International journal of engineering science*, 22(2), 149–164.

Karapiperis, K., Ortiz, M., and Andrade, J. E., 2021. Data-Driven nonlocal mechanics: Discovering the internal length scales of materials. *Computer Methods in Applied Mechanics and Engineering*, 386, 114039.

Katagiri, J., Matsushima, T., and Yamada, Y., 2010. Simple shear simulation of 3D

irregularly-shaped particles by image-based DEM. *Granular Matter*. 12(5), 491–497.

Kazama, M., and Noda, T., 2012. Damage statistics (Summary of the 2011 off the Pacific Coast of Tohoku Earthquake damage). *Soils and Foundations*, 52(5), 780–792.

Kazama, M., Morimoto, H., Mori, T., Sento, N., and Shinozaki, T., 2006, December. Micro mechanical interpretation of liquefaction resistance of over-consolidated granular assemblies. In *International Symposium on Geomechanics and Geotechnics of Particulate Media-Geomechanics and Geotechnics of Particulate Media*. 217–223.

Kazama, M., Yamaguchi, A. and Yanagisawa, E., 2000. Liquefaction resistance from a ductility viewpoint, *Soils and Foundations*, 40(6), 47–60.

Kiyota, T., Sato, T., Koseki, J., and Abadimarand, M., 2008. Behavior of liquefied sands under extremely large strain levels in cyclic torsional shear tests. Soils and Foundations, 48(5), 727–739.

Kokusho, T., 2013. Liquefaction potential evaluations: energy-based method versus stress-based method. *Canadian Geotechnical Journal*, 50(10), 1088–1099.

Kokusho, T., and Kaneko, Y., 2018. Energy evaluation for liquefaction-induced strain of loose sands by harmonic and irregular loading tests. *Soil Dynamics and Earthquake Engineering*, 114, 362–377.

Kramer S. L, 1996. *Geotechnical earthquake engineering*. Prentice Hall, Upper Saddle River.

Kruyt, N. P., and Rothenburg, L., 1996. Micromechanical definition of the strain tensor for granular materials. *Journal of Applied Mechanics*. 63(3), 706–711.

Kuhn, M. R., 1999. Structured deformation in granular materials. *Mechanics of materials*, Elsevier, 31(6), 407–429.

Kumar, S. S., Murali Krishna, A. and Dey, A., 2020. Assessment of dynamic response of cohesionless soil using strain-controlled and stress controlled cyclic triaxial tests. *Geotech. Geol. Eng.*, 38 (2), 1431–1450.

Lee, K.L., and Albaisa, A., 1974. Earthquake induced settlements in saturated sands. *Journal of the Geotechnical Engineering Division*. 100(4), 387–406.

Lei, D., Huang, J., Xu, W., Wang, W., and Zhang, P., 2018. Deformation analysis of shear band in granular materials via a robust plane shear test and numerical simulation. *Powder Technology*, 323, 385–392.

Li, X. S., and Dafalias, Y. F.,2012. Anisotropic critical state theory: role of fabric. *Journal of engineering mechanics*, 138(3), 263–275.

Li, X., and Li, X. S., 2009. Micro-macro quantification of the internal structure of granular materials. *Journal of engineering mechanics*, American Society of Civil Engineers, 135(7), 641–656.

Love, A. E. H., 1927. *A treatise of mathematical theory of elasticity*, Cambridge University Press, Cambridge, U.K.

Manne, A., and Neelima Satyam, D., 2015. A review on the discrete element modeling of dynamic laboratory tests for liquefaction assessment. *Electronic Journal of Geotechnical Engineering*. 20(1), 21–46.

Martin, E. L., Thornton, C., and Utili, S., 2020. Micromechanical investigation of liquefaction of granular media by cyclic 3D DEM tests. *Géotechnique*, 70(10), 906–915.

Martin, G. R., Finn, W. L. and Seed, H. B., 1975. Fundamentals of liquefaction under cyclic loading. *Journal of Geotechnical and Geoenvironmental Engineering*, 101, 423–438.

Matsuda, H., Hendrawan, A. P., Ishikura, R., and Kawahara, S., 2011. Effective

stress change and post-earthquake settlement properties of granular materials subjected to multi-directional cyclic simple shear. *Soils and Foundations*. 51(5), 873–884.

Mitchell, J., and Soga, K., 2005. *Fundamentals of Soil Behavior*. 3rd edn. New York, NY, USA: John Wiley and Sons.

Morimoto, H., Okada, N., and Kazama, M., 2001. Evaluation of elastic energy of granular assembles subjected to various consolidation histories by DEM. *Powders and Grains.*

Nagase, H., Ishihara, K., 1988. Liquefaction-induced compaction and settlement of sand during earthquakes. *Soils and Foundations.* 28(1), 65–76.

Nakai, K., Asaoka, A., and Sawada, Y., 2016. Liquefaction damage enhanced by interference between the body wave and surface wave induced from the inclined bedrock. *Japanese Geotechnical Society Special Publication*. 2(19), 723–728.

Nakase, H., Takeda, T., and Oda, M., 1999. A simulation study on liquefaction using DEM. In *Earthquake geotechnical engineering*. 637–642.

Nemat-Nasser, S. and Shokooh, A., 1979. A unified approach to densification and liquefaction of cohesionless sand in cyclic shearing. *Canadian Geotechnical Journal.* 16(4), 659–78.

Ng, T. T., and R. Dobry, 1994. Numerical simulations of monotonic and cyclic loading of granular soil. *Journal of Geotechnical Engineering*, ASCE. 120 (2), 388–403.

Nguyen, H. B. K., Rahman, M. M., and Fourie, A., 2021. The critical state behaviour of granular material in triaxial and direct simple shear condition: A DEM approach. *Computers and Geotechnics*, 138, 104325.

Nguyen, H. B. K., Rahman, M. M., and Fourie, A., 2021. The critical state behaviour of granular material in triaxial and direct simple shear condition: A DEM

approach. *Computers and Geotechnics*, 138, 104325.

Nhan, T. T., Matsuda, H., and Sato, H., 2017. A model for multi-directional cyclic shear-induced pore water pressure and settlement on clays, *Bulletin of Earthquake Engineering*, 15(7), 2761–2784.

Nicot, F., Hadda, N., Guessasma, M., Fortin, J., and Millet, O., 2013. On the definition of the stress tensor in granular media. *International Journal of Solids and Structures*, 50(14-15), 2508–2517.

Novotny, O., 1999. *Seismic surface waves*. Bahia, Salvador: Instituto de Geociencias, 61.

Novotny, O., 1999. *Seismic surface waves*. Bahia, Salvador: Instituto de Geociencias, 61.

Oda, M., 1972. The mechanism of fabric changes during compressional deformation of sand. *Soils and Foundations*, 12(2), 1–18.

Oda, M., and Iwashita, K., 2000. Study on couple stress and shear band development in granular media based on numerical simulation analyses. *International journal of engineering science*, 38(15), 1713–1740.

Oda, M., Nemat-Nasser, S., and Konishi, J., 1985. Stress-induced anisotropy in granular masses. *Soils and Foundations*, The Japanese Geotechnical Society, 25(3), 85–97.

O'Sullivan, C., 2011. *Particulate discrete element modelling: a geomechanics perspective*. CRC Press.

O'Sullivan, C., Cui, L., O'Neill, S. C., 2008. Discrete element analysis of the response of granular materials during cyclic loading. *Soils and Foundations*. 48(4), 511–530.

Polito, C., Green, R. A., Dillon, E., and Sohn, C., 2013. Effect of load shape on relationship between dissipated energy and residual excess pore pressure generation in cyclic triaxial tests. *Canadian Geotechnical Journal*, 50(11), 1118-1128.

Pujol, J., 2003. *Elastic Wave Propagation and Generation in Seismology*, Cambridge University Press.

Pyke, R., Chan, C. K., and Seed, H. B., 1975. Settlement of sands under multidirectional shaking. *Journal of the Geotechnical Engineering Division*. 101 (4), 379–398.

Radjai, F., 2009. Force and fabric states in granular media. In M. Nakagawa and S. Luding (Eds.), *Proceedings of the 6th International Conference on Micromechanics of Granular Media Golden*, *Colorado, 13-17 July 2009*, pp. 35–42. AIP Conference Proceedings.

Radjai, F., Jean, M., Moreau, J. J., and Roux, S. (1996). Force distributions in dense two-dimensional granular systems. *Physical review letters*, 77(2), 274.

Radjai, F., Wolf, D. E., Jean, M., and Moreau, J. J., 1998. Bimodal character of stress transmission in granular packings. *Physical Review Letters*. 80, 61–64.

Rauch, A. F., 1997. *EPOLLS: an empirical method for predicting surface displacements due to liquefaction-induced lateral spreading in earthquakes* (Doctoral dissertation, Virginia Tech).

Robertson, P. K., and Fear, C. E., 1996. Soil liquefaction and its evaluation based on SPT and CPT. Draft of paper presented at the *NCEER Workshop on Evaluation of Liquefaction Resistance*, Salt Lake City, Utah, January 4–5.

Roscoe, K.H., Schofield, M.A., and Worth, C.P., 1958. On the yielding of soils. *Géotechnique.* 8(1), 22–53.

Rothenburg, L. and Kruyt, N. P., 2004. Critical state and evolution of coordination number in simulated granular materials. *International Journal of Solids and Structures*, 41, 5763–5774.

Rycroft, C., 2009. Voro++: *A three-dimensional Voronoi cell library in C++*. Lawrence Berkeley National Lab. (LBNL), Berkeley, CA (United States).

Satake, M., 1982. Fabric tensor in granular materials. In *Proc., IUTAM Symp. on Deformation and Failure of Granular materials*, Delft, The Netherlands.

Satake, M., 1982. Fabric tensor in granular materials. *IUTAM Conference on Deformation and Flow of Granular Materials*, 1982, AA Balkema, 63–68.

Schofield, A. N., and Wroth, P., 1968. *Critical state soil mechanics*. London: McGraw-hill.

Seed, H. B. and Lee, K. L., 1966. Liquefaction of saturated sands during cyclic loading. *Journal of the Soil Mechanics and Foundations Division*, 92(6), 105–134.

Seed, H. B., 1979. Soil liquefaction and cyclic mobility evaluation for level ground during earthquakes. *Journal of the Geotechnical Engineering Division,* 105(2), 201–255.

Seed, H. B., Martin, G. R., and Pyke, R. M., 1978. Effect of multidirectional shaking on pore pressure development in sands. *Journal of the Geotechnical Engineering Division*. 104(1), 27–44.

Seed, H. B., Pyke, R. and Martin, G. R., 1975. Effect of multi-directional shaking on liquefaction of sands. Earthquake Engineering Research Center, University of California.

Seed, H. B., Pyke, R., and Martin, G. R., 1975. *Effect of multi-directional shaking on liquefaction of sands*. Earthquake Engineering Research Center, University of California.

Sento, N., Kazama, M., Uzuoka, R., 2004. Experiment and idealization of the volumetric compression characteristics of clean sand after undrained cyclic shear. *Doboku Gakkai Ronbunshu*. 2004(764), 307–317.

Shafipour, R., and Soroush, A., 2008. Fluid coupled-DEM modelling of undrained behavior of granular media. *Computers and Geotechnics*. 35(5), 673–685.

Shamoto, Y., Sato, M., and Zhang, J., 1996. Simplified estimation of earthquake-induced settlements in saturated sand deposits. *Soils and Foundations*. 36(1), 39–50.

Shamoto, Y., Zhang, J.M. and Goto, S., 1997. Mechanism of large post-liquefaction deformation in saturated sand. *Soils Found.* 37(2), 71–80.

Sitharam, T. G., and Dinesh, S. V., 2003. Numerical simulation of liquefaction behaviour of granular materials using Discrete Element Method. *Journal of Earth System Science*, 112(3), 479.

Sitharam, T. G., J. S. Vinod, and B. V. Ravishankar (2009). Postliquefaction undrained monotonic behaviour of sands: experiments and DEM simulations. *Géotechnique.* 59 (9), 739–749.

Sitharam, T., S. Dinesh, and N. Shimizu, 2002. Micromechanical modelling of monotonic drained and undrained shear behaviour of granular media using three-dimensional DEM. *International Journal for Numerical and Analytical Methods in Geomechanics*. 26, 1167–1189.

Soroush, A., and Ferdowsi, B., 2011. Three dimensional discrete element modeling of granular media under cyclic constant volume loading: a micromechanical perspective. *Powder technology*, 212(1), 1–16.

Staroszczyk, R., 2016. Rayleigh Waves Transformation in Liquefying Water-saturated Sands. *Archives of Hydro-Engineering and Environmental Mechanics*, 63(2-3), 173–190.

Su, D., and Li, X. S., 2008. Impact of multidirectional shaking on liquefaction potential of level sand deposits. *Géotechnique*, 58(4), 259–267.

Sugano, T., and Yanagisawa, E., 1992. Cyclic undrained shear behavior of sand under surface wave stress conditions. In *Proc. of the 10th WCEE*. 3, 1323–1327.

Sun Q. C, and Wang G. Q., 2009. *Introduction to the mechanics of granular matter*. Beijing: Science Press. (in Chinese)

Thornton C., 2000. Numerical simulations of deviatoric shear deformation of granular media. *Géotechnique.* 50(1), 43–53

Thornton, C., and Antony, S. J., 1998. Quasi-static deformation of particulate media. *Philosophical Transactions of the Royal Society of London. Series A: Mathematical, Physical and Engineering Sciences*, 356(1747), 2763–2782.

Thornton, C., and Sun, G., 1993. Axisymmetric compression of 3D polydisperse systems of spheres. *Powders and grains*, 93, 129–134.

Thornton, C., and Zhang, L., 2010. On the evolution of stress and microstructure during general 3D deviatoric straining of granular media. *Géotechnique*, 60(5), 333-341.

Tokimatsu, K., and Asaka, Y.,1998. Effects of liquefaction-induced ground displacements on pile performance in the 1995 Hyogoken-Nambu earthquake. *Soils and Foundations*, 38, 163–177.

Tokimatsu, K., and Yoshimi, Y., 1982. Liquefaction of sand due to multidirectional cyclic shear. *Soils and Foundation*s, 22(3), 126–130.

Tokimatsu, K., Seed, H. B., 1987. Evaluation of settlements in sands due to earthquake shaking. *Journal of geotechnical engineering*. 113(8), 861–5878.

Tordesillas, A., Shi, J., and Tshaikiwsky, T., 2011. Stress–dilatancy and force chain

evolution. *International Journal for Numerical and Analytical Methods in Geomechanics*, 35(2), 264–292.

Towhata I., 2008. *Geotechnical earthquake engineering*. Springer series in geomechanics and geoengineering. Springer, Berlin.

Towhata, I., and Ishihara, K., 1985. Shear work and pore water pressure in undrained shear. *Soils and Foundations*. 25(3):73–84.

Trifunac, MD., 1971. Response envelope spectrum and interpretation of strong earthquake ground motion. *Bulletin of the Seismological Society of America*. 61(2), 343–356.

Umar, M., Kiyota, T., Chiaro, G., and Antoine, D., 2019. Undrained monotonic behavior of sand in large strain torsional shear apparatus. *Bulletin of Earthquake Resistant Structure Research Center*, Institute of Industrial Science, University of Tokyo, 52, 1–10.

Uthayakumar, M., and Vaid, Y. P., 1998. Static liquefaction of sands under multiaxial loading. *Canadian Geotechnical Journal*. 35(2), 273–283.

Uzuoka, R., Shimizu, Y., Kamura, A., Sento, N., and Kazama, M., 2010. A unified prediction for liquefaction and settlement of saturated sandy ground. In: *4th International Conference on Earthquake Geotechnical Engineering*, Thessaloniki, Greece.

Ventouras, K., and Coop, M. R., 2009. On the behaviour of Thanet Sand: an example of an uncemented natural sand. *Géotechnique*, Thomas Telford Ltd, 59(9), 727–738.

Verdugo, R., and González, J., 2015. Liquefaction-induced ground damages during the 2010 Chile earthquake. *Soil Dynamics and Earthquake Engineering*, 79, 280–295.

Vucetic, M., 1994. Cyclic threshold shear strains in soils. *Journal of Geotechnical engineering*, 120(12), 2208–2228.

Wang, G., and Wei, J., 2016. Microstructure evolution of granular soils in cyclic mobility and post-liquefaction process. *Granular Matter*, 18(3), 1–13.

Wang, G., and Wei, J., 2016. Microstructure evolution of granular soils in cyclic mobility and post-liquefaction process. *Granular Matter*, Springer, 18(3), 51.

Wang, R., Fu, P., Zhang, J. M., and Dafalias, Y. F., 2016. DEM study of fabric features governing undrained post-liquefaction shear deformation of sand. *Acta Geotechnica*, 11(6), 1321–1337.

Wang, Z., Fang, H., and Zhao, S., 1983. Macroscopic features of earthquake induced soil liquefaction and its influence on ground damage. *Canadian Geotechnical Journal*. 20(1), 61–68.

Wei, J., Huang, D., and Wang, G., 2020. Fabric evolution of granular soils under multidirectional cyclic loading. *Acta Geotechnica*, 15, 2529–2543.

Wei, X., Zhang, Z., Wang, G., and Zhang, J., 2019. DEM study of mechanism of large post-liquefaction deformation of saturated sand. *Rock and Soil Mechanics*. 40(4), 1596–1602 (in Chinese).

Yamamuro, J. A. and Covert, K. M., 2001. Monotonic and cyclic liquefaction of very loose sands with high silt content. *J. Geotech. Geoenviron. Eng*., 127 (4), 314–324.

Yanagisawa, E., 1983. Influence of void ratio and stress condition on the dynamic shear modulus of granular media. *Advances in the mechanics and the flow of granular materials*, 2, 946–960.

Yang, J. and Sze, H. Y., 2011. Cyclic behaviour and resistance of saturated sand under non-symmetrical loading conditions. *Géotechnique.* 61 (1), 59–73.

Yang, M., Taiebat, M., Mutabaruka, P., and Radjaï, F., 2021. Evolution of granular materials under isochoric cyclic simple shearing. *Physical Review E*, 103(3), 032904.

Yang, M., Taiebat, M., Mutabaruka, P., and Radjai, F., 2022. Evolution of granular media under constant-volume multidirectional cyclic shearing. *Acta Geotechnica*, 17(3), 779–802.

Yimsiri, S. and K. Soga, 2010. DEM analysis of soil fabric effects on behaviour of sand. *Géotechnique.* 60 (6), 483–495.

Yoshida, N., 2020. *Liquefaction Phenomenon: From Mechanism to Numerical Analysis.* Morikita Shuppan Kabushiki Kaisha.

Yoshimi, Y., Tokimatsu, K., and Hosaka, Y., 1989. Evaluation of liquefaction resistance of clean sands based on high-quality undisturbed samples. *Soils and Foundations*, 29, 93–104.

Zhang, H. P., and Makse, H. A., 2005. Jamming transition in emulsions and granular materials. *Physical Review E*, 72(1), 011301.

Zhou, Y., Li, Y., Ding, H., Chen, Y., Ling, D., Ishikawa A., and Shamoto Y., 2014. Characterization of reconsolidation volumetric strain of liquefied sand and validation by centrifuge model tests. *Chinese Journal of Geotechnical Engineering*. 36(10), 1838–1845.

Towhata, I., 1999. *Photographs and Motion Picture of the Niigata City Immediately after the earthquake in 1964.* Japanese Geotechnical Society (CD-Rom).

APPENDIX I

The evolution of the magnitude and distribution of normal contact forces in the measurement cube of the specimen with $e = 0.75$ in the 1^{st} and 11^{th} cycle are illustrated here. The radial lines represent the contact force directions, and each concentric circle indicates the proportion of contact forces aligned in a particular direction range (10° per interval). The color of sector areas indicates the mean value of the projection of contact forces in each direction range on a given plane. The orange arrow illustrates the direction of the projection of major principal stress on each plane.

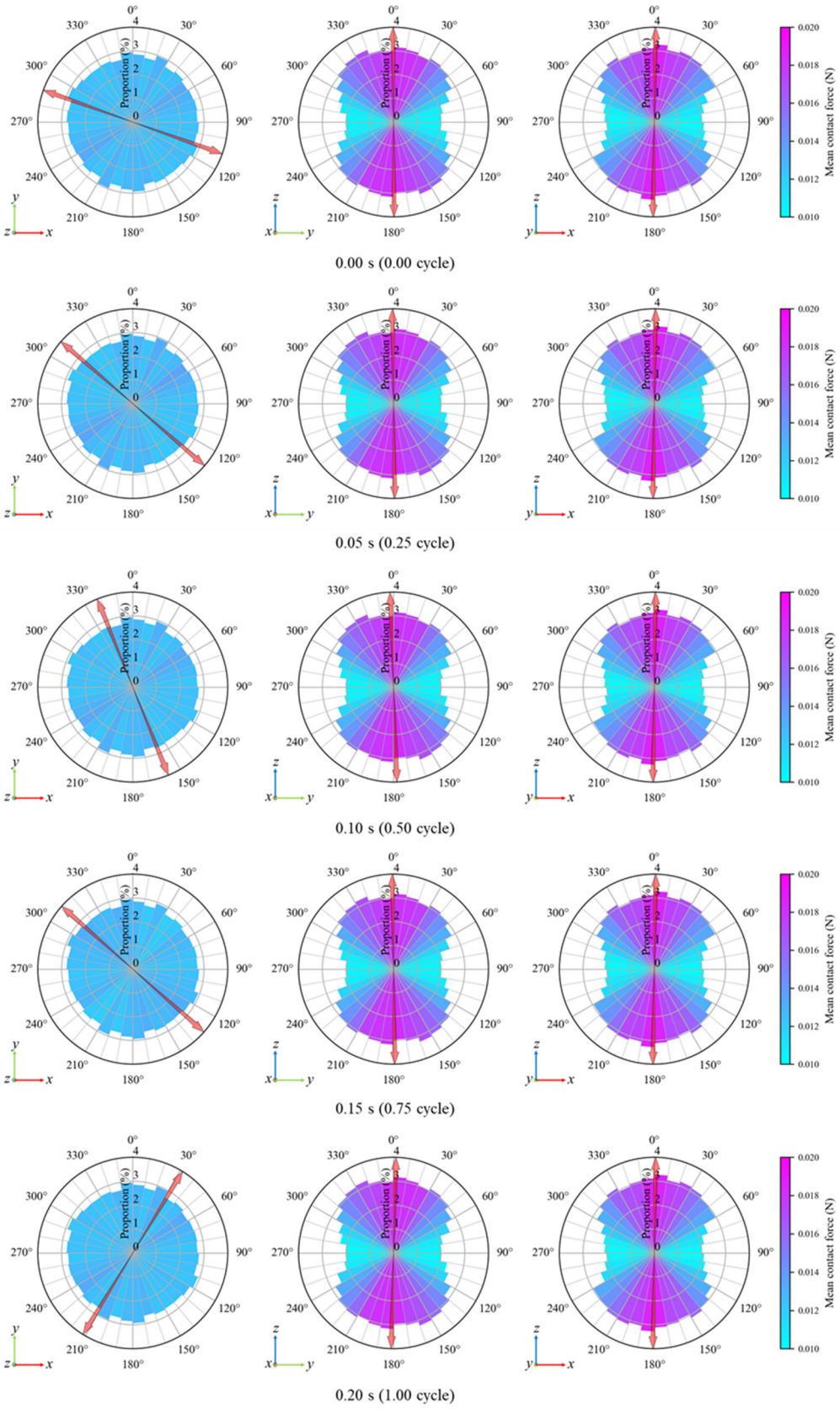

Fig. A. 1. Rose diagram under Love-wave strain condition with AR = 0.25 (the 1st cycle).

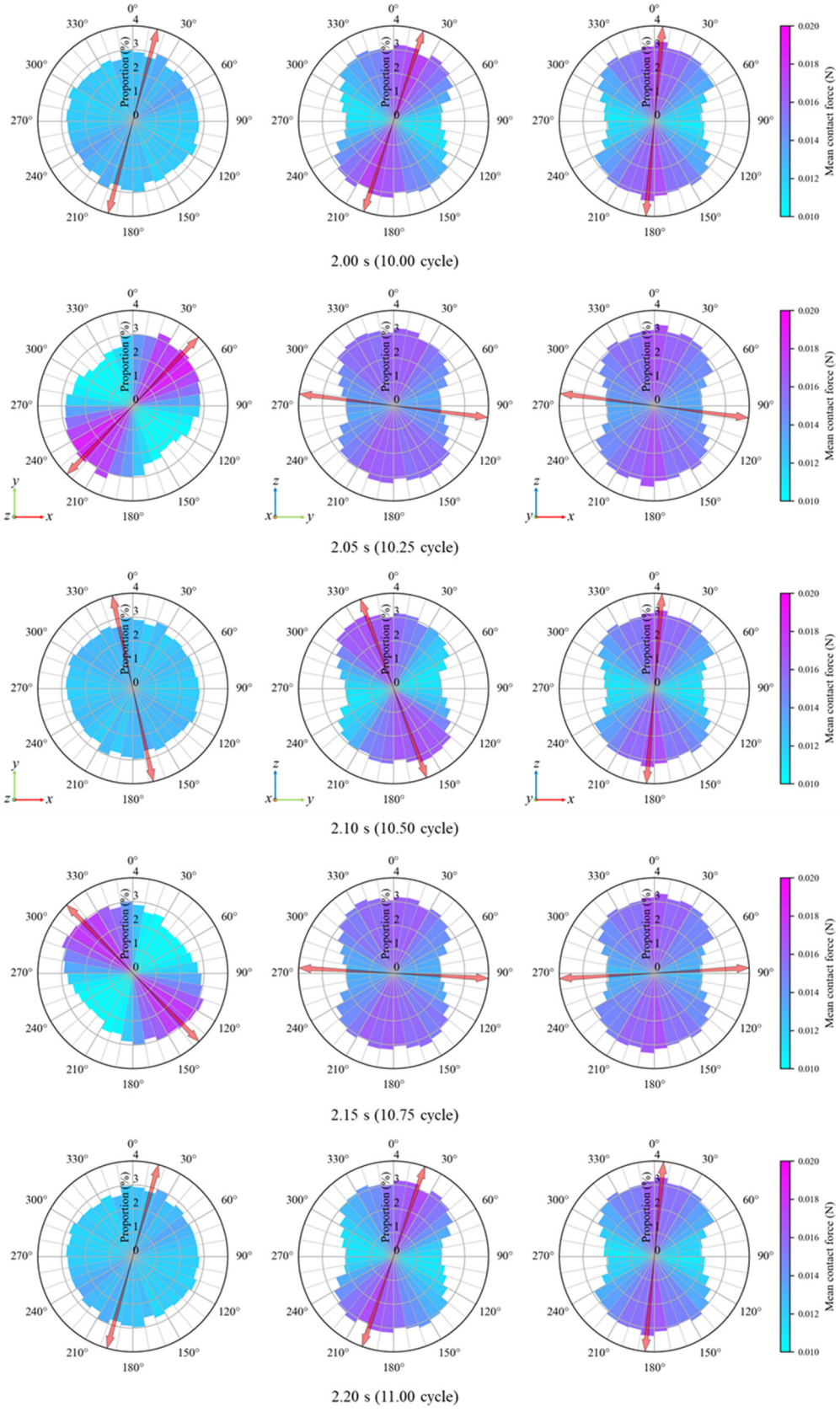

Fig. A. 2. Rose diagram under Love-wave strain condition with AR = 0.25 (the 11st cycle).

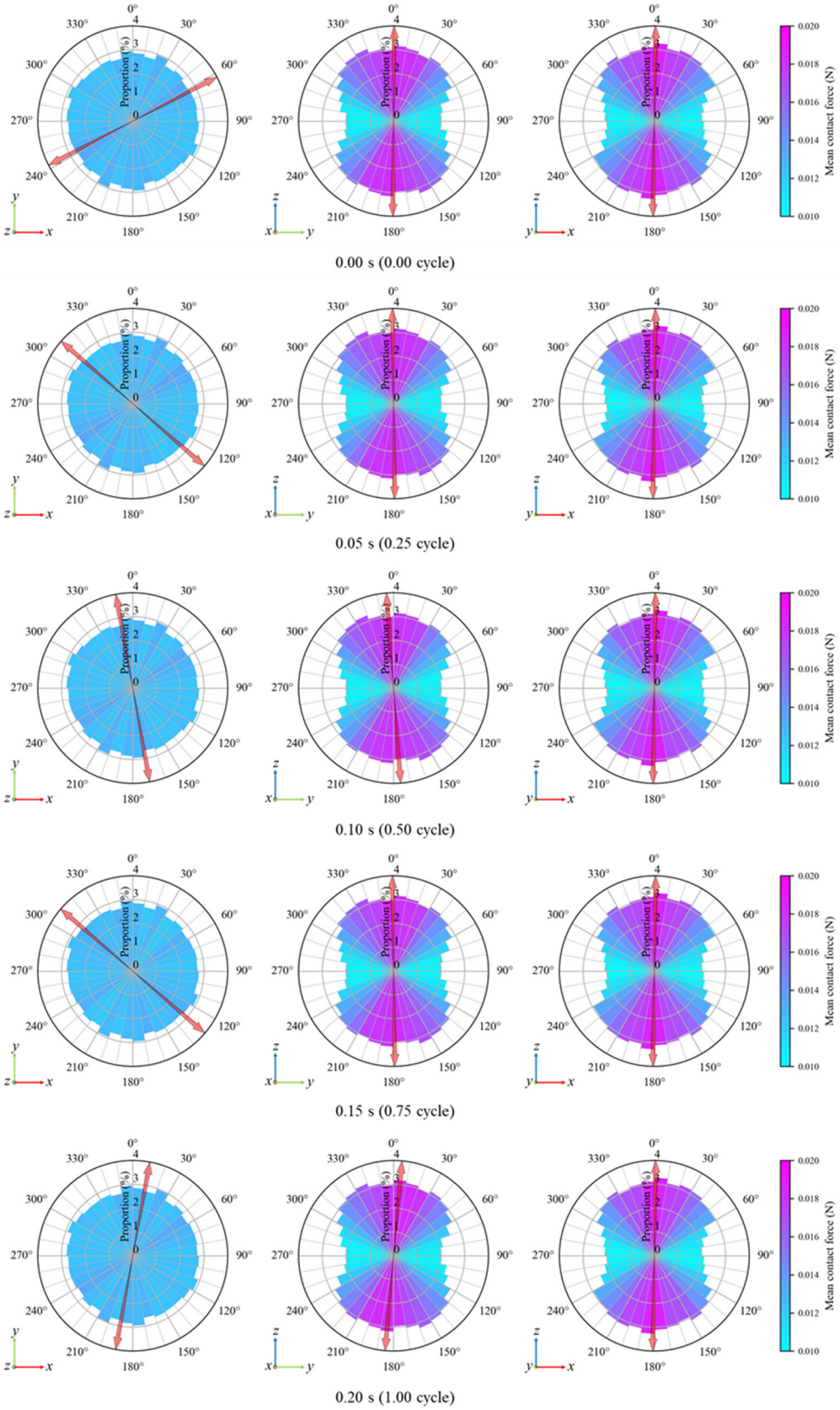

Fig. A. 3. Rose diagram under Love-wave strain condition with AR = 1 (the 1st cycle).

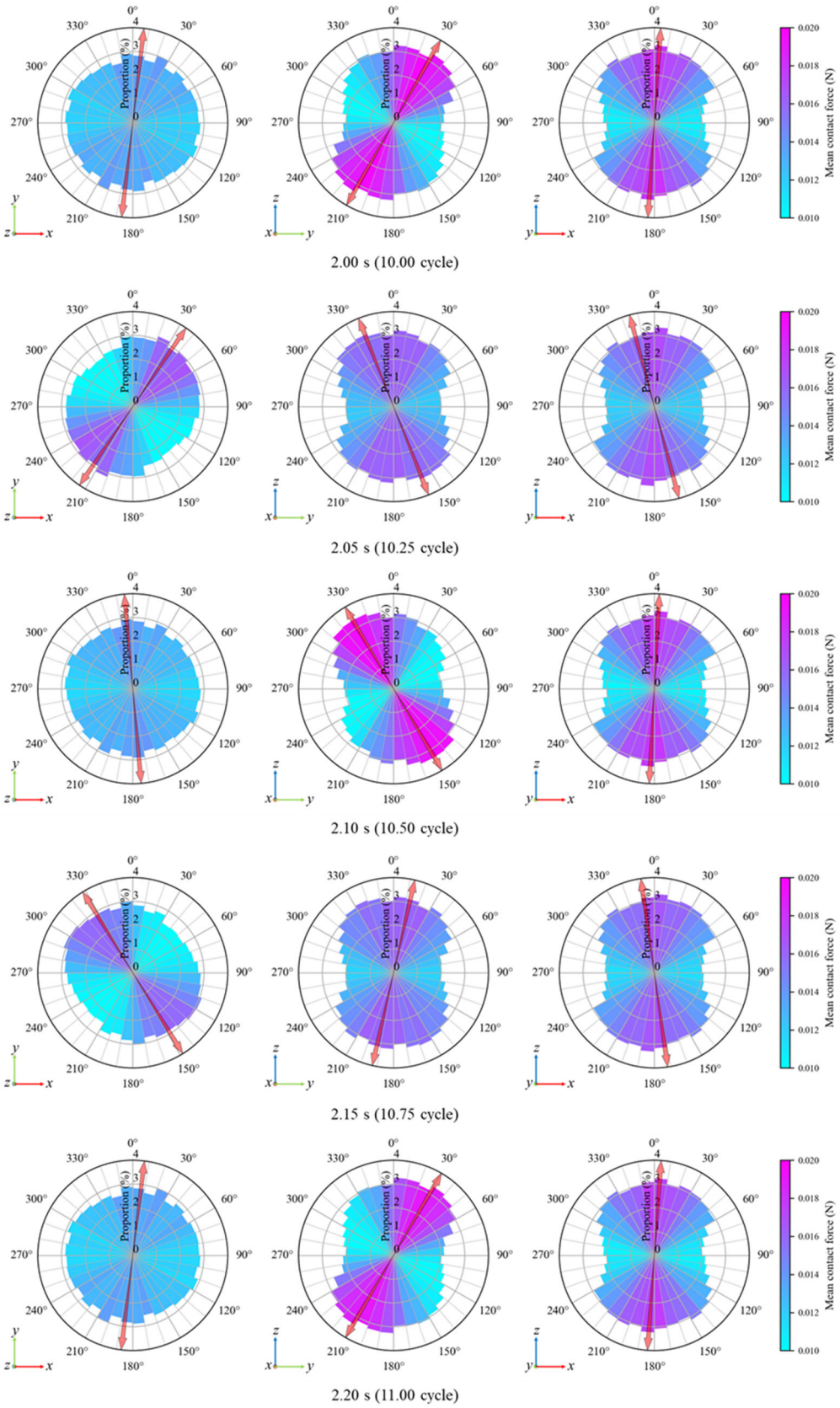

Fig. A. 4. Rose diagram under Love-wave strain condition with AR = 1 (the 11st cycle).

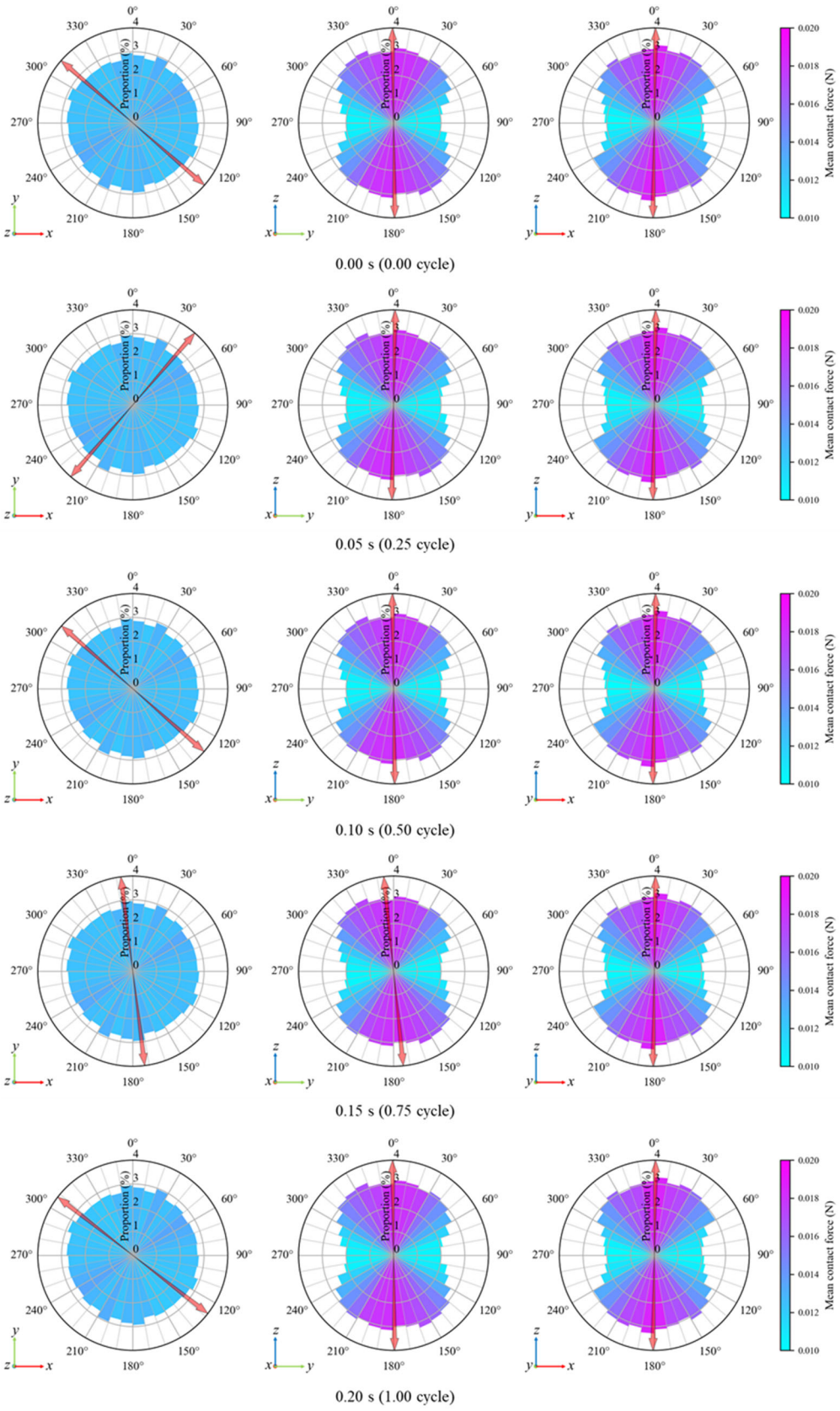

Fig. A. 5. Rose diagram under Love-wave strain condition with AR = 4 (the 1st cycle).

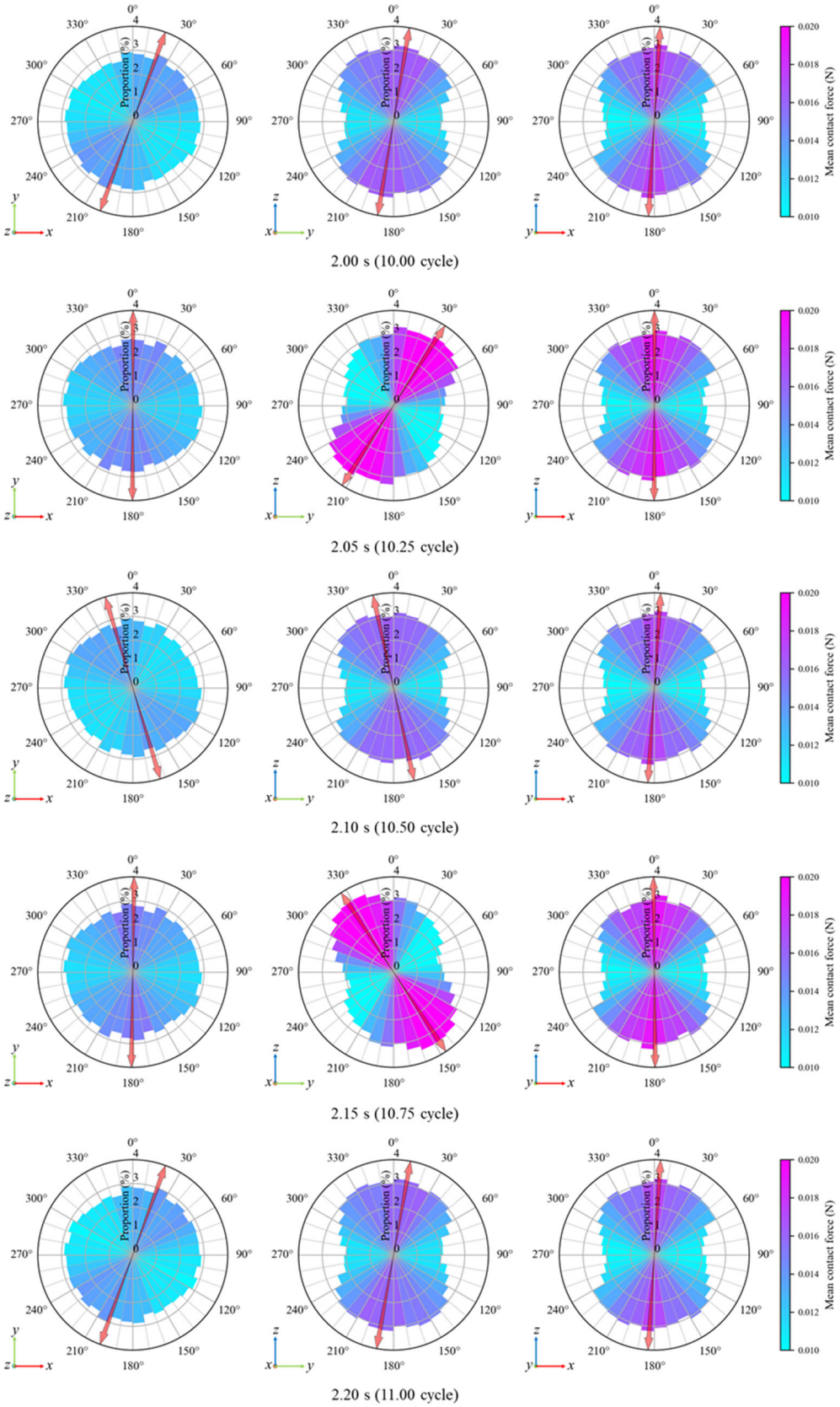

Fig. A. 6. Rose diagram under Love-wave strain condition with AR = 4 (the 11st cycle).

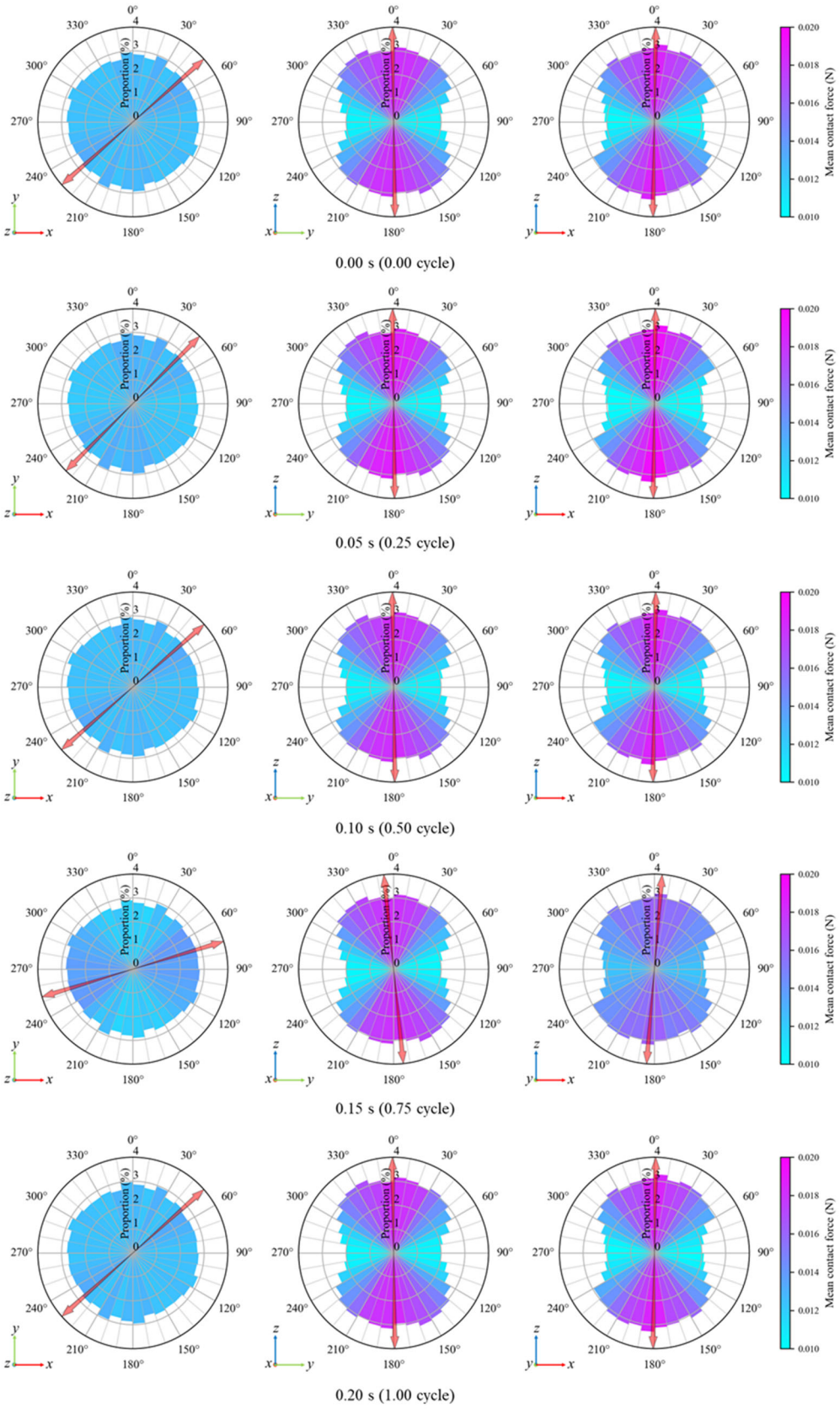

Fig. A. 7. Rose diagram under Rayleigh-wave strain condition with RSN = 0 (the 1st cycle).

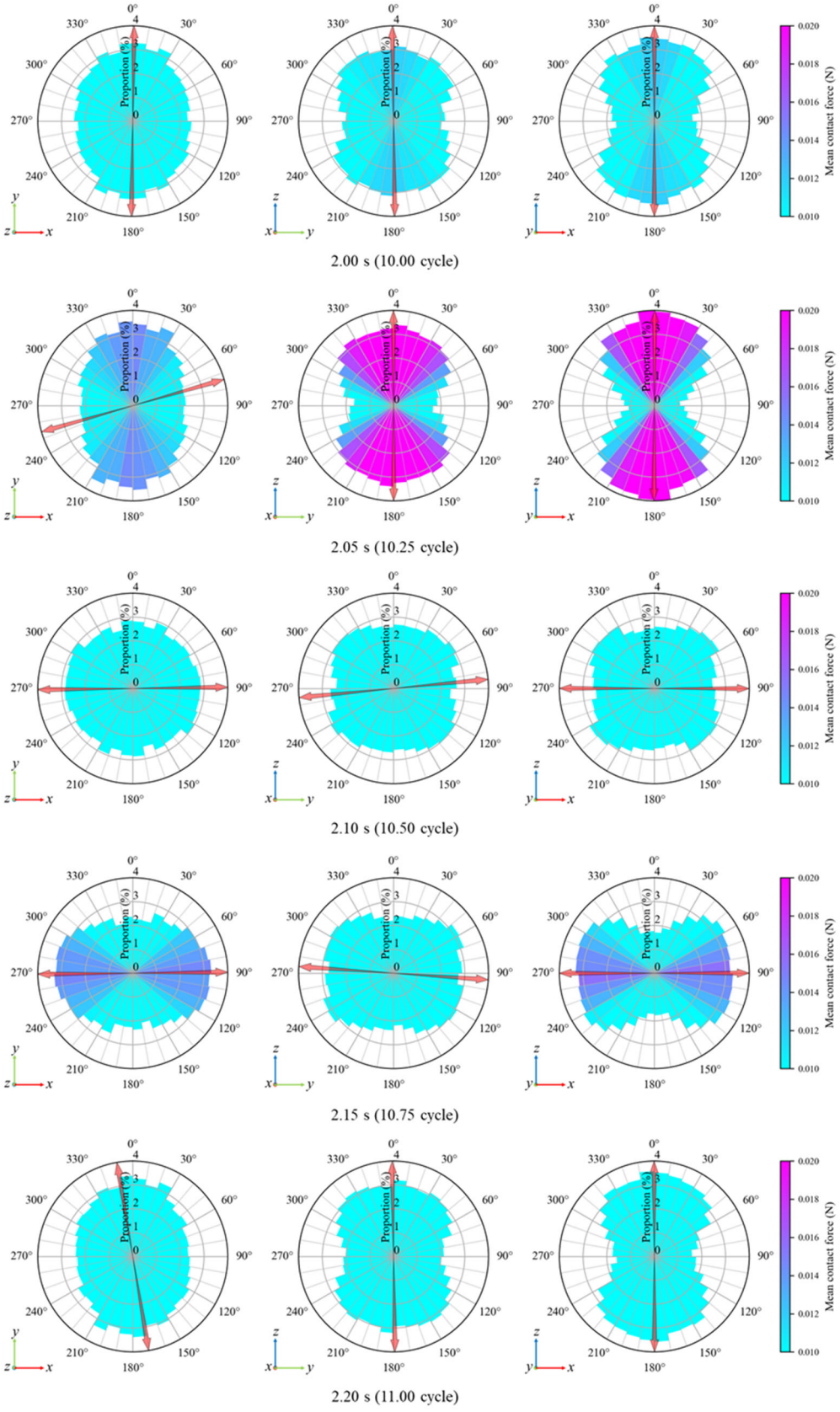

Fig. A. 8. Rose diagram under Rayleigh-wave strain condition with RSN = 0 (the 11st cycle).

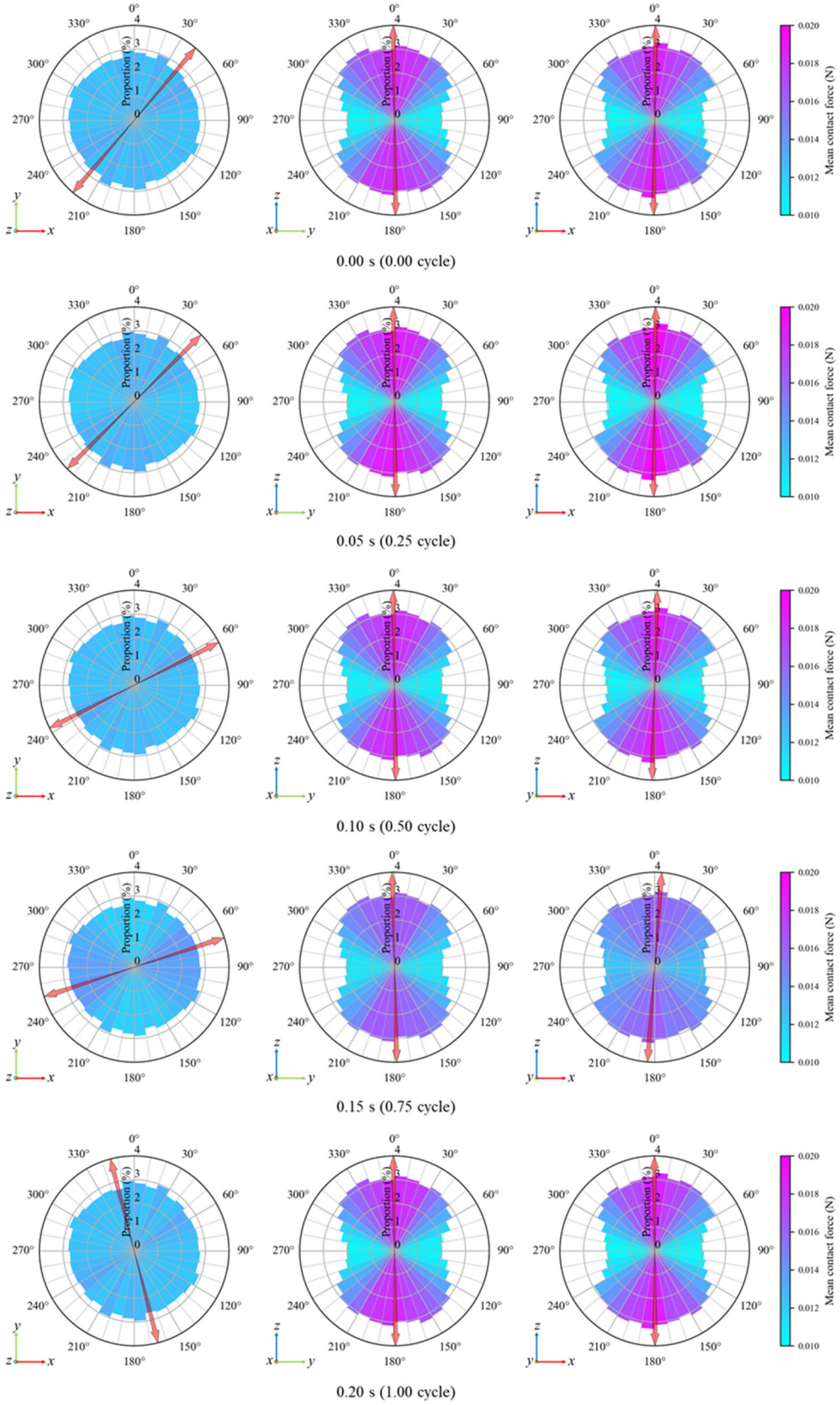

Fig. A. 9. Rose diagram under Rayleigh-wave strain condition with RSN = 0.25 (the 1st cycle).

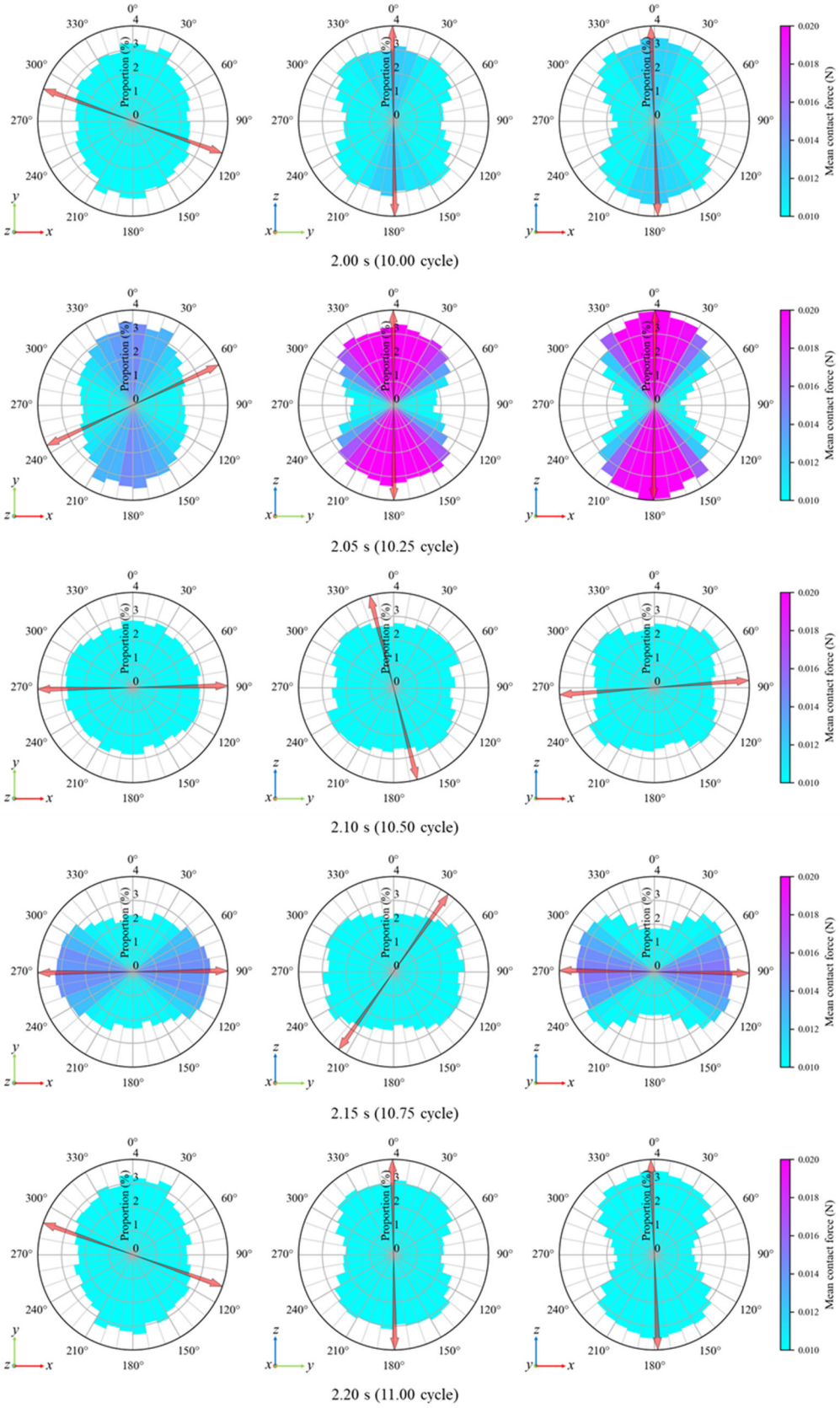

Fig. A. 10. Rose diagram under Rayleigh-wave strain condition with RSN = 0.25 (the 11st cycle).

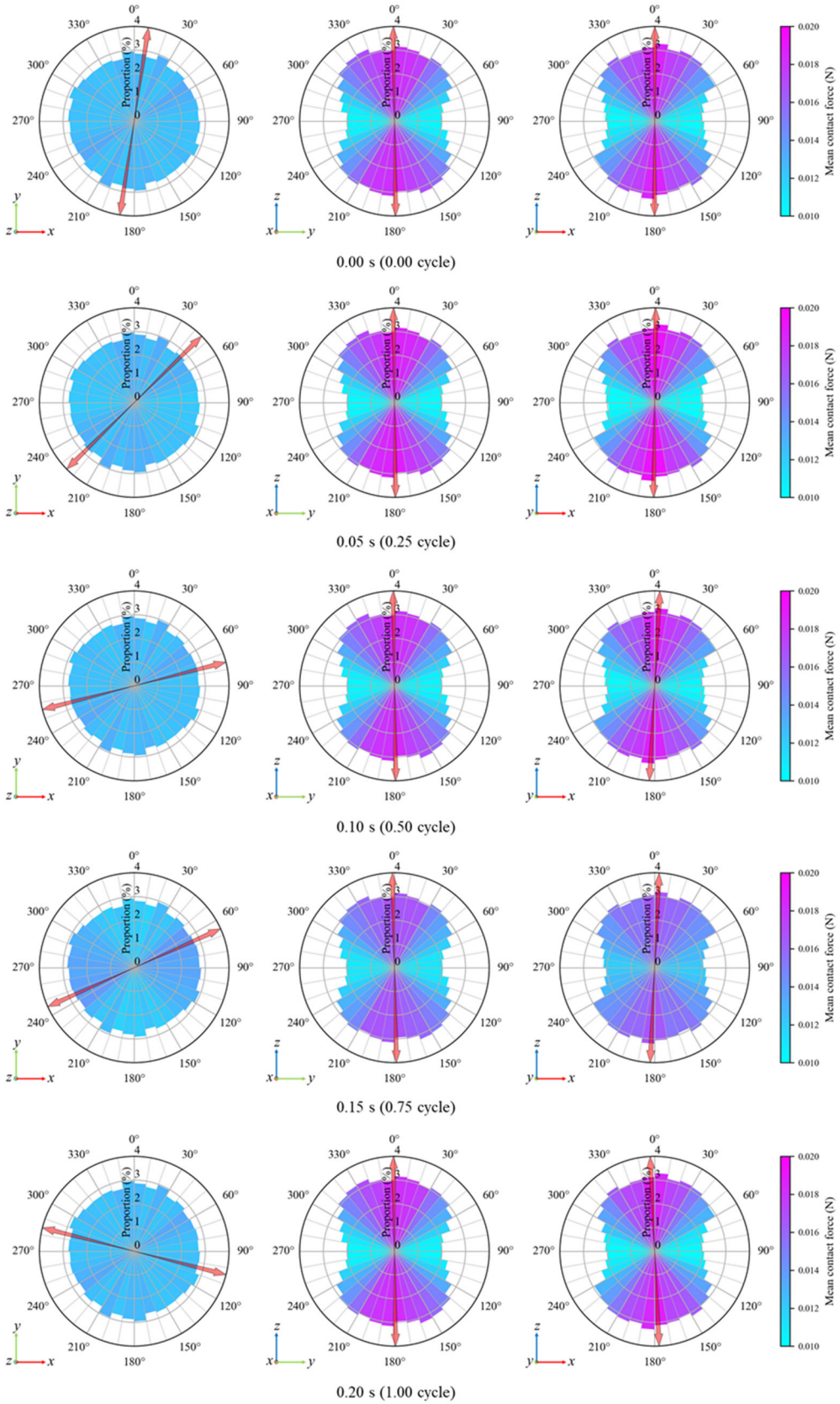

Fig. A. 11. Rose diagram under Rayleigh-wave strain condition with RSN = 1 (the 1st cycle).

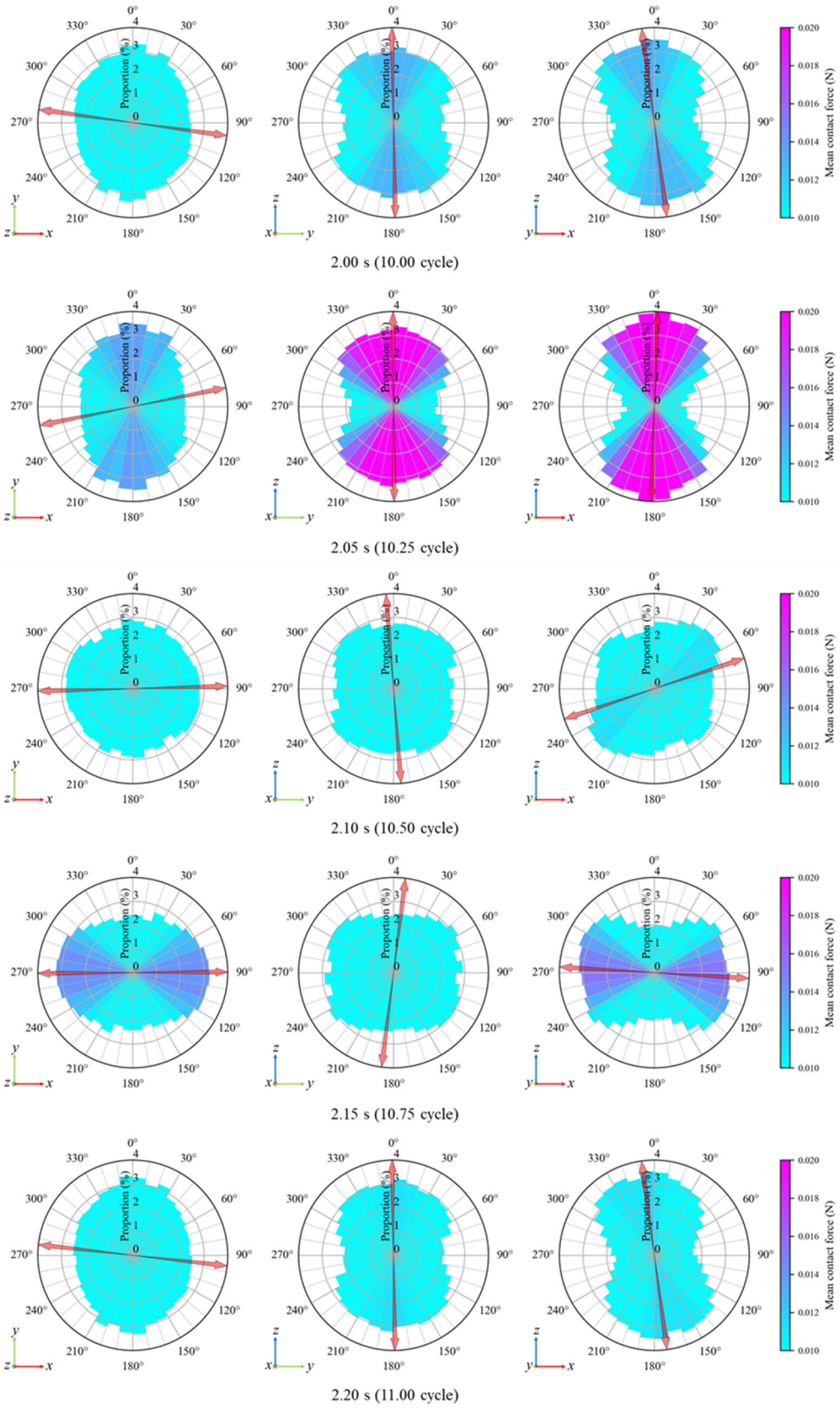

Fig. A. 12. Rose diagram under Rayleigh-wave strain condition with RSN = 1 (the 11st cycle).

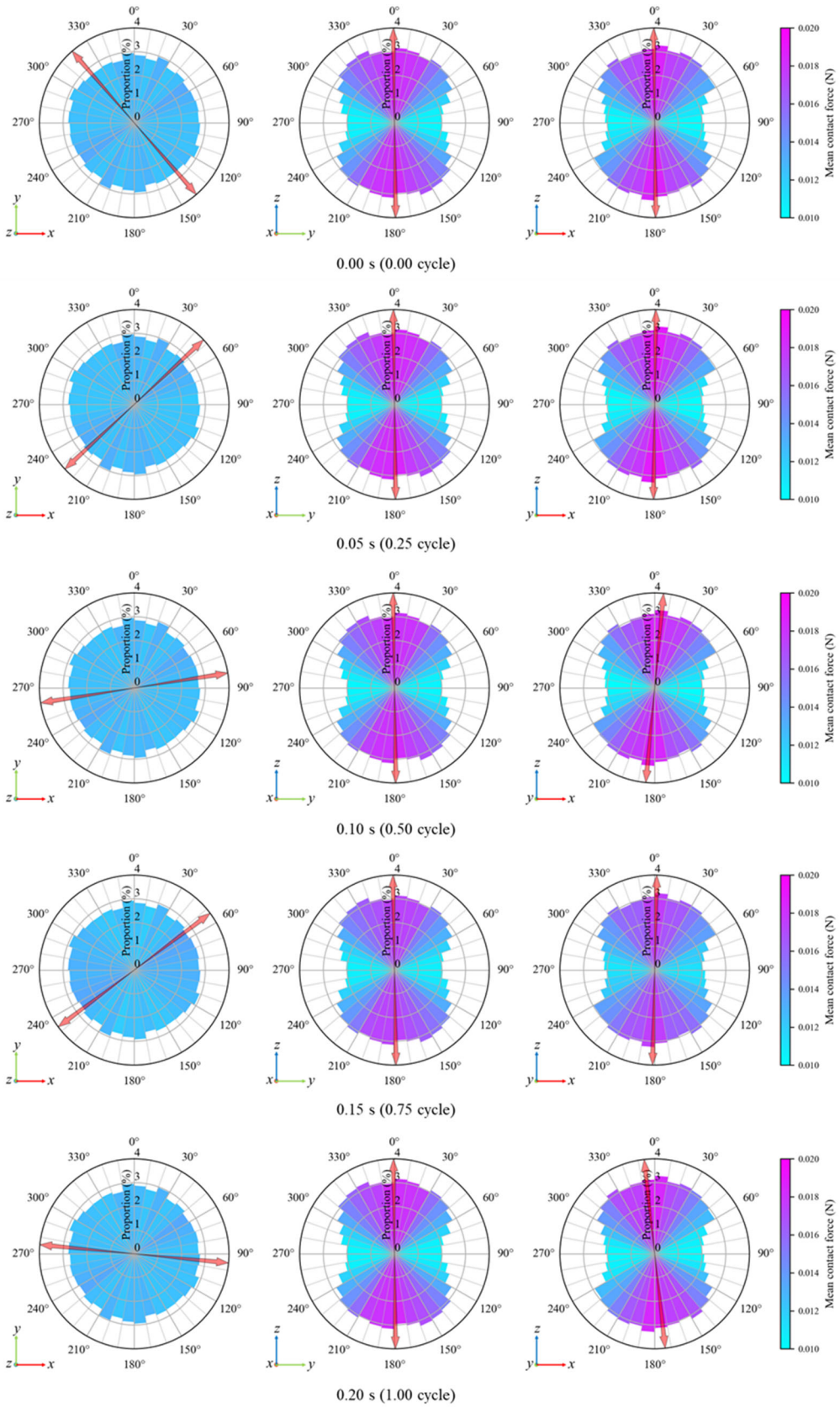

Fig. A. 13. Rose diagram under Rayleigh-wave strain condition with RSN = 4 (the 1st cycle).

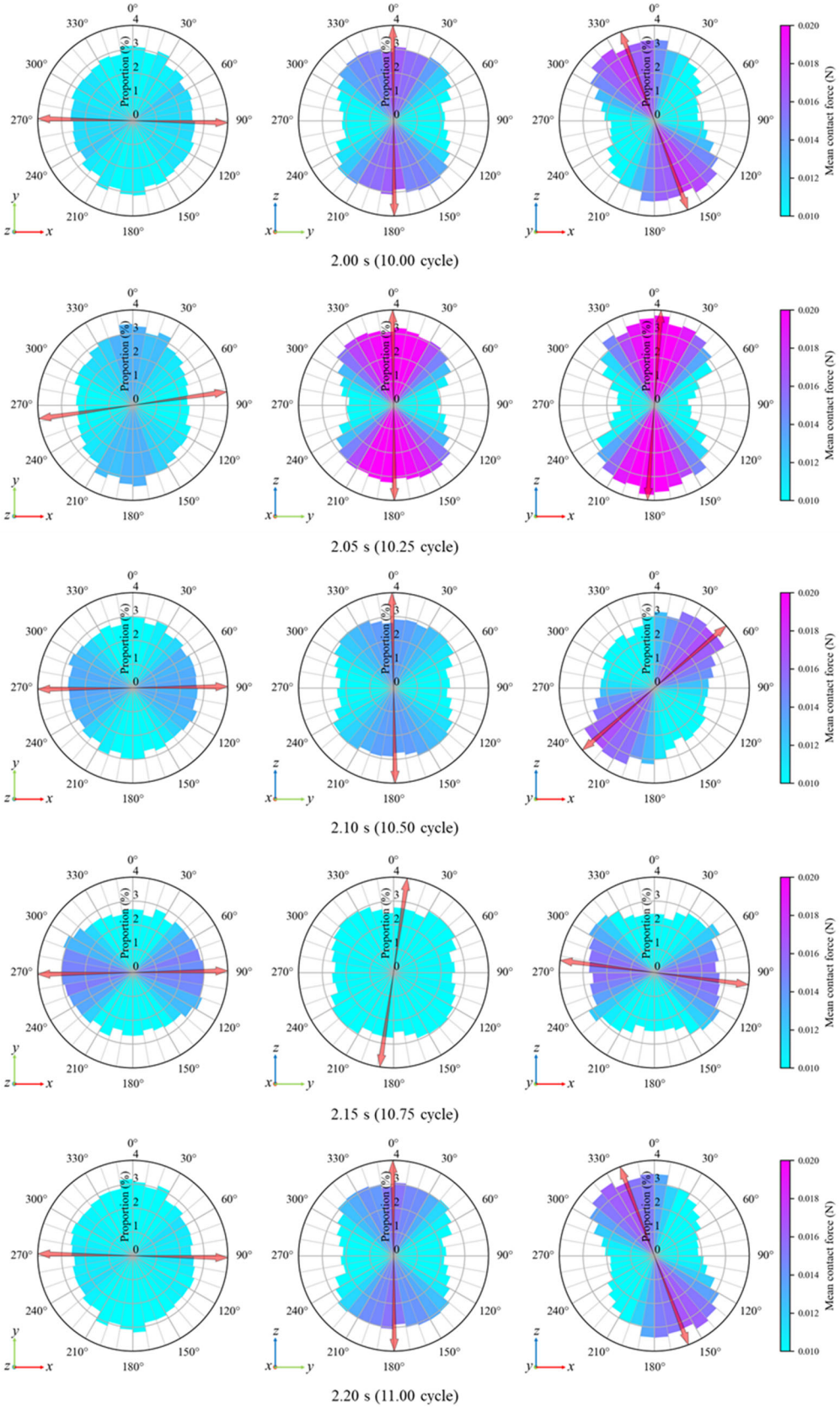

Fig. A. 14. Rose diagram under Rayleigh-wave strain condition with RSN = 4 (the 11st cycle).

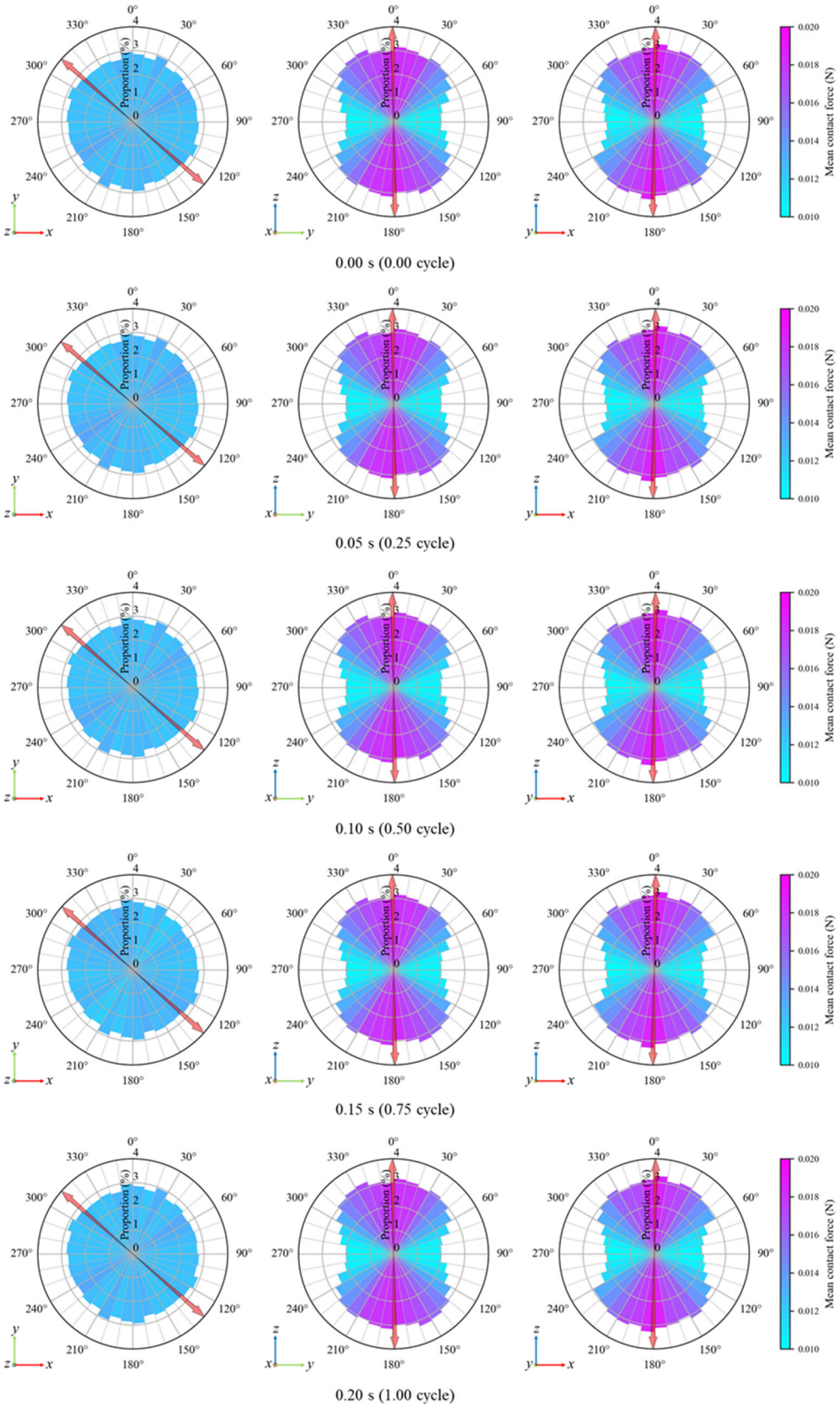

Fig. A. 15. Rose diagram under SHH-wave strain condition (the 1st cycle).

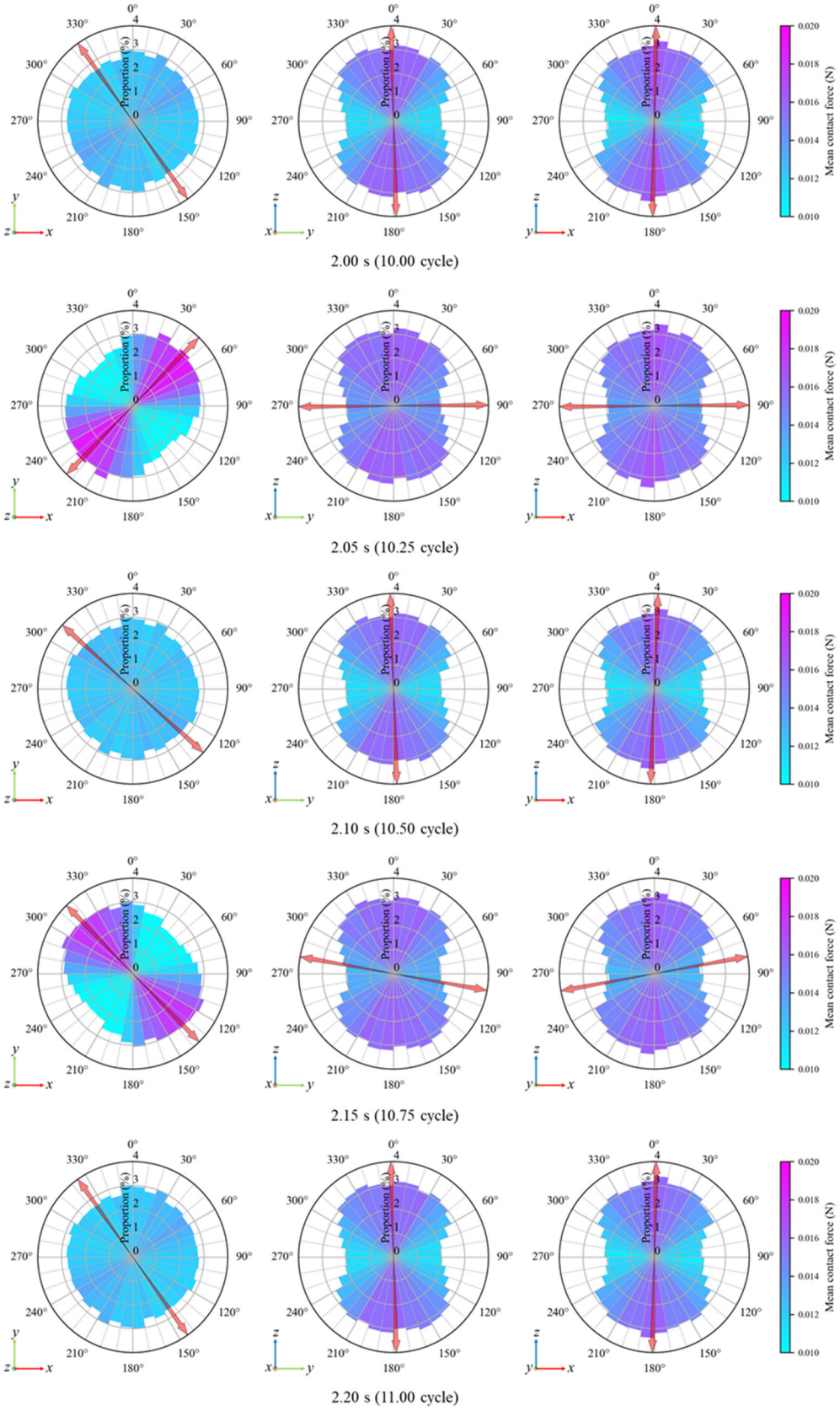

Fig. A. 16. Rose diagram under SHH-wave strain condition (the 11st cycle).

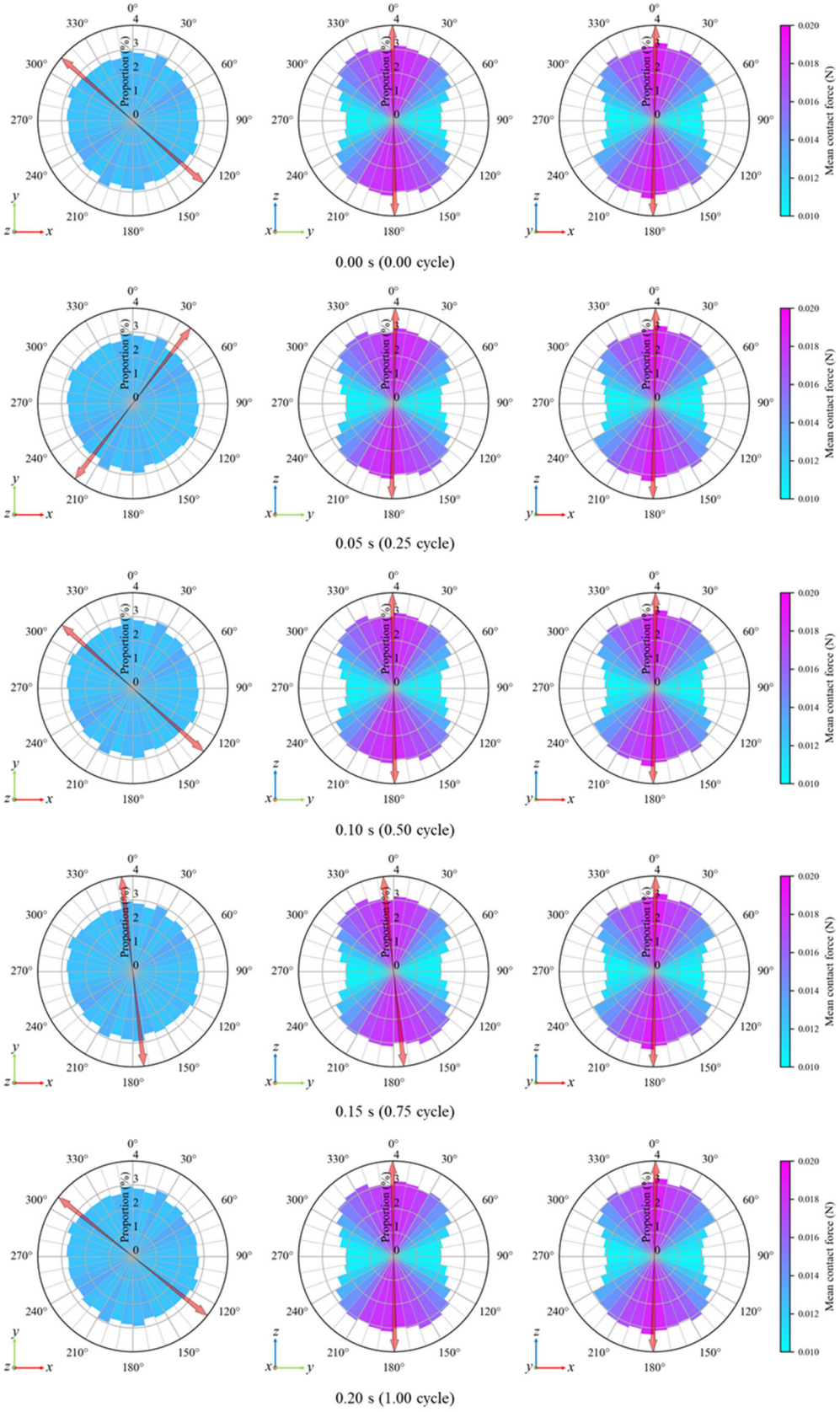

Fig. A. 17. Rose diagram under SHV-wave strain condition (the 1st cycle).

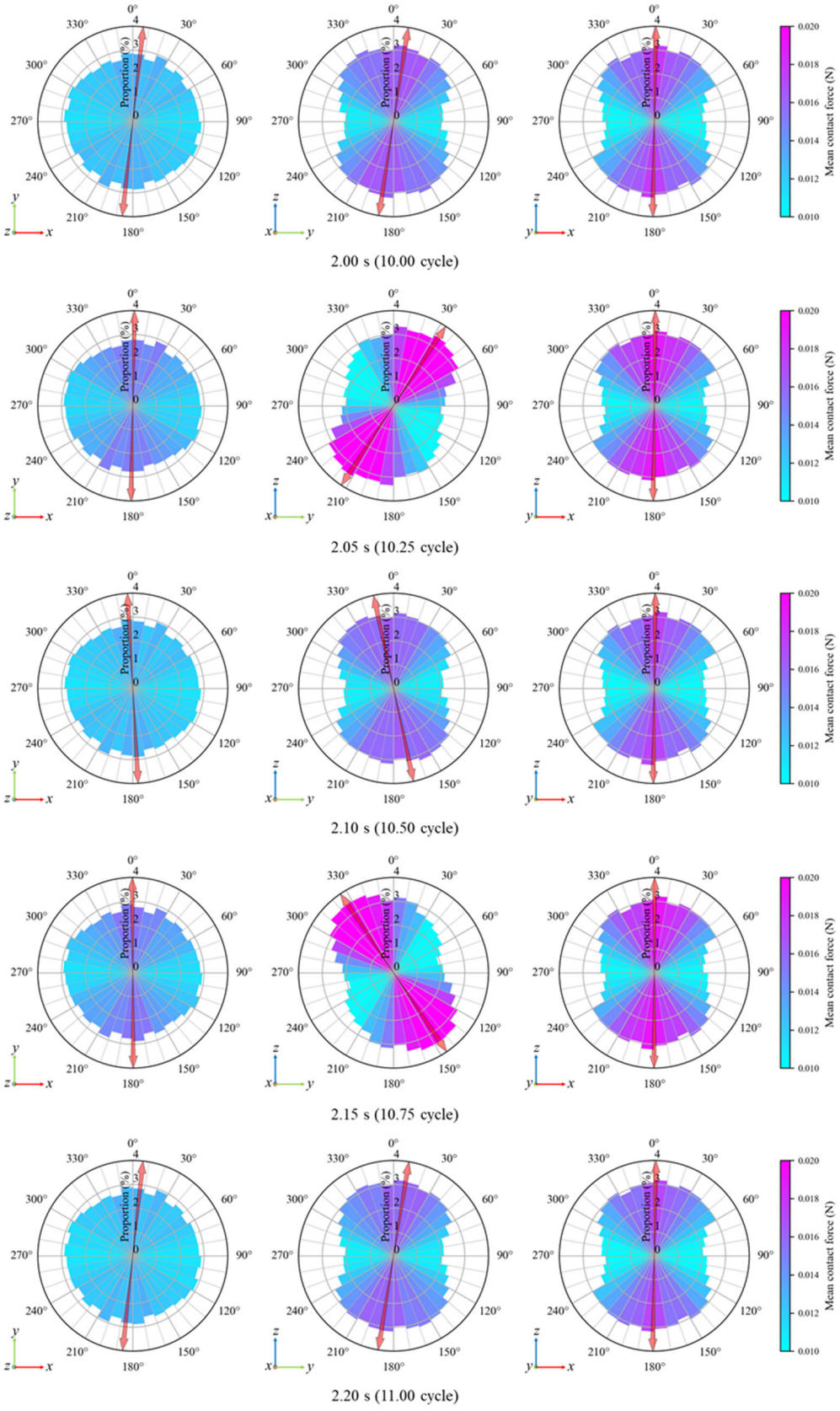

Fig. A. 18. Rose diagram under SHV-wave strain condition (the 11st cycle).

APPENDIX II

The evolution of the projections of the directions of ε_1, σ_1, and Φ_1 on the strain application plane (e = 0.75), and their relationship with ESRR during cyclic loading are illustrated here.

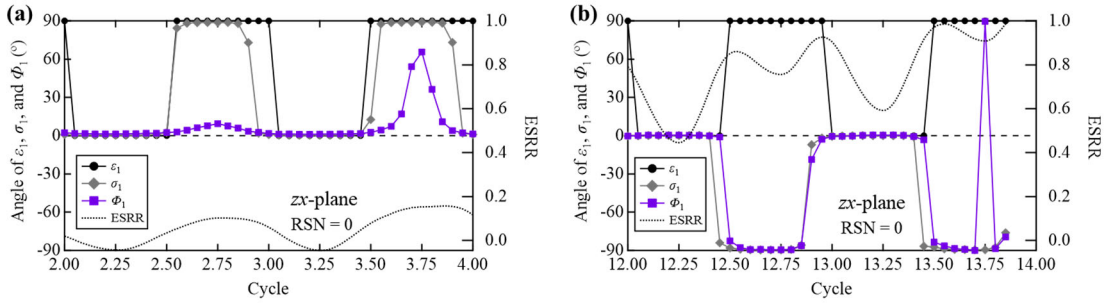

Fig. A. 19. Evolution of the projections of the directions of ε_1, σ_1, and Φ_1 on the zx-plane (e = 0.75), and their relationship with ESRR under Rayleigh-wave strain condition with RSN = 0 during: (a) 2–4 cycle; (b) 12–14 cycle.

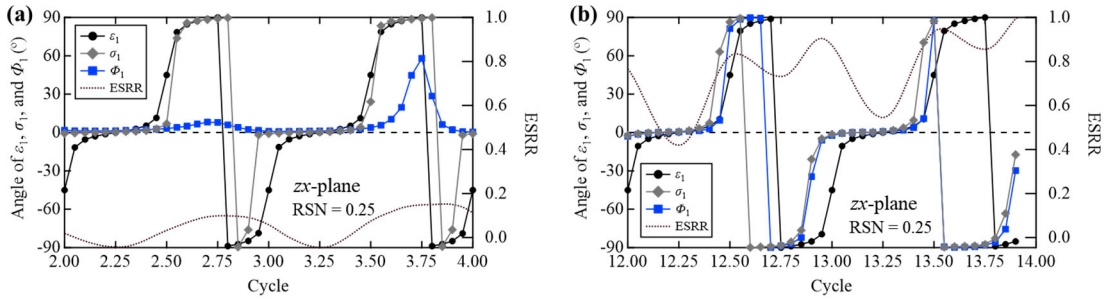

Fig. A. 20. Evolution of the projections of the directions of ε_1, σ_1, and Φ_1 on the zx-plane (e = 0.75), and their relationship with ESRR under Rayleigh-wave strain condition with RSN = 0.25 during: (a) 2–4 cycle; (b) 12–14 cycle.

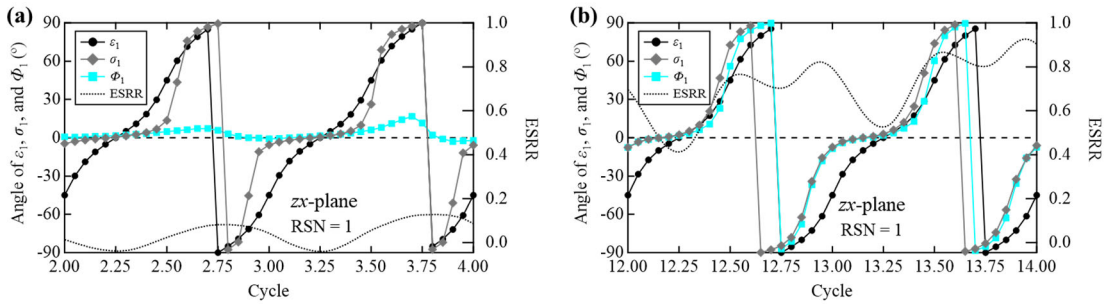

Fig. A. 21. Evolution of the projections of the directions of ε_1, σ_1, and Φ_1 on the *zx*-plane (e = 0.75), and their relationship with ESRR under Rayleigh-wave strain condition with RSN = 1 during: (a) 2–4 cycle; (b) 12–14 cycle.

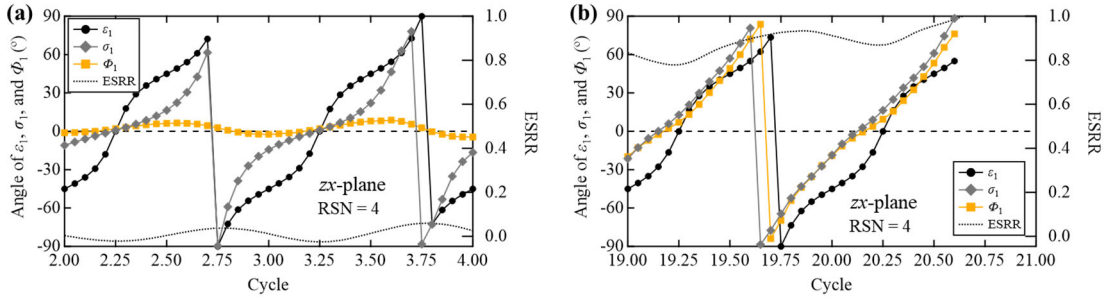

Fig. A. 22. Evolution of the projections of the directions of ε_1, σ_1, and Φ_1 on the *zx*-plane (e = 0.75), and their relationship with ESRR under Rayleigh-wave strain condition with RSN = 4 during: (a) 2–4 cycle; (b) 19–21 cycle.

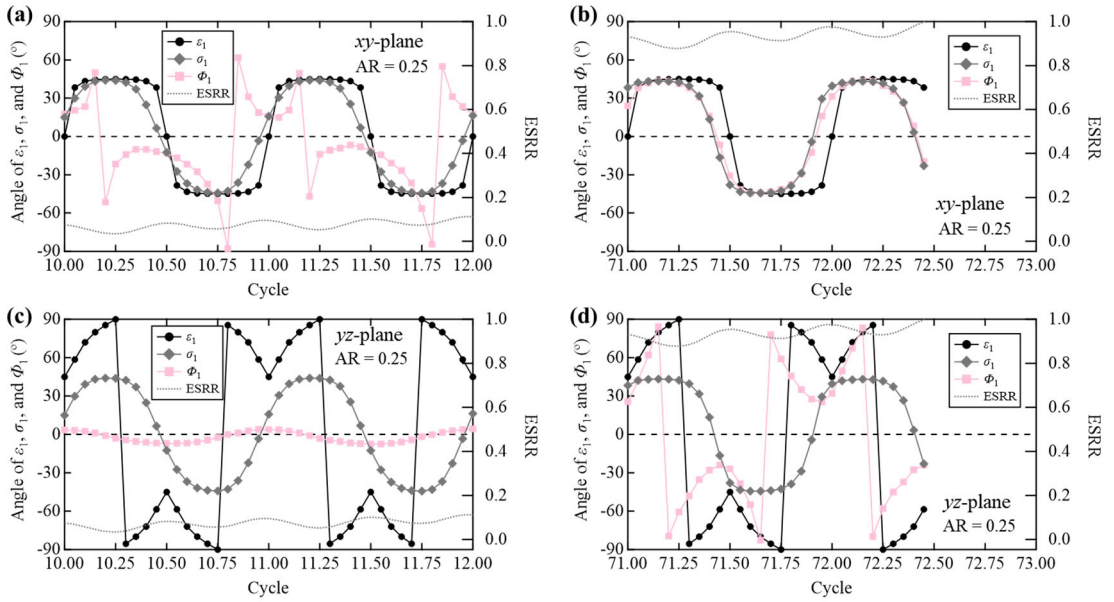

Fig. A. 23. Evolution of the directions of ε_1, σ_1, and Φ_1, and their relationship with ESRR under Love-wave strain condition with AR = 0.25 (e = 0.75): (a) projection on the *xy*-plane during 10–12 cycle; (b) projection on the *xy*-plane during 71–73 cycle; (c) projection on the *yz*-plane during 10–12 cycle; (d) projection on the *yz*-plane during 71–73 cycle.

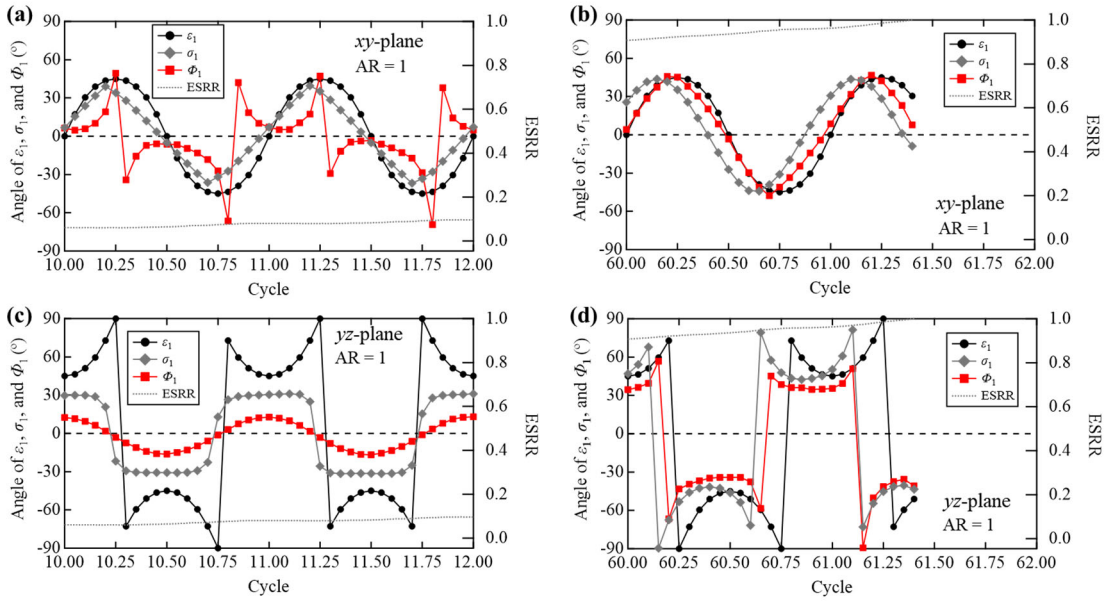

Fig. A. 24. Evolution of the directions of ε_1, σ_1, and Φ_1, and their relationship with ESRR under Love-wave strain condition with AR = 1 (e = 0.75): (a) projection on the *xy*-plane during 10–12 cycle; (b) projection on the *xy*-plane during 60–62 cycle; (c) projection on the *yz*-plane during 10–12 cycle; (d) projection on the *yz*-plane during 60–62 cycle.

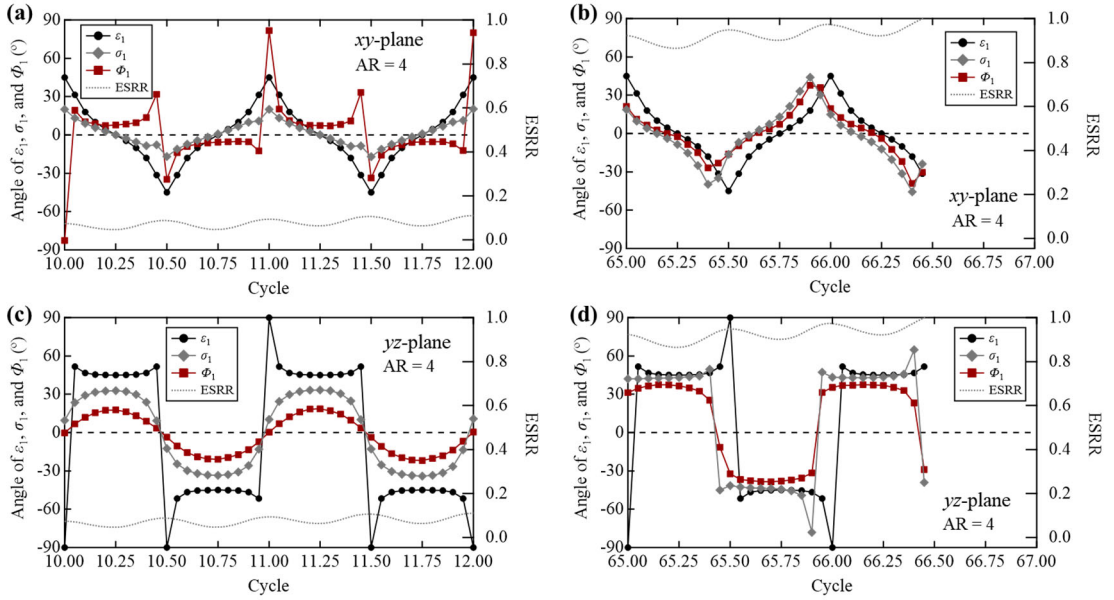

Fig. A. 25. Evolution of the directions of ε_1, σ_1, and Φ_1, and their relationship with ESRR under Love-wave strain condition with AR = 4 (e = 0.75): (a) projection on the *xy*-plane during 10–12 cycle; (b) projection on the *xy*-plane during 65–67 cycle; (c) projection on the *yz*-plane during 10–12 cycle; (d) projection on the *yz*-plane during 65–67 cycle.

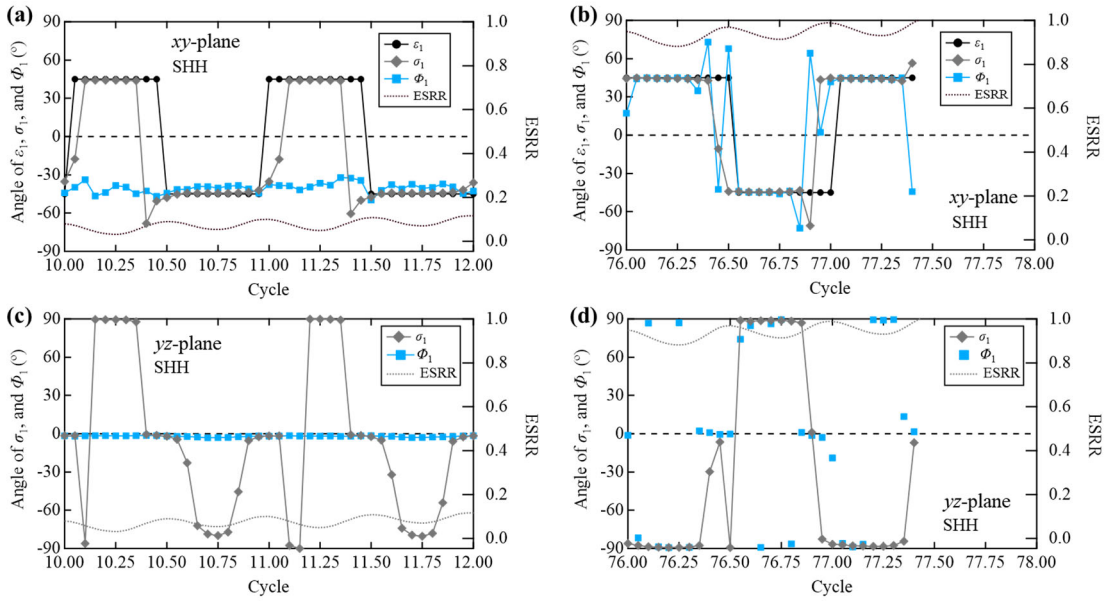

Fig. A. 26. Evolution of the directions of ε_1, σ_1, and Φ_1, and their relationship with ESRR under SHH-wave strain condition (e = 0.75): (a) projection on the *xy*-plane during 10–12 cycle; (b) projection on the *xy*-plane during 76–78 cycle; (c) projection on the *yz*-plane during 10–12 cycle; (d) projection on the *yz*-plane during 76–78 cycle.

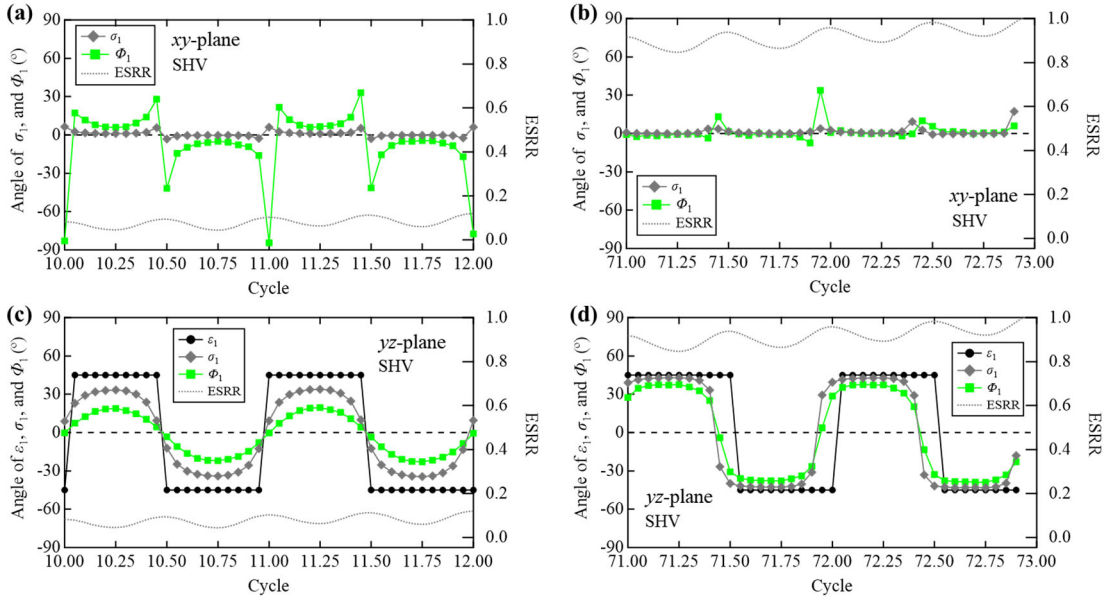

Fig. A. 27. Evolution of the directions of ε_1, σ_1, and Φ_1, and their relationship with ESRR under SHV-wave strain condition (e = 0.75): (a) projection on the *xy*-plane during 10–12 cycle; (b) projection on the *xy*-plane during 71–73 cycle; (c) projection on the *yz*-plane during 10–12 cycle; (d) projection on the *yz*-plane during 71–73 cycle.

APPENDIX III

The evolution of the magnitude and distribution of projection of normal contact forces on the *zx*-plane in the measurement cube of the specimen in undrained monotonic shear is illustrated here.

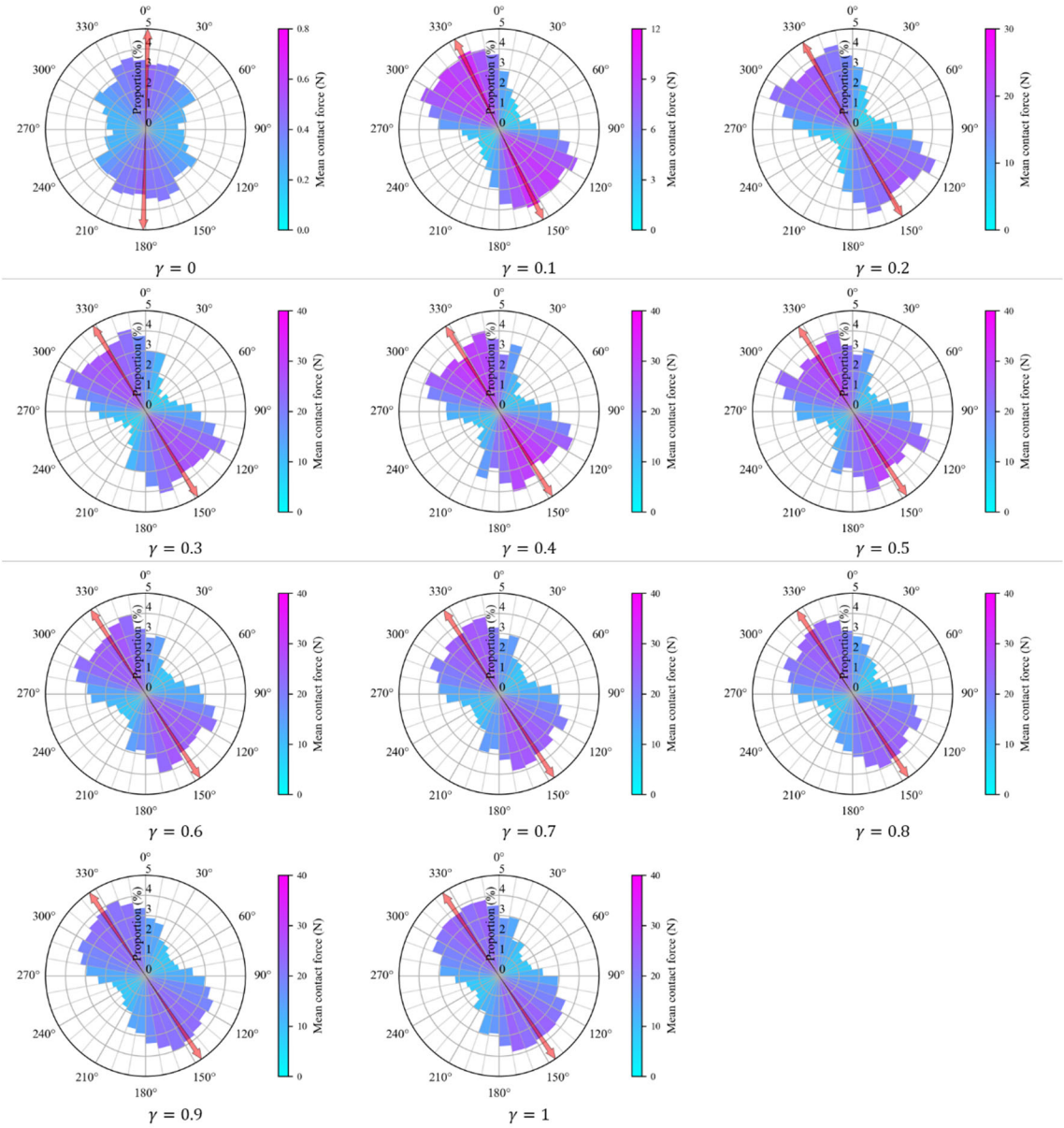

Fig. A. 28. Magnitudes and distributions of projection of normal contact forces on the *zx*-plane.